TECHNISCHE UNIVERSITÄT WIEN

VIENNA UNIVERSITY OF TECHNOLOGY

DISSERTATION

Hydrothermal Synthesis of Nanocrystalline Barium Titanate and the Production of thin Ceramic-Polymer Dielectric Films

ausgeführt zum Zwecke der Erlangung des akademischen Grades eined Doktors der technischen Wissenschaften unter der Leitung von

Ao. Prof. DI Dr. Roland Haubner
Institut 164
Institut für chemische Technologien und Analytik

eingereicht an der Technische Universität Wien
Fakultät für Technische Chemie

von

Amir Habib

Matrikelnummer 0427753

Haus Döbling
Vegagasse 20, E/709, pf 313
1190 Wien

Wien, Juli 2008

In The Name of Allah
The most Beneficient,
The most Merciful

ACKNOWLEDGMENT

KURZFASSUNG

BaTiO$_3$ Nanopartikel wurden mittels Hydrothermal und Solvothermische–Synthese hergestellt. Die Pulver wurden auf ihre Perovskitstruktur, Größe und Morphologie untersucht. Durch Variation der Syntheseparameter wie Temperatur, Reaktionszeit und Größe des TiO$_2$-Prekursors, konnten Wachstumsmechanismen für das BaTiO$_3$ aufgezeigt werden. Aus den Pulvern wurden dünne dielektrische Keramik-Polymer Filme für organische Feldeffekttransistoren hergestellt wobwi das BaTiO$_3$ als dielektrischer high-k Füllstoff in Polymethylmethacrylat (PMMA) dient.

Bei Verwendung der Hydrothermalsynthese reagierte feines TiO$_2$ Ausgangspulver aufgrund der größeren Oberfläche schneller. Höhere Reaktionstemperaturen und längere Reaktionszeiten erlaubten eine vollständige Umsetzung zu BaTiO$_3$. Die aus XRD-Messungen berechneten Kristallitgrößen des BaTiO$_3$ wurde mit steigender Synthesetemperatur geringer, wobei kein Einfluss der Reaktionsdauer festgestellt wurde. Proben welche bei niedrigeren Temperaturen hergestellt wurden zeigen einen Kern aus TiO$_2$ in BaTiO$_3$. Die Größe und Morphologie des BaTiO$_3$ wird auch vom TiO$_2$ Ausgangspulver beeinflusst. Aufgrund der Resultate wird ange- nommen, dass das BaTiO$_3$ durch direkte Reaktion oder durch Umkristallisation gebildet wird.

Die Verwendung von dünnem stäbchenförmigem TiO$_2$ in der Hydrothermalsynthese und TiO$_2$ (P25 Degussa) in der Solvothermen-Synthese führte zu BaTiO$_3$–Kristallitgrößen größer als die Korngröße des Ausgangspulvers. Dies kann durch Umkristallisation (lösen und abscheiden) erklärt werden. Phasenreines BaTiO$_3$ wurde aus Ethanol / Wassermischungen bei einem Barium : Titan Verhältnis 2 : 1 erreicht. Höhere Reaktionstemperaturen und längere Reaktionszeiten begünstigen die tetragonale BaTiO$_3$-Phase.

Durch die Funktionalisierung des BaTiO$_3$ Pulvers mit Polymethylmethacrylat co-methacrylsäure in Tetrahydrofuran oder Toluol oder Chlorbenzol reagieren Hydroxylgruppen am BaTiO$_3$ und die Oberflächenenergie kann herabgesetzt werden. Dies erlaubt die Herstellung stabiler Disper- sionen in PMMA. Dicke und dünne Schichten aus BaTiO$_3$ in PMMA wurden durch Dip-Coating oder Aufspinnen hergestellt und die Anteile an Füllstoff und PMMA in den Filmen wurde variiert. Durch BaTiO$_3$ im Polymer konnte die Dielektrizitätskonstante deutlich erhöht werden.

Bei 20 Vol.% BaTiO$_3$ in PMMA und 3.25 Gew.% PMMA in THF wurde bei Filmen mit etwa 300 nm Dicke eine Dielektrizitätskonstante von 9 und eine Kapazität von 32 nF/cm^2 bei 10 kHz gemessen. Die Oberflächenrauhigkeit dieser Schichten beträgt 50 bis 70 nm. Ein Anstieg der Dielektrizitätskonstante wurde auch beobachtet wenn tetragonals BaTiO$_3$ (~ 120 nm) anstelle von kubischem BaTiO$_3$ (~ 60 nm) verwendet wird. Der dielektrische Verlust beträgt 0.04 bei 10 kHz.

ABSTRACT

BaTiO$_3$ nanoparticles are synthesised via hydrothermal and solvothermal route. The powders are characterised for their perovskite structure, size and morphology. Changes in synthesis parameters like temperature, time, and particle size of titania precursor give an insight into BaTiO$_3$ formation mechanism. Barium titanate powders are used as nanofillers in Poly(methylmethacrylate) (PMMA) for fabrication of thin high-k gate dielectric films for organic field effect transistors.

Using the hydrothermal route fine grained TiO$_2$ precursor reacted faster due to large surface area for reaction of Ba with TiO$_2$. Higher reaction temperatures and longer reaction time helped to complete the reaction to BaTiO$_3$. The crystallite size of BaTiO$_3$ calculated from XRD measurements is observed to decrease at higher temperature, while no trends regarding the dependence of crystallite size on time can be predicted. Samples synthesized at low temperature shows unreacted core of TiO$_2$ in BaTiO$_3$, while size and morphology of BaTiO$_3$ depend on the initial TiO$_2$ precursor. This suggests an in-situ transformation mechanism or short range dissolution-precipitation for the growth of BaTiO$_3$ from particulate precursors.

The use of spindle like TiO$_2$ in hydrothermal synthesis and TiO$_2$ (P25 Degussa) in solvothermal synthesis resulted in BaTiO$_3$ crystal size larger than the initial titania precursor which can be explained by a dissolution-precipitation crystal growth. In solvothermal synthesis with equal ethanol / water contents use of barium to titanium ratio equal to 2 results in phase pure BaTiO$_3$. High reaction temperature and longer reaction time favours tetragonal phase stability of BaTiO$_3$.

The post functionalization of BaTiO$_3$ nanofillers with Poly(methylmethacrylate-co-methacrylic acid) in tetrahydrofuran or toluene or chlorobenzene helped to reduce surface energies of nanoparticles by weak interactions of methacrylic acid to BaTiO$_3$ hydroxyl groups. This leads to stable dispersions in PMMA. Thick and thin films are obtained using dispersions at various filler fraction of BaTiO$_3$ in PMMA and different weight percent PMMA in solvent by dip coating and spin on technique at different speeds. Inclusion of BaTiO$_3$ in polymer nanocomposite resulted in increase in dielectric constant of thin films

At 20 % volume fraction of BaTiO$_3$ in PMMA and 3.25 % weight fraction of PMMA in THF a dielectric constant of 9 and capacitance density of 32 nF/cm^2 at 10 kHz is achieved in thin film (approx. 300 nm). The surface roughness of such layers remains around 50 nm to 70 nm. An increase in dielectric constant is observed for thick and thin films at lower filler loadings when tetragonal BaTiO$_3$ (approx. 120 nm) is used instead of cubic BaTiO$_3$ (approx. 60 nm). The dielectric loss for the layers remains as low as 0.04 at 10 kHz.

TABLE OF CONTENTS

1 Introduction

1.1 Aim of the Work: Improvement of organic field effect transistors by new high-K composite dielectrics

One important goal in the development of organic field effect transistors (OFETs) is the lowering of the gate voltage needed to

1. Increase the source-drain-current on its maximum by attaining higher concentration of accumulated charge carriers in the source-drain channel.

2. Avoid leakage source to drain currents while the transistor is in off mode.

High mobilities can be achieved at low operating voltages in pentacene IGFETs, when relatively high dielectric constant gate insulators are used [1]. One way to achieve this is to replace the currently used dielectrics by new materials. Simple oxides such as ZrO_2, HfO_2 and complex oxides such as $BaTiO_3$ or $SrTiO_3$ are used as high-k dielectrics. Using materials with a high dielectric constant enables the formation of layers, which are equally thin as the currently used dielectrics, but showing a greater physical thickness. Materials having perovskite structure e.g. $BaTiO_3$ are often used as gate insulators. $BaTiO_3$ layers are prepared by using sputtering or by sol-gel method. Since the layers prepared by the latter method can only be transformed into crystalline state by using thermal treatment, the preparation of dielectric layers on the organic substrate is not possible. The preparation of $BaTiO_3$ layers by using the first method is cost intensive and disadvantageous regarding the more exact tailoring of the particle properties. The $BaTiO_3$ were successfully synthesised using hydrothermal crystallization technique, the layers obtained by using hydrothermal method are not homogeneous and bear weak mechanical stability. Until now, no synthesis method of $BaTiO_3$-PMMA composites used as dielectrics in OFETs has been reported. Due to the comparably better dielectric properties of the perovskites it is foreseen to replace current dielectric layers by layers consisting of $BaTiO_3$ particles embedded in a PMMA matrix. To synthesise a dielectric $BaTiO_3$-PMMA layer offering good mechanical stability to the organic substrate at low temperatures, a preparation route consisting of hydrothermal crystallization of $BaTiO_3$ nanoparticles followed by dispersing them in PMMA matrix can be used. The most critical step in the formation of the above described organic-inorganic hybrid materials is the bonding between the inorganic particles and the organic matrix. It is therefore, necessary to modify the surface of $BaTiO_3$ particles to better link to the polymer matrix.

1.2   Organic field effect transistors

Organic field-effect transistors (OFETs) were first described in 1987 [2]. OFETs adopted the architecture of thin-film transistors (TFTs). Organic TFTs alias OFETs are just one class of organic devices, of which rectifiers, light-emitting diodes, photo detectors, solar cells, electro-optic switches and sensors are other representative examples [3].

OFETs now compete with amorphous silicon FETs [2], are expected to be a post-silicon technology. OFETs have received considerable attention recently because they can be fabricated at reduced temperature and potentially reduced cost compared to hydrogenated amorphous silicon thin-film (a-Si:H) transistors. Low fabrication temperature allows a wide range of substrate possibilities and makes OTFTs an attractive technology for many low-cost electronics applications, particularly those that require or may benefit from flexible polymeric substrates such as radio frequency identification tags, smart cards, electronic paper, and flat panel displays [4, 5]. Organic field-effect transistors (OFETs) are based on solution-processible polymers as well as small molecular semiconductors .These devices have been developed to realize low-cost, large-area electronic products [1].

The basic operating scheme of an OFET is given in Fig. 1.
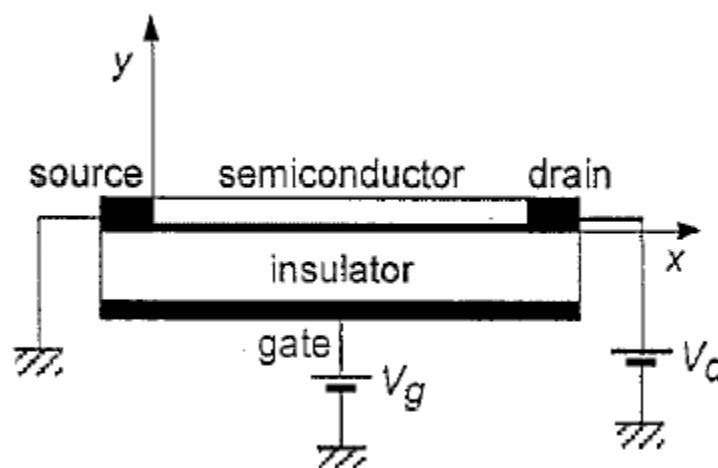
Figure 1-1   Schematic view of an organic field effect transistor

A field-effect transistor is basically a capacitor, where one plate is constituted by the gate electrode, and the other one by the semiconducting film [6]. When a voltage V_g is applied between source and gate, majority carriers accumulate at the insulator semiconductor interface, leading to the formation of a conducting channel between source and drain. If we restrict ourselves to low drain voltages V_d, the induced charge remains nearly constant all along the conducting channel, and the drain current I_d, is given by Equation given below, where Z and L are the channel width and length, C_i, is the capacitance of the insulator, μ the field-effect mobility, and V_0 the so-called threshold voltage that accounts for voltage drops of various origin across the insulator-semiconductor interface.

$$I_d = \frac{Z}{L} C_i \mu (V_g - V_0) V_d$$

The transconductance g_m which is defined as the derivative of I_d, with respect to V_g, Equation below, can be used to estimate the field-effect mobility at low V_d.

$$g_m = \frac{\partial I_d}{\partial V_g} = \frac{Z}{L} C_i \mu V_d$$

It is clearly evident that the mobility is gate voltage dependent, and the above equations are valid for $V_d \ll V_g$ only [6].

A generic embodiment of a OFETdevice is shown in Figure 1-2 (a) bottom and (b) top contact geometries. The 'off' state is defined as the case of little or no current flowing between the source and drain electrodes at a given source–drain voltage, while the 'on' state refers to the case where substantial source–drain current flows at that voltage. Switching between the two states is accomplished by the application and removal of an electric field from the gate electrode across the gate dielectric to the semiconductor–interface, effectively charging a capacitor.

When the OFET operates in the so-called accumulation mode, the charges injected from the source, are mobile and conduct the source–drain 'channel' current. For 'p-type' semiconductors, where the organic molecules would be considered electron donors, the carriers are holes, while electron-accepting organics are 'n-type' and form channels of electrons. In absence of a gate field, there is no channel and ideally no source–drain conduction. In practice, however, there can
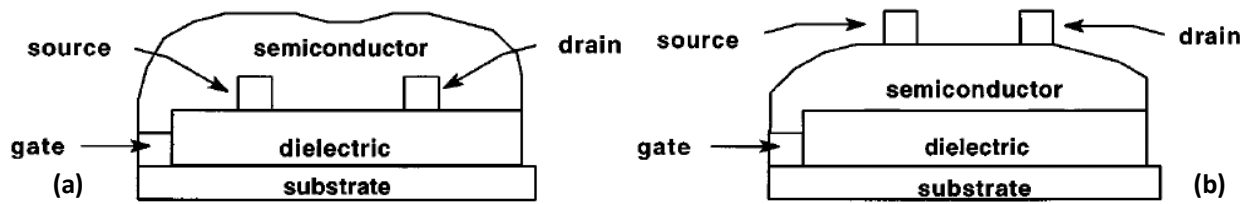
Figure 1-2   Schematic structure of an organic FET with (a) 'bottom' and (b) 'top contact' geometry. The substrate is conductive. The dielectric could be SiO_2 / PMMA / polymer nanocomposite. The source, drain and gate contacts are typically gold, but other metals or conductive composites can be used. Organic semiconductor can be pentacene or others conducting polymers

be adventitious off-currents caused by impurities in the semiconductor and by leakage pathways [3]. Because of relatively low mobility of the organic semiconductor layers, OFETs cannot rival the materials and technology used in applications requiring very high switching speeds, however organic semiconductors like pentacene and thiophene oligomers have exhibited the OFETs performance with good environmental stability [1].

Pentacene TFTs have produced the highest field-effect mobility values reported for organic semiconductor insulated gate field effect transistors (IGFETs), which in some cases are greater than 0.6 $cm^2V^{-1}s^{-1}$ and on/off current ratio (I_{on}/I_{off}) of 10^8. These values of mobility and on/off ratios are similar to the ones reported for hydrogenated amorphous silicon (a-Si:H) TFT. However, the operating voltage required to achieve such high performance from pentacene devices is too high (a voltage swing from -100 V to +100 V is required) in comparison with a-Si:H and for practical applications in general [1].

1.3   Explanation of the problem and remedy

Dimitrakopoulos et al. [1] studied the gate voltage dependence of mobility in pentacene devices. They demonstrated that high performance pentacene IGFETs can exhibit high mobility and good current modulation at low operating voltage, when relatively high dielectric constant gate insulators are used. The gate voltage dependence in these devices is attributed to higher concentration of the charge carriers accumulated in the channel instead of the gate field.

Due to the higher charge carrier densities, that are induced at the insulator-semiconductor interface by high-k dielectrics, the supply voltage can be reduced without scaling down the channel lengths [7].

For materials with higher dielectric constant, the capacitance of dielectric will be higher as per following relation;

$$C = \varepsilon_0 \varepsilon_r t / A$$

As well according to basic principal of capacitors

$$V = Q/C$$

The capacitor with larger capacitance needs lower voltage to accumulate high charge. The choice of high dielectric material instead of presently used dielectrics will help to accumulate enough charge at the semiconductor-insulator interface to draw maximum source drain current at low gate voltage without leakage current in off mode of the transistor.

2   Literature

2.1   Barium titanate

After the discovery of ferroelectricity in barium titanate in the 1940s [8], barium titanate has been an extensively studied and widely utilized electroceramic. Nowadays multilayer ceramic capacitors (MLCCs) based on $BaTiO_3$ are one of the most important electronic components in surface mounted electronic circuits. Common electronic appliances contain many MLCCs, *e.g.*, a typical watch contains 2 to 4, a video camera or cell phone 250, a laptop computer 400 and an automobile over 1000 [9].

It has a perovskite structure ABO_3 (Figure 2-1) in which positively charged A cations (blue- Ba) and negatively charged O anions (red- Oxygen) occupy body-centered cubic lattice sites, while smaller B cations (green-Ti) occupy an interpenetrating lattice in which they are surrounded by six oxygens in an octahedral arrangement.
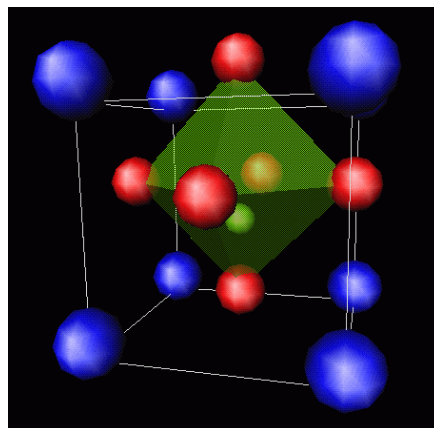
Figure 2-1 ABO_3 perovskite structure (blue- barium, red- oxygen, green- titanium)

$BaTiO_3$ is a polymorph and undergoes crystalline phase transitions with temperature:
Rhombohedral -90 ˚C$\rightarrow$ orthorhombic 0 ˚C $\rightarrow$ tetragonal 120 ˚C$\rightarrow$ cubic 1460 ˚C$\rightarrow$ hexagonal [10].

Because of the practical temperature ranges, the tetragonal phase and the tetragonal to cubic phase transition region are important. The tetragonal to cubic transition temperature is usually called a Curie point. The Curie point is generally located between 120 ˚C and 130 ˚C. In the temperature range for the cubic phase, i.e., above the Curie point, the ideal perovskite structure

of a cubic and symmetrical unit cell is stable. Between 0 ˚C and 130 ˚C, $BaTiO_3$ shows a distorted perovskite structure in which the Ti^{4+} and O^{-2} ions are displaced in the opposite direction from their original positions, whereas the barium ion does not change its position. This result in a large change of the Ti-O bond length compared to a small change in the Ba-O bond during the cubic to tetragonal phase changes [9]. A perovskite lattice structure, the displacement of the Ti^{4+} and O^{2-} ions and the slight distortion of oxygen octahedral during the cubic to tetragonal phase transition are shown in Figure 2-2.
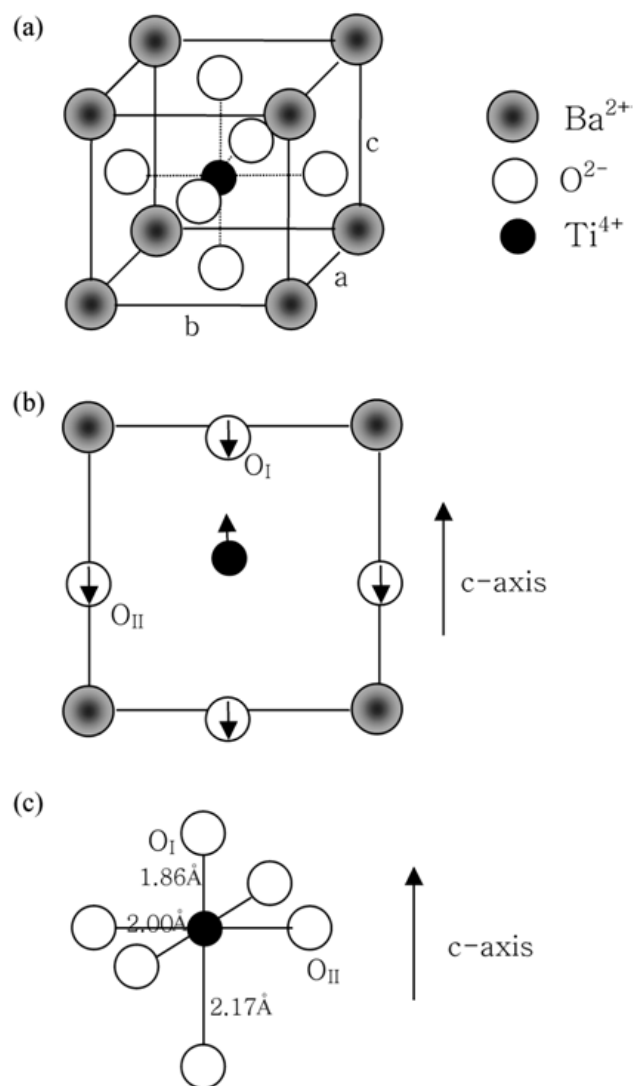
Figure 2-2   (a) Perovskite structure of $BaTiO_3$ above Curie point, (b) a-axis projection of tetragonal $BaTiO_3$ with atomic displacements, and (c) change in lattice along c-axis [9]

These ionic displacements also result in a change in lattice dimensions, and a negative linear thermal expansion coefficient along the c-axis, while a thermal expansion coefficient is usually positive due to a-, b-axes expansion. As shown in Figure 2-3, the crystal structure of $BaTiO_3$ becomes less and less tetragonal as the temperature increases toward the tetragonal to cubic transition temperature [11]. Cubic $BaTiO_3$ shows paraelectric properties, while tetragonal $BaTiO_3$ shows ferroelectric properties which are more interesting properties of $BaTiO_3$ for dielectric applications. The relative dielectric constant variations along a-, b- and c-axes of the single crystalline $BaTiO_3$ are given in Figure 2-4.
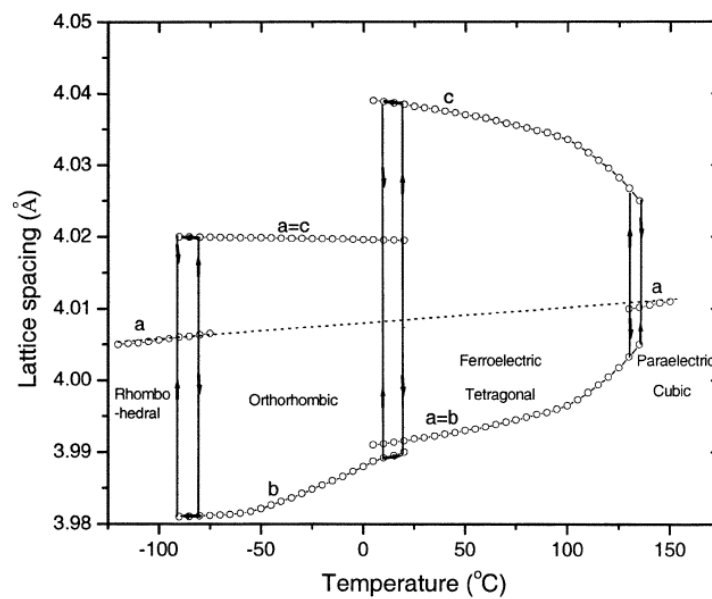
Figure 2-3   Lattice parameters of single crystal $BaTiO_3$ as a function of temperature [11].
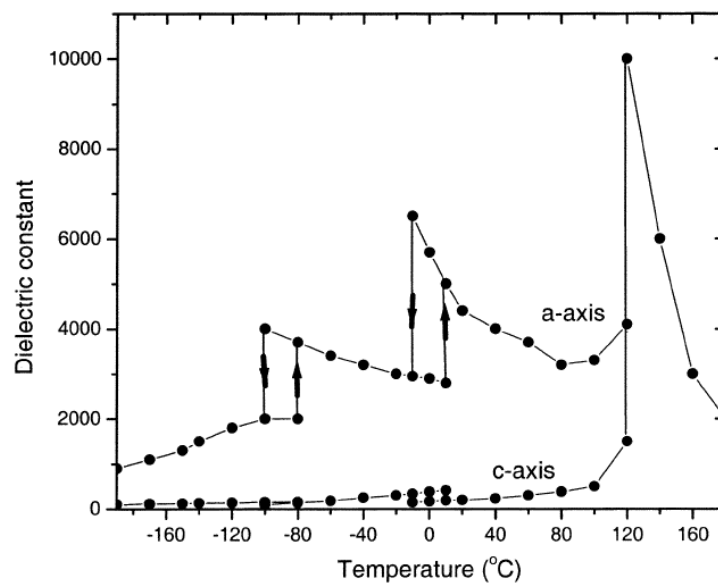
Figure 2-4:   Relative dielectric constant ε_a and ε_c for single crystal $BaTiO_3$ as a function of temperature [12].

The dielectric constant along the c-axis is less than that along the a-axis may be due to the fact that oxygen ions in the c-axis, which is also cell polar axis, make strong ionic attractions with the center Ti^{4+} ion. This gives an interaction force between the Ti^{4+} and O^{2-} ions which makes vibration difficult because of a "pinning" effect under an external AC source. On the other hand, oxygen ions in the a- and b-axes are relatively free to vibrate perpendicularly to this c-axis; consequently, the dielectric constants along a- and b-axes are higher. In the vicinity of the Curie point, the stability of the lattice decreases and the amplitude of the vibration become higher. This induces a high dielectric constant at the Curie point. The dielectric constant of polycrystalline, non-polarized $BaTiO_3$, is an average of both curves in Figure 2-4 due to the random orientation of the individual crystals [12].

Although the basic dielectric properties of $BaTiO_3$ are well known, but the physical parameters related to the phase transition are affected by chemical purity, surface defects, particle size and sintering conditions [13, 14].

Ferroelectricity is a reversible spontaneous polarization in the absence of an electric field. Spontaneous polarization in a ferroelectric arises from a noncentrosymmetric arrangement of ions in its unit cell that produces an electric dipole moment. Adjacent unit cells tend to polarize in the same direction and form a region called a ferroelectric domain. Above the Curie temperature, these materials have a centrosymmetric structure and therefore lose all spontaneous polarization i.e., paraelectric. As the temperature is lowered through the Curie point, a phase transformation takes place from the paraelectric state to the ferroelectric state. The center ion is displaced from its body-centered position and the cubic unit cell deforms to assume one of the noncentrosymmetric structures such as tetragonal, rhombohedral or monoclinic structures. When an alternating electric field is applied to a ferroelectric, the polarization shows a hysteretic behavior with the applied field Figure 2-5. In this initial stage, the ferroelectric domains that are oriented favorably with respect to the applied field direction grow at the expense of other domains. This continues until total domain growth and reorientation have occurred. At this stage, the material has reached its saturation polarization P_{sat}. If the electric field is then removed, some of the domains do not return to their random configurations and orientations. The polarization at this stage is called the remnant polarization, P_r. The strength of the electric field required to return the polarization to zero is the coercive field, E_c [15].
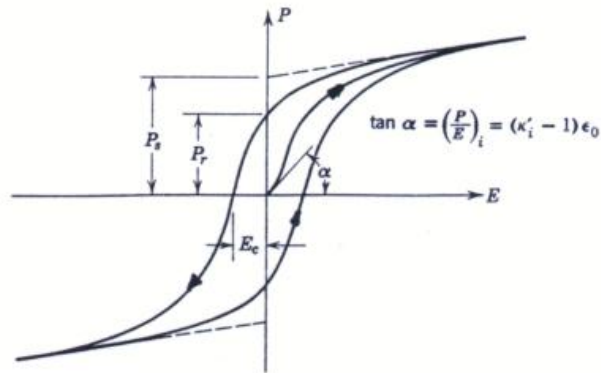
Figure 2-5   A typical ferroelectric hysteresis loop

2.1.1   Hydrothermal synthesis of BaTiO$_3$

Hydrothermal synthesis is a useful method for preparing a myriad of ceramic materials e.g., ferroelectric and relaxor from different precursors e.g., oxides, nitrates and alkoxides. The hydrothermal synthesis is attractive for powder synthesis because the combined effects of solvent, temperature, and pressure on ionic reaction equilibria can form desirable products while inhibiting the formation of undesirable compounds. It also helps to get anhydrous powders in single process step and does not require elaborate apparatus or expensive reagents [16-18].

Hydrothermal synthesis involves reactions, mostly of ionic nature between heterogeneous phases. The interaction between solid and fluid phases determines the physical characteristics of the powder. Therefore, the powder properties can be controlled by using chemical process variables such as temperature, pressure, reactant concentration, pH, etc.

The outstanding dielectric and ferroelectric properties of barium titanate make it desirable primary material for a variety of applications including multilayer ceramic capacitors, thermistors and electro optic devices [19].

A great interest is shown in controlled synthesis of well crystalline BaTiO$_3$ powder with suitable particle size, uniform size distribution and morphology. Hydrothermal synthesis is attractive due to its feature such as single step process and high-yield of the anhydrous product.

Extensive research has been directed towards hydrothermal synthesis of $BaTiO_3$. The resulting product is usually a metastable cubic perovskite with particles size below 1.0 µm under special conditions temperature and time [19].

There are various method of fine powder preparation, including co precipitation, spray drying, freeze drying, sol gel and hydrothermal processes. Among these methods the hydrothermal process is very attractive. It is a bottom up approach, where fine particles are formed from much smaller particles, such as clusters, molecules, ions and atoms [20, 21].

The hydrothermal approach could become very interesting for finer powder preparation because of low temperature synthesis and non agglomerated powders.

In the beginning the hydrothermal synthesis of $BaTiO_3$ was performed at relatively elevated temperatures of 380 ˚C to 500 ˚C and pressures of 300 atm to 500 atm [22]. However, later the synthesis temperature decreased drastically to 85 ˚C at equilibrium water vapour pressure (15-65 atm.) [23, 24]. In general hydrothermal method has the potential for producing extremely fine particles with high crystallinity, high purity and narrow size distribution. In this method an aqueous $Ba(OH)_2$ solution with suspended TiO_2 fine particles is hydrothermally treated and $BaTiO_3$ is formed dissolution-deposition route; i.e., $Ba(OH)_2$ reacts with titania under hydrothermal conditions to form $BaTiO_3$. During the process the concentrations of cations and hydroxide must increase to the super saturation range where the nucleation products are stable. Then the monodispersed grains are formed by subsequent uniform growth on the existing nuclei, which were provided by adsorption of solute species, agglomeration and Ostwald ripening [25]. Thus the dissolution of TiO_2 particle affects the super saturation range, the nucleation and the growth of $BaTiO_3$ particles. The dissolution rate of titania and its constituent to a great extant governs the formation of $BaTiO_3$ monodispersed grains [26]. However, once the nuclei of $BaTiO_3$ from the supersaturation solution are formed, the aqueous suspension is only stable under strongly alkaline conditions at pH $\geq$ 13. Otherwise, due to the thermodynamic instability of $BaTiO_3$ in water complete decomposition of $BaTiO_3$ to TiO_2 and $Ba(OH)_2$ is expected. In practice, however, usually thin but water impermeable layers of TiO_2 are formed on the surface of $BaTiO_3$ particles which prevents the $BaTiO_3$ grains from complete disintegration. In an aqueous suspension of hydrothermally processed $BaTiO_3$ Ba leaching is expected due to higher surface area of smaller sized grains.

2.1.2 Thermodynamic modelling of hydrothermal synthesis of BaTiO₃

Lencka et al. [17] presented thermodynamic model of electrolyte solutions in 1993, thereby giving the stability diagrams for the hydrothermal synthesis of $BaTiO_3$ to predict the optimum synthesis conditions (i.e., feedstock composition, pH, temperature and pressure) to minimize the need for trail-and-error experimentation. These diagrams show the regions of reagent concentrations and pH for which various species predominate in the system indicating thermodynamically stable products. The stability diagrams show predominance fields for several species as a function of pH and total molality of reactant species in the solution at constant temperature. All possible reactions that may occur in the hydrothermal medium are summarized in Table 2-I.

Table 2-I   Relevant equilibiria in the Ba-Ti hydrothermal system

Relevant Equilibiria in the Ba-Ti Hydrothermal System	
1	$H_2O \leftrightarrows H^+ + OH^-$
2	$H_2O(g) \leftrightarrows H_2O$
3	$TiO_2(s) + OH^- \leftrightarrows HTiO_3$
4	$Ba(OH)_2(s) \leftrightarrows Ba^{2+} + 2OH$
5	$BaOH^+ \leftrightarrows Ba^{2+} + 2OH$
6	$BaTiO_3 + H_2O \leftrightarrows Ba^{2+} + 2OH^- + TiO_2$
7	$Ba(OH)_2 \cdot 8H_2O \leftrightarrows Ba^{2+} + 2OH^- + 8H_2O$
8	$BaO(s) + 2H^+ \leftrightarrows Ba^{2+} + H_2O$
9	$Ba_2TiO_4(s) + 2H_2O \leftrightarrows 2Ba^{2+}\ 4OH^- + TiO_2(s)$
10	$CO_2(g) \leftrightarrows CO_2(aq)$
11	$CO_2(aq) + H_2O \leftrightarrows H^+ + HCO_3^-$
12	$HCO_3^- \leftrightarrows H^+ + CO_3^{2-}$
13	$BaCO_3(aq) \leftrightarrows Ba^{2+} + CO_3^{2-}$
14	$BaHCO_3^+ \leftrightarrows Ba^{2+} + HCO_3^-$
15	$Ti^{4+} + H_2O \leftrightarrows TiOH^{3+} + H^+$
16	$TiOH^{3+} + H_2O \leftrightarrows Ti(OH)_2^{2+} + H^+$
17	$Ti(OH)_2^{2+} + H_2O \leftrightarrows Ti(OH)_3^+ + H^+$
18	$Ti(OH)_3^+ + H_2O \leftrightarrows Ti(OH)_4(aq) + H^+$
19	$Ti(OH)_4(aq) \leftrightarrows TiO_2(s) + 2H_2O$

The standard state thermodynamic properties were used to construct stability diagrams for Ba-Ti system. They calculated stability diagrams showing which species predominate at a given T, pH, and total concentration of either Ba (mBa_T) or Ti (mTi_T) assuming autogenous pressure in all cases. The stability diagrams were obtained by solving the equilibrium and balance equations for different input concentrations to cover the whole mBa_T vs. pH or mTi_T vs. pH plane. Calculations were performed at 25 ˚C and 90 ˚C. Figure 2-6 and Figure 2-7show the results obtained using the complete thermodynamic model (solid lines) and results using the ideal solution approximation at 25 ˚C and 90 ˚C respectively.

The boundaries between aqueous Ba^{2+} and solid $BaTiO_3(s)$, aqueous Ba^{2+} and $BaOH^+$, and aqueous $BaOH^+$ and solid $BaTiO_3(s)$ are shown in the figures. Solution non-ideality has an important effect on the location of phase boundaries.
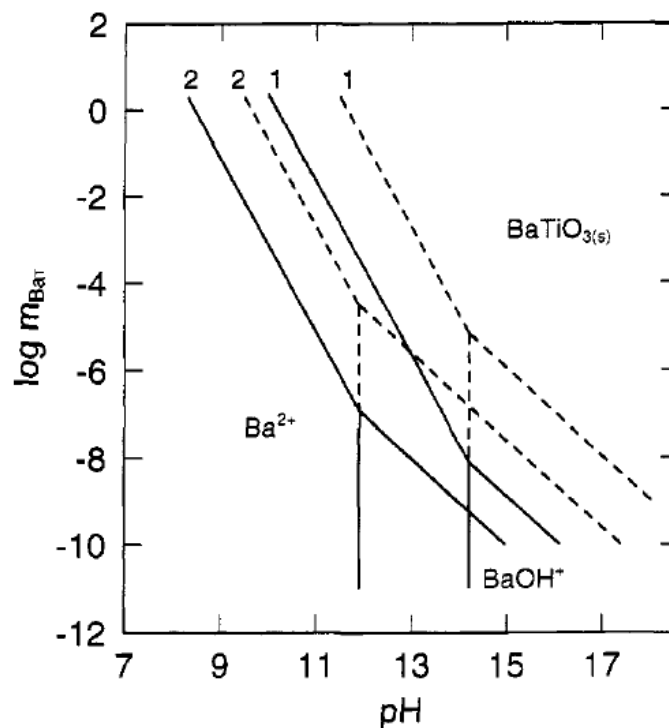
Figure 2-6   Calculated stability diagram for the Ba-Ti hydrothermal system using an ideal-solution approximation at 25 ˚C (1) and 90 ˚C (2). The solid and dashed lines denote the results obtained using the data from two different sources.
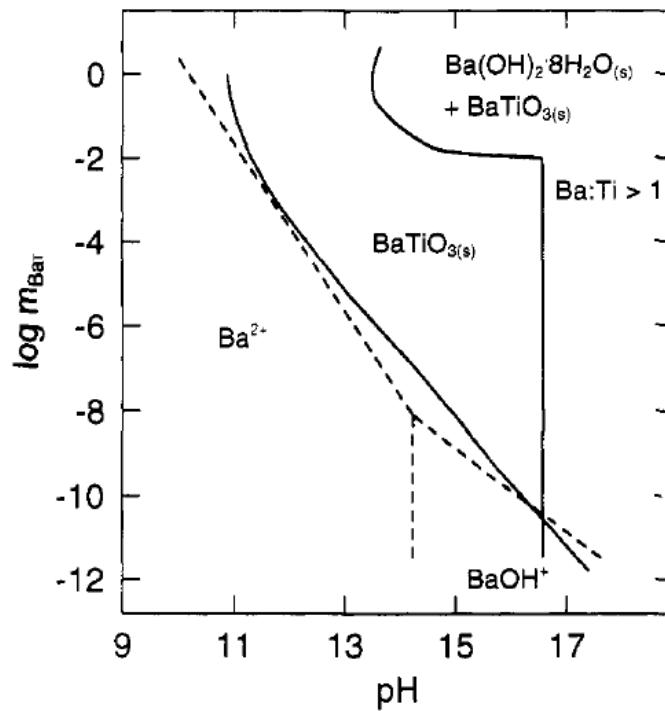
Figure 2-7   Calculated stability diagram for the Ba-Ti system at 25 ˚C, using modelled activity
coefficients for comparison, the ideal-solution results are shown as dashed lines.
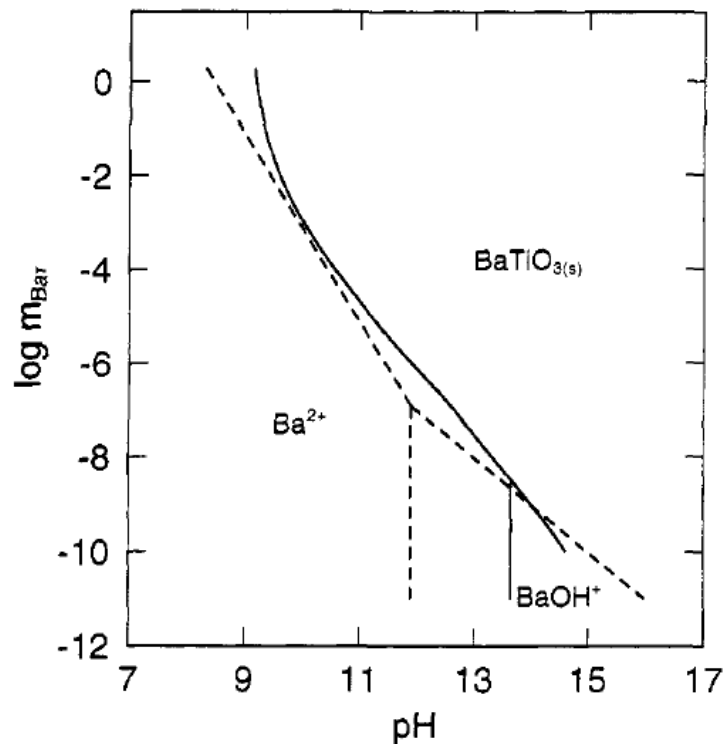
Figure 2-8   Calculated stability diagram for the Ba-Ti system at 90 ˚C using modelled activity
coefficients, for comparison the ideal-solution results are shown as dashed lines.

The stability diagrams illustrate the effect of process variables such as mBa_T, pH, T and the Ba/Ti ratio on the synthesis of barium titanate. $BaTiO_3(s)$ can be obtained in the whole range of mBa_T provided that pH is appropriately chosen. The higher is the total concentration of Ba in the solution (mBa_T), the lower can be the pH to cause the precipitation of $BaTiO_3(s)$. For example, pH that is necessary to precipitate $BaTiO_3(s)$ from a 1molal solution of barium is 9.2 at 90 ˚C; it increases to 11.2 for a 10^{-5} molal solution of barium.

$Ba(OH)_2(s)$ is the most obvious feedstock, along with titanium dioxide $TiO_2(s)$ to synthesis barium titanate $BaTiO_3(s)$. However an aqueous solution of $Ba(OH)_2(s)$ may not be sufficiently alkaline for the synthesis of $BaTiO_3(s)$ Figure 2-9. If mBa_T is greater than 0.0017 pt 'A' (Figure 2-9) , the alkalinity of a $Ba(OH)_2(s)$ solution is sufficient for the preparation of $BaTiO_3(s)$. For lower values of mBa_T, additional mineralizers, such as NaOH or KOH should be added.
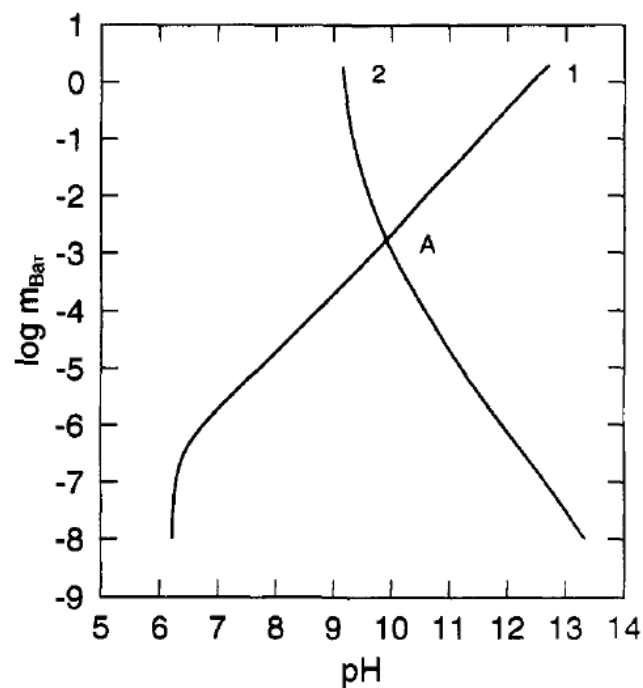
Figure 2-9   Comparison of the pH of a $Ba(OH)_2(s)$ solution (curve 1) with the pH that is necessary to precipitate $BaTiO_3(s)$ from the solution (curve 2).

The formation of $BaTiO_3(s)$ consumes equimolar amounts of Ba and Ti (Ba : Ti = 1). If different relative amounts of Ba and Ti are used (Ba : Ti ≠ 1), the location of phase boundaries does not change, however, the Ba to Ti ratio may have important effect on the synthesis. The excess amount of Ti (Ba : Ti < 1) will cause contamination of $BaTiO_3(s)$ with $TiO_2(s)$, which is stable in

hydrothermal conditions. Moderate excess amounts of barium (Ba/T > 1) will increase the pH of the solution, which is desirable for the hydrothermal synthesis as it makes it possible to avoid the use of mineraliser. However, the excessive amount of barium may cause precipitation of other undesirable species like barium carbonate.

The phase boundaries are shifted towards lower pH values with an increase in temperature. Also, the temperature determines the appearance or disappearance of additional solid species (e.g., $Ba(OH)_2 \cdot 8H_2O(s)$). In comparison with temperature, the pressure has a minor effect because all reactions involved in the synthesis proceed in a condensed phase with limited compressibility.

Figure 2-10 show stability diagrams for Ti-H_2O system as a function of solution pH at 90 ˚C. $Ti(OH)_2^{2+}$ is the predominant species for pH < 2.45 whereas $Ti(OH)_4(aq)$ is predominant for pH >2.45. Also, $Ti(OH)_3^{+}$ occurs in significant, although smaller, quantities for 1 > pH < 4.6. For the conditions of practical hydrothermal synthesis (i.e., pH > 9 and $mTi_T > 10^{-5}$ m), $TiO_2(s)$ is stable. This confirms that the ratio Ba to Ti should not be smaller than one to avoid the contamination of $BaTiO_3(s)$ with remaining $TiO_2(s)$ [17].
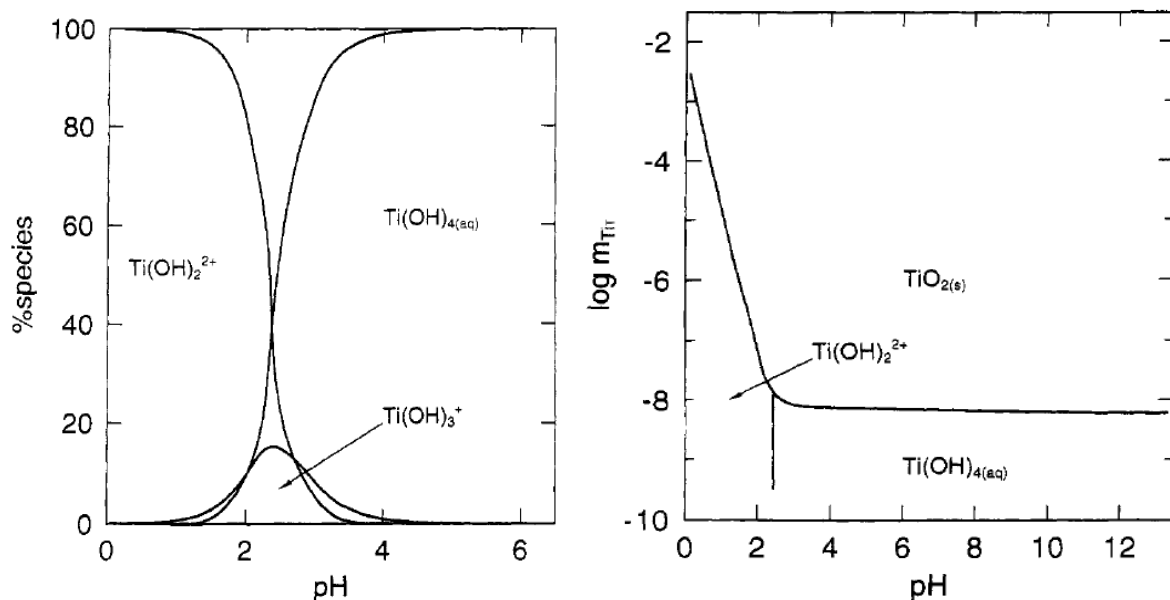
Figure 2-10 Calculated phase stability diagram for Ti-H_2O system at 90 ˚C

Effect of CO_2 (g) on the synthesis of $BaTiO_3$(s) is reported as CO_2 (g) acts as a contaminant because of its appreciable concentration in the atmosphere. Using standard state data for $BaCO_3^-$(s), $BaCO_3$(aq), CO_2(aq), $BaHCO_3^+$, HCO_3^-, CO_3^-, H_2O(g) and CO_2(g) calculations done by Lencka and Riman [17] for open system and for reactions proceeding in a closed system (i.e., autoclave with about 20 % of its volume filled with air containing atmospheric carbon dioxide.). The results obtained for an open system showed that desired $BaTiO_3$(s) does not form at all because $BaCO_3$(s) is inherently more stable. In the closed system Figure 2-11, which drastically reduces the availability of CO_2(g), $BaCO_3$(s) tends to precipitate at concentrations of Ba higher than ca. 10^{-5} molal. $BaCO_3$ precipitate at lower pH values than those needed to precipitate $BaTiO_3$(s) Figure 2-11. Therefore, the precipitated $BaTiO_3$(s) will be always contaminated with some amount of $BaCO_3$(s) if the solution is concentrated with respect to Ba (i.e., if $mBa_T > 10^{-5}$). This suggest that the exposure to CO_2 (g) should be always avoided while synthesis of $BaTiO_3$(s).
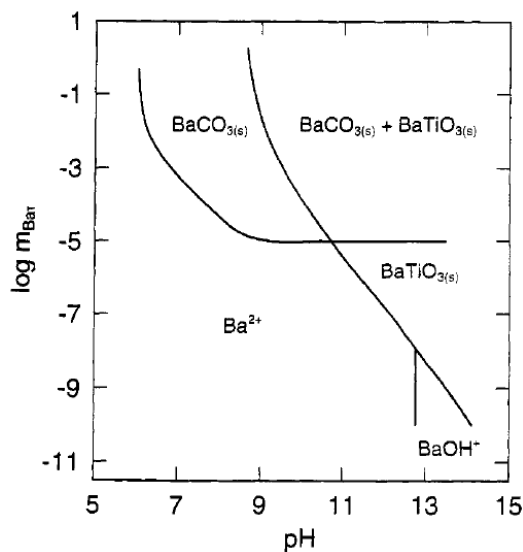
Figure 2-11   Calculated stability diagram for the Ba-Ti system in a sealed vessel containing 20 % volume air (CO_2 (g)-containing) at 90 ˚C.

2.1.3   Hydrothermal synthesis of $BaTiO_3$ nanopowders

Wet-chemical, hydrothermal processing with inorganic precursors offers a promising approach to preparing ultra-fine (sub micrometer-size), crystalline ceramics by using an aqueous medium under strong alkaline conditions. Numerous ceramic powders can be conveniently synthesized

by the hydrothermal method, which allows for the preparation of phase-pure products under low temperatures (100 ˚C) and facile control of reaction condition such as concentration, pH, and temperature. In contrast to the expensive sol–gel route with alkoxides, the inorganic salts of barium and titanium used by Wada et al. [27]. and Eckert et al. [16] are relatively inexpensive. Wada et al. were able to produce barium titanate by adding barium hydroxide to a gel network of hydrous titanium tetra hydroxide, while Eckert et al. prepared barium titanate via hydrothermal conversion of commercial titania particles in solutions of barium hydroxide octahydrate.

The hydrothermal methods using titania gel or commercial titania particles are effective relative to kinetics and producing submicrometer-sized particles of $BaTiO_3$ composition. Urek et al. [28] synthesised fine powders of barium titanate hydrothermally while using barium hydroxide and barium acetate along with titanium ethoxide in different alkaline media. The preparation of $BaTiO_3$ from hydroxide alkoxide precursors yielded nanocrystalline powders in the range of 40 nm with $BaCO_3$ as impurities, while the powders with higher surface area were reported to be synthesised using barium acetate.

Micheal Hu et al. [29] adopted a ''two-stage'' approach for preparing monodispersed barium titanate: (1) dielectric-tuning solution precipitation of titania microspheres and (2) low-temperature hydrothermal conversion of titania microspheres in barium hydroxide solutions to achieve the production of monodispersed microspheres of nanocrystalline barium titanate.

Chen et al. [30] synthesized spherical $BaTiO_3$ particles by using a low-temperature (≤100 ˚C) hydrothermal method from spherical titania particles. The change to dielectric constant of the liquid was used to produce spherical TiO_2 particles in submicrometer size from $TiCl_4$, followed by hydrothermal conversion in a barium hydroxide solution. The size and morphology of the $BaTiO_3$ particles were the same as those of the precursor TiO_2 particles, which was attributed to the in-situ transformation mechanism for the conversion of TiO_2 to $BaTiO_3$.

$BaTiO_3$ hydrothermal synthesis involving the modified metal alkoxide precursor by addition of acetylacetone was reported by J. Moon et al. [31]. A synthesis procedure for barium titanate-using titanium isopropoxide precursor modified with acetylacetone and barium acetate was devised. Co-precipitated gels were obtained from these precursors by addition of KOH solution. Direct precipitation of cubic $BaTiO_3$ from such suspensions was obtained under hydrothermal conditions. Phase-pure barium titanate were synthesized under high alkaline conditions (i.e., pH

>13.0) at temperatures as low as 50 ˚C with in 12 h. The higher reaction temperatures was reported to accelerate the crystallization process while particle size of the synthesized powder ranged from 50 nm to 350 nm that could be controlled by proper selection of the hydrothermal synthesis conditions such as concentration, temperature, and time.

2.1.4   Kinetics and mechanism of hydrothermal synthesis of BaTiO$_3$

Two possible mechanisms have been generally proposed for the hydrothermal conversion of titania to barium titanate.

1. *In situ transformation:* involving diffusion of Ba^{2+} through the BaTiO$_3$ shell layer formed around the titania particle, followed by reaction with the TiO$_2$ core. The overall conversion rate could be controlled by either diffusion rate or reaction rate. Barium titanate particles obtained by this mechanism should maintain their size and morphology similar to those of the precursor titania particles.

2. *Dissolution–precipitation:* involving dissolution of TiO$_2$ into Ti(OH)$_x^{4-x}$ species, precipitative BaTiO$_3$ nucleation (heterogeneous or homogeneous in nature) by reaction with barium ions or complexes in solution, followed by recrystallization or growth. Barium titanate particles obtained by this route are usually different from the precursor titania particles with regard to their size and shape [16, 29]. Hertl [32] reported the kinetics of BaTiO$_3$ proposing the in-situ transformation mechanism for hydrothermal conversion of TiO$_2$ to BaTiO$_3$. While using Ba(OH)$_2$ and particulate TiO$_2$ as precursors he found that the rate determining step at high concentration of Ba(OH)$_2$ is the topochemical reaction of Ba^{2+} with TiO$_2$ at the interface, whereas at low concentration of Ba(OH)$_2$ the diffusion of Ba ions through the BaTiO$_3$ product layer limits the reaction rate. He found that particle size of BaTiO$_3$ is inversely proportional to initial concentration of Ba(OH)$_2$. Eckert et al. [16] evaluated a reaction mechanism of hydrothermal formation of BaTiO$_3$ using the same precursors for various reaction times (1 h to 72 h). On the basis of chemical composition, morphology, sub micrometer-scale distribution of intermediate-stage products and kinetic analysis using Johnson-Mehl Avrami equation [33, 34] they tried to find evidence of reaction mechanism. Their analysis revealed two reaction regimes. In first regime, at early stage of BaTiO$_3$ formation dissolution-precipitation was observed to be the transformation mechanism. While in the second regime, an in-situ transformation mechanism dominated at longer reaction times. Over all they favoured the dissolution-precipitation to be responsible for formation of BaTiO$_3$ via hydrothermal route. They calculated crystallite sizes of BaTiO$_3$ and found it to be in the range of 35 nm to 50 nm. However, according to them no trends of crystallite sizes relative to reaction time at a particular temperature were evident.

Transformation mechanisms proposed for hydrothermal synthesis of BaTiO$_3$ are (i) in-situ transformation and (ii) dissolution-precipitation, shown in Figure 2-12 and Figure 2-13 respectively.

The in-situ transformation assumes that TiO_2 reacts initially with dissolved barium. This produces a continuous layer of $BaTiO_3$ through which additional barium must diffuse for reaction to continue, until the TiO_2 supply is exhausted. The product layer may be either a dense or porous layer or of monocrystalline or polycrystalline nature. Hydrothermal synthesis was assumed by Hertl [32], to occur by in-situ transformation; the two possible rate controlling processes he considered were diffusion of the barium species and TiO_2. As the reaction progresses, one can envision that the product layer will slow, if not halt, the velocity of the reaction.

The dissolution-precipitation model involves multiple steps. For anhydrous TiO_2 precursor, Ti-O bonds must be broken via hydrolytic attack to form hydroxytitanium complexes ($Ti(OH)_x{}^{4-x}$) capable of dissolution and reaction with barium ions or complexes (Ba^{2+} or $BaOH^+$) in solution to precipitate $BaTiO_3$. In contrast, use of hydrous TiO_2 reactant bypasses some or most of the hydroxylation step. $BaTiO_3$ nucleus may either originate on the TiO_2 substrate (heterogeneous nucleation) or form directly in the bulk solution (homogeneous nucleation).When heterogeneous nucleation occurs, the dissolving TiO_2 particle can be encapsulated, thereby limiting the supply of soluble TiO_2 species available to react with the barium species. As with the in-situ transformation model, this diffusional barrier serves to slow, if not halt the hydrothermal reaction [16].
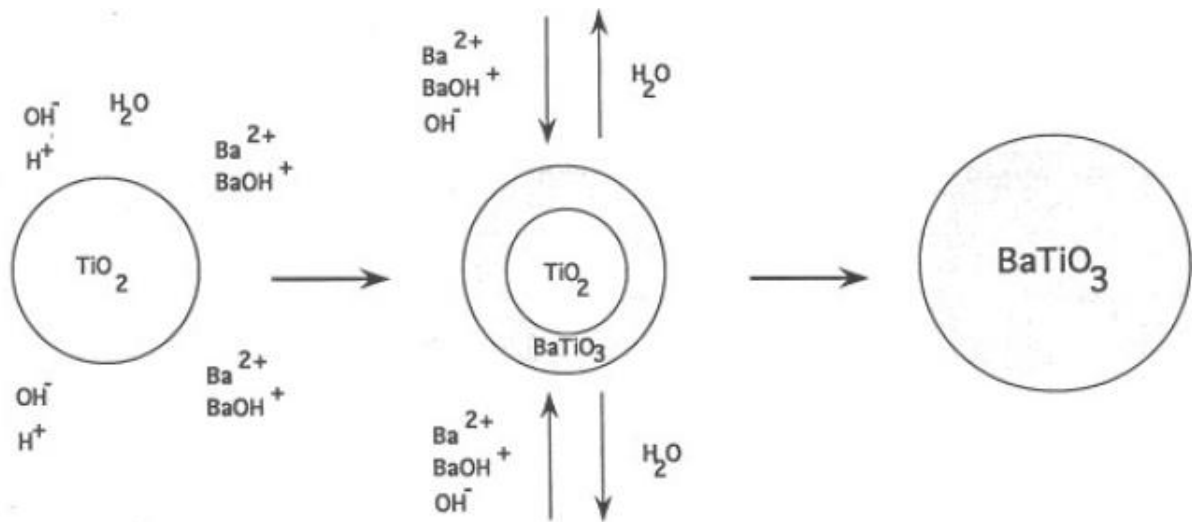
Figure 2-12 Schematic sketch of the in-situ reaction mechanism [16].
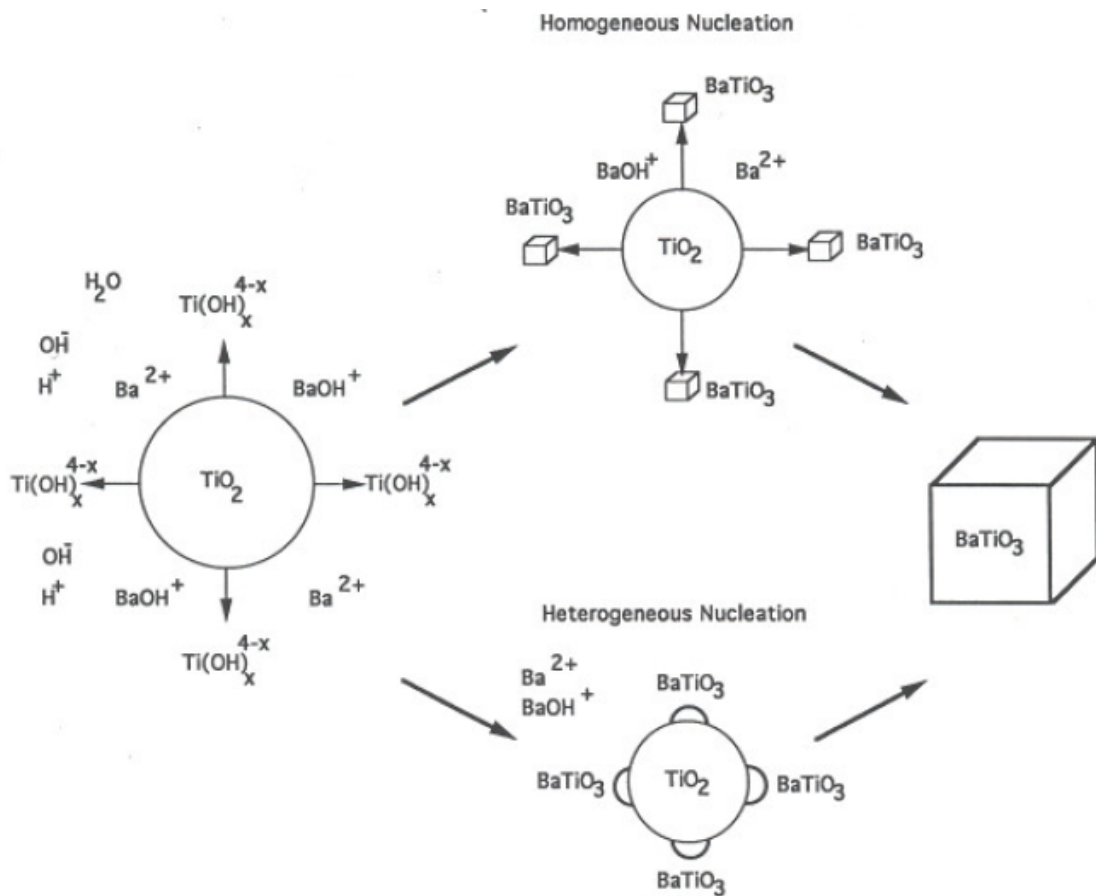
Figure 2-13 Schematic sketch of the dissolution-precipitation reaction mechanism [16].

2.1.5   Effect of particle size and cubic/tetragonal phase stabilization in polymorph BaTiO₃

The overriding goal in barium titanate processing is to create smaller, more uniform particles to allowing finer ceramic layers to achieve device miniaturization without the loss of dielectric properties, using fast, low-temperature synthesis mechanisms. Controlling the phase, composition homogeneity, particle size and monodispersity, microstructure, and the cost of particle production are important concerns in developing techniques for synthesizing barium titanate [29]. The use of ferroelectric ceramics and thin films in microwave devices requires that they possess frequency-stable, low-loss dielectric properties [35].

$BaTiO_3$ exists in various crystallographic modifications. Two crystalline phases of barium titanate are especially important for applications in the microelectronics industry i.e., the tetragonal phase of barium titanate due to its ferroelectric properties, and the paraelectric cubic form. The stable crystalline polymorph of $BaTiO_3$ at room temperature is the tetragonal form, which possesses a high dielectric constant at temperatures between 0 ˚C and 130 ˚C. Above 130 ˚C the unit cell converts to a paraelectric cubic structure [36-38]. At room temperature, the dielectric constant for $BaTiO_3$ ceramics prepared from fine powders can be in the range from 1500 to 6000, depending on the grain size. At microwave frequencies, ferroelectric polycrystalline ceramic materials typically exhibit a large dielectric relaxation, characterized by a decrease in the relative permittivity (ε_r) and a peak in the dielectric loss (tan δ) [35].

Among the various methods for producing sub-micrometer $BaTiO_3$ powder, the hydrothermal technique is well known. This technique produces fine particles of $BaTiO_3$ with acceptable particle morphology and composition. The hydrothermal synthesis involves the reaction of Ba precursors and a titanium source. The reaction has to be carried out in a strongly alkaline solution and crystalline $BaTiO_3$ has been reported to from at temperatures between 85 ˚C and 250 ˚C within hours. However, in all the syntheses, the crystalline product recovered is cubic. A thermal treatment of as-synthesized metastable cubic form above l000 ˚C is needed to stabilize the tetragonal form [19].

Hydrothermal synthesis of $BaTiO_3$ resulting in the stabilization of the tetragonal form at room temperature has only been reported for syntheses that are carried out above 450 ˚C [22, 39]. Previous studies have shown that below 250 ˚C, the metastable cubic $BaTiO_3$ is observed at room temperature [40-42]. To stabilize tetragonal $BaTiO_3$, it is important that crystal sizes

exceed 1 µm so as to accommodate the strains caused by the transformation from cubic to tetragonal structure [8, 19, 43-46]

The cubic phase stabilization instead of tetragonal phase at room temperature is attributed to two origins: (1) size effect reflecting a thermodynamic phase transition due to an isotropic pressure and (2) hydroxyl ion incorporation on oxygen sites of $BaTiO_3$.

The reasons for the existence of a limiting size in order to exhibit tetragonality is being debated and is related to strains that develop in the particle that prevent it from assuming the tetragonal form, as well as the presence of OH impurities in the lattice leading to defects and resulting micro strains that keep the particles cubic.

The difference between the cubic and tetragonal form arises from the inequality in the 'a' and 'c' axes in the latter polymorph. To accommodate the dimensionality change in the c direction as the sample is synthesised, synthesis temperatures in the range of 600 °C will result in formation of large (sub-millimetre) tetragonal crystals of $BaTiO_3$. Temperatures of hydrothermal synthesis exceeding 200 °C lead to the first appearance of the tetragonal phase. Kajiyoshi et al.[39] have shown that the crystals formed on Ti substrates increased in size from 0.3 µm to 2 µm, as the hydrothermal synthesis temperature increased from 400 °C to 800 °C. Uchino et al. [13] noted that particles with average sizes greater than 0.2 µm were tetragonal with Curie transition temperatures of 130 °C. Arlt and co-workers [8] noted that the dielectric constant of sintered samples decreased with grain sizes lower than 1 µm and proposed that this occurs because the ferroelectric structure changes to a pseudocubic form.

It has been reported by Christensen [22] that the tetragonal form can be directly synthesized by the hydrothermal method at temperatures between 450 °C and 600 °C, with the process being favoured at the higher temperatures.

Dutta et al. [19] showed that inclusion of chloride ions in the reactant composition for hydrothermal synthesis leads to formation of the tetragonal form of $BaTiO_3$ at synthesis temperatures as low as 240 °C.

Wu et al. [47] prepared tetragonal $BaTiO_3$ hydrothermal using $Ba(OH)_2 \cdot H_2O$ and TiO_2 (anatase), in the absence of anions (chloride ions), at 220 °C after several days reaction time. They as well

observed that increasing the Ba : Ti molar ratio from 1:1 to 4:1 and alkaline concentrations from 1.0 M to 3.0 M promotes the formation of tetragonal $BaTiO_3$.

Xu et al. [48] prepared tetragonal $BaTiO_3$ powders hydrothermally at 240 ˚C after 12 h, using $BaCl_2·H_2O$ and $TiCl_4$. The formation of tetragonal $BaTiO_3$ powders is promoted by the increase in NaOH excess concentration (from 0.5 M to 2.0 M) and decrease in initial $TiCl_4$ concentration (from 0.625 M to 0.15 M). After reaction, the powders were phase-pure $BaTiO_3$, with no impurities, such as Cl^{1-} and CO_3^{2-}.

Few successful cases of tetragonal $BaTiO_3$ powder synthesis below 100 nm size have been reported [49, 50]. A 70 nm barium titanate powder hydrothermally synthesized with chloride source materials at 240 ˚C was noted to be tetragonal [50]. 70 nm is the smallest barium titanate powder having high tetragonality synthesized in a hydrothermal condition. Kwon et al. [51] reported the preparation of superfine (lower than 100 nm) highly tetragonal $BaTiO_3$ powder up to 1.0088 (*c/a*) at 210 ˚C using 50 % ethanol to water as solvent via a solvothermal method without precipitating agent. They used barium hydroxide octahydrate and anatase as precursors in ethanol-DI water mixture. Solvent ratio used in volume percent was changed from 100 % EtOH to 80 %, 60 %, 50 %, 40 %, 20 % and 0 % with DI water.

The OH^- must play a vital role in this process since in its absence $BaTiO_3$ is not formed. The mechanism of formation of $BaTiO_3$ from Ba^{2+} and Ti species is not well understood. Two proposed mechanisms involve a condensation reaction of $Ti(OH)_6^{2-}$ with Ba^{2+} [40] and migration of Ba^{2+} into the TiO_2 structure with resulting breakage of TiOTi bonds and incorporation of Ba^{2+} [41]. In the latter mechanism, the role of OH^- could be to facilitate the hydrolysis of TiOTi bonds. The dynamic nature of the interaction between TiO_2, Ba^{2+}, and OH^- leads to a crystallization mechanism involving nucleation, growth, and crystal dissolution.

It is recognized that synthesis at higher temperatures (>450 ˚C) will lead to formation of larger crystals [22].

There have been controversies [13, 49, 50, 52] about the critical barium titanate size where it loses its tetragonality due to size effect. Hsiang and Yen [53] determined the critical size to be 49 nm using a transmission electron microscope, which was consistent with the result of Zhang et al. [49] using X-ray diffraction techniques.

2.1.6   Size effects in ferroelectrics

It is Generally believed that there is a decrease in tetragonal distortion with decreasing particle size below approximately 1 μm. Arlt et al. [8] reported that permittivity below Curie point shows a pronounced maximum $\varepsilon\varepsilon_r$ ~5000 at grain sizes 0.8 μm to 1 μm while at grain sizes < 0.7 μm the permittivity strongly decreases and the lattice gradually changes from tetragonal to pseudocubic. Uchino et al. [13] showed that the transformation from tetragonal to cubic symmetry occurred at a critical particle size of 0.12 μm at 75˚C. Begg et al. [54], however, indicated that a hydrothermal $BaTiO_3$ powder with a particle size larger than 0.27 μm was completely tetragonal and with a particle size less than 0.19 μm was a fully cubic phase as shown by XRD and SEM. Kobayashi et al reported that critical crystallite size of transformation from cubic to tetragonal structures for $BaTiO_3$ prepared by sol gel method is approximately 40 nm [55]. More details on the critical particle size *vs*. the phase transition are presented in Table 2-II.

All reports show some difference in the critical particle size. This critical size difference may come from the different residual elastic strain energy, chemical impurity level and crystalline defects. Two models have been proposed to describe the room temperature stabilization of the cubic structure in fine-grained $BaTiO_3$. One is the phenomenological surface layer model [56], and the other is the pure phase model [13, 57]. The phenomenological surface layer model is based on the structural transition between the outer cubic surface layer of fixed thickness and the tetragonal core, with a gradient of tetragonality existing between the two regions. As the particle size decreases, the relative ratio of cubic to tetragonal region is increased and eventually only a stable cubic region remains at a critical particle size. As an example, Takeuchi et al. [58], using a $BaTiO_3$ powder formed by a solid-state reaction, estimated the thickness of the surface cubic layer as 5.1 nm, independent of the particle size by XRD measurement.

Table 2-II   Critical particle sizes for the cubic to tetragonal phase transition

Researcher	Results	Preparation method	Measurement method
Arlt *et al.* [8]	≤0.5 µm pseudo cubic	oxalate	XRD, εr Measurement
Uchino *et al.* [13]	≤0.12 µm cubic >0.12 µm tetragonal	hydrothermal, solid-state co precipitation	XRD, BET
Hennings and Schreinemacher [59]	0.2~0.4 µm cubic ≤0.15 µm cubic ≥0.20 µm tetragonal	hydrothermal solid-state solid-state	XRD
Begg *et al.* [54]	≤0.19 µm cubic ≥0.27 µm tetragonal	hydrothermal	XRD, SEM, HRTEM
Takeuchi *et al.* [58]	(0.32~1.22) µm coexistence	solid-state	XRD
Lobo *et al.* [60]	≥0.2 µm tetragonal	sol-gel	XRD, εr Measurement
Li and Shih [61]	≤0.056 µm cubic ≥0.071µm tetragonal	alkoxide-hydroxide	XRD
Jiang *et al.* [62]	(0.105~0.130) µm Cubic to tetragonal change (0.01~3.5) µm cubic	sol-gel stearic-acid gel	Raman spectroscopy XRD
Lu *et al.* [63]	0.08 µm Cubic with some tetragonal	hydrothermal	XRD, DSC Raman spectroscopy
Xu *et al.*[50]	≈70nm tetragonal	hydrothermal use of Cl^{1-} ions	
Hsaing and Yen[53]	≈49nm tetragonal		TEM
Kwon *et al.* [51]	≈80nm tetragonal	solvothermal	XRD, BET, PSD

The pure phase model does not require the coexistence of the cubic and tetragonal structures. There are two mechanisms to explain this model; strains imposed by the presence of lattice hydroxyl ions [57] and the role of the surface [13]. Regarding the hydroxyl ion effects, Vivekanandan and Kutty [57] explained the source of lattice strain from point defects caused by the presence of hydroxyl ions and the corresponding cation vacancies. According to Vivekanandan and Kutty, the residual hydroxyl ions in the oxygen sub-lattice, the structure is retained during hydrothermal $BaTiO_3$ synthetic process, is compensated by cation vacancies, and results in strain leading to the metastable presence of the cubic phase at room temperature. Although one can remove hydroxyl ions completely by annealing in air at 900 ˚C for 15 hours, $BaTiO_3$ still remains as a cubic phase by the retained strain of compensating cation vacancies. Only with annealing above 1000 ˚C, is the tetragonal phase acquired.

However, retention of the supposed charge-compensating cation vacancies is difficult to visualize once the hydroxyl ions have been removed from the lattice. Therefore, Begg et al. [54] used Vivekanandan and Kutty's model to explain the deficiency with regard to the role of hydroxyl ions/cation vacancies in the stabilization of the cubic structure. Begg et al. [54] observed that the tetragonal hydrothermal $BaTiO_3$ powder contained more hydroxyl ions than the cubic phase $BaTiO_3$.

The surface effect model is based on the surface tension associated with the very fine powder stabilizing the cubic phase at room temperature. Uchino et al. [13] observed that a decrease of room temperature tetragonality and the Curie point are a function of the reduction in particle size. According to Uchino et al. [13], this surface tension is sufficiently high to decrease the tetragonality and the Curie point associated with small particle size barium titanate.

In summary, due to the importance of fine sized tetragonal $BaTiO_3$, many researchers have been interested in the cubic to tetragonal phase transition of this powder. However, all the research reports show different results on the critical particle size produced by different synthetic methods and different measurement methods. This critical size difference may come from the different residual elastic strain energy, chemical impurity levels and crystalline defects [9].

2.1.7   Phase transformation in four steps

Ferroic crystals have movable domain walls which result in hysteretic behavior. In terms of particle size effects, ferromagnetic materials are by far the best studied, and it is anticipated that ferroelectrics will follow the magnetic analog as size is reduced. At large particle sizes, twinning lowers the volume energy of the particle, with the appearance of complex domain structures possessing several types of walls. As size is reduced further, it becomes increasingly difficult to recover the wall energy from the volume term, consequently, it is expected that the number of domains will decrease, at first by one type, and then the others. The first transformation is then from a polydomain particle to a single domain particle. Upon further reduction in size, the next expected transformation is from a single domain crystallite to a superparaelectric phase. From the magnetic analog, this *superparaelectric* phase would then be expected to behave as an unpolarized, but highly orientable single domain, possessing a high dielectric constant.

Finally, since ferroelectricity is a cooperative phenomenon, it is reasonable to suppose that the system will be forced to revert to a paraelectric state at a critical size too small to sustain the cooperative interactions necessary for ferroelectric behavior. In summary, the size dependence of ferroelectric particles should exhibit four states, predicted from the magnetic analog: multidomain, single domain, superparaelectric, and paraelectric [35].

Intuitively, grain size effects are expected to differ from particle size effects mainly because the boundary conditions within a ceramic differ from those which govern a free particle.

Most significantly, grains in ceramic are three dimensionally clamped by surrounding grains. In the case of $BaTiO_3$, as the ceramic cools through the cubic-tetragonal phase transition, a tetragonal lattice distortion is introduced, resulting in large strains in the individual grains. This leads to rather complicated domain structures which strongly influence the electric permittivity. Typically, large grain (0.20 µm) polycrystalline ceramic $BaTiO_3$ exhibits a relative permittivity of, ε_r approx. 1500 to 2000 at room temperature.

Various investigators [64-66] however, have observed ε_r to increase with decreasing grain size, peak at some critical size, and then decrease with continued size reduction [8, 67, 68].

Frey et al. [69] considered in detail the role of nonferroelectric interfaces in submicron, fine grain ceramic $BaTiO_3$. The grain size dependent Curie–Weiss characteristics and dielectric properties in the ferroelectric state were measured. In this work, a significant enhancement in the apparent dielectric constant ε_r, was observed upon decreasing grain size from 1.7 to 0.5 µm, where ε_r reached a maximum of 4000. Below 0.5 µm, ε_r appeared to decrease, however, remaining above 2000 for a grain size less than 100 nm. With decreasing grain size, it was shown that the true dielectric constant of the ferroelectric grains increased to 4800 at a grain size of 0.5 µm, and remained constant for all grain sizes less than 0.5 µm down to 70 nm. Frey et al. concluded that in the submicron grain size region, domain twinning significantly decreased with an associated increase in internal residual stress, which acts to enhance ε_r For grain sizes less than 0.5 µm, it was proposed that the ceramics were comprised of substantially single-domain, highly stressed grains.

2.2 Poly(methylmethacrylate) (PMMA)

PMMA is a vinyl based polymer. It softens when heated this category of polymers is referred to as thermoplastic meaning they can be made to flow if hot.

If the –OH group of vinyl alcohol is substituted by a carboxylic acid group –COOH it will result into Acrylic acid. On polymerization it gives poly acrylic acid. If one of the hydrogens on the main carbon-carbon chain is substituted by a methyl –CH_3 group, polymethacrylic acid (PMA) results which is used as a dispersant when the molecular weight is low. The methyl ester of PMA is PMMA (Figure 2-14), which is a common plastic (i.e., polymer) and used to make hair brushes, jewellery, optical fibres and resist/dielectric material in electronic industry [70].

PMMA is a versatile polymeric material that is well suited for many imaging and non-imaging microelectronic applications. PMMA is most commonly used as a high resolution positive resist for direct write e-beam as well as x-ray and deep UV micro lithographic processes. PMMA is also used as a protective coating for wafer thinning, as a bonding adhesive and as a sacrificial layer.
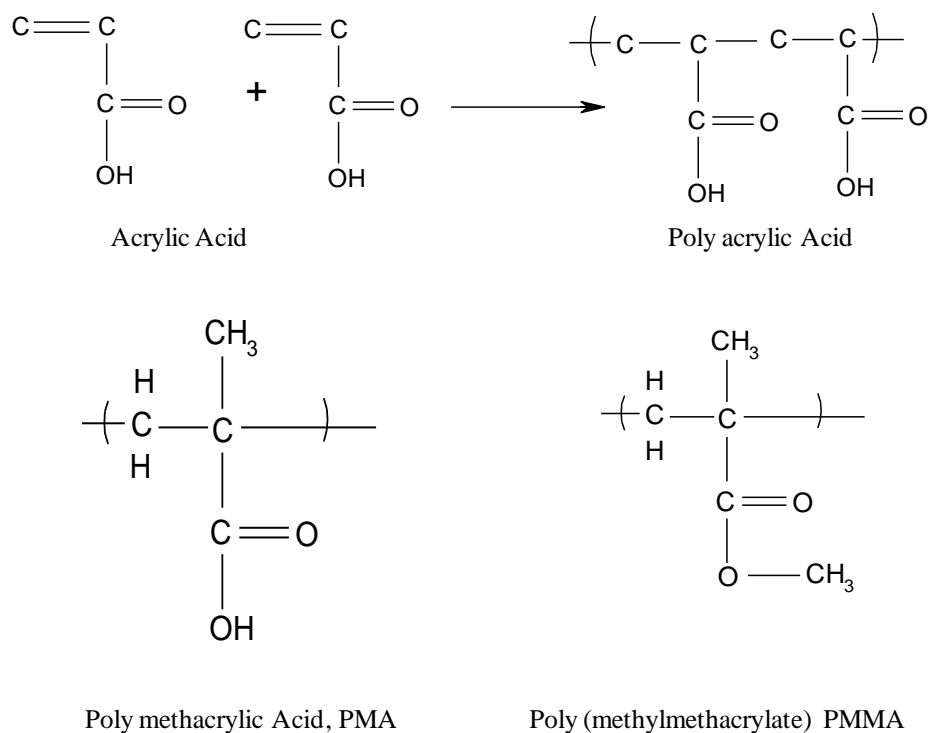
Figure 2-14 Polymerization of acrylic acid to achieve PMA and PMMA

PMMA has been also used as a protective layer for wafer thinning. Its thermal and mechanical stability, together with a high resistivity (>2 E15 Ωcm) and suitable dielectric constant, similar to that of silicon dioxide (ε= 2:6 at 1 MHz, ε= 3:9 at 60 Hz), make PMMA a good candidate as a dielectric layer in MIS (metal-insulator-semiconductor) structures. Besides, PMMA can be easily deposited on large areas by spin-coating and baked at low temperatures (<170 ˚C) [71].

2.2.1   Properties of PMMA

- Hard, rigid, transparent (very clear to see through)
- Softening point at 125 ˚C
- Absorbs very little visible light but there is a 4% reflection at each polymer-air interface for normal incident light.
- PMMA is a polar material and has a rather high dielectric constant and power factor
- A good electrical insulator at low frequencies but less satisfactory at higher frequencies
- good water resistance
- PMMA prepared by free radical polymerization is amorphous and is therefore soluble in solvents with similar solubility parameters such as benzene, toluene, chloroform, methylene chloride, esters, ethyl acetate, and amyl acetate.
- PMMA has good resistance to alkalis (sodium hydroxide, etc.), aqueous inorganic salts (the Pacific Ocean) and dilute acids.
- PMMA has a better resistance to hydrolysis than PMA probably by virtue of the shielding of the methyl group.
- PMMA's outstanding good outdoor weather resistance is marketably superior to other thermoplastics.
- When heated about 200 ˚C, decomposition becomes appreciable and at 350- 450 ˚C, a nearly quantitative yield of monomer is readily obtained. Thus, the recovery of monomer from scrap is feasible.
- Because it's a thermoplastic, it can be molten and molded (at 100 to 150 ˚C) into anything we want.
- A syndiotactic polymer (A polymer whose monomer units are oriented alternately dextro and levo or a polymer structure in which monomer units attached to the polymer backbone alternate in a-b-a-b fashion on one side of the backbone and, if present on the other side, are arranged in a b-a-b-a fashion.) can be polymerized. At lower temperatures, the stereochemistry of the polymer can be controlled by means of the solvent.

Material	Dielectric constant	Dissipation factor	Frequency [Hz]	Break down strength [KV/cm]
PMMA	3.3-3.9	0.04-0.06	50	140
	2.2-3.2	0.004-0.04	1000000	

2.2.2 Solvents for PMMA

A safer solvent for PMMA is anisole.

Not so safe are chloro-benzene, hexane.

PMMA is also soluble in acetone, benzene, chloroform, MEK, THF.

2.3 Polymer nanocomposites

After passing through different ages of development like stone age, bronze age, iron age, steel age(industrial revolution) silicon age and silica age (telecommunication revolution) we are entering into a new era, where scientist instead of understanding a particular material are looking for optimizing the relative contributions afforded by material combinations.

The nanoscience and technology is providing us unique opportunities to create revolutionary material combinations. These new materials are only possible when the length scale of morphology and fundamental physics associated with property coincide on the nanoscale. The combination of fundamental understanding of materials and realization of fabrication and processing techniques that provide simultaneous structural control on the nano-, micro- and macro- length scales is the core of the exciting area of nano-engineered materials.

The reinforcement of polymers using inorganic / organic fillers is common to achieve improved mechanical electrical and magnetic properties. In contrast to conventional micron filled polymer composites the fillers are on the order of few nanometres. Uniform dispersion of these nanofillers provides high surface area for link between nanoelements and host polymer. This high interfacial area and the finite size effect differentiate nanocomposites to their micron filled composites.

Multifunctional materials require a trade off between desired performance, mechanical properties, cost and processibilty.

Polymer nanocomposite is a vast field depending on the potential nanoelements, polymeric resins and their applications. Development of these materials require a balance between four independent areas; constituent selection, fabrication, processing and performance.
Polymer nanocomposite methodologies:

1. In-situ routes
2. Exfoliation

Despite large number of combinations or matrices and potential reinforcing nanoelements with different chemistry, shape, size, and properties, all Polymer nanocomposites share common

features with regard to fabrication, methodologies, processing, morphology characterization and fundamental physics.

The objective of exfoliation is to uniformly disperse and distribute the inorganic (initially comprise of aggregate of the nanoparticles) within the polymer. The final Polymer nanocomposite structure results from the transformation of an initially microscopically heterogeneous system to a nanoscopically homogenous system.

Four approaches to fabricate Polymer nanocomposites using exfoliation;

1. Solution process.
2. Mesophase mediated processing.
3. In-situ polymerization and
4. Melt processing.

Each has its advantages with respect to processing steps required for the desired final form of PNC Powder, film, paste. The fundamental challenge is to provide a general guideline including thermodynamic, kinetic and rheological considerations, for morphology control using these fabrication processes. So it is required to carefully choose surface functionalization to control polymerization rates and initiation points so that separation of the aggregates of nanoelements occurs before or during polymerization. This is because the cross linking reactions determine the morphology. Additional complications arise from preferential portioning of components to the nanoelement surface in these multi component resin systems, thus modifying reactivities and creating unknown gradients in network topology.

The key to any of these fabrication processes is the engineering of the polymer-nanoparticle interface where surfactants are commonly used. These surface modifiers mediate interlayer interactions by effectively lowering the interfacial free energy. They may as well serve to catalyze interfacial interactions, initiate polymerizations, or serve as anchoring points for the matrix and thereby improve the strength of the interface between the polymer and inorganic. The choice of the optimal modifier is yet based on observation and experience.

Developing an understanding of the characteristics of this inter phase region, its dependence on nanoelement surface chemistry, the relative arrangement of constituents and ultimately, its relationship to Polymer nanocomposite properties, is a current research frontier in nanocomposites. Equally important is the development of a general understanding of the

morphology-property relationship for mechanical, barrier, and thermal response to these systems. This necessitates the determination of the critical length and temporal scale with which continuum description of a physical process must give way to mesoscopic and atomistic view of these nanoscale systems- a current challenge for computational material science [72].

2.3.1 What makes nanocomposites unique?

Firstly nanofillers are small mechanical, optical, and electrical defects compared to micron scale fillers. Below 50nm many fillers do not scatter light significantly, so it is possible to achieve composites with altered electrical or mechanical properties that maintain optical clarity [73]. Secondly many properties of material are said to be intrinsic-depend upon how the matter being assembled above a critical length scale. When the nanoparticles decrease below this size, the properties of the particles can differ significantly from the bulk material; thus variation in melting temperature, colour, magnetization and charge capacity are often observed [74, 75].

Third, the small size of the filler leads to exceptionally large interfacial area in the composites. Figure 2-15 (a) shows the surface area per unit volume as function of particle size for spherical particles that are ideally dispersed. In addition Figure 2-15 (b) the inter particle spacing decreases such that at small volume fractions of filler, the inter particle spacing is similar to the radius of gyration of the polymer (~100 A°).

The high surface area becomes even more significant when one considers that there is an interaction zone (IZ) surrounding the filler. This is a region in which the structure and properties have been altered because of the presence of the filler. It could be a region of altered chemistry, polymer conformation, chain mobility, degree of cure, or crystallinity. This approximated value of this zone is reported to be in the range of 2 to 9 nm [76]. If we assume that this IZ is about 10 nm in thickness, then at 2.5 volume % of a 20 nm equiaxed nanoparticle well dispersed, 37 % of the polymer has different properties from the bulk polymer. Therefore, the IZ can be significant portion, if not the entire bulk, of the matrix. Thus the nanofillers can alter the expected properties of the composites considerably

The physical nature and extent of this IZ has recently been probed through some recent work on multi walled carbon nanotubes (MWNTs). In this study, a solvent processing method was used to make MWNT polymer nanocomposites. Upon observation of the composite fracture surface,
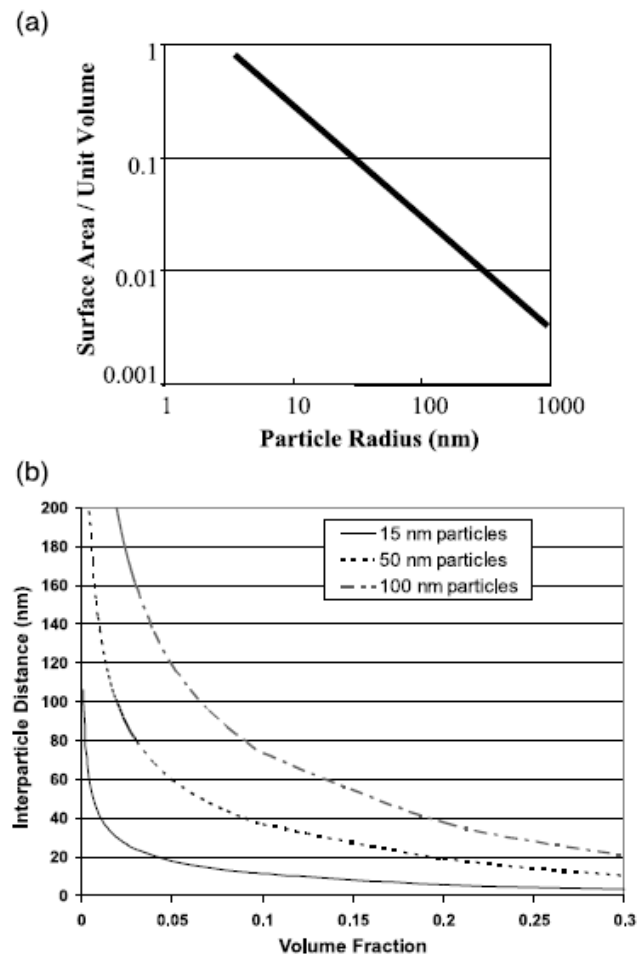
Figure 2-15   a) The surface area per unit volume as a function of particle size for spherical
               particles showing the large surface area in nanoparticles. b) The inter particle
               spacing of nanoparticles arranged on a simple cubic lattice showing the variation
               with particle size and volume fraction [72].
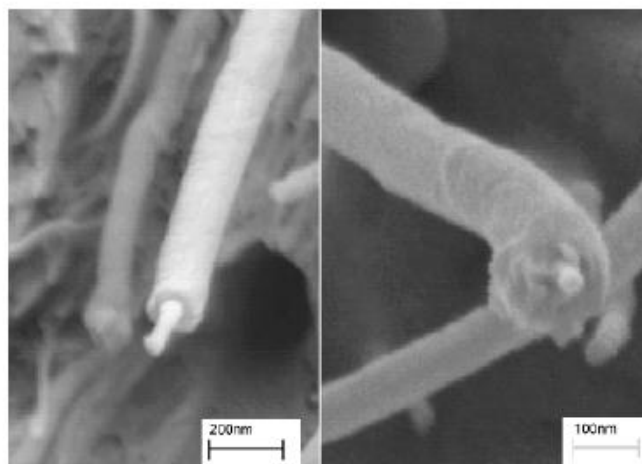
Figure 2-16   Polymer-coated nanotubes observed in the fracture surface of MWNT reinforced
              polycarbonate composite [77].

a polymer layer was observed on the nanotubes Figure 2-16 that had pulled out of the opposing side of the fracture. This ''sheath'' was confirmed to be polymer from the matrix, but with obviously altered thermal and mechanical properties from the bulk. The thickness of this interfacial layer increased with chemical modification of the nanotubes [72].

2.3.2   Thermodynamic aspects of dispersion

The dispersion of nanoparticles in a polymer is a result of favorable enthalpy of mixing resulting from the increased molecular contacts between the polymer and the dispersed nanoparticle as compared with the case of aggregated nanoparticles, because of the increased accessible area on the nanoparticle caused by dispersion [78]. Mackay et al. [78] results indicate that nanoparticles prepared from cross-linked polymers are capable of dispersing in polymers if the size of the nanoparticle is smaller than the radius of gyration of the polymer matrix. The effect, as elucidated by these authors, is only expected in nanoparticles and vanishes at the two limits of extremely small particles as well as for macroscopic particles.

To understand the thermodynamic behavior of nanocomposites comprising flexible polymers and spherical nanoparticles Schweizer et al [79] used the polymeric reference site modal. Miscibility is predicted as a result of a steric stabilization mechanism that results from a small polymer coating strongly adsorbed onto the nanoparticle. Interestingly, they note that the miscibility is relatively independent of polymer molecular weight for weak polymer-nanoparticle interactions, and in the case of strong bridging induced attraction, an increase in miscibility is observed with increasing molecular weight.

During the study of control of dewetting dynamics by adding nanoparticle fillers Sharma et al. [80] concluded that when interaction between particles and polymers is strong, dewetting i.e., the rapture of film from substrate is arrested. While unfavorable interaction exists between particles and the polymer, separation of particles from the polymer and dewetting of the films proceeds. Repulsive interaction destabilizes the films and increase the rate and magnitude of dewetting.

2.3.3   Experimental strategies to disperse nanoparticles in polymeric matrices

The dispersion of nanoparticles in polymeric matrices is the fundamental challenge surrounding the development of polymer nanocomposites. In addition to the development of methods to

characterize the dispersions of the nanoparticles, techniques for dispersing aggregated or ordered nanoparticles while not compromising the inherent advantages of the nanoparticles (such as their unique mechanical, thermal, and optical/electrical properties and extremely large internal surface area) remain a significant challenge.

The inter particle interactions are clearly a function of the chemical nature of the nanoparticles, with the shape of the nanoparticles, the distance between the nanoparticles, and the polydispersity of particle sizes being the most prominent secondary contributors. There is a strong dependence of the interaction energies on the shape and aspect ratio of the nanoparticles. Further, many nanoparticles form low-dimensional crystals or tight agglomerates that render their dispersion even more difficult [81].

Some of the most prominent methods to achieve dispersion of nanoparticles in polymer matrices are the functionalization of nanoparticles using weak (Van der Waals, π-stacking) interactions and the ionic interactions and covalent functionalization.

2.3.4   Controlling interparticle forces to create stable suspensions

Stabilising a colloidal suspension means that the inter particle potential is made repulsive, and there is a high-energy barrier to reach the primary minimum Figure 2-17.

The methods of stabilisation are [82]:

1. electrostatically

2. electrosterically

3. sterically

4. depletional

5. masking Van der Waals forces

The energy diagrams for these methods of stabilisation can be drawn by adding the different components that influence the stability.

For electrostatic stabilisation small ions in simple salts are used and therefore do not have a steric effect. The stabilisation arises purely from the repulsion between the double-layers that are formed by non-adsorbing counter-ions. The more ions adsorb at the surface, the less the amount of electrostatic repulsion. The energy diagram is shown in Figure 2-17. At low salt concentration

there is no secondary minimum but a barrier that prevents coagulation into a primary minimum. This barrier height decreases as the pH approaches the iso-electric point (pHiep). If large molecules with charge carrying groups adsorb at the surface the stabilisation becomes electrosteric. The electrostatic repulsion arises from the dissociated groups of the molecule that are not bound to the surface. The thicker the layer that is formed by the adsorbed ions, the larger is the steric part of the stabilisation. Polyelectrolytes containing many -COO--groups are mostly used for this type of stabilisation. The -COO--groups that bind to the surface do not contribute to the electrostatic stabilisation by the polyelectrolyte. The energy diagram for electrosteric stabilisation does not contain a primary minimum, as the particles in suspension cannot reach each other due to the presence of molecules at the surface. Only if the molecules are removed from the surface, a primary minimum will result. A secondary minimum can be present if the amount of steric or electrostatic stabilisation is not high [82].

If all the charge carrying groups of a large molecule are bound to the surface no electrostatic stabilisation is present, and the repulsion becomes purely steric. Thus purely steric stabilisation arises from adsorbing large molecules whose charge carrying groups are all bound to the surface or from large non-dissociating molecules that are adsorbed at the surface. Here as well thicker the layer of adsorbed molecules, the larger the steric stabilisation is. The steric stabilisation energy will be less compared to the electrosteric stabilisation energy with equally thick layers, due to the lack of electrostatic stabilisation. The energy diagram will not contain a primary minimum. As with electrosteric stabilisation, the particles cannot touch each other. A primary minimum can only be reached if there is no or little adsorption present. The width of the steric barrier normally cannot be varied for a given system.

This steric barrier can only be varied by varying the used adsorbent. Depending on the used adsorbent there will or will not be a secondary minimum. Depletion stabilisation arises when relatively high amounts of large molecules that do not adsorb at the surfaces of the colloidal particles are dissolved in the suspension. Mostly large polymers like poly vinyl alcohol (PVA) are used for this.

In most cases the depletion stabilisation mechanism is not the only stabilisation mechanism present, but here the energy diagram purely due to the stabilisation mechanism will be considered. A primary minimum is present, and a certain barrier height to reach this minimum. This barrier height depends on the concentration of the free molecule that causes the depletion

stabilisation. With decreasing concentration the barrier height will decrease, eventually leading to depletion flocculation into the primary minimum [83]. The masking of Van der Waals forces by using additives is not a real stabilisation mechanism, as it leads to coagulation of the particles into a secondary minimum. However, when present, this mechanism will not be the only stabilisation. Masking of Van der Waals forces can arise when molecules are adsorbed at the surface of suspended particles. If the adsorbed molecules have dielectric properties intermediate between those of the particle and the liquid, then the Van der Waals forces between the suspended particles will be diminished. However, the absorbance of the molecules will most often also lead to steric or electrosteric stabilisation, leading to a stable suspension whose stability is partly due to the masking of the Van der Waals forces. This last stabilisation mechanism will always be less important than the other present stabilisation mechanisms (Figure 2-18).
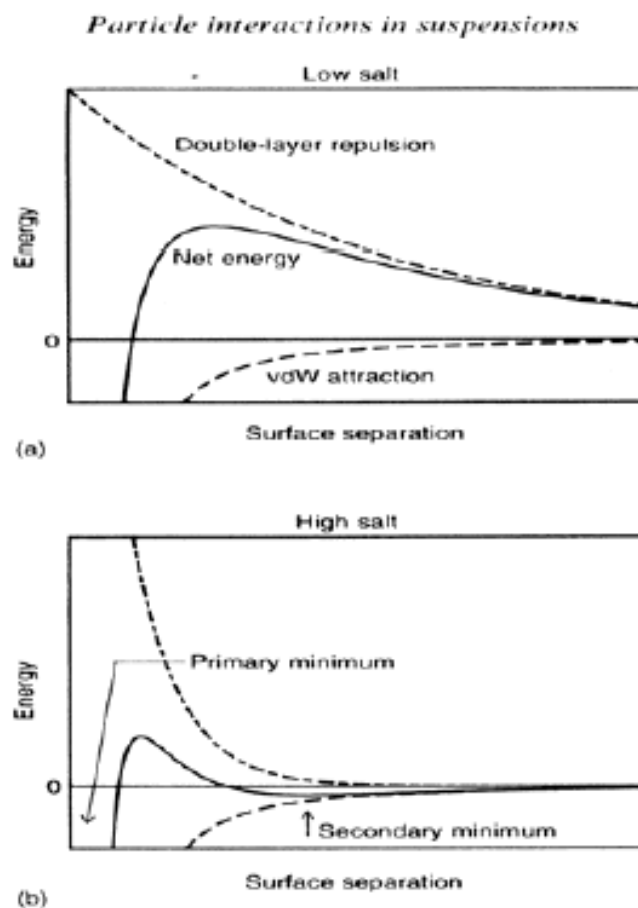
Figure 2-17   Interaction energy between colloidal particles in suspension depending on the salt concentration [82].
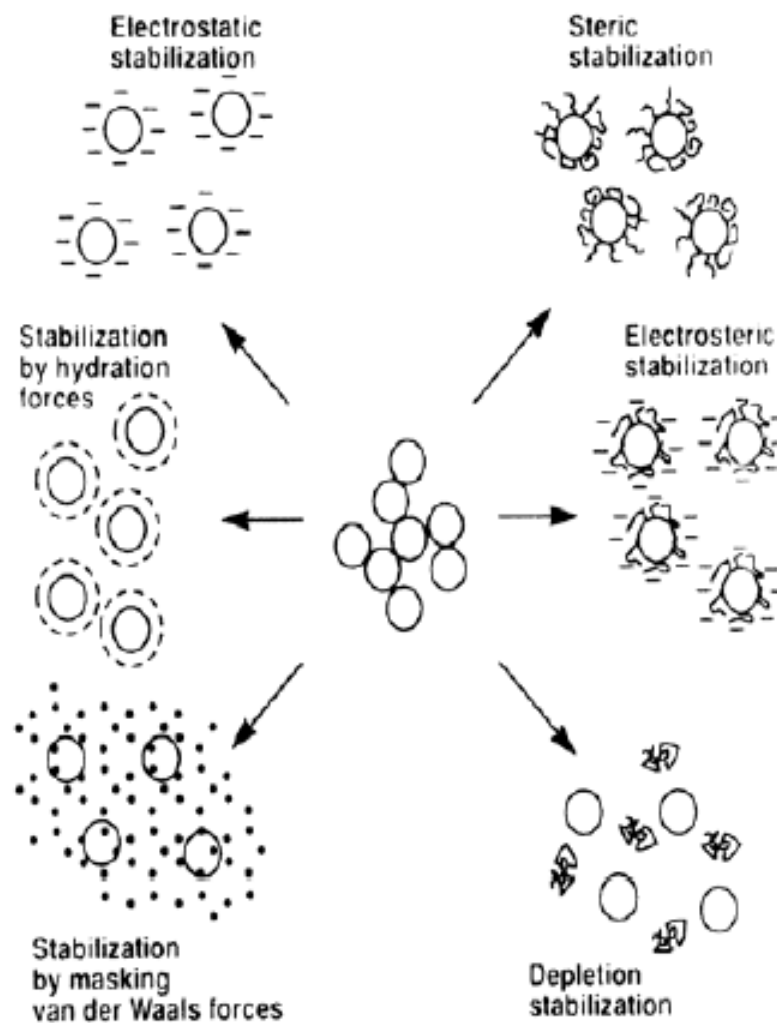
Figure 2-18 Methods of stabilising colloidal ceramic particles in liquids [83].

2.3.5   Functionalization of nanoparticles using weak interactions

The use of surfactants and polymers interacting with weak forces with nanoparticles has received much attention in dispersing nanoparticles because of significant discoveries in the dispersion of carbon and boron nitride (BN) nanotubes and, more recently, in the use of nanoemulsions to disperse single nanoparticles.

This method clearly preserves many of the attractive properties of the nanoparticles, and in some cases, the stabilizing surfactant or polymers can be removed after dispersion. A good example of this method is the non-covalent supramolecular modification of carbon nanotubes (CNTs) by

poly(*m*-phenylenevinylene)-*co*-(2,5 - dioctoxy - *p* - phenylenevinylene) (PmPV)–based polymers and starch-based amylose polymers,[17] resulting in CNT dispersion in organic and aqueous solutions, respectively.

Surfactant-assisted stabilization of CNTs, it has been observed that the solubilization occurs for anionic, cationic, and Non-ionic surfactants at concentrations significantly lower than the critical micelle concentration. The mechanisms for such dispersions are speculated to be by the formation of rod-like micelles with the nanoparticle embedded at the core of the micelle, the formation of hemi-micelles on the outside of the nanoparticles, and the random adsorption of the surfactants onto the nanotubes. Although direct imaging using electron microscopy appears to be ambiguous regarding the dispersion mechanism, small-angle neutron scattering measurements suggest that random (disordered) adsorption of the surfactant is responsible for the dispersion,[19] and these measurements have been supported recently by computer simulation studies. Regardless of the dispersion mechanism, this use of surfactants and polymers interacting with weak forces with nanoparticles has been a powerful method to disperse nanotubes in solvent and polymeric matrices.

2.3.6   Ionic interactions and covalent functionalization

Ionic and covalent functionalization of nanoparticles has been perhaps one of the most extensively studied methods for the dispersion in polymer matrices. For instance, hydroxyl-terminated silica nanoparticles have been treated with organosilanes, and naturally occurring and synthetic layered silicates with hydrated metals populating the interlayer galleries have been ion - exchanged with cationic surfactants with long alkyl or aromatic groups to render them hydrophobic and organophilic.

2.3.7   Mechanical stresses

Mechanical stresses generated by melt state shear, ultrasonication in solution, and solid- state pulverization are extremely effective in the dispersion of aggregated nanoparticles. In particular, ultrasonication has proven extremely popular in the dispersion of CNTs and is one of the few physical methods useful in the dispersion of nano tubes despite the known shortening of the CNTs when subjected to powerful ultrasonication leading to breakdown of the nanoparticle

agglomerates and subsequent individualization and dispersion of the nanoparticles in the polymer matrix.

2.3.8 Ultrasonic deagglomeration of BaTiO₃ powder

Markovic et al reported deagglomeration of $BaTiO_3$ powder ~ 1.4 μm, synthesized by solid-state reaction by high-intensity ultrasound irradiation (ultrasonication) The crystal structure, crystallite size, morphology, particle size, particle size distribution, and specific surface area of the $BaTiO_3$ powder deagglomerated for different ultrasonication times (0, 10, 60, and 180 min) were determined. It was found that the particles size of the $BaTiO_3$ powder was influenced by ultrasonic treatment, while its tetragonal structure was maintained. Therefore, they proposed ultrasonic irradiation as an environmental-friendly, economical, and effective tool for the deagglomeration of barium titanate [84].

2.3.9 Characterization of dispersion states

The most prominent ways to quantitatively characterize the dispersion state of nanocomposites include;

1. Microscopy (electron and force),
2. Scattering (x-ray, neutron, and light),
3. Chemical spectroscopic methods,
4. Electrical and dielectric characterization,
5. Mechanical spectroscopy.

Depending on the details of the nanoparticle, each of these methods can provide unique information on the state of dispersion, ranging from nanometer to micrometer in size scale.

Electron microscopy has been most extensively used to determine the nanoscale dispersion in different nanocomposites and, in many cases, to qualitatively demonstrate the development of well-dispersed systems.

Many of these methods have been extended for the use of atomic force microscopy methods in characterizing dispersions of nanotubes and spherical nano dispersions in polymers and require many sets of images and detailed data analysis. Additionally, the development of three-dimensional reconstruction [85], stereology, and high-resolution transmission electron

microscopy and scanning electron microscopy methods have all enabled significant improvements in the understanding of the 3D distribution and dispersion of the nanoparticles. Radiation scattering and diffraction methods were applied to quantify the dispersion state of the nanoparticles in the matrix. XRD is seldom used as the definitive proof of exfoliation even in those cases, because issues such as surface sensitivity and orientation of the platelets can result in ambiguous results. On the other hand, small-angle x-ray and neutron scattering (SAXS and SANS) have been used to understand the dispersion of nanoparticles such as clays and nanotubes [81].

2.4 Surfactants

2.4.1 Characteristic features of surfactants

Surfactants are used in various areas of chemical industry like motor oils in automobile, pharmaceuticals, and detergents, drilling mud used in prospecting for petroleum and floatation agent for benefaction of ores. Recently there have been wide applications of surfactants in the high-tech areas like electronic printing, magnetic recording, microelectronics and viral research.

A surface active agent (surfactant) is a substance that, when present at low concentration in a system has the property of adsorbing onto the surfaces or interfaces of the system, and of altering to a marked degree the surface or interfacial free energies of those surfaces (or interfaces). The interfacial free energy is the minimum amount of work required to create an interface between two phases.

The interfacial free energy per unit area is what we measure when we determine the interfacial tension between two phases. The interfacial free energy per unit area is the minimum work required to create that unit area of the interface. The interfacial tension is also a measure of the difference in nature of the two phases meeting at the interface (or surface). The greater the dissimilarity in their natures the greater the interfacial tension between them.

When we measure the surface tension of a liquid, we are measuring the interfacial free energy per unit area of the boundary between the liquid and air above it. When we expand an interface, the minimum work required to create the additional amount of that interface is the product of the interfacial tension γ_I and the increase in area of the interface; $W_{min} = \gamma_I * \Delta$ interfacial area. A surfactant is therefore a substance that at low concentrations adsorbs at some or all of the interfaces in the system and significantly changes the amount of work required to expand those interfaces. Surfactants usually act to reduce interfacial energy rather than to increase it, although there are instances when they are used to increase it.

2.4.2 Conditions under which interfacial phenomenon and surfactants become significant

The physical, chemical and electrical properties of matter confined to phase boundaries are often profoundly different from those of the same matter in the bulk. For many systems, even those containing a number of phases , the fraction of total mass that is localized at phase boundaries

(interfaces, surfaces) is so small that the contribution of these abnormal properties to the general properties and behaviour of the systems is negligible. There are, however, many important circumstances under which these different properties play a significant role.

One such circumstance is when the phase boundary area is so large relative to the volume of the system that a substantial fraction of the total mass of the system is present at boundaries e.g., in emulsions, foams, and dispersions of solids. In the case of nanoparticles where due to large surface area one cannot ignore the interfacial phenomena. Where a high percentage of atoms are surface or interface atoms. For example, about 50% of the atoms in spherical 5-nm particles are surface atoms. In this circumstance, surfactants can always be expected to play a major role in the system.

Another such circumstance is when the phenomena occurring at phase boundaries are so unusual relative to the expected bulk phase interactions that the entire behaviour of the system is determined by interfacial processes e.g., heterogeneous catalysis, corrosion, detergency, or flotation.

2.4.3   General structural features and behaviour of surfactants

The molecules at a surface have higher potential energies than those in the interior. This is because they interact more strongly with the molecules in the interior of the substance than they do with the widely spaced gas molecules above it. Work is therefore required to bring a molecule from the interior to the surface. Surfactants have a characteristic molecular structure consisting of a structural group that has very little attraction for the solvent, known as a lyophobic group, together with a group that has strong attraction for the solvent, called the lyophilic group. This is known as an amphipathic structure (Figure 2-19). When a molecule with an amphipathic structure is dissolved in a solvent; the lyophobic group may distort the structure of the solvent, increasing the free energy of the system. When that occurs, the system responds in some fashion in order to minimize contact between the lyophobic group and the solvent.
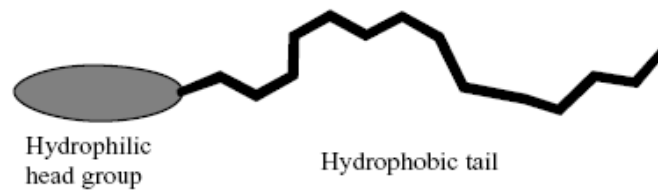
Figure 2-19 Schematic illustration of a surfactant

In the case of a surfactant dissolved in aqueous medium, the lyophobic (hydrophobic) group distorts the structure of the water (by breaking hydrogen bonds between the water molecules and by structuring the water in the vicinity of the hydrophobic group). As a result of this distortion, some of the surfactant molecules are expelled to the interfaces of the system, with their hydrophobic groups oriented so as to minimize contact with the water molecules. The surface of the water becomes covered with a single layer of surfactant molecules with their hydrophobic groups oriented predominantly toward the air. Since air molecules are essentially nonpolar in nature, as are the hydrophobic groups, this decrease in the dissimilarity of the two phases contacting each other at the surface results in a decrease in the surface tension of the water. On the other hand, the presence of the lyophilic (hydrophilic) group prevents the surfactant from being expelled completely from the solvent as a separate phase, since that would require dehydration of the hydrophilic group. The amphipathic structure of the surfactant therefore causes not only concentration of the surfactant at the surface and reduction of the surface tension of the water, but also orientation of the molecule at the surface with its hydrophilic group in the aqueous phase and its hydrophobic group oriented away from it.

The chemical structures of groupings suitable as the lyophobic and lyophilic portions of the surfactant molecule vary with the nature of the solvent and the conditions of use. In a highly polar solvent such as water, the lyophobic (hydrophobic) group may be a hydrocarbon or fluorocarbon or siloxane chain of proper length, whereas in a less polar solvent only some of these may be suitable (e.g., fluorocarbon or siloxane chains in polypropylene glycol). In a polar solvent such as water, ionic or highly polar groups may act as lyophilic (hydrophilic) groups, whereas in a nonpolar solvent such as heptane they may act as lyophobic groups. As the temperature and use conditions (e.g., presence of electrolyte or organic additives) vary, modifications in the structure of the lyophobic and lyophilic groups may become necessary to

maintain surface activity at a suitable level. Thus, for surface activity in a particular system the surfactant molecule must have a chemical structure that is amphipathic in that solvent under the conditions of use.

The hydrophobic group is usually a long-chain hydrocarbon residue, and less often a halogenated or oxygenated hydrocarbon or siloxane chain; the hydrophilic group is an ionic or highly polar group. Depending on the nature of the hydrophilic group, surfactants are classified as:

- *Anionic*. The surface-active portion of the molecule bears a negative charge, for example, $RCOO^-Na^+$ (soap), $RC_6H_4SO_3^-Na^+$ (alkylbenzene sulfonate).

- *Cationic*. The surface-active portion bears a positive charge, for example, $RNH_3^+Cl^-$ salt of a long-chain amine), $RN(CH_3)_3^+Cl^-$ (quaternary ammonium chloride).

- *Zwitterionic*. Both positive and negative charges may be present in the surface-active portion, for example, $RN^+H_2CH_2COO^-$ (long-chain amino acid), $RN^+(CH_3)_2CH_2CH_2SO_3^-$ (sulfobetaine).

- *Nonionic*. The surface-active portion bears no apparent ionic charge, for example, $RCOOCH_2CHOHCH_2OH$ (monoglyceride of long-chain fatty acid), $RC_6H_4(OC_2H_4)_xOH$ (polyoxyethylenated alkylphenol), $R(OC_2H_4)_xOH$ (polyoxyethylenated alcohol).

2.4.4 General use of charge types

Most natural surfaces are negatively charged. Therefore, if the surface is to be made hydrophobic (water-repellent) by use of a surfactant, then the best type of surfactant to use is a cationic. This type of surfactant will adsorb onto the surface with its positively charged hydrophilic head group oriented toward the negatively charged surface (because of electrostatic attraction) and its hydrophobic group oriented away from the surface, making the surface water-repellent. On the other hand, if the surface is to be made hydrophilic (water-wet able), then cationic surfactants should be avoided. If the surface should happen to be positively charged, however, then anionic will make it hydrophobic and should be avoided if the surface is to be made hydrophilic.

Nonionics adsorb onto surfaces with either the hydrophilic or the hydrophobic group oriented toward the surface, depending upon the nature of the surface. If polar groups capable of H bonding with the hydrophilic group of the surfactant are present on the surface, then the surfactant will probably be adsorbed with its hydrophilic group oriented toward the surface,

making the surface more hydrophobic; if such groups are absent from the surface, then the surfactant will probably be oriented with its hydrophobic group toward the surface, making it more hydrophilic.

Zwitterionics, since they carry both positive and negative charges, can adsorb onto both negatively charged and positively charged surfaces without changing the charge of the surface significantly. On the other hand, the adsorption of a cationic onto a negatively charged surface reduces the charge on the surface and may even reverse it to a positive charge (if sufficient cationic is adsorbed). In similar fashion, the adsorption of an anionic surfactant onto a positively charged surface reduces its charge and may reverse it to a negative charge. The adsorption of a nonionic onto a surface generally does not affect its charge significantly, although the effective charge density may be reduced if the adsorbed layer is thick.

Differences in the nature of the hydrophobic groups are usually less pronounced than those in the nature of the hydrophilic group. Generally, they are long-chain hydrocarbon residues.

Shanefield [70] suggests that a good dispersant should be soluble in the dispersing medium, have strong affinity to the particle surface and soft enough to fend off other neighboring particles. The benefits of a good dispersant are better utilized when added directly to the solvent, allowing the dispersant to react with the bare particle surface in the solvent medium itself. The dispersant-first rule of Cannon et al. 8 suggests that efficient deagglomeration can be achieved in shorter times by dispersing the powder in the solvent before adding the polymer (binder). Hence, an epoxy solution in PGMEA was added to the optimized suspensions as a subsequent step.

2.4.5   Polymer Surfactants

Surface active polymers. or polymeric surfactants, have gained in popularity during the last two decades. They are now used commercially in many different applications, among which the stabilization of dispersions and rheology control are probably the most widespread.

Surface Active Polymers can be designed in different ways

A polymer with surface active properties can be built along three *main* routes: with hydrophobic chains grafted to a hydrophilic backbone polymer. with hydrophilic chains grafted to a hydrophobic backbone and with alternating hydrophilic and hydrophobic segments. The three types will be treated individually below [86].

The classiflcation of surface active polymers into the three types mentioned above should not be seen as a clear-cut division. In reality, two or more types may be combined into one product. For example, a surface active macromolecule may have a backbone polymer consisting of alternating hydrophilic and hydrophobic segments and, in addition, contain hydrophilic or hydrophobic side chains, i.e. the molecule may at the same time be both a block and a graft copolymer. A graft copolymer may also contain both hydrophilic and hydrophobic grafts. The important feature from a physicochemical point of view is that the molecule is able to orient itself so as to expose its hydrophilic regions into a polar environment and its hydrophobic segments into a lipophilic phase. By doing so. the interfacial tension will be reduced. i.e. the polymer is by definition a surfactant.

Polymeric surfactants have attractive properties

The growing interest in polymeric surfactants can be said to emanate from two characteristic features:

1.   They have a very strong driving force to go to interfaces, with this tendency to collect at interfaces being not as dependent on the physical variables as that observed for normal. low molecular weight surfactants. This means that:

    a. The products are effective at low total concentrations:

    b. The products show little sensitivity to salts, temperature changes. etc.

2.   They can have very long chains and still be retained at interfaces. Thus, such products are very efficient stearic stabilizers for dispersed systems and effective non-fouling agents on solid surfaces.

According to Goodwin [87] synthetic polymers are also used as stabilizers. Homopolymers are not much use as stabilizers, as if they are readily soluble in the continuous phase they will not form strong effective attachments to the surface. Hence, we emulate the smaller molecules like surfactants and make the polymers contain some lyophobic blocks along the chain. Frequently, these polymers are of relatively low molecular weight, typically in the range of 5×10^3 to 50×10^3.

A polymer in solution increases the viscosity of that solution and high-molecular weight material is particularly effective at this so that only a small amount is required. When molecular weights $> 10^6$ are utilized, however, problems in rheological behavior become apparent. For example, droplets do not break away from the bulk cleanly – we have a 'stringy' behavior which is due to a marked resistance to stretching. That is, the extensional viscosity is high and applications such as spraying become difficult. One solution to this problem is to use a lower-molecular-weight

polymer and make it behave like a system of much higher molecular weight under quiescient conditions, but like a lower-molecular-weight material upon application. This is achieved by having a small mole percentage of lypophobic polymer material on the backbone of the polymer, which results in a weak assembly of these regions so that all of the polymer molecules are associated with each other. This has similarities to the self-assembly of surfactant molecules and is becoming increasingly widely utilized.

It is interesting to note that when soluble polymers are added as a rheology modifier to a colloidal dispersion, a synergistic effect is often observed. That is, the relative increase in viscosity of the dispersion is markedly greater than the relative increase found for the polymer solution on its own. What occurs here is that solution polymer, which does not adsorb to the disperse phase, produces a weak reversible aggregation of the disperse phase and this increased interaction is observed as a further change in the rheological behavior.

Polymers with charged groups are known as polyelectrolytes and these can be added as stabilizing agents for particulate dispersions or to cause aggregation. For example, poly(acrylic acid) produces a good dispersion of china clay by adsorbing onto the edges which carry a positive charge. Positively charged polyacrylamide can be used to remove negatively charged particulates by a bridging mechanism which holds particles together and makes them easy to separate. The polymer concentration required to do this is extremely low. Too high a level could give complete coverage of the surfaces by the cationic polymer and provide (unwanted) stability of the system.

2.5   Ceramic-polymer composite dielectric layers – a review

Development of electronic devices working at high operating frequencies, require new high-dielectric constant (high-K) materials that combine good dielectric properties with both mechanical strength and ease of processing. The unique combination of dielectric and mechanical properties is hard to achieve in a one component material. Pure polymers are easy to process into mechanically robust components but generally suffer from a low dielectric constant. On the other hand, typical high-K materials, such as ferroelectric ceramics, are brittle and require high-temperature processing, which is often not compatible with current circuits integration technologies. The ideal solution would be a high-K material that is mechanically robust and processable at ambient temperatures. This has raised a great interest in hybrid materials, such as ferroelectric ceramic/polymer composites, that may combine desired properties of the components.

The dielectric properties of the filler and the polymer, greatly affect the properties of the ceramic polymer composite.Choice of high-k dielectric material is always of interest. $BaTiO_3$ is widely used ferroelectric in the electronic industry. Other materials like PMN-PT, TiO_2, and, ZrO_2 are also the option as fillers. The choice of nanofillers have advantages over their counterparts i.e., micron fillers, as nanofillers are small electrical and mechanical defects. At the same time nanofillers may be a disadvantage when they lose their dielectric properties due to size effect, as in the case of $BaTiO_3$, it is widely reported [13, 49, 52, 67] that with the reduction of particle size the crystal structure of the $BaTiO_3$ is affected. $BaTiO_3$ loses its tetragonality in the nanometer regime (60-70 nm). The decrease in tetragonality results in poorer ferroelectric response of the finer ceramic. The processing of polymer nanocomposites for thin film <500 nm require that particle below 50 nm may be incorporated in the polymers to obtain smoother and defect free films. Thus there will be a tradeoff between the dielectric constant and achievable film while choosing filler size.Work of Ogitani et al. [88] suggests the selection of a polymer matrix with as high a dielectric constant as possible in order to get the best dielectric properties.

The processing of these materials is another important factor in formation ceramic polymer composite. A good dispersion of the ceramic filler implies better and more homogeneous packing resulting in a higher reliability and more uniform properties of the film. Colloidal dispersion using compatible surface treatment agents can be utilized to obtain better dispersion

and thus higher dielectric constants. Higher permittivity composites can also be obtained using higher permittivity polymers.

Composites with efficient packing are also expected to give a higher dielectric constant. This has been experimentally verified by the work of Agarwal et al. [89]. In their work, dielectric constants of the composites were found to vary between 30 and 74 depending on the dispersion and packing characteristics.

Simple theoretical equations of the dielectric properties for a particulate composite predict that higher dielectric constants can be achieved with increasing filler content. However, it can be envisaged that an optimum amount of polymer may be necessary to completely fill the particle network. Polymer volume fractions smaller than the optimum content result in a lower dielectric constant, presumably because of the residual porosity in such composites. This is depicted in Figure 2-20 which shows the variation of dielectric constant with increasing polymer content.

A lot of effort is devoted to achieve ceramic polymer composite, several authors tried different fillers and matrices to obtain good dielectric layers from 100 nm-few mm thick. One difference is quite obvious in these studies that where the layer thickness reaches to the lower limit, it is often difficult to achieve higher filler loading in polymer. Few examples with a chronological order are quoted below.
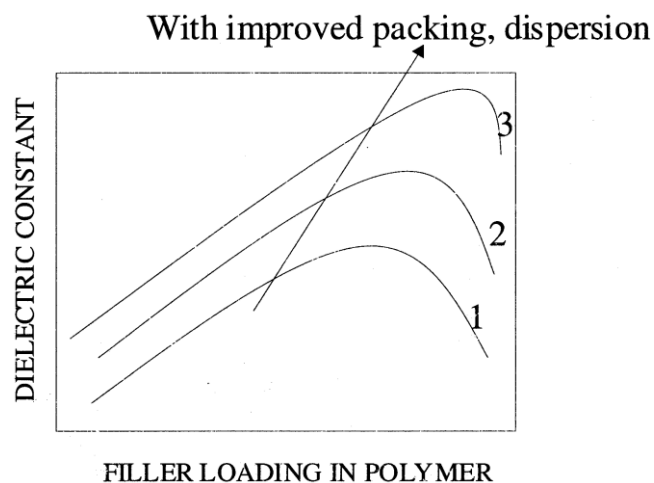
Figure 2-20 Schematic variation of dielectric constant from minimum to maximum with 0 to 100 % filler content [90].

Khastgir et al. [91] reported the dielectric properties of thick layer ~5 mm dielectric polymer nanocomposites (BaTiO$_3$ ~100-500 nm and a telecheric polydimethylsiloxane (t-PDMS)). The BaTiO$_3$, t-PDMS, and 5 % of the cross linking reagent mixture was put between two electrodes, and heated up to 80 to 100 °C under a DC electric field of 4 kV/cm.

During this procedure, t-PDMS was cross linked at about 80°°C, and orientation and configuration of the BaTiO$_3$ particles were fixed. The BaTiO$_3$ content of the elastomer was around 14 % volume fraction.

The suspension before cross linking exhibits high dielectric constant at 100 Hz. This high dielectric constant was attributed to the orientational polarization of BaTiO$_3$ particles. With increasing temperature the cross linking reaction occurred above 47°C (320 K), and ε' decreased dramatically. When the temperature was decreased, the dielectric constant did not recover to the original value and became ca. 5, irrespective of frequency. The dramatic decrease of ε' by cross linking of the PDMS matrix is due to freezing-in of the rotational degree of freedom of BaTiO$_3$ particles.
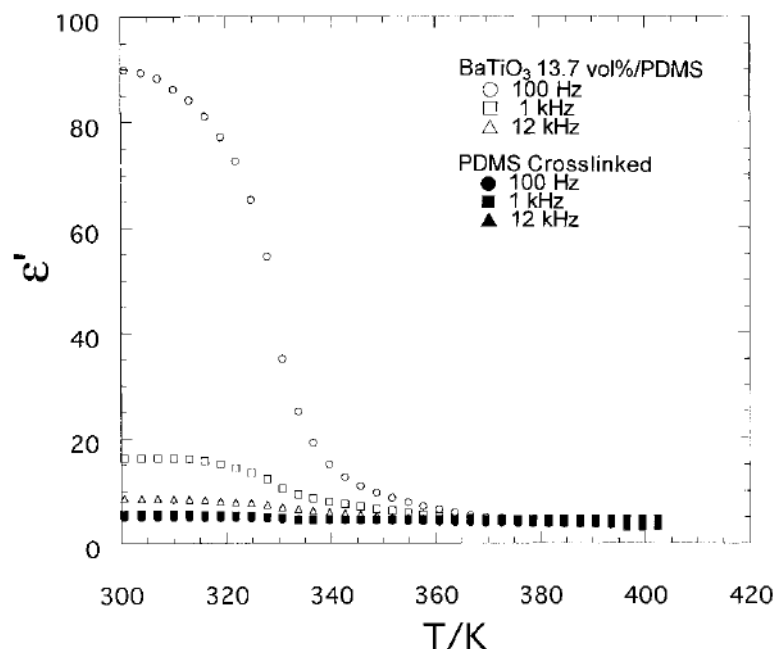
Figure 2-21   Temperature dependence of dielectric constant ε' of the BaTiO$_3$/t-PDMS/crosslink catalyst system. Open keys indicate ε' of the suspensions of BaTiO$_3$/t-PDMS/catalyst measured in the heating direction. Decrease of ε' around 330 K is due to the crosslink reaction of t-PDMS. Filled keys represent ε' of the system after t-PDMS is cross linked [91].

Khastgir et al. [91] reported that ε' decreases slightly with increasing frequency, this dielectric relaxation at room temperature was attributed to $BaTiO_3$ particles as relaxation of PDMS occurs at around -103 ˚C (170 K). ε' and ε" increased with $BaTiO_3$ concentration, i.e., at 1 kHz. ε' varies from 2.84 for the pure silicon rubber to 5.96 for a sample containing 13.7 volume % of $BaTiO_3$.
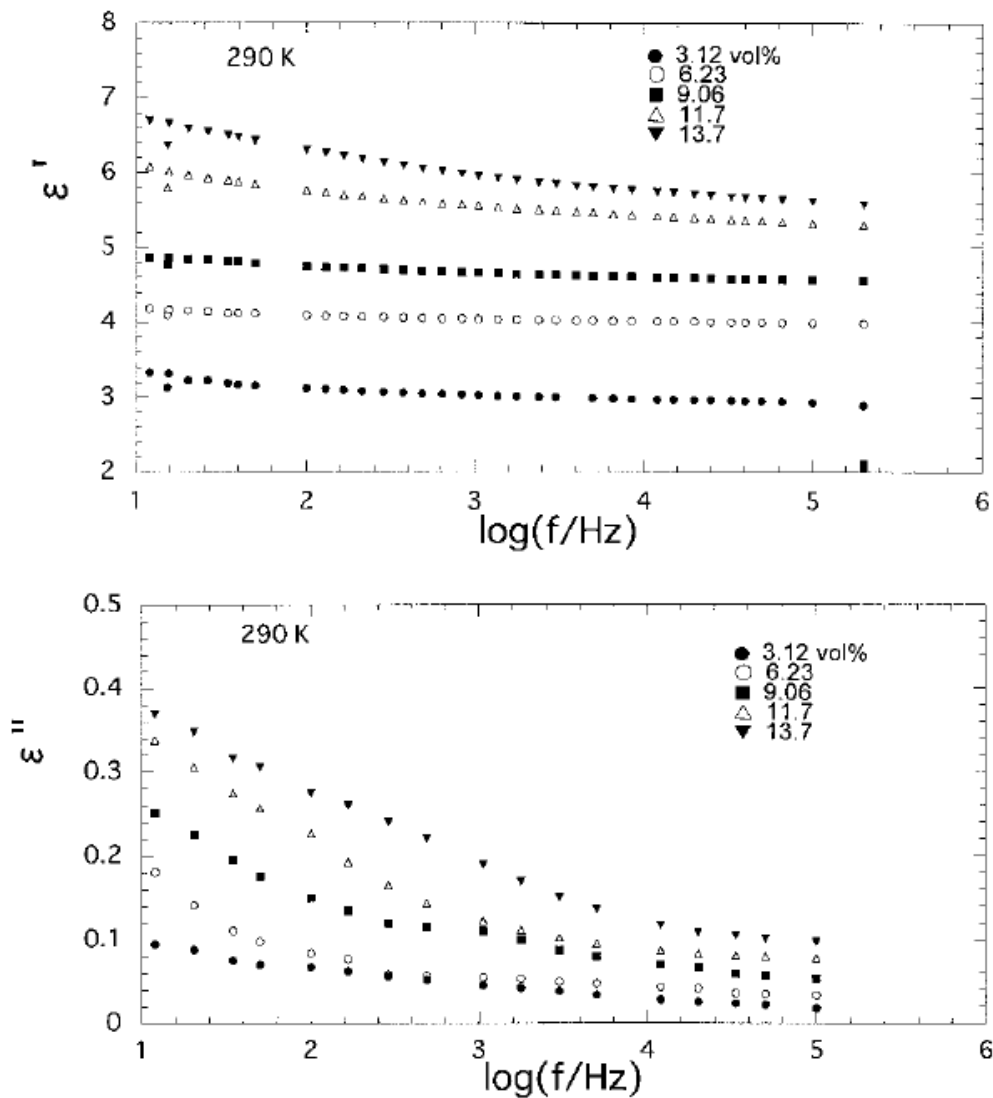
Figure 2-22   Frequency dependence of ε' and ε"at 17 ˚C for silicon rubbers containing $BaTiO_3$ [91].
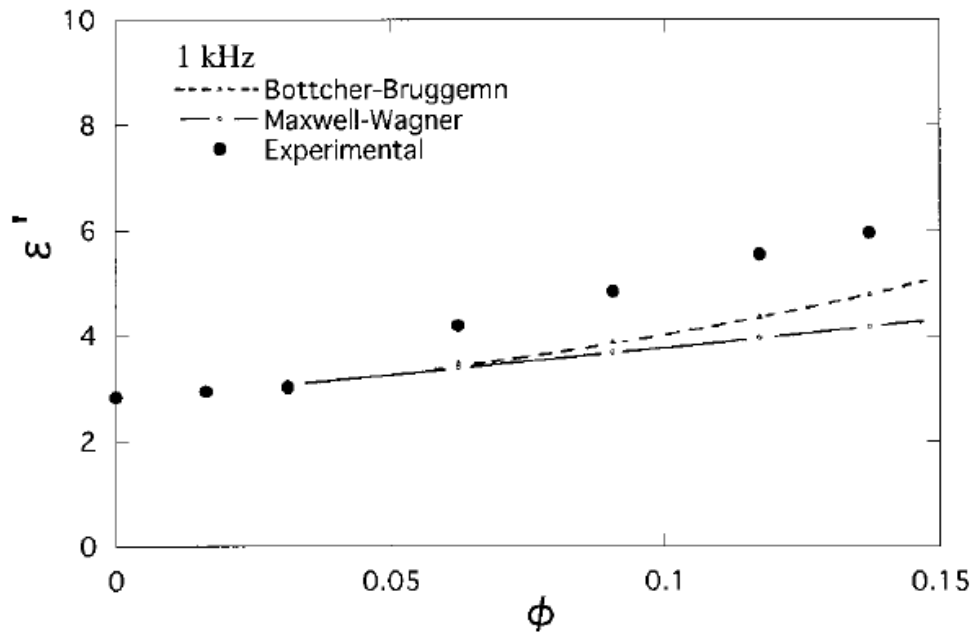
Figure 2-23   Comparison of observed ε' for silicon rubbers containing $BaTiO_3$ with the Bottcher–Bruggermn theory and the Maxwell–Wagner theory [91].

The experimental values of ε' was found to be slightly higher than the theoretical values i.e., the proposed mixing laws of Maxwell Wagner and Bottcher and Bruggeman [92] (Figure 2-23).

Rao et al. [93] reported polymer nanocomposite using Lead magnesium niobate-lead titanate (PMN-PT) as ceramic filler (average particle size 800 nm , ε_r around 17800) and two different epoxies (ε around 3 to 4) The epoxy-PMN-PT composites with different ceramic volume loading (30 %, 50 %, 60 %, 70 %, and 80 %) were mixed by ball milling for four days. Capacitors then fabricated on silicon wafer by spin on technique ~10 µm thickness. Dielectric constant values were calculated from the capacitance data at 10 kHz. A high dielectric constant (ε_r around 16 to 82) has been reported at 30 to 80 % volume fraction.

Bhattacharya et al. [94] achieved a dielectric constant in the range of 3.5 to 50 with increase in filler (PMN–PT average particle size 800 nm) loading up to 50 % volume fraction for photo-definable epoxy nanocomposite system where the dielectric constant of the host polymer was 3.5. The capacitors were stable up to a frequency range of 120 Hz to 100 kHz. For loading higher than 40 % volume fraction, authors used solvent to thin the base epoxy resin. Layer thickness was in the range of 10-20 µm.

Figure 2-24 shows dielectric constants as a function of filler loading in the photo-definable epoxy at 100 kHz composite system. A capacitance density of (6 to 8) nF/cm^2 was achieved.

Dielectric constant of epoxy nanocomposites at 100 KHz
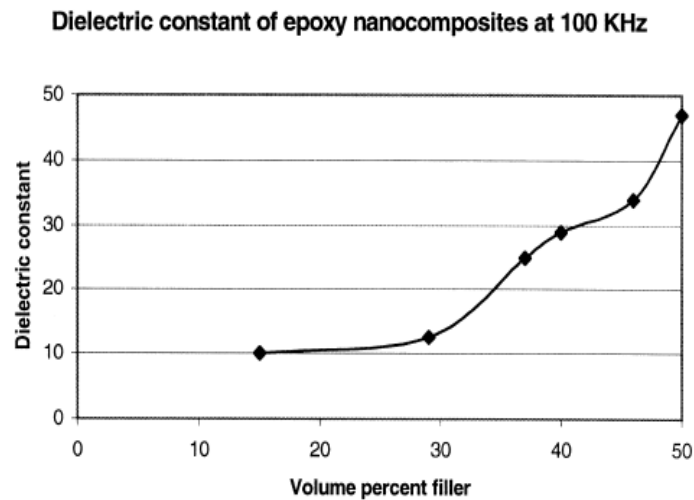
Figure 2-24   Dielectric constants as a function of filler loading in a Probimer 4959/PMN-PT composite [94].

In the same year Popielarz et al. [95] reported dielectric properties of BaTiO$_3$/polymer composites over a broad frequency range (100 Hz to 10 GHz and at -140 °C to +150 °C). BaTiO$_3$/monomer suspensions were used to obtain layers (wet thickness 100 µm) on wafers equipped with aluminum electrodes. They found that for the same BaTiO$_3$ loading polar polymers have high dielectric constant at low frequencies but there was no or little effect of polymer at gigahertz frequencies. Dielectric losses of the composites show a maximum at some intermediate frequency within megahertz to gigahertz range that reflects the relaxation behavior of the polymer matrix. Whereas, the magnitude of the losses increases with increasing polarity of the polymer component and at constant frequency and temperature, the composites follow a linear relationship between logarithm of their dielectric constant and volume fraction of the ferroelectric filler.

The highest volume fraction of 45 % was achieved for BaTiO$_3$ with 1 µm average particle size in some monomers (e.g., PEGDA) without losing the material processability. At that concentration the dielectric constant of the corresponding composite reached about 30 at 10 GHz (Figure 2-25).

The magnitude of dielectric loss is an important material parameter for making capacitors. Ideally, in a capacitor the dielectric losses should be as low as possible. It is well-known that

BaTiO$_3$ ceramic does not show significant dielectric losses up to megahertz frequencies, while the BaTiO$_3$ loss tangent reaches a maximum within the gigahertz to terahertz frequency range. Hence, the dielectric losses of the BaTiO$_3$/polymer composites observed within low frequency range (Figure 2-26) originate primarily from the polymer component.

For high-frequency applications where the dielectric losses need to be minimized, composites with non-polar polymer matrices will perform better.
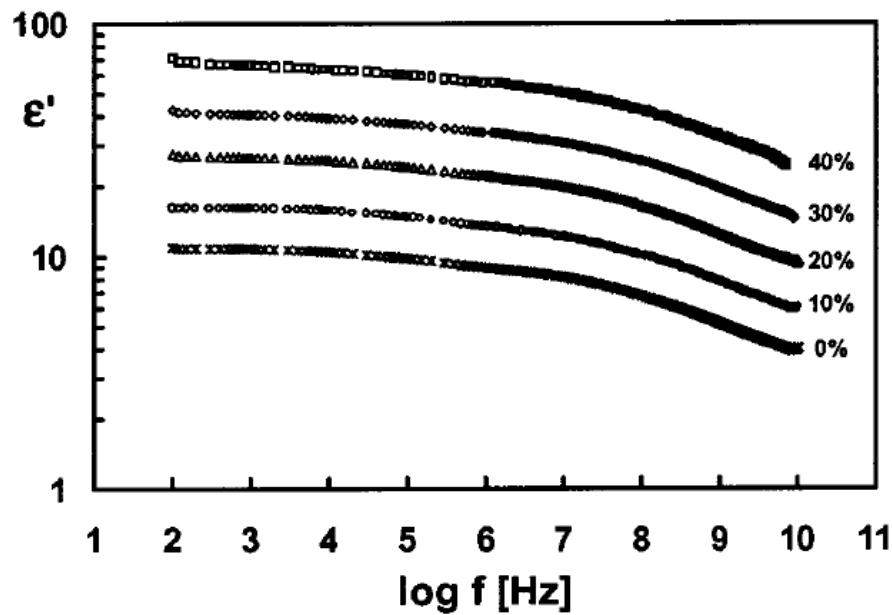
Figure 2-25   Dielectric constant of BaTiO$_3$/PEGDA composites as a function of frequency for various volume fractions of BaTiO$_3$ [95].
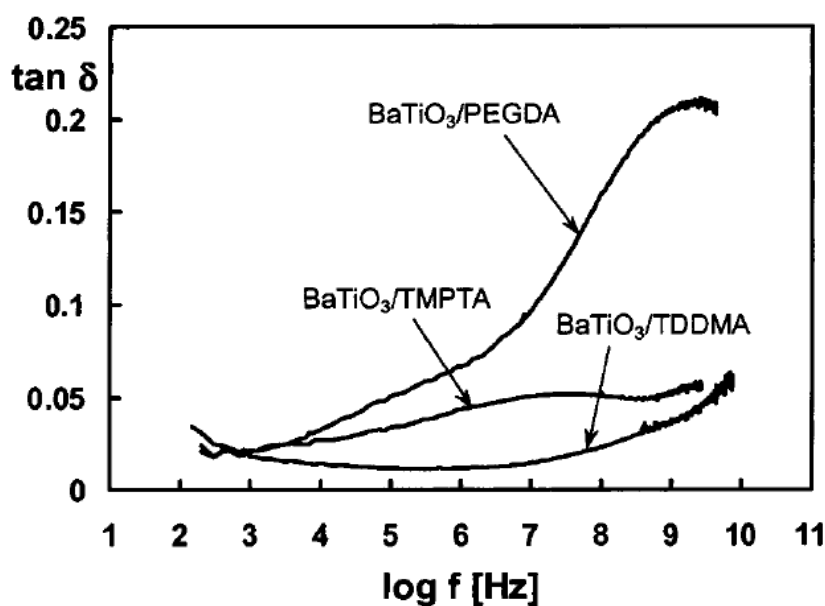
Figure 2-26   Comparison of the dielectric losses (tan δ) of 30 % BaTiO$_3$/polymer composites and the corresponding pure polymer matrices [95].

In the year 2002 Vrejoiu et al. [96] reported the production of $BaTiO_3$–polymer composite layers by the spin-on technique (thickness 3 μm to 10 μm). Perfluorocyclobutene (poly 1,1,1-triphenyl ethane perfluorocyclobutyl ether) (PFCB), was used as the polymer host material. The room temperature dielectric permittivity of 2.8-33 for the ceramic filler loading of 0 to 60% by volume was achieved. The dielectric properties of the films were observed to be almost insensitive to temperature variations in the range 20 ° to 180 °C. The adhesion of layers to the substrate was relatively weak and layers peeled off during sample cutting. The composite layers showed an increasing modulation of the film thickness with increasing filler content.
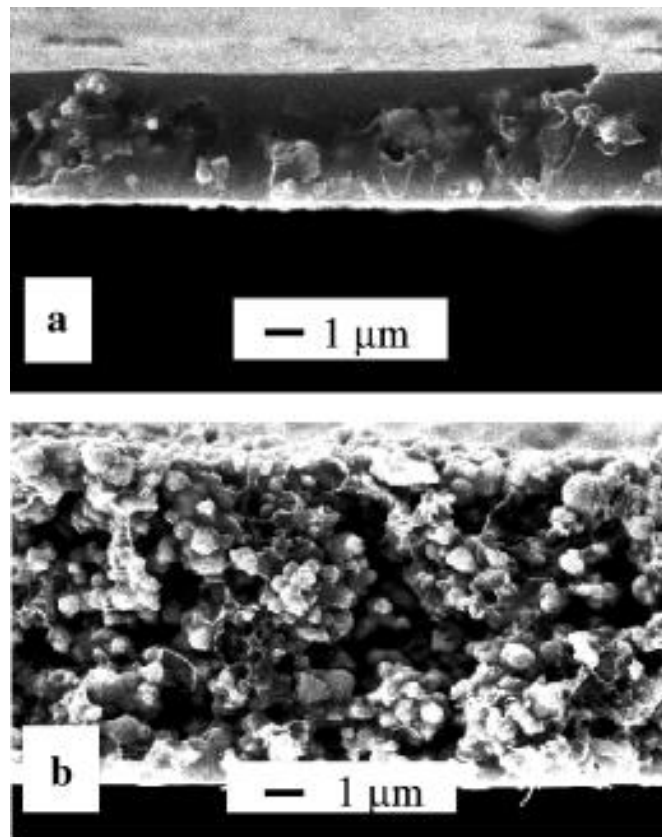
Figure 2-27   Cross section electron micrographs of free-standing $BaTiO_3$– PFCB composite layers. Ceramic filling is 10 and 50 vol% for images **a** and **b**, respectively [96].
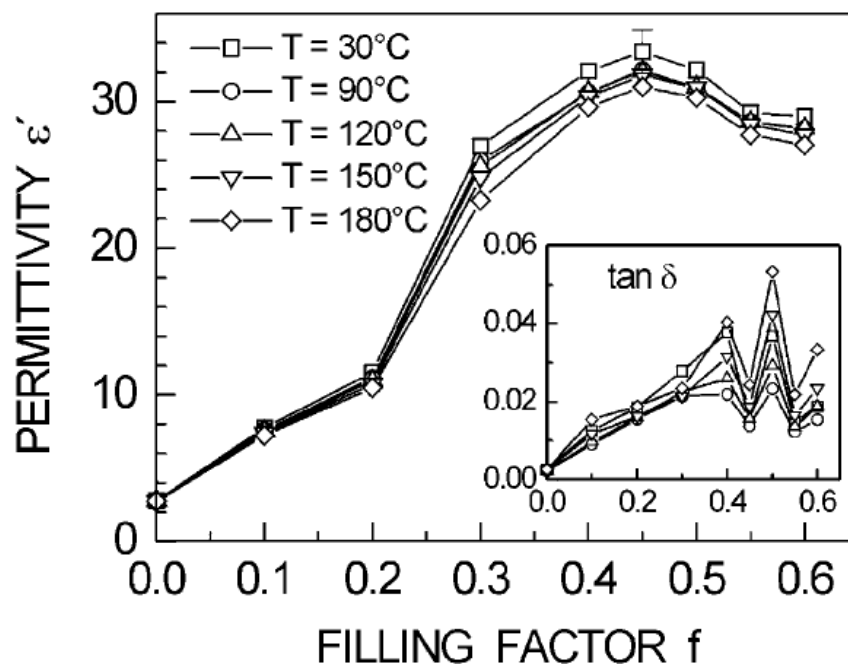
Figure 2-28   The dielectric permittivity of composite layers increases with ceramic filling (f ≤ 0.45) and reveals only a slight decrease at higher temperatures. The uncertainty of layer thickness introduces an error $\Delta\varepsilon/\varepsilon_{\_} \leq 5\%$. The inset shows the variation of the loss tangent with ceramic filling [96].

In the year 2003 Windlass et al. [90] reported to achieve high capacitance density in their composite films (thickness approx. 2 μm) with efficient filling of polymers(epoxies) with high dielectric constant ceramic powders PMN-PT and barium titanate. They optimized weight percent of dispersant by monitoring the viscosity of the suspension in propylene glycol methyl ether acetate (PGMEA).

A high positive Zeta potential was observed in their suspensions, which indicate a strong contribution of electrostatic stabilization. A dielectric constant greater than 135 was achieved in PMN-PT/epoxy system. Suspensions were made with the lowest PGMEA content using bimodal distribution technique i.e., filling the interstitial empty spaces between large particles with finer particles, helped to obtain ultra-thin capacitor films (< 2 μm) with capacitance of 35 nF/cm^2.

Recently Kobayashi et al. [97] reported the formation of high dielectric thin film of polymer nanocomposites, the polymer-poly vinylidene fluoride (PVDF - ε_r around 12) was loaded with nanometer sized barium titanate (crystal size approx. 10.5 nm to 34.6 nm). Since the average size of the particles observed by TEM was close to the crystal size by XRD, the particles are

considered to mainly consist of single crystals) particles synthesized with a complex alkoxide method already suspended in NMP (PVDF 5 wt % in NMP solution). Polymer/*N*-methyl-2-pyrrodinone solution suspending the $BaTiO_3$ particles was spin-coated on ITO (tin-doped indium oxide) glass substrates to prepare polymer-based composite films of submicron meters thickness (150-500 nm). The good dispersion of the particles in the PVDF film yielded a smooth surface of the film i.e., a root mean square roughness less than 20 nm at a particle volume fraction of 30 %. With the increase in the $BaTiO_3$ crystal size from 10.5 to 34.6 nm at a particle volume fraction of 30 % increased the dielectric constant of the film increased from 20.1 to 31.8. The dissipation factor of the PVDF composite film was found to be 0.05 at 10^4 Hz.
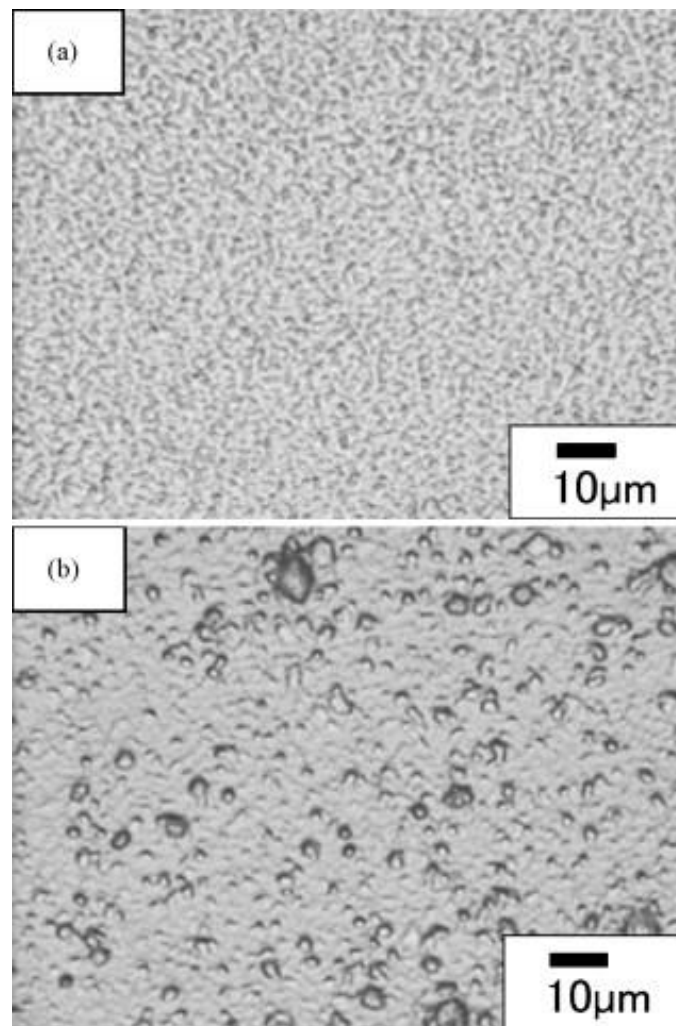
Figure 2-29   Optical micrographs of (a) $BaTiO_3$–PVDF and (b) $BaTiO_3$–SPAI composite films. $BaTiO_3$ crystal size: 27.3 nm, volume fraction 30 %, spin speed 3000 rpm and drying temperature 150 °C [97].

Theoretical models have been proposed in the literature for predicting the effective dielectric constant of polymer ceramic nanocomposites for simulating the electrical and mechanical properties of the composites. In most cases, composite dielectrics are chaotic or randomly dispersed systems of several components. The most commonly used equation is the Lichtenecker logarithmic law in mixing and is written for a two-component system is shown as Equation 2-1. Equation 2-2 is a modified-form of Lichtenecker equation, where 'k' is a fitting constant subject to composite material. It is reported that it has value around 0.3 for most well-dispersed polymer–ceramic composites [93].

Equation 2-1

$$Log\varepsilon_{eff} = Vf_a Log\varepsilon_a + f_b Log\varepsilon_b$$

Equation 2-2

$$Log\varepsilon_{eff} = Log\varepsilon_a + f_b(1-k)Log\frac{\varepsilon_b}{\varepsilon_a}$$

ε_{eff} is the effective dielectric constant of the composite, f_i, is the volume fraction of material i $(i=a, b)$, and ε_i is the dielectric constant of that material.

Some authors [91, 93, 98] tried to use effective-medium theory (EMT) to predict dielectric constant of polymer ceramic nanocomposite.

Effective-medium theories can be applied to a wide variety of problems in the general area of condensed matter. In case of an arbitrary composite system consisting of a random distribution of homogeneous materials possessing their own properties, the properties of the composite can be extracted from equations describing the dielectric response of the system of interest [98]. The Maxwell–Garnett [99], and the Bruggeman theory [92], are the most widely used methods for calculating the bulk dielectric properties of composite materials. They have the same generic expression for an effective medium with two components, a and b, with dielectric functions ε_a and ε_b, and with volume fractions f_a and f_b, respectively,

$$\frac{(\varepsilon_{eff} - \varepsilon)}{(\varepsilon_{eff} + 2\varepsilon)} = fa\frac{(\varepsilon_a - \varepsilon)}{(\varepsilon_a - 2\varepsilon)} + fb\frac{(\varepsilon_b - \varepsilon)}{(\varepsilon_b + 2\varepsilon)}$$

Where, ε_{eff} is the dielectric function of the effective medium. The quantity ε is a dielectric function that is assigned to different values according to the model.

(i) For the Maxwell–Garnett model, one of the components is chosen as a host medium, for example component a, in which inclusions of the other components are embedded. Then ε is equal to ε_a and the corresponding term of the right-hand side of equation above thus vanishes. This model is generally used in the case of particles of component 'b' randomly distributed in the continuous medium 'a' and sufficiently far from each other to avoid direct mutual interactions.

$$\frac{(\varepsilon_{eff} - \varepsilon_a)}{(\varepsilon_{eff} + 2\varepsilon_a)} = fb \frac{(\varepsilon_b - \varepsilon_a)}{(\varepsilon_b + 2\varepsilon_a)}$$

$$\varepsilon_{eff} = \varepsilon_a \frac{(2\varepsilon_a + \varepsilon_b + 2f_b(\varepsilon_b - \varepsilon_a)}{((2\varepsilon_a + \varepsilon_b - f_b(\varepsilon_b - \varepsilon_a)}$$

(ii) For the Bruggeman model, the effective medium itself acts as the host medium (self-consistent approach) and then ε is equal to ε_{eff} . In this case the left-hand side of Eq. above vanishes. This model is generally used in the case of particles of both 'a' and 'b' components randomly distributed in the sample.[98]

$$0 = f_a \frac{(\varepsilon_a - \varepsilon_{eff})}{(\varepsilon_a - 2\varepsilon_{eff})} + f_b \frac{(\varepsilon_b - \varepsilon_{eff})}{(\varepsilon_b + 2\varepsilon_{eff})}$$

In order to account for the morphology of ceramic particles, a shape factor 'n' is introduced by Rao et al. [93].

$$\varepsilon_{eff} = \varepsilon_b \left[1 + \frac{f_a(\varepsilon_a - \varepsilon_b)}{\varepsilon_b + n(1 - f_a)(\varepsilon_a - \varepsilon_b)} \right]$$

Equation above is the EMT model for the effective dielectric constant prediction of polymer ceramic nanocomposite. The only restriction of using this model is that the particle size should be very small, which is suitable to nanocomposite.

Khastgir et al employed the Wagner theory to compare their system by using the approximation $\varepsilon_b \gg \varepsilon_a$.

$$\Rightarrow \varepsilon_{eff} = \varepsilon_a \frac{2\varepsilon_a + \varepsilon_b + 2f_b(\varepsilon_b - \varepsilon_a)}{2\varepsilon_a + \varepsilon_b - f_b(\varepsilon_b - \varepsilon_a)}$$

When $\varepsilon_b \gg \varepsilon_a$, equation reduces to

$$\Rightarrow \varepsilon_{eff} = \varepsilon_a \frac{(1 + 2f_b)}{(1 - f_b)}$$

They suggested that, the error of the estimation of ε_b does not affect much the theoretical value.

2.6   Thin dielectric films

According to Gregor [100] a thin polymer dielectric film is a solid layer of more or less homogeneous composition which is less than 3 µm thick, uniform in thickness, coherent in structure and adherent upon a supporting surface. The definition foreshadows the primary employment of such films, as capacitor dielectrics, for thin film circuit insulation, and for basic investigation of electrical conductivity and surface phenomena.

2.6.1   General properties of thin dielectric films

Thin dielectric films possess some characteristic properties independent of their composition. Perhaps the most significant property is the fact that the thickness is very small compared to other dimensions; hence the electric field in the insulator can be quite large. Thus the insulator is often subjected to field strengths well beyond those at which the bulk material undergoes dielectric breakdown. This phenomenon of increasing dielectric strength with decreasing insulator thickness is well-known and has been discussed extensively by Whitehead [101] and O'Dwyer [102]. It is generally accepted that when the dimensions of the insulator become smaller than the energetic electron path in the insulator, the dielectric strength increases since avalanche and thermal breakdown are less likely to occur. Thus intrinsic breakdown becomes the predominant mechanism in very thin films. Another aspect of thin-film dielectric behavior is that the actual potential distribution in the insulator at the metal-insulator interface varies over a region which is not negligible compared to the total insulator thickness. Hence the geometric capacitance and the measured capacitance for such a structure may be considerably different.
This problem is discussed by Ku and Ulmann [103].

Since the film thickness is small, compared to area coverage, the problem of "pinholes," or regions where the film does not cover the underlying surface, is quite significant. This, of course, is common to all thin films, inorganic as well as organic, but there are several specific points which are worth discussing in detail. Inorganic insulating films are usually produced by deposition techniques such as evaporation, vapor growth, sputtering, etc. The exceptions are materials such as thermally grown SiO_2 and anodic Ta_2O_5. Almost all polymer films are produced by chemical reaction at the surface, either from conversion of monomer to polymer or through an increase in average polymer molecular weight or an increase in polymer cross linking. Indeed, all three processes may take place in the same film deposition. The important point is that polymer film deposition processes are not self healing, so great care must be used in

substrate preparation and cleanliness to insure that the polymer film can be deposited uniformly over the entire surface. Although there are other contributing factors, the presence of pinholes determines the minimum thickness at which a polymer film will provide reliable electrical insulation. This minimum thickness varies from one type of film and process to another, but is of the order of 100 ˚A. Second, there are special instances where very thin polymer insulation can be achieved.

Finally, the absence of large stresses in most polymer films reduces the likelihood of cracking or rupture after deposition. This is a serious problem with many inorganic films.

An important property displayed by thin-film insulators **is** their ability to conduct appreciable non-ohmic currents due to the mechanisms of electron tunneling, field emission, space-charge-limited conduction and impurity conduction [100].

2.6.2   Polymer dielectric layers

The polymer film should have a low electrical conductivity and a small dissipation factor, with few peaks in the dispersion curve versus frequency. It is desirable that the intrinsic breakdown voltage be high. The dielectric constant requirements depend on the use to which the film is put, but in general this constant is to be kept as low as possible. In all these properties, the polymer films to be discussed vary from good to excellent.

In addition to such general electrical properties, polymer films also have some advantageous physico-chemical features. Thus, many polymer films are able to undergo plastic deformation when a stress is applied, minimizing residual stress in the films. This property also is advantageous in reducing the amount of inherent stress after deposition or growth. One of the important factors in this case is the amorphous structure of most polymers.

There are a number of disadvantages in the use of polymer insulating films as well. Perhaps the most severe is the temperature limitation due to the presence of such relatively labile bonds as C-C and C-H in almost all polymer structures. While advances in the chemistry of polymers may push the maximum temperature limit upward to some extent, polymer films at present are limited to operating temperatures below about 150 ˚C.

The chemical stability of polymer films is determined by the nature of the polymer and of the attacking substance.

2.7 Substrate for thin film deposition

2.7.1 Self assembled monolayer

Bare surfaces of metals and metal oxides tend to adsorb adventitious organic materials readily because these adsorbates lower the free energy of the interface between the metal or metal oxide and the ambient environment. These adsorbates also alter interfacial properties and can have a significant influence on the stability of nanostructures of metals and metal oxides; the organic material can act as a physical or electrostatic barrier against aggregation, decrease the reactivity of the surface atoms, or act as an electrically insulating film. Surfaces coated with adventitious materials are, however, not well defined: they do not present specific chemical functionalities and do not have reproducible physical properties (e.g., conductivity, wet ability, or corrosion resistance).

Self-assembled monolayer (SAM) provides a convenient, flexible, and simple system with which to tailor the interfacial properties of metals, metal oxides, and semiconductors. SAMs are organic assemblies formed by the adsorption of molecular constituents from solution or the gas phase onto the surface of solids or in regular arrays on the surface of liquids (in the case of mercury and probably other liquid metals and alloys); the adsorbents organize spontaneously (and sometimes epitaxial) into crystalline (or semi crystalline) structures. The molecules or ligands that form SAMs have a chemical functionality, or "head group", with a specific affinity for a substrate; in many cases, the head group also has a high affinity for the surface and displaces adsorbed adventitious organic materials from the surface. The high affinity of thiols for the surfaces of noble and coinage metals makes it possible to generate well-defined organic surfaces with useful and highly alterable chemical functionalities displayed at the exposed interface [104].
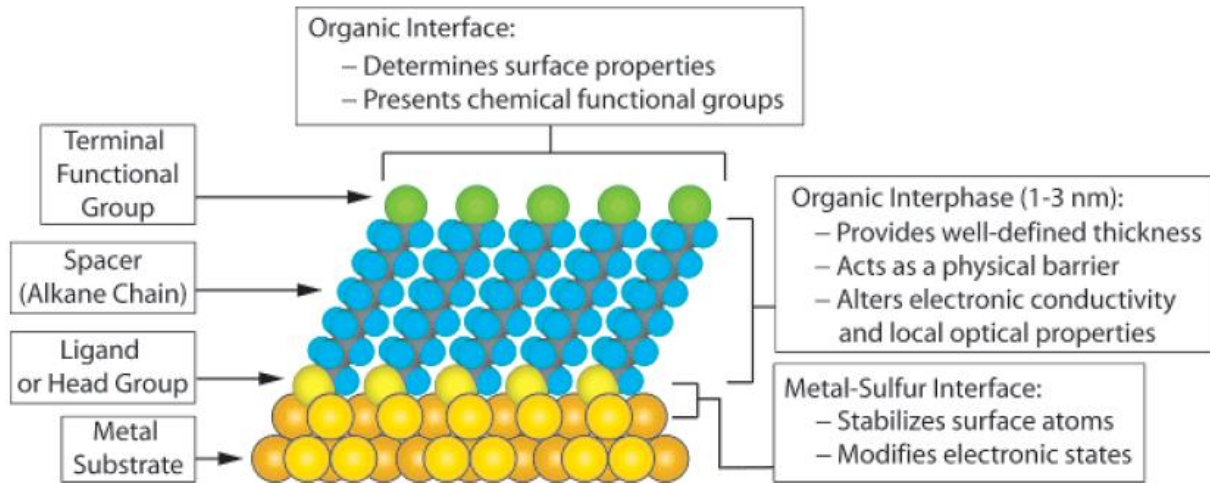
Figure 2-30   Schematic diagram of an ideal, single-crystalline SAM of alkanethiolates supported on a gold surface

2.7.2   Tin-doped Indium oxide (ITO)

Indium tin oxide (ITO, or tin-doped indium oxide) is a mixture of indium(III) oxide (In_2O_3) and tin(IV) oxide (SnO_2), typically 90 % In_2O_3, 10 % SnO_2 by weight. Highly conductive and transparent thin films are widely used as electrode layers in optoelectronic devices, such as in flat panel displays, liquid crystal displays, organic light emitting diodes, touch panels, solar cells, electro chromic devices [105].

3 Experimental Procedure

3.1 Hydrothermal synthesis of BaTiO$_3$ nanoparticles

Ba(OH)$_2$·8H$_2$O Barium Hydroxide Octahydrate, was used as barium precursor while various precursors of titania (TiO$_2$ Tronox powder, P25 Degussa powder and, spindle like rutile) were used for hydrothermal synthesis of BaTiO$_3$.

3.1.1 Use of TiO$_2$ Tronox powder and TiO$_2$ P25 Degussa powder for synthesis of BaTiO$_3$

Ba(OH)$_2$·8H$_2$O Barium Hydroxide Octahydrate, obtained from Sigma Aldrich was used as barium precursor whereas two different precursors of titania TiO$_2$ Tronox powder and TiO$_2$ P25 Degussa powder, were used for hydrothermal synthesis of BaTiO$_3$. SEM micrographs are shown here in Figure 3-1 , while Table 3-I shows the size and phases of the used TiO$_2$ powders. The Ba to Ti ratio was kept one in most of our experiments here otherwise it will be mentioned. As synthesis of BaTiO$_3$ consumes equimolar ratio of Ba and Ti. 19.75 g of Ba(OH)$_2$·8H$_2$O and 5 g of TiO$_2$ were added to to a Teflon vessel along with 30 ml distilled water. No mineraliser was used to adjust the pH of the solution. The concentration of Ba is such that the alkalinity of Ba(OH)$_2$ aqueous solution is sufficient for the precipitation of BaTiO$_3$. The pH of the solution at this concentration of Ba is in the range 9 to 10.

Table 3-I   Properties of two TiO$_2$ precursors used for hydrothermal synthesis of BaTiO$_3$

Type	Brand Name	Particle Size	Phase
A	TiO$_2$ Tronox	125 nm	Anatase
B	TiO$_2$ P25 Degussa	25 nm	Rutile 30 %
			Anatase 70 %
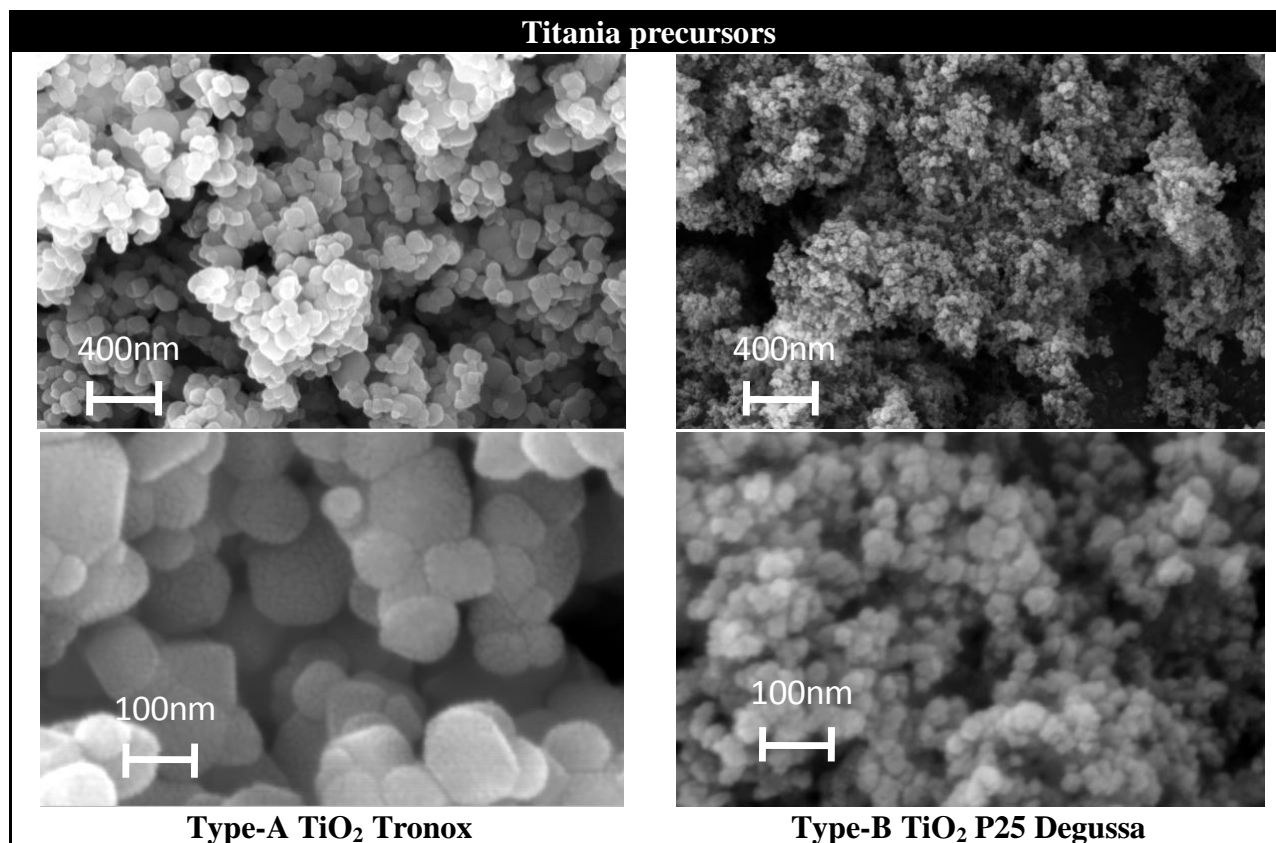
Figure 3-1   SEM micrographs of two TiO$_2$ precursors used for hydrothermal synthesis of
BaTiO$_3$

The mixed Ba and Ti precursor were treated at different temperatures 60 ˚C, 90 ˚C, 120 ˚C and 150 ˚C for different reaction times 16 h, 24 h, 48 h, and in some case for longer times in Autoclave BLH800 (Figure 3-2 Berghof- Germany, operated by computer using P4 MESS software to log temperature and pressure) having maximum volume of 250 ml, maximum pressure of 150 bar and highest attainable temperature of 250 ˚C. All the reaction took place for said times after the temperature have achieved a said value. In all our reactions the temperature rises to +10 ˚C above the prescribed temperature in the first hour of the experiment and then kept constant and the adjusted temperature for the whole reaction time mentioned here. The reactions took place at autogenously attained pressure in the vessel during heating at a particular temperature; no external pressure was applied during the reaction. The obtained slurry is washed with 100 ml of 1 M formic acid and then dried at 100 ˚C under ambient atmosphere. The cake was grinded using an agate mortar to achieve BaTiO$_3$ powder.

Figure 3-2   Autoclave BLH800 from Berghof- Germany, operated by computer using P4 MESS software to log temperature and pressure.

3.1.2 Use of spindle like TiO$_2$ (rutile phase) as Ti-precursor

Hydrothermal synthesis of BaTiO$_3$ was performed using spindle like TiO$_2$ Figure 3-3 as Ti-precursor, whereas Ba(OH)$_2$·8H$_2$O was used as Ba- precursor in equimolar ratio to titanium precursor, no mineraliser was used. Both precursors were added along with 30 ml double distilled water to a Teflon vessel in the autoclave. The reaction proceeded at 90 ˚C for 48 h without stirring to note the morphology change of obtained product in comparison to morphology of the titania precursor used in the reaction. The obtained slurry was washed with 100 ml of 1M formic acid and then washed with distilled water to remove BaCO$_3$. The powder was dried and grinded with agate mortar to obtain BaTiO$_3$ powders.
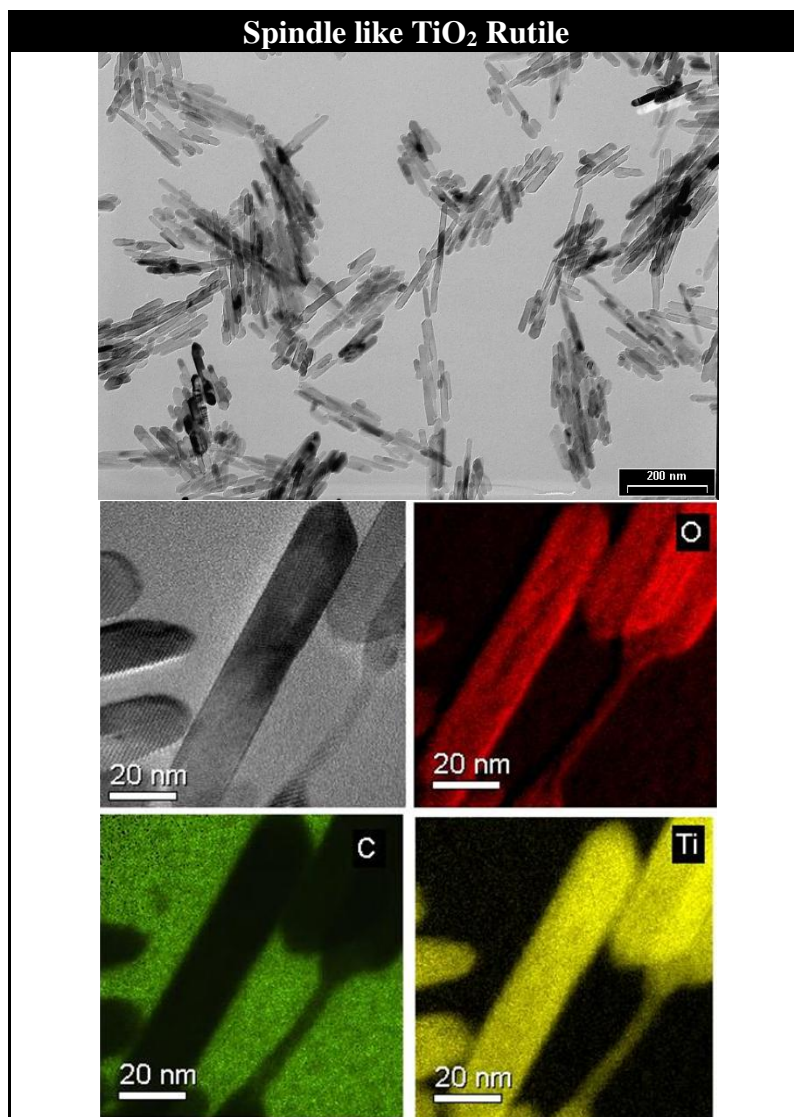
Figure 3-3   HR TEM images and elemental mapping of spindle like TiO_2 rutile phase used for
hydrothermal synthesis of $BaTiO_3$

3.1.3   Use of barium stearate and titanium tetrachloride

Barium stearate $(C_{17}H_{35}COO^-)_2 \ Ba^{2+}$ was used instead of Barium Hydroxide, as barium precursor, while titanium tetrachloride $(TiCl_4)$ was used as titanium precursor. The Ba : Ti ratio was kept 1. KOH was used as mineraliser to raise the pH of the solution to 10, water was used as solvent in the reaction. The solution was kept in autoclave at 190 ˚C for 24 h. Obtained slurry was dried and kept for XRD examination.

3.2   Solvothermal synthesis of BaTiO$_3$

The use of solvents other than water, were as well tested to achieve the tetragonal phase and different morphology of nanoparticles of BaTiO$_3$. An ethanol-water mixture was used under different temperature and time.

Ba(OH)$_2$.8H$_2$O Barium Hydroxide Octahydrate, as barium precursor and TiO$_2$ P25 Degussa powder were used for solvothermal synthesis of BaTiO$_3$. The Ba to Ti ratio was kept 2 : 1 in our experiments. Both precursors were weighed and added to a Teflon vessel along with distilled water and ethanol in equal amounts i.e., 30 ml each. No mineraliser was used to adjust the pH of the solution. The mixed Ba and Ti precursor were treated at different temperatures 185 ˚C for 2 and 6 days, and at 235 ˚C for 1 day in autoclave BLH800. All the reaction took place for said times after the temperature have achieved a particular value.

The obtained slurry is washed with 100 ml of 1 M formic acid and then dried in oven at 100 ˚C under normal conditions. The cake was grinded using agate mortar to achieve BaTiO$_3$ powders.

3.3 Dispersion of BaTiO$_3$ in PMMA

3.3.1 Dispersion of BaTiO$_3$ nanoparticles in different solvents

Several solvents tested to disperse the obtained BaTiO$_3$ powders are listed below;

1. Ethanol (EtOH)
2. Tetrahydrofuran (THF)
3. Acetone
4. Hexane
5. Toluene
6. Isopropanol
7. Chlorobenzene (MCB)

Equal amount of BaTiO$_3$ powder (0.05 g) was weighed and added to 10 ml of solvent in small bottles and sonicated for 15 min each in ultrasonication bath under ambient conditions. The bottles were placed to see sedimentation over the time.

EtOH and Acetone were added in different ratios (1:1, 2, 3, 4, 5, 10 = EtOH: Acetone) and tested to disperse BaTiO$_3$ nanopowders in order to achieve best combination of different solvents for dispersing BaTiO$_3$ powders.

3.3.2 Choice of solvent for dissolution of poly(methyl methacrylate) (PMMA) and different molecular weights (MWs) of PMMA

PMMA was dissolved in different solvents namely acetone, tetrahydrofuran (THF), chlorobenzene (MCB) and toluene in different concentrations 10 g/L, 20 g/L, 200 g/L and 400 g/L to obtain PMMA solution in a particular solvent for its future use in polymer composites. The said amount was added to a beaker along with a solvent and refluxed at or below the boiling point of a particular solvent to obtain a PMMA solution.

Different molecular weights of PMMA were obtained from ACROS and Sigma Aldrich and used to obtain PMMA solutions. The different molecular weights (MW) of PMMA used are listed below:

- ACROS 35000 MW
- Sigma Aldrich 120,000 MW
- Sigma Aldrich 350,000 MW

3.3.3   Vacuum drying of BaTiO₃ powders

To improve the dispersibility of BaTiO$_3$ the already dried powders were again dried in vacuum furnace (0.1 mbar) at 110 ˚C for 5 days and vacuum dried powders were kept in plastic bottles in the desiccators for future use. The dried beads of silica gel were used as desiccant.

3.3.4   Ultrasonication as mode for deagglomeration of BaTiO₃ nanopowders

Ultrasonication technique is used for deagglomeration of BaTiO$_3$ powders. A known amount of BaTiO$_3$ powders is added to a certain solvent and sonicated at room temperature for 15 to 30 min. Ultrasonication is used in all our experiements without surfactant, with surfactant, and with polymer.

3.3.5   Post functionalization of BaTiO₃ particles

Stearic acid (Octadeconic acid C$_{18}$H$_{36}$O$_2$) was used for the post functionalization of already obtained BaTiO$_3$ powders. Stearic Acid is a commonly used surfactant and tested to disperse BaTiO$_3$ in PMMA.

A known amount of BaTiO$_3$ was added to an already obtained solution of stearic acid in acetone / THF. The weight of the surfactant used was 4 times the weight of BaTiO$_3$ (400 weight percent of BaTiIO$_3$). The BaTiO$_3$ powder was dispersed in the solution by ultrasonic activation for 15 min.

PMMA in acetone / THF were then added and ultrasonic treatment was done for15 minute. The weight percent of PMMA in suspension was kept equal to 0.56. 1 to 10 volume percent fraction of BaTiO$_3$ in PMMA was varied

In case of PMMA in Acetone EtOH-Acetone was used to disperse BaTiO$_3$ first and then PMMA in acetone was added.

In case of PMMA in THF stearic acid was dissolved in THF and BaTiO$_3$ already sonicated in THF were mixed with PMMA in THF.

3.3.6   Choice of surfactant for dispersions

Different surfactants were tested to find the best surfactant for dispersing $BaTiO_3$ nanoparticles in solvents which are suitable for dissolving PMMA.

Different ionic, cationic and non–ionic surfactants listed below in Table 3-II were added to solvents. In the next step $BaTiO_3$ was added (surfactant: $BaTiO_3$ = 10: 1) and ultrasonicated for 15 min. The dispersions were kept for a certain period to observe the effect of surfactant.

Brij 35 P was used in to test dispersing $BaTiO_3$ powder along with PMMA. Brij 35 P 10 times the weight of $BaTiO_3$ was added to 10 ml THF and stirred on hotplate to dissolve Brij in THF. After dissolution of Brij 35 P, $BaTiO_3$ 9 % volume fraction of PMMA was added to this solution and stirred in ultrasonic bath for 15 min. About 0.56 weight percent PMMA in solvent was added from an already obtained PMMA solution in THF and sonicated for 15 more minutes. The stable dispersion was used for dip coating the glass slides. The layers were characterized using SEM.

Table 3-II   Different surfactants were tested to achieve a stable dispersion of $BaTiO_3$ in THF

Sr.Nr.	Name		Type	Formula
1. Brij	Tricosaethyleneglycol dodecylether	HLB	Non-ionic	$CH_3(CH_2)_{10}CH_2(OHCH_2CH_2)n$ OH
	35 P	16.9		
	78	15.3		
	700	18		
	76	12		
	30	9		
2.Cetrimonium bromide	Hexadecyltrimethylammonium Bromide		Cationic	$(C_{16}H_{33})N(CH_3)_3Br$
3. Stearic Acid	Octadecanoic acid		Non-ionic	$CH_3(CH_2)_{16}COOH$
4. SDS	Sodium dodecyl Sulfate		Anionic	$NaC_{12}H_{25}SO_4$
5. Co-Polymer	Poly(methyl methacrylate-co methacrylic acid		Non-ionic	$CH_2C(CH_3)(CO_2CH_3)]_X$ $[CH_2C(CH_3)(CO_2H)]_Y$

3.3.7 Varying Surfactant to BaTiO₃ concentration

After finding suitable surfactant, the concentration of surfactant had to be optimised. For that different concentration ratios of surfactant were tested. The ratio of the surfactant to BaTiO$_3$ was varied in the range 5, 3.33, 2 and 1 times the weight of the filler in the dispersion while the concentration of PMMA in all the case was kept equal to 0.374 weight percent of the solvent used to obtain dispersions. As surfactants are usually used in low concentrations, 10 % , 5 % and 2.5 % weight of BaTiO$_3$ was as well tested to obtain dispersions.

3.3.8 Brij HLB observations

A set of experiment was performed to confirm the best brij surfactant on the basis of hydrophilic lypophilic balance (HLB) criteria. The Hydrophilic-lipophilic balance of a surfactant is a measure of the degree to which it is hydrophilic or lypophilic, determined by calculating values for the different regions of the molecule. An HLB value of 0 corresponds to a completely hydrophobic molecule, and a value of 20 would correspond to a molecule made up completely of hydrophilic components. Different Brij samples namely Brij 35 p, 78, 700, 76, and 30 were obtained from sigma Aldrich with different HLB values. A known amount of BaTiO$_3$ was added in THF already containing Brij 5 % weight of BaTiO$_3$ in dissolved form. THF was sonicated for 15 min and kept overnight to observe the sedimentation on different samples containing different HLB values of Brij.

3.3.9 Copolymer as surfactant

Poly(methylmethacrylate-co-methacrylic acid) (PMMA-co-MA) MW 34 000 was used as polymer surfactant in different ratios 2.5 %, 5 %, 10 %, 20 %, 50 %, and, 100 % weight of BaTiO$_3$. The different BaTiO$_3$ samples cubic BaTiO$_3$, tetragonal and R90-iii were used to check best dispersed sample in polymeric surfactant in THF.

3.3.10 Comparison of non ionic surfactants Brij, PMMA-co-MA, and Brij+PMMA-co-MA

It was found that the non-ionic surfactants are helpful in achieving stable dispersion. Three different set of systems for BaTiO$_3$ dispersion was tested i.e., a) Brij, b) PMMA-co-MA and c) Brij with PMMA-co-MA. A known amount of BaTiO$_3$ was used to disperse in solution of each surfactant in the ratio of 5 % weight of BaTiO$_3$ and sonicated for 15 min each and kept standing overnight to observe settling down of BaTiO$_3$ powder.

3.3.11 Variation of volume percent fraction of BaTiO₃ in PMMA

In case of polymer nanocomposites, it was found that at even low volume percent fraction of filler improve the mechanical and physical properties of polymer matrix are enhanced [106]. The uniform dispersion of nanofillers in the polymer matrices is a general prerequisite for achieving desired characteristics.At higher concentration chance of agglomerating nanoparticles increases, which results in micro particles held by matrix. The better dispersion offers to hold higher concentration of filler particles with low agglomeration. The filler fraction were varied over 1-30 volume percent fraction of BaTiO₃ in PMMA. The formula for calculation of volume percent fraction of BaTiO₃ in PMMA used in this work is given by equation below;

$$Vol\,\%\,of\,BaTiO3\ =\frac{Vol\,of\,BaTiO3}{Vol\,of\,BaTiO3+Vol\,of\,PMMA}*100$$

'Vol', stands for the volume. Volume of BaTiO₃ was calculated using mass (g) of BaTiO₃ and density of the powders (6.017 g / ml) whereas the mass and density of PMMA (1.2 g/ml) were used to calculate volume of PMMA used in the system.

3.3.12 Variation of weight percent of PMMA in Solvent

The concentration of PMMA solution was varied from 0.5 % to 14 % weight of the solvent. In this range of weight percent PMMA the viscosity of the system is not so high that make the thin film (~100-1000nm) formation by dip or spin coating impossible. The formula for calculation of weight fraction of PMMA in solvent used is as below;

$$Wt\,\%\,of\,PMMA\,in\,Solvent\ =\frac{Wt\,of\,PMMA}{Wt\,of\,PMMA+Wt\,of\,Solvent}*100$$

Where, 'Wt' stands for weight.

3.3.13 Use of THF as solvent for obtaining dispersions for thin and thick films

THF has a low boiling point of 69 ˚C, dielectric constant of 7.52,a density of 0.886 g/cm³ and can dissolve PMMA well. It is used in most of dispersions to obtain BaTiO₃-PMMA polymer nanocomposite. At 1 % to 30 % volume fraction of BaTiO₃ in PMMA and 1.7 % to 12 % weight

of PMMA in solvent (for details see Table 4-XI and Table 4-XIV). THF is used to dissolve PMMA with different molecular weights i.e., MW 35 000, 120 000, and 350 000.

In first step surfactant (PMMA-co-MA) 2.5 % weight of $BaTiO_3$ was dissolved in a known amount of sovlent. After mixing it well A certain volume percent fraction of $BaTiO_3$ in PMMA was added to solution and agitated ultrasonically for 15 min. Subsequently PMMA in THF is added according to a certain desired weight percent in the mixture and again agitated in ultrasonication tub for 15 min. The dispersions obtained were used for obtaining layers directly.

3.3.14 Use of toluene as solvent for obtaining dispersions for thin and thick films

Toluene has boiling point of 110 ˚C, dielectric constant of 2.4, and density of 0.867 g/cm^3. It is a good solvent for PMMA. It is as well tested for obtaining dispersions using cubic and tetragonal $BaTiO_3$ in PMMA with different molecular weights MW 35 000 and 350 000.

In the first step 40 % weight of PMMA-co-MA was dissolved in toluene, subsequently $BaTiO_3$ was added to this solution and sonicated for 15 min. The solution was kept overnight to observe the settling down of $BaTiO_3$ particles over time.

Different dispersions were obtained using toluene as solvent at 2 volume percent fraction of $BaTiO_3$ in PMMA, while the weight percent of PMMA in toluene was kept 8.8. Different molecular weights of PMMA i.e. 35 000 and 350 000 were used in these dispersions. Cubic and tetragonal $BaTiO_3$ was used to see the effect of cubic to tetragonal $BaTiO_3$ on electrical properties of polymer composite. Thick films were obtained using sliding apparatus. Thin films using dip coating were obtained.

3.3.15 Use of chlorobenzene as solvent for obtaining dispersions for thin films

Monochlorobenzene or chlorobenzene (MCB) has a boiling point of 130 ˚C. A study is conducted here to dissolve PMMA MW 35 000 in MCB and obtaining dispersion of $BaTiO_3$ nanoparticles with surfactant i.e., PMMA-co-MA acid. Thin films were obtained using spin on technique and characterized using SEM and optical profilometery to compare effect of MCB as solvent with other solvents used here.

3.4   Obtaining thin and thick layer using stable dispersions

3.4.1   Thin layers using dip coater

Thin layer were achieved using the stable dispersions of BaTiO$_3$-PMMA at various dip coating speeds (85, 60, and 30) mm / min using the dip coater operated with computer program at room temperature. The substrate is held over the dipping solution and moved down slowing into the solution at a particular speed of dip and kept immersed in the solution for 15 s to 30 s so the temperature of the substrate and solution become same. After approximately 30 s the substrate is pulled out of the dispersion at the speed with which it was immersed in the solution. During pulling off from dispersion the solvent evaporates depending on the heat of evaporation of solvent used for dispersion. After the drying of the film on substrate, substrate is removed from the holder and samples are saved for characterization.

Usually film thickness during dip coating depends on viscosity of dispersion, boiling point of solvent (i.e., a rough estimate of heat of evaporation) used for dispersion, coating speed, temperature at which dip coating is done and moisture in the air at time of dipping.

The more viscous dispersion and high boiling point of solvent result in thick films while low viscosity of dispersion and low boiling point of solvent help to obtain thin films.

The lower dipping speed result in thin films as minimum amount of dispersion stay sticking during slow removal of the substrate from the solution ,whereas at higher speeds the thick films are obtained due to excess solution remain stick to substrate at higher drag speed during dip coating. The high temperature and dry conditions help fast removal of solvent from drying film on substrate results in thin films whereas at low temperature moisture in air slow down evaporation of solvent result in thicker films.

3.4.2   Thin layers using spin coater

Thin layer were as well obtained using the stable dispersions of BaTiO$_3$-PMMA at various spin coating speeds 4000 rpm, 6000 rpm, and 8000 rpm for 30 s at different accelerating speeds 1000 rpm^2, 2000 rpm^2 and 4000 rpm^2 using the spin coater at room temperature. The substrate is held on a stage with vacuum generated by a vacuum pump attached to stage to hold the sample. By dropping few drops of dispersion on the freshly cleaned substrate mostly glass / ITO the rotation

of stage is started using computer generated program of speed of revolution, accelerating rate and time for rotation. The rotation of substrate on stage removes excess solution from the substrate and removal of solvent during revolution dry the film on the substrate.

Film thickness obtained during spin coating as well depends on viscosity of dispersion, boiling point of solvent used for dispersion, spinning speed, speed of acceleration, temperature at which spin coating is done and moisture in the air.

3.4.3   Thick layers using wet films application

Thick layers were obtained using the dispersion by sliding apparatus on glass plates. The glass plates were cleaned with deconex and distilled water and dried before deposition of layers. Few drops of dispersion were spread over the glass within the area of the sliding apparatus and the sliding apparatus was slide over the glass manually. The wet thickness of the obtain layer was 200 μm due to gap of the sliding apparatus used. The layers were dried at room temperature for 1 h and then removed using ethanol spray on the layer. Afterward double distilled water was poured on the layer to take it off from the glass plate. The layer started peeling off from glass after the application of ethanol and DD water.

The layer were dried and kept for testing electrical properties. The dispersion used for obtaining thick film had 2 % volume fraction of $BaTiO_3$ in PMMA, while the weight percent of PMMA (MW 350 000) in solvent was 8.8. Effort to use lower MW of PMMA i.e., 35 000 for filler loading to 4 % and 8 % volume fraction of $BaTiO_3$ resulted in layers which were impossible to peel off from the glass substrate for characterization. Two different solvent THF and toluene were used to obtain dispersion for thick films.

3.4.4   Various substrate used for obtaining thin layers

For achieving better adhesion of our thin films to substrates, several substrates were tested. The substrate used for our work:

- Test grade Si-wafers with orientation <100>, thickness of 625 micron
- Microscopic glass slide
- ITO on glass
- Gold sputtered Si- wafers
- Self assembled monolayer of thiols deposited on gold surface

3.4.4.1 ITO on glass

ITO on glass was obtained from Delta technologies Ltd. USA. The polished float glass with SiO_2 passivated ITO coated on one surface with R_s=20 Ω and unpolished float glass SiO_2 passivated ITO coated on one surface R_s =4.8 Ω were used.

3.4.4.2 Self assembled monolayer to improve adhesion of thin films to gold sputtered substrate

1 Hexadecanethiol was obtained from sigma Aldrich. The most common protocol for preparing SAMs on gold, is immersion of a freshly prepared or clean substrate into a dilute (1-10 mM) ethanolic solution of thiols for 12-18 h at room temperature. Dense coverage of adsorbates are obtained quickly from milli molar solutions (milliseconds to minutes), but a slow reorganization process requires times on the order of hours to maximize the density of molecules and minimize the defects in the SAM [104] Freshly cleaned substrates of Au sputtered Silicon wafers were submerged in a solution of thiol in absolute ethanol (1mM/10mM) overnight about 10 hours. The substrates were removed after 10 hours and washed with ethanol and dried to be used for depositing thin films of our polymer nanocomposite system.

3.4.5 Cleaning substrate before deposition of $BaTiO_3$ –PMMA layers

The substrates were cleaned with various approaches to achieve best layers. Two methods usually helped to obtain clean substrate for coating thin films.

The detergent deconex / water / ethanol were used for cleaning the glass or ITO. Substrate were immersed in each and sonicated for 5 min. Then it was dried with condensed dried air (CDA)

The second method adopted was to clean the substrate using acetone by applying manually acetone to cotton bud and cleaning the surface from any dust or organic stuff. In the end a layer of OPTICLEAN[R] polymer is applied and let it to polymerize for 2 min to 5 min. The polymer was then peeled off from the surface just before depositing the film.

3.4.6 Heat treatment of layers

The obtained layers were heated in oven at 130 ˚C for (15, 30, 45 and 60) min. The temperature of furnace was reached to said value before placing the samples in the furnace. The sample were taken out after drying at a particular temperature and cooled down at room temperature.

3.5   Characterisation of powders and layers

3.5.1   Characterisation of powders by XRD

The crystal structure, phase composition and, crystallite size measurements for the sample powders were done using an X-ray diffractometer [X´Pert MPD from Panalytical (Philips) with software package "X´Pert"] using Cu $K\alpha$ radiation with maximum output 60 kV and 60 mA. Absolute scan with step mode was used, the starting 2θ angle was 5° and end angle was 85° with step size equal to 0.025° and time per step is 2 s with incident beam width 15 mm at 40 kV and 45 mA, supporting base used was Si-crystal.

3.5.2   Characterisation of powders by TEM

The investigations were accomplished with the highly resolution transmission electron microscope (Tecnai F20 using the accelerating voltage of 200 kV). The determination of the powder size and morphology took place on the basis the bright field and/or dark field images. The chemical composition was analyzed with energy dispersive X-ray (EDX) analysis, electron energy loss spectroscopy (EELS) and/or energy-filtered transmission electron microscopy (EFTEM) - procedures. The crystal structure was analysed by the high resolution images (crystal plane images) and appropriate diffraction analysis. **Sample preparation;** For TEM investigations, the specimens were prepared by dispersing a small amount of the powders in ethanol, mixing under ultrasonic agitation and pipetting a drop of this dispersion on a copper mesh covered with a porous carbon film.

3.5.3   Characterisation of powders by SEM

High resolution scanning electron microscopy – HRSEM ZEISS – Gemini Supra VP was used to observe the particle size and morphology of sample powders. The specimens were prepared by sputtering thin film (~2-4 nm) of either carbon black or platinum/gold to observe high resolution images and avoid the charging and breaking in case of thin polymer films.

3.5.4   Characterisation of layers by SEM / FIB

HRSEM ZEISS – Gemini Supra VP was used to observe thin and thick layers. SEM images helped to see the dispersion of $BaTiO_3$ in PMMA. Distribution of $BaTiO_3$ over the surface of film and within the films is observed. The milling of cross section is done using focused ion beam (FIB) technique to observe film thickness and distribution of $BaTiO_3$ within the films.

3.6   Electrical properties of thick and thin layers

3.6.1   Capacitance measurement of thick layers

Thick layers obtained using various $BaTiO_3$-PMMA suspensions were tested for electrical properties using Quad tech Precision LCR meter 7600. The measurements were performed using constant mode at 1 volt. The frequency sweep range was 10 Hz to 2 MHz. The polymer nanocomposite samples were held between two electrodes with a diameter of 15 mm. The air and PMMA were used as reference. The instrument was calibrated in open and short mode before measurements.

3.6.2   Capacitance measurement of thin layers

Thin layer obtained via dip coating and spin on technique on ITO coated glass were characterized for their electrical properties using HIOKI 3532-50 or Agilent 4284A precision LCR meter. The top electrode was deposited by evaporating aluminium (Al) or platinum (Pt) metal in vacuum chamber. The electrode deposited samples were mounted on a needle probe apparatus and connected to LCR meter at ambient conditions.

Impedance Z and phase angle φ are measured during a sweep of the applied frequency from 42 Hz to 5 MHz using HIOKI 3532-50 LCR meter, while 1000-10,000 Hz using Agilent 4284A precision LCR meter (frequency range from 20 Hz to 1 MHz). The capacitance is calculated by the use of an equivalent circuit shown in Figure 3-4.
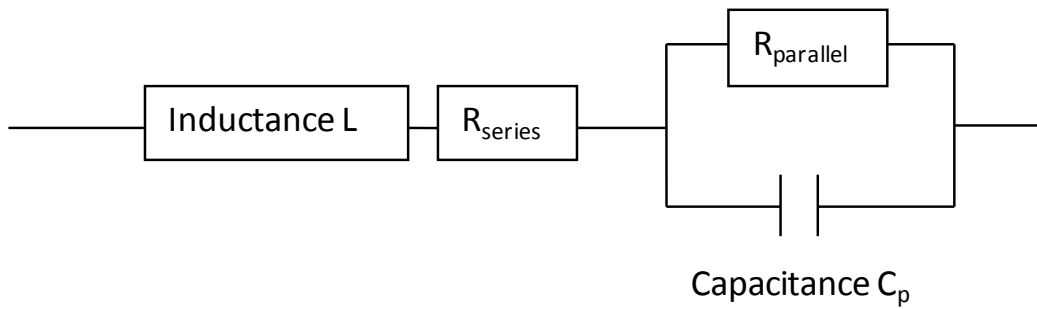
Figure 3-4   Equivalent circuit for Impedance measurement and calculation of the capacitance

$$Z = R_s + i\omega L + Z_p$$

$$\frac{1}{Z} = \frac{1}{R_p} + i\omega C$$

$$\varphi = \arctan\frac{Im\,Z}{Re\,Z}$$

Z is the overall impedance, Z_p the impedance of parallel circuit, R_s the serial resistance and R_p the parallel resistance. The dielectric constant was measured using the capacitance in parallel (Cp) by the following equation;

$$C = \varepsilon_0\varepsilon_r A/t$$

Where C = capacitance, ε_0 = permitivity of free space and ε_r = relative permitivity of layer, A = area of the electrode and t = thickness of layer.

The electric power is lost in all dielectric materials, usually in the form of heat. Dissipation factor (DF) is expressed as the ratio of the resistive power loss to the capacitive power, and is equal to the tangent of the loss angle.

It is also referenced as the loss tangent or tan δ, and approximate power factor.

$$DF \quad or \quad tan\delta = R_s / Z$$

DF is the ratio of a capacitor's equivalent series resistance (R_s) to its capacitive reactance i.e., (Z).
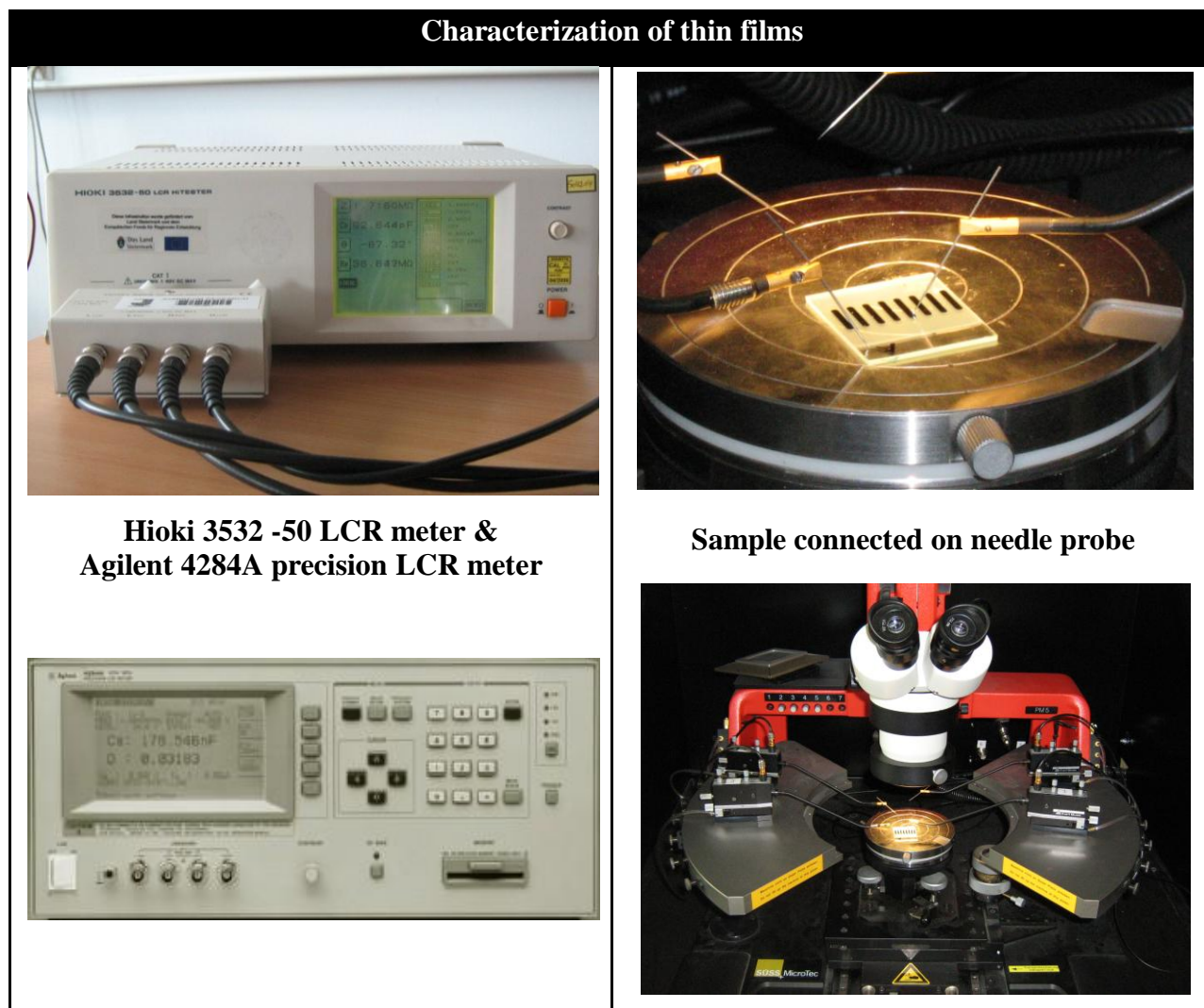
Figure 3-5   LCR meters and needle probe apparatus used to characterize thin film deposited with Al/Pt as top electrode, whereas ITO acts as bottom electrode.

4 Results

4.1 Hydrothermal synthesis

Hydrothermal synthesis is famous for ease of process and stiochiometric control over the production of sub micrometer $BaTiO_3$ particles with uniform particle size distribution. The powder properties can be controlled by utilizing chemical process variables such as temperature, pressure, reactant concentrations, pH, etc [17]. In our case we tried to obtain nanometeric $BaTiO_3$ particles using various Ti precursors, TiO_2 Tronox (ave. particle size 125 nm) and TiO_2 P25 Degussa (ave. particle size 25 nm), and spindle like TiO_2 rutile phase. Barium hydroxide was mostly used as barium precursor, whereas barium stearate was as well tested to obtain in situ surface functionalized $BaTiO_3$ nanoparticles.

In first step TiO_2 Tronox and TiO_2 P25 Degussa were used to carry out a systematic study of hydrothermal synthesis of $BaTiO_3$.

4.1.1 Ti-Precursor Type-A: TiO_2 Tronox

While using TiO_2 Tronox Ti precursor following set of experiments was performed and various samples listed in Table 4-I were obtained. All the samples were obtained using no mineraliser except for sample 8 i.e., (A90-3M) of Table 4-I where 3 M KOH was used.

The XRD diffraction pattern reveals the phase stabilized over various reaction times at different temperatures. The completion of the reaction and presence of unreacted anatase and impurities tell the degree to which the reaction is completed. The reaction at 60 ˚C with type-A precursor yields an incomplete reaction (Figure 4-1). Even after 48 h unreacted anatase is observed by XRD analysis, yet some $BaTiO_3$ perovskite cubic structure can be seen at this temperature after 16 h. $BaCO_3$ in form of witherite phase is present as an impurity

The reactions samples obtained at 90 ˚C after 16 h show that $BaTiO_3$ perovskite cubic structure, while the longer reaction time ensures the completion of reaction. At 120°˚C and 150°˚C for type-A precursor as well yielded $BaTiO_3$, with some TiO_2 as anatase present in the samples. The amount of anatase decreases as the reaction is given longer time.

The crystallite size measurement is performed using Scherrer's equation for two peaks (100) and (110) and obtaining the mean of the two values. The crystallite size of obtained $BaTiO_3$ is in the range of 40 nm to 95 nm (Table 4-II).

Table 4-I $BaTiO_3$ obtained using TiO_2 Tronox and $Ba(OH)_2 \cdot 8H_2O$ under different temperature and time

Sr.Nr.	Temperature °C	Time h	Ti-Precursor A	Sample	Remarks
1.	60	16	A	A60-16 h	
2.	60	24	A	A60-24 h	
3.	60	48	A	A60-48 h	
4.	90	16	A	A90-16 h	
5.	90	24	A	A90-24 h	
6.	90	48	A	A90-48 h	
7.	90	72	A	A90-72 h	
8.	90	48	A	A90-3 M	KOH used as Mineraliser
9.	120	16	A	A120-16 h	
10.	120	24	A	A120-24 h	
11.	120	48	A	A120-48 h	
12.	135	24	A	A135-24 h	
13.	120	46	A	A120-46 h	
14.	150	16	A	A150-16 h	
15.	150	24	A	A150-24 h	
16.	150	48	A	A150-48 h	

The XRD patterns show that the obtained $BaTiO_3$ in is cubic (i.e., powder diffraction file Nr. 31-0174 from International Centre for Diffraction Data).

XRD patterns for the samples A90-48 h and A90-3M are very similar. 3M KOH was used as a mineraliser in case of sample A90-3M whereas the sample A90-48 h was synthesised without any mineraliser. The use of mineraliser does not show significant effect on the $BaTiO_3$ formation. The crystallite size measured for A90-3M was found to be about 85 nm, which is larger as compared to crystallite size of sample A90-48 h i.e., 60 nm.

Figure 4-1   X-ray diffraction patterns for BaTiO$_3$ obtained using type-A Ti precursor at 60,90,120 and 150 ˚C, for 16, 24, and 48 h reaction times (■ BaTiO$_3$, ▲ anatase, ● BaCO$_3$).

Table 4-II   Crystallite size variation of $BaTiO_3$ obtained using type-A Ti precursor with temperature and time

Temp/Time	16 h	24 h	48 h	72 h
60°°C	67 nm	73 nm	95 nm	-
90°°C	-	52 nm	60 nm	54 nm
120°°C	43 nm	45 nm	53 nm	-
150°°C	41 nm	41 nm	52 nm	-

The TEM micrographs for sample A 90-48h shows agglomerates of $BaTiO_3$ dispersed on carbon net. Particle are in the range of 50 nm to100 nm with irregular morphology with some cubes evident. The pores in the particles are as well evident. The bright and dark field images of $BaTiO_3$ help to observe the texture of the particle surface (Figure 4-2). High energy beam focused during observation was unable to break apart these porous particles, which indicate that the particles are mechanically stable. High resolution TEM images show lattice planes i.e., fully crystallized particles of $BaTiO_3$. The orientation of planes does not changes over the whole particle, which indicate that the particles are single crystal (Figure 4-3).

The EFTEM and EDX spectrum reveals that the elemental distribution is homogeneous and the particles are fully reacted The EDX spectrum of particles of obtained $BaTiO_3$ shows an even distribution of Ba, Ti, and , O in the particles (Figure 4-4).

A90˚ C 48h
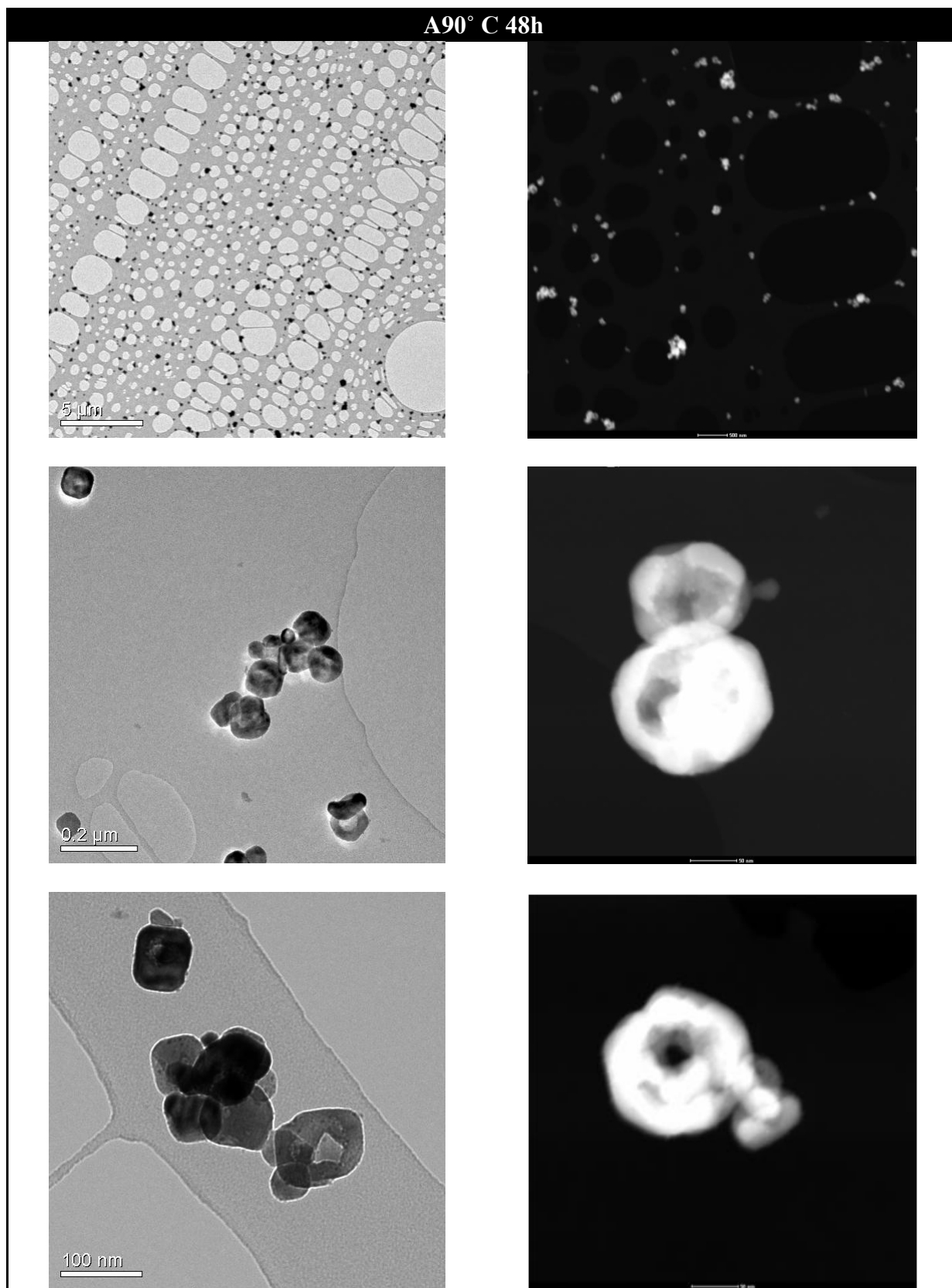
Figure 4-2   TEM bright and dark field images of BaTiO$_3$ obtained using Ti Precursor type-A at 90 ˚C for 48 h.

A90° C 48 h
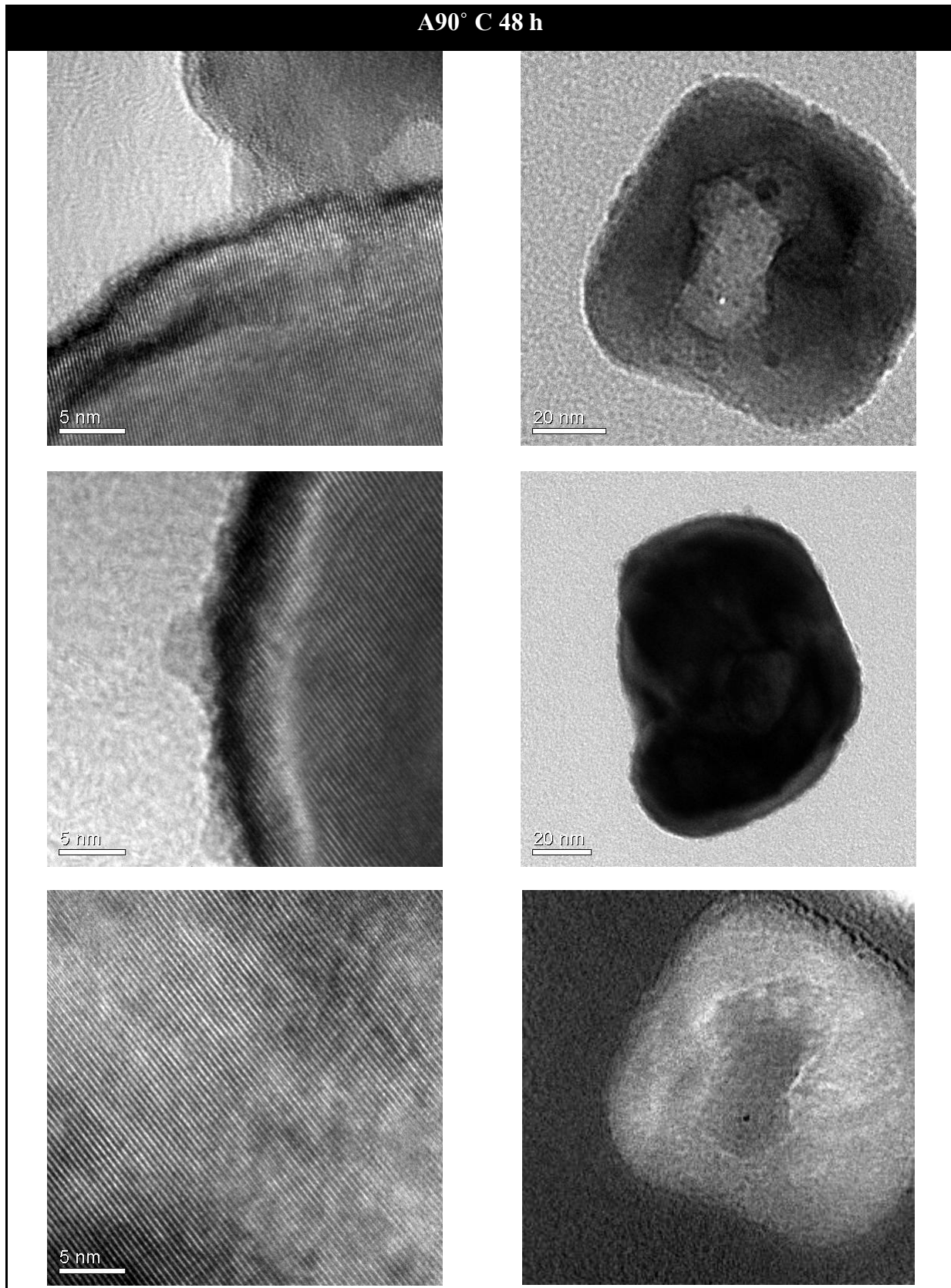
Figure 4-3   High resolution TEM micrographs show the fully crystalline BaTiO$_3$ at 90 °C for 48 h using Ti precursor type-A

Figure 4-4   EDX spectrum for BaTiO$_3$ obtained at 90 ˚C for 48 h using Ti precursor type-A.
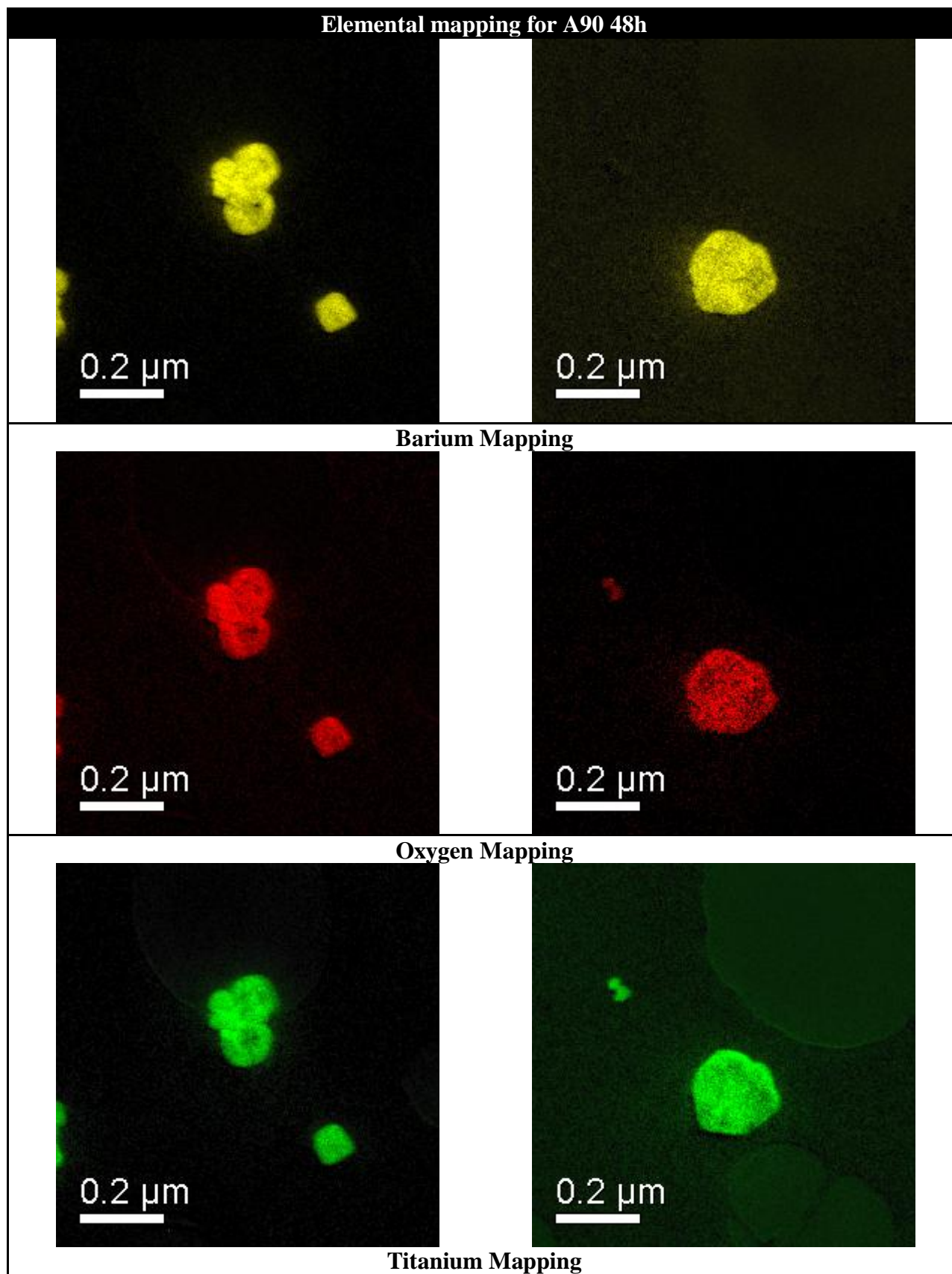
Figure 4-5   EFTEM elemental mapping of Ba, O, and Ti for BaTiO₃ obtained at 90 ˚C for 48 h
              using Ti precursor type-A

SEM micrographs help to observe the overall morphology of $BaTiO_3$ particles obtained at 90 ˚C, 120 ˚C, and 150 ˚C for 48 h (Figure 4-6 and Figure 4-7). The SEM micrographs obtained using Ti precursor type-A at 90 ˚C show that the powders are of uniform size distribution with particles size in the between 100 nm to 200 nm. The particles are aggregated into strong clusters. The morphology of the particles appears to be round or cubic. Pores can be observed in the samples produced at 90 ˚C for 48 h. More internal pores are observable for samples synthesized at high temperatures i.e., at 120 ˚C for 48 h and 150 ˚C for 24 h. SEM micrographs for A150-24 h shows tight agglomerated of $BaTiO_3$ powders with porous morphology. The size of the particles is in the range of 100 nm to 200 nm as shown in Figure 4-6.

SEM images for A150-24 h
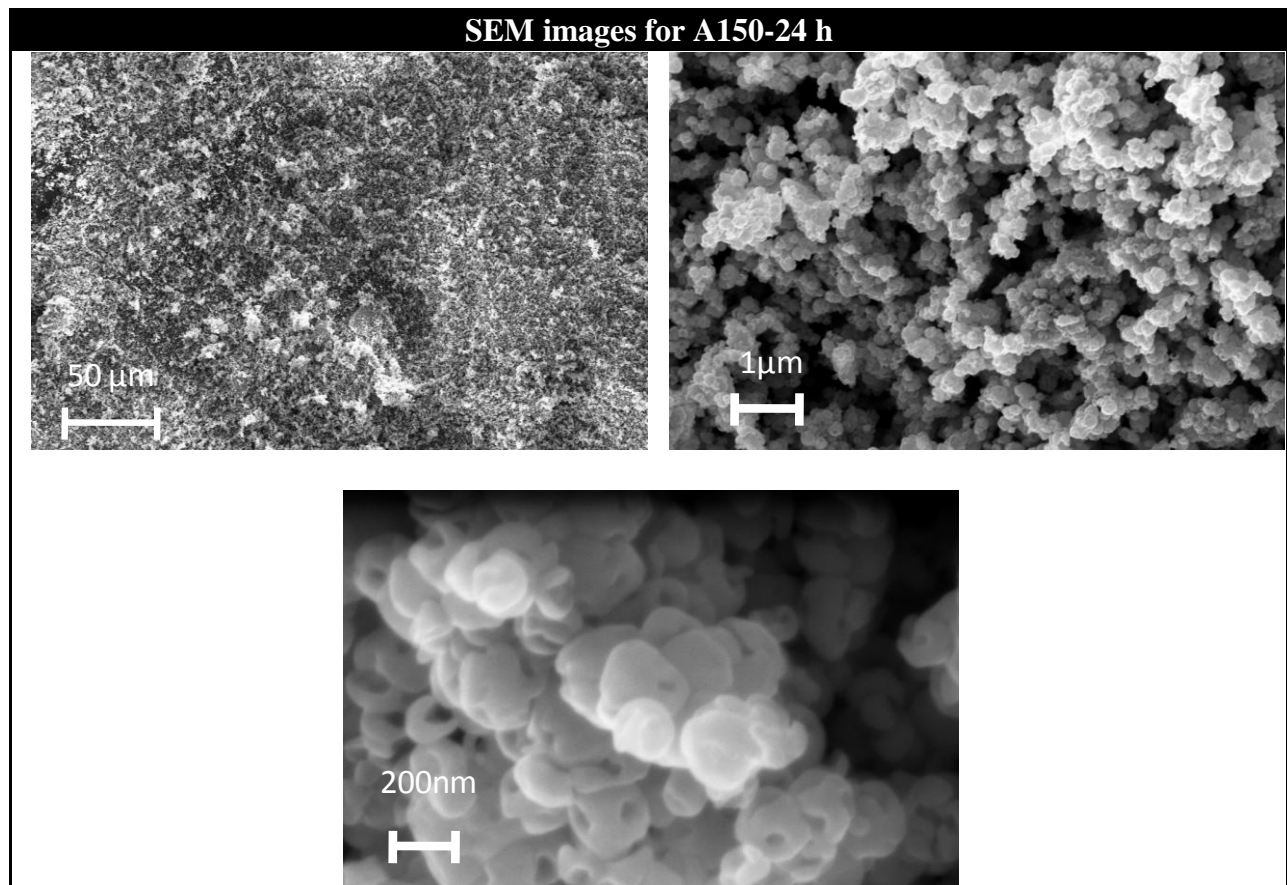
Figure 4-6   SEM micrographs for $BaTiO_3$ obtained at 150 ˚C for 24 h using Ti precursor type-A.

SEM images for A90-48 h	SEM images for A120-48 h
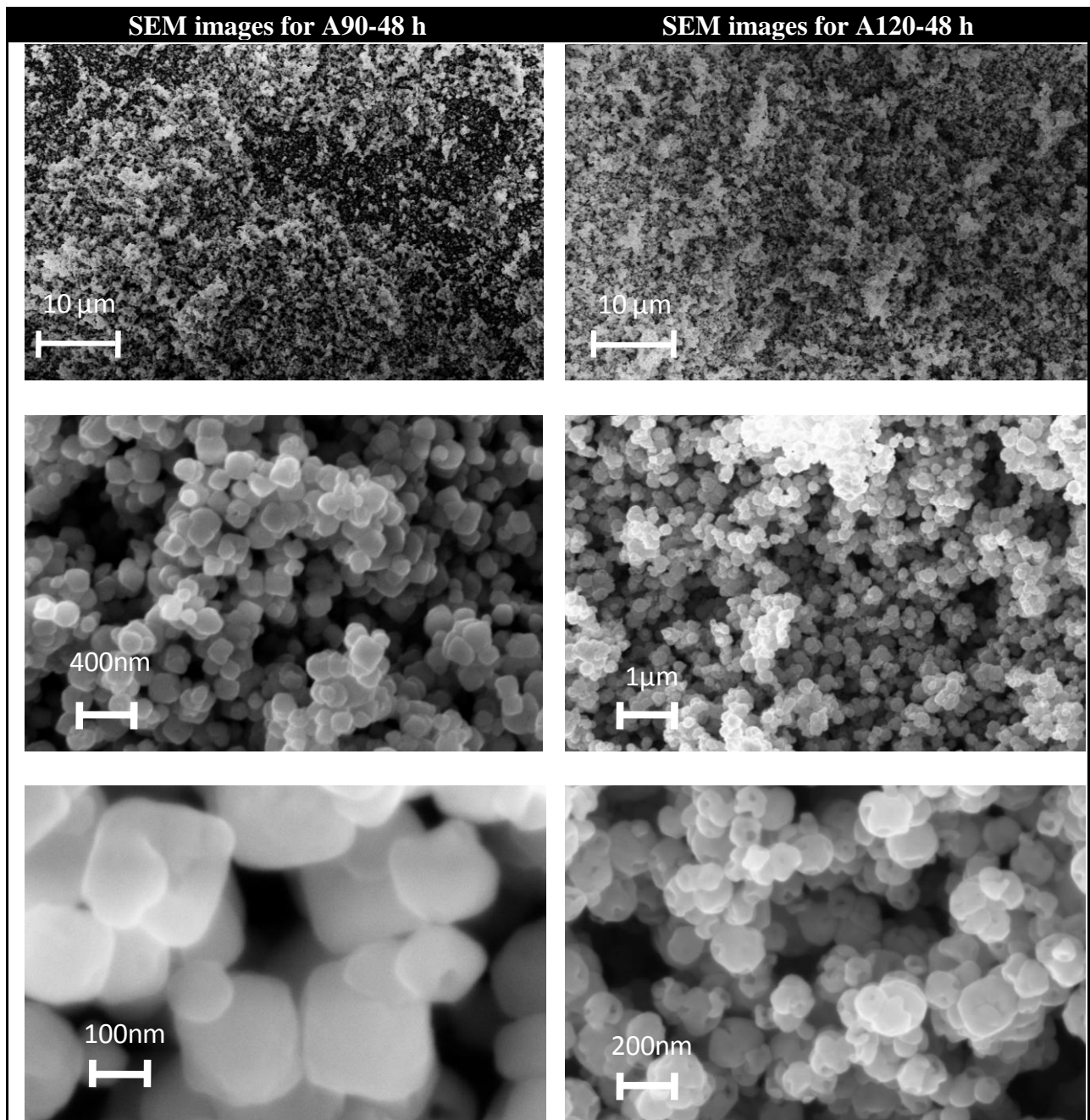
Figure 4-7   SEM micrographs for BaTiO$_3$ obtained at 90 ˚C and 120 ˚C for 48 h using
               Ti precursor type-A

4.1.2 Ti-Precursor type-B: TiO$_2$ P25 Degussa

While using TiO$_2$ P25 Degussa Ti precursor, the following set of experiment was performed and various samples obtained are listed in Table 4-III.

Table 4-III   BaTiO$_3$ obtained using TiO$_2$ P25 Degussa and Ba(OH)$_2\cdot$8H$_2$O under different temperature and time conditions

Sr.Nr.	Temperature ˚C	Time h	Ti-Precursor A or B	Sample	Remarks
1.	60	16	B	B60-16 h	
2.	60	24	B	B60-24 h	
3.	60	48	B	B60-48 h	
4.	60	72	B	B60-72 h	
5.	90	16	B	B90-16 h	
6.	90	24	B	B90-24 h	
7.	90	48	B	B90-48 h	
8.	90	40	B	B90-40 h	
9.	120	16	B	B120-16 h	
10.	120	24	B	B120-24 h	
11.	150	16	B	B150-16 h	
12.	150	24	B	B150-24 h	
13.	150	48	B	B150-48 h	

The characterization of obtained BaTiO$_3$ particles using XRD reveals that BaTiO$_3$ perovskite structure has started appearing even at 60 ˚C after 16 hours reaction time with anatase and rutile as impurities (Figure 4-8). For longer reaction time at 60 ˚C reaction appearing to near completion with minimum amount of unreacted anatase and rutile present in the final product.

At 90 ˚C for 24 h the reactions appears to be fully complete as indicated by XRD patterns, while some barium formate peaks are observed due to washing of obtained BaTiO$_3$ powders with formic acid.
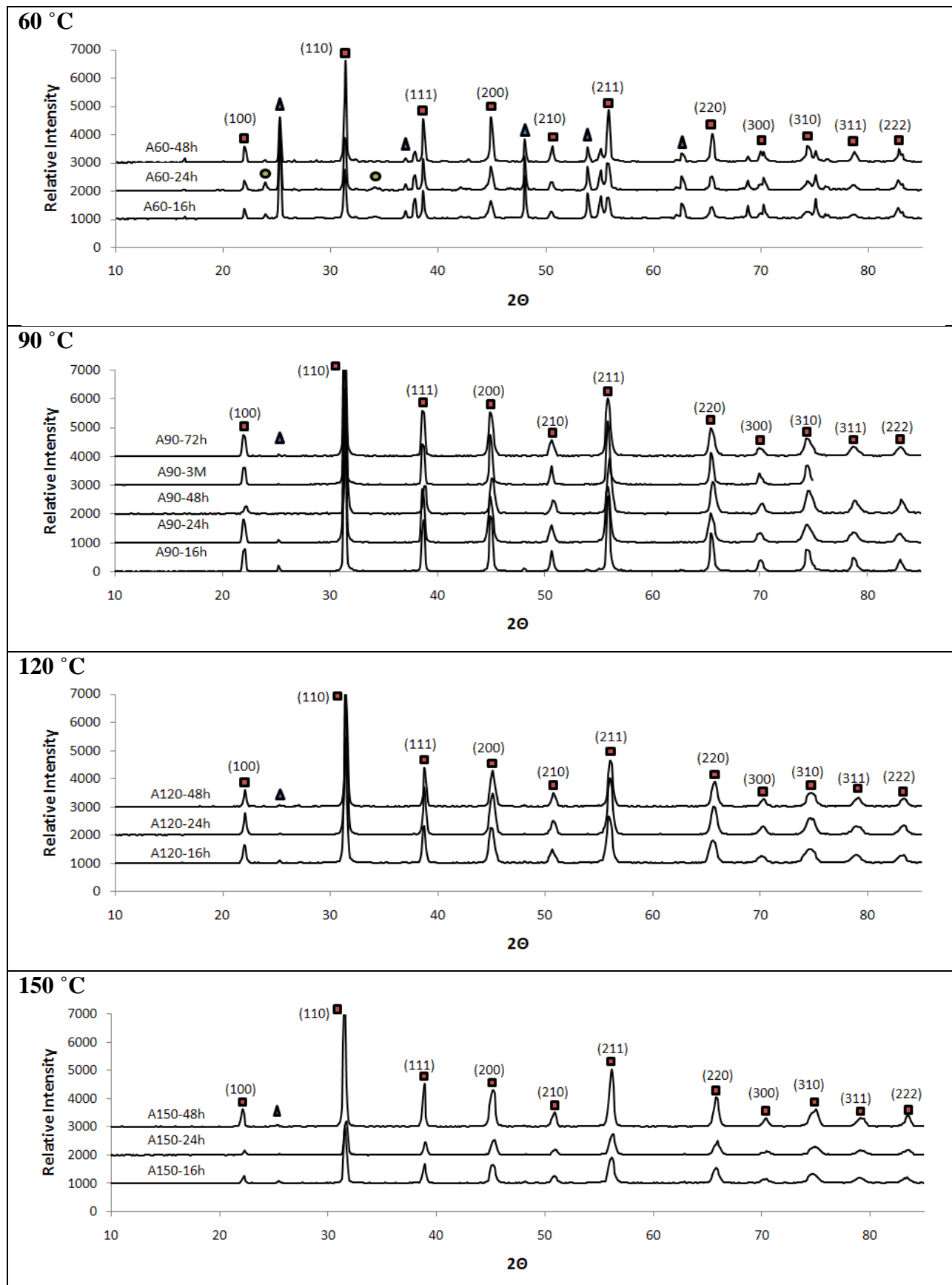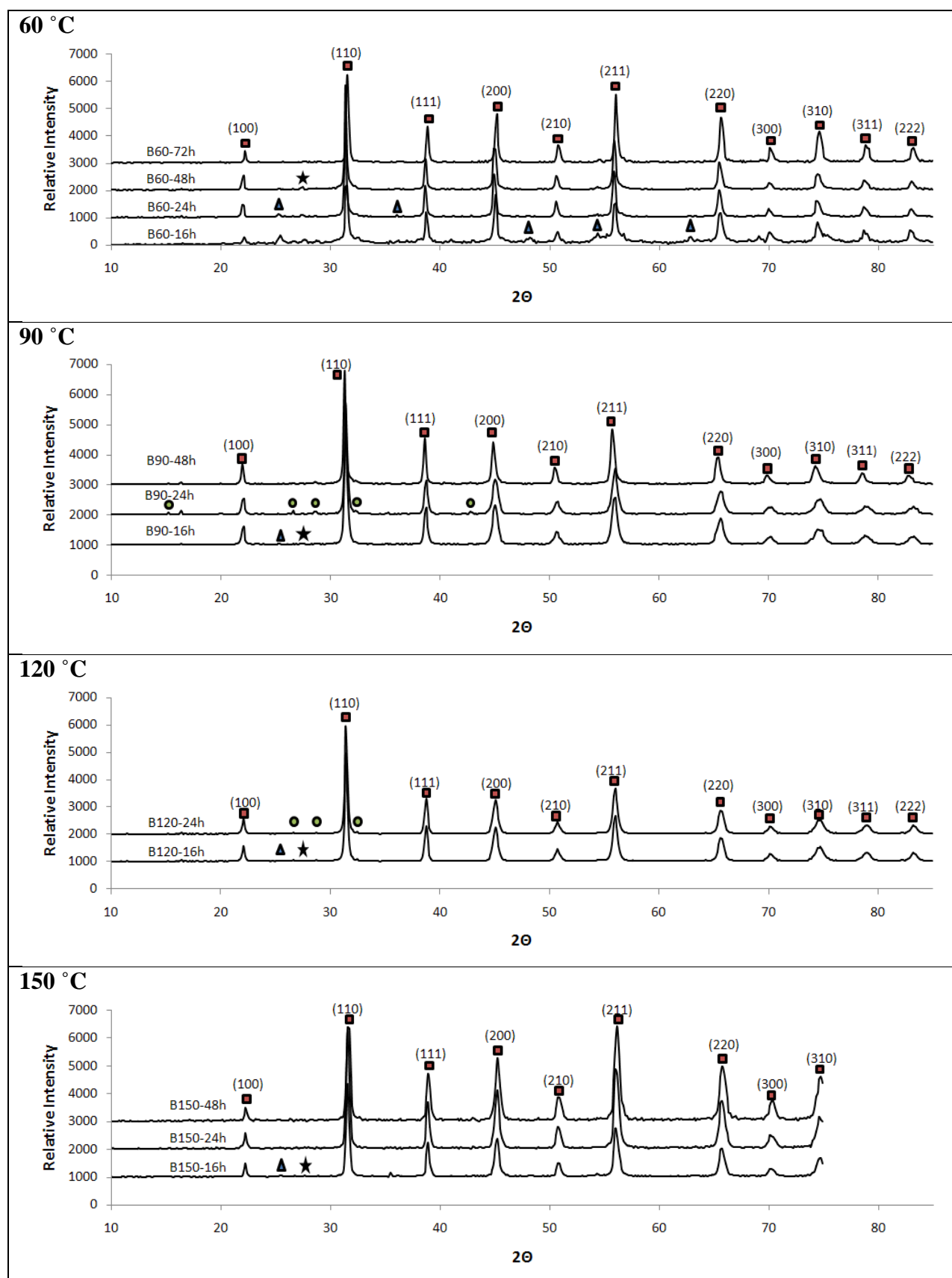
Figure 4-8   X-ray diffraction patterns for BaTiO₃ obtained using type-B Ti precursor at 60, 90, 120 and 150 ˚C for 16, 24, and 48 h reaction times (■BaTiO$_3$, ▲ anatase, *Rutile, ● barium formate; Ba (CHO$_2$)$_2$).

In case of type-B precursor the longer reaction time and higher temperature helped to complete the reaction. The $BaTiO_3$ crystallite sizes were calculated using Scherrer's equation for two peaks (100) and (110) and averaging over the two values. Crystallite size for the type-B precursor samples is in the range 34 nm to 62 nm (Table 4-IV).

Table 4-IV   Crystallite size variation of $BaTiO_3$ obtained using type-B Ti precursor with temperature and time

Temp/Time	16 h	24 h	48 h
60 ˚C	36 nm	60 nm	62 nm
90 ˚C	34 nm	36 nm	48 nm
120 ˚C	38 nm	49 nm	-
150 ˚C	40 nm	37 nm	35 nm

TEM observations of $BaTiO_3$ samples using type-B precursor at 60 ˚C for 48 h show no sharp edges hence indicating an incomplete reaction (Figure 4-9). The amorphous and crystalline regions can be observed by HRTEM images. The elemental mapping using EDX spectrum EFTEM images allows observing unreacted TiO_2 at the core of particles which gives an impression that diffusion of Ba-ions has not yet completed at 60 ˚C for 48 h reaction (Figure 4-10 and Figure 4-11). Observation of sample type-B precursor, 90 ˚C for 48 h shows irregular morphology and pores. EFTEM images of sample indicate that the particles are fully formed with uniform distribution of Ba, Ti and O (Figure 4-12 and Figure 4-13).

Samples of $BaTiO_3$ obtained from type-B precursor at 150 ˚C for 48 h show compact particles with no pores. The morphology of the particles has changed from spherical to facetted, fully formed particles (Figure 4-14). The compactness and fully crystallized form of the particles is evident from the high resolution TEM image computer generated diffractogram (Figure 4-15). Homogeneous distribution of Ba, Ti and O can be observed in EFTEM elemental mapping shown in Figure 4-16.

TEM images for B 60 ˚C 48 h
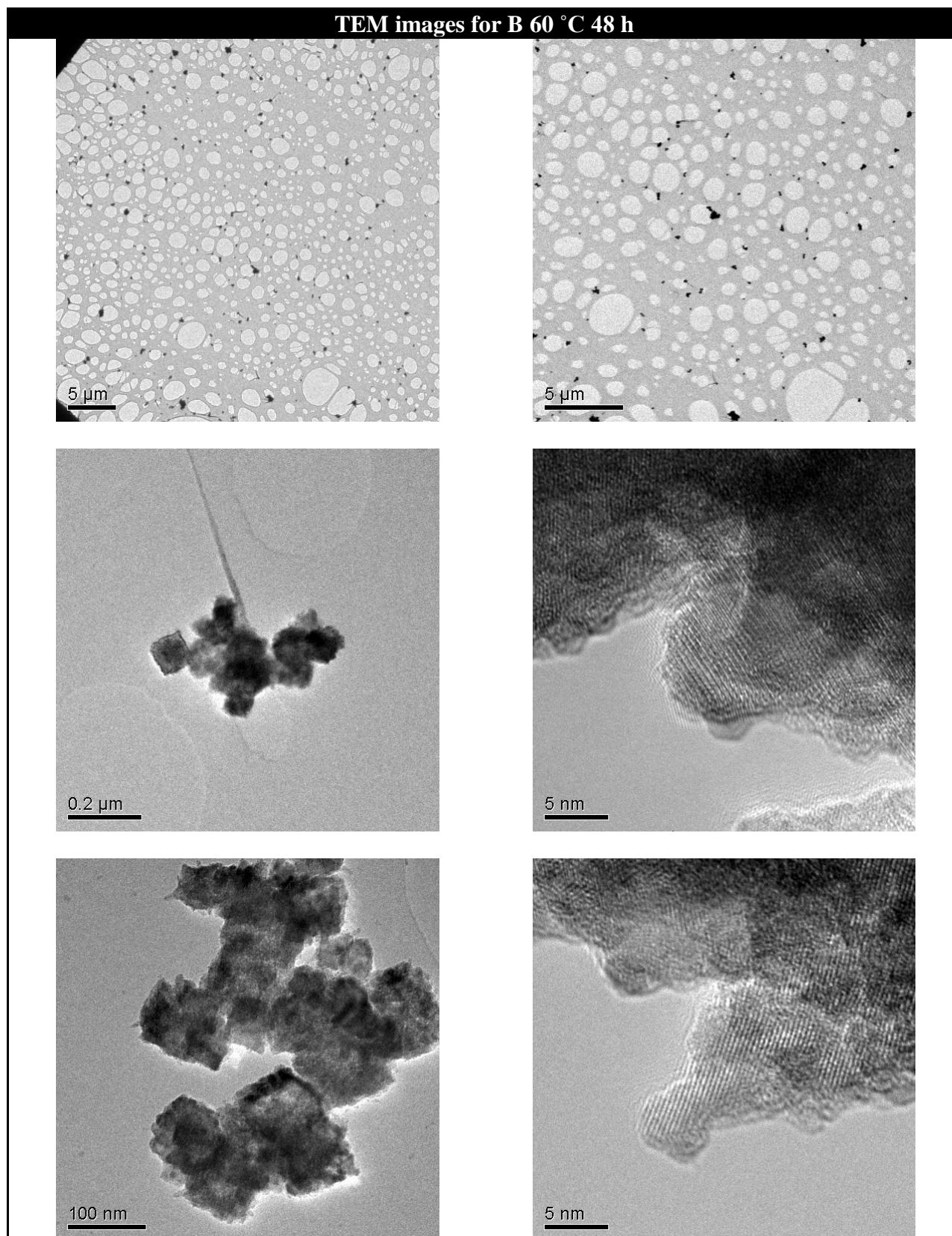
Figure 4-9   TEM bright field and HRTEM images of BaTiO3 obtained using Ti Precursor Type-B at 60 ˚C for 48 h

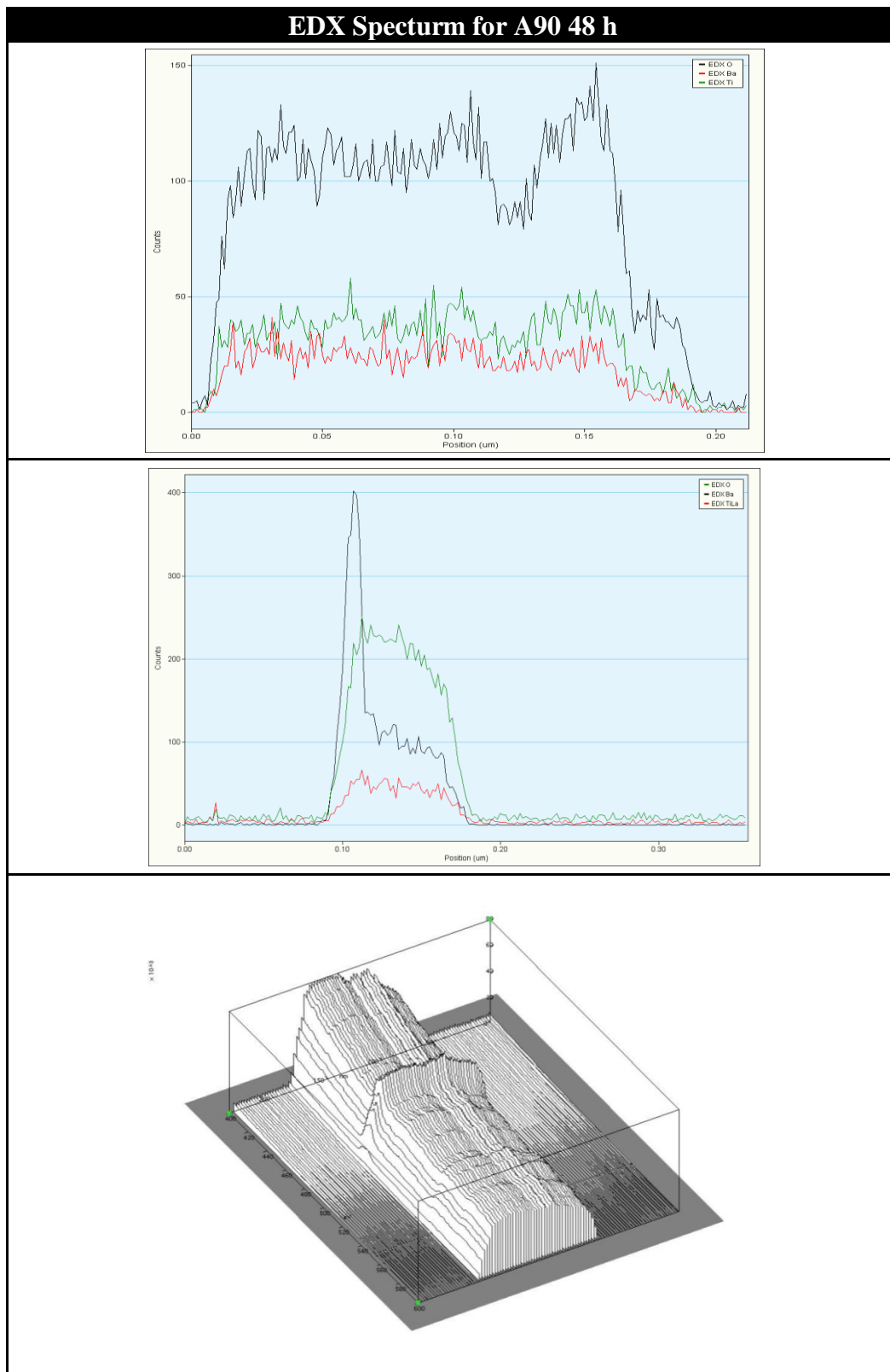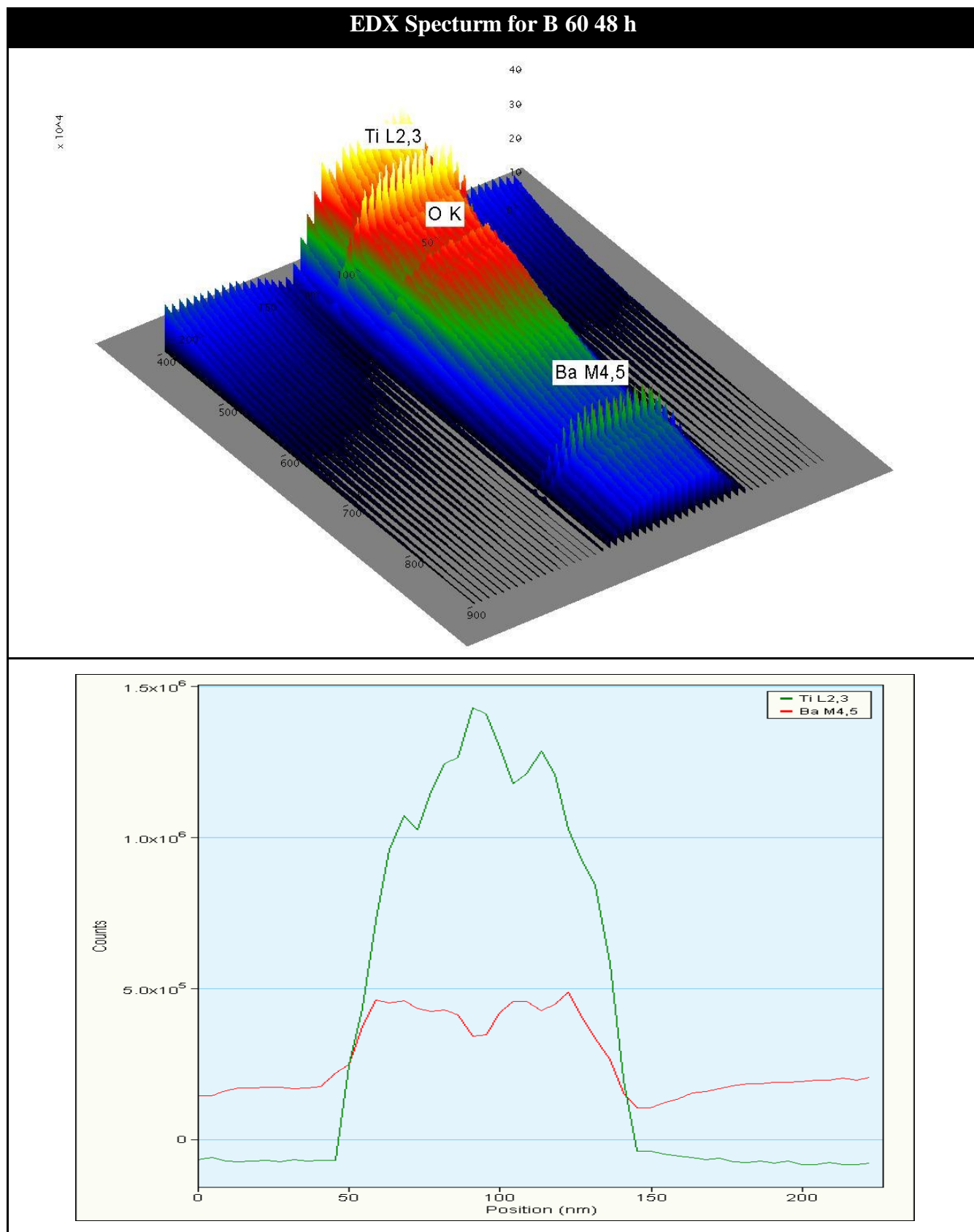Figure 4-10   EDX spectrum for BaTiO$_3$ obtained at 60 ˚C for 48 h using Ti precursor type-B
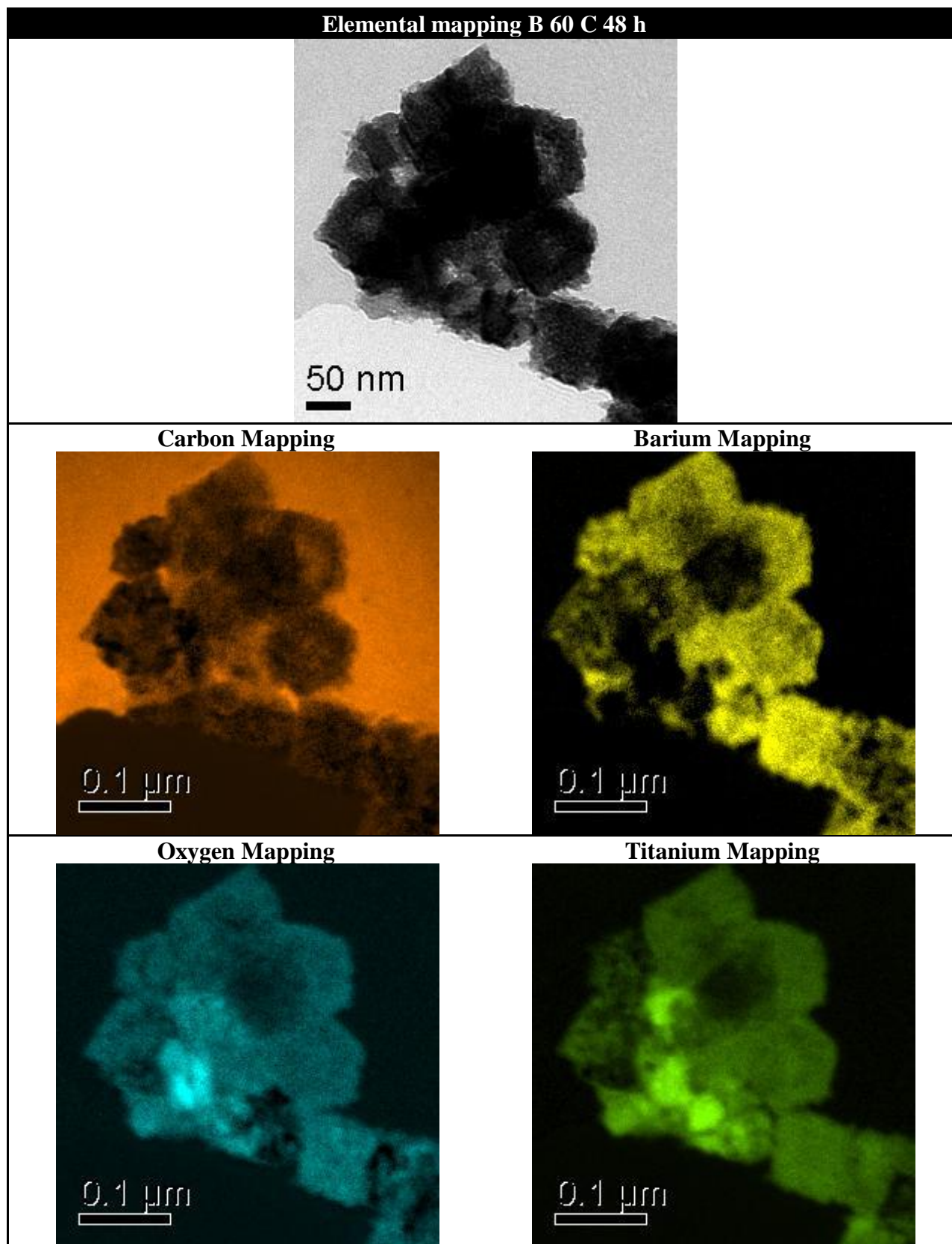
Figure 4-11   EFTEM Elemental mapping of Ba, O, and Ti for BaTiO$_3$ obtained at 60 ˚C for 48 h
using Ti precursor type-B
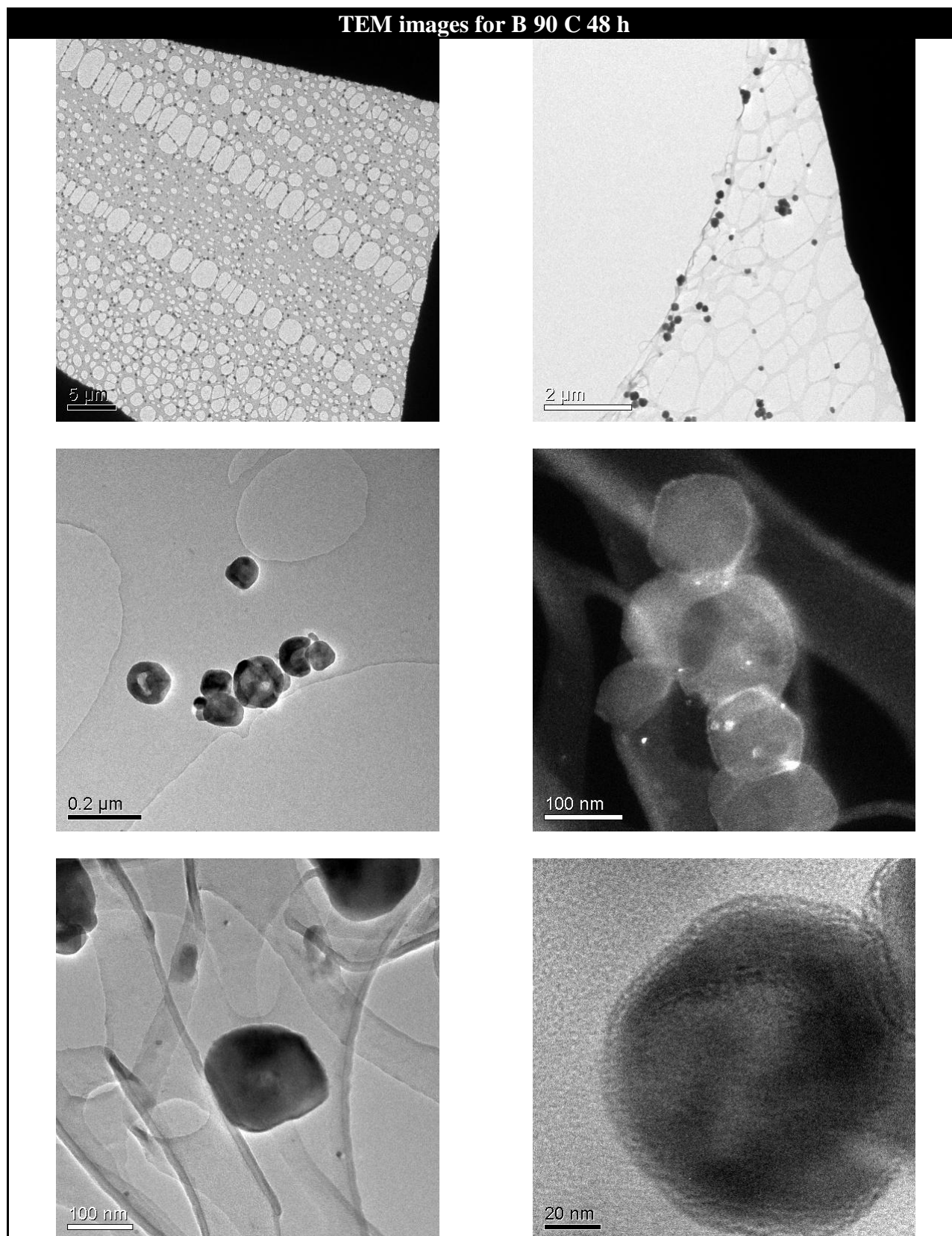
Figure 4-12 TEM bright and dark field images of BaTiO$_3$ obtained using Ti Precursor type-B at 90 ˚C for 48 h
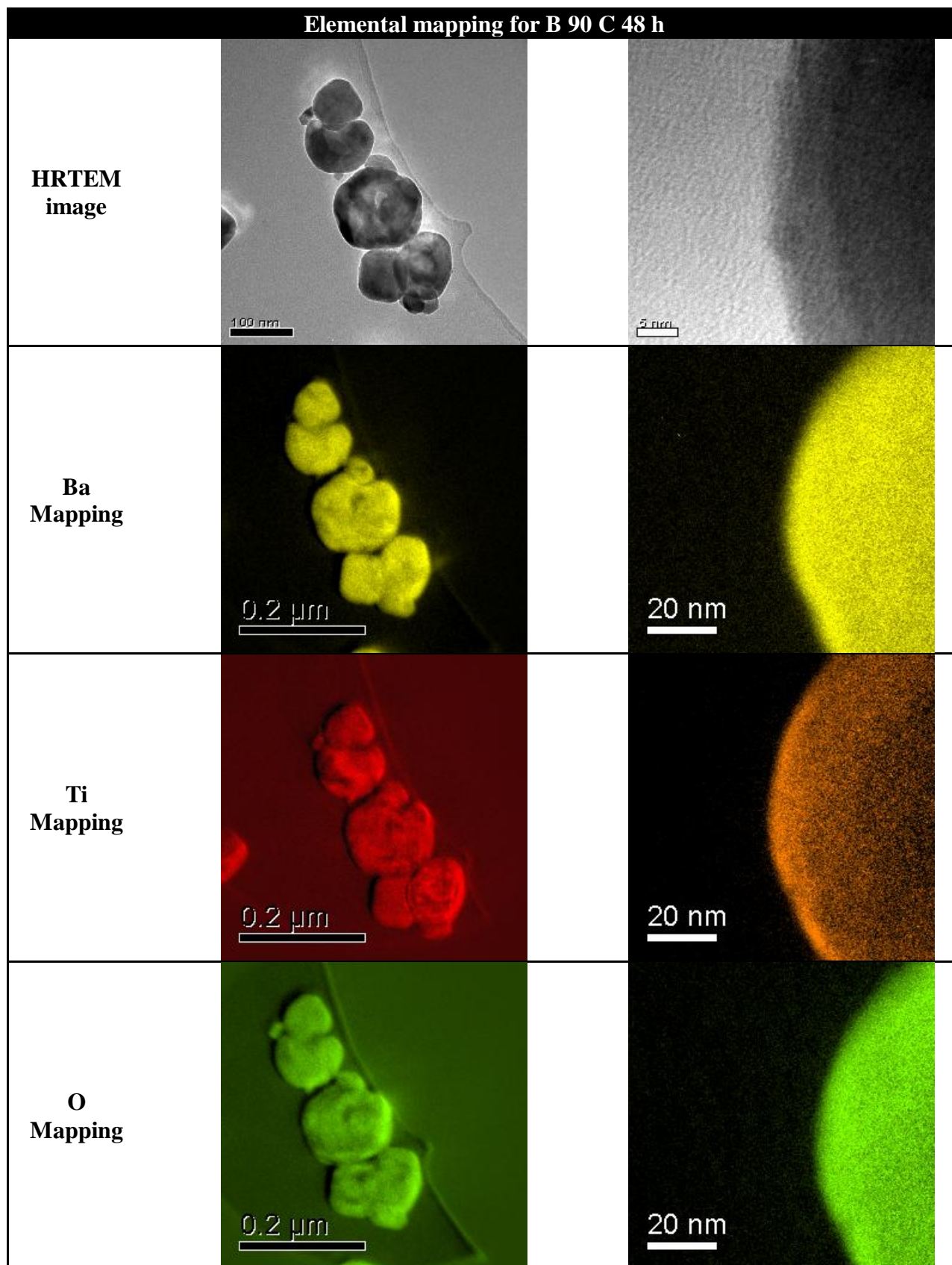
Figure 4-13 Elemental mapping of Ba, O, and Ti for BaTiO$_3$ obtained at 90 ˚C for 48 h using Ti precursor type-B

TEM images for B 150 C 48 h
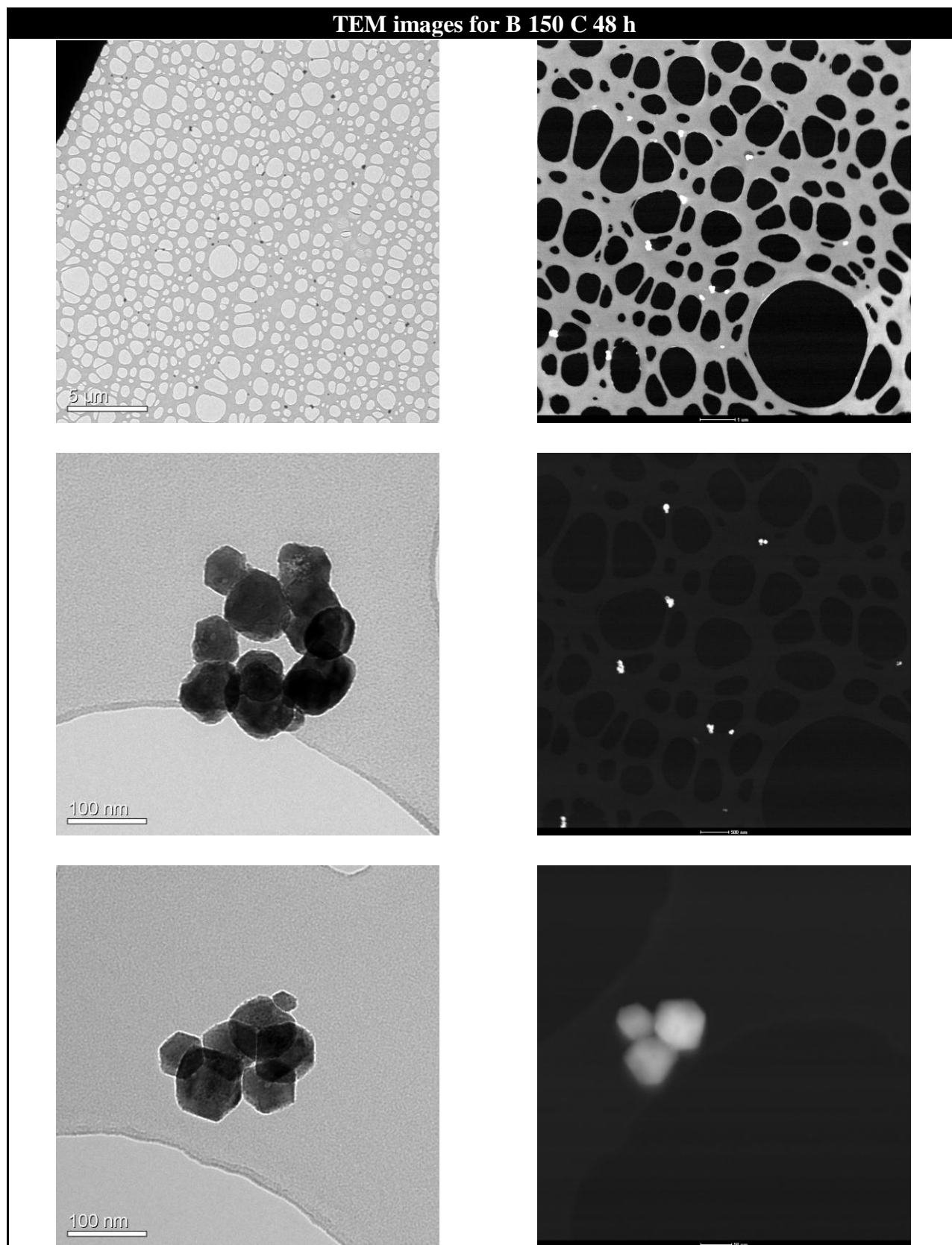
Figure 4-14   TEM bright and dark field images of BaTiO$_3$ obtained using Ti precursor type-B at 150 ˚C for 48 h

HRTEM images for B 150 48 h
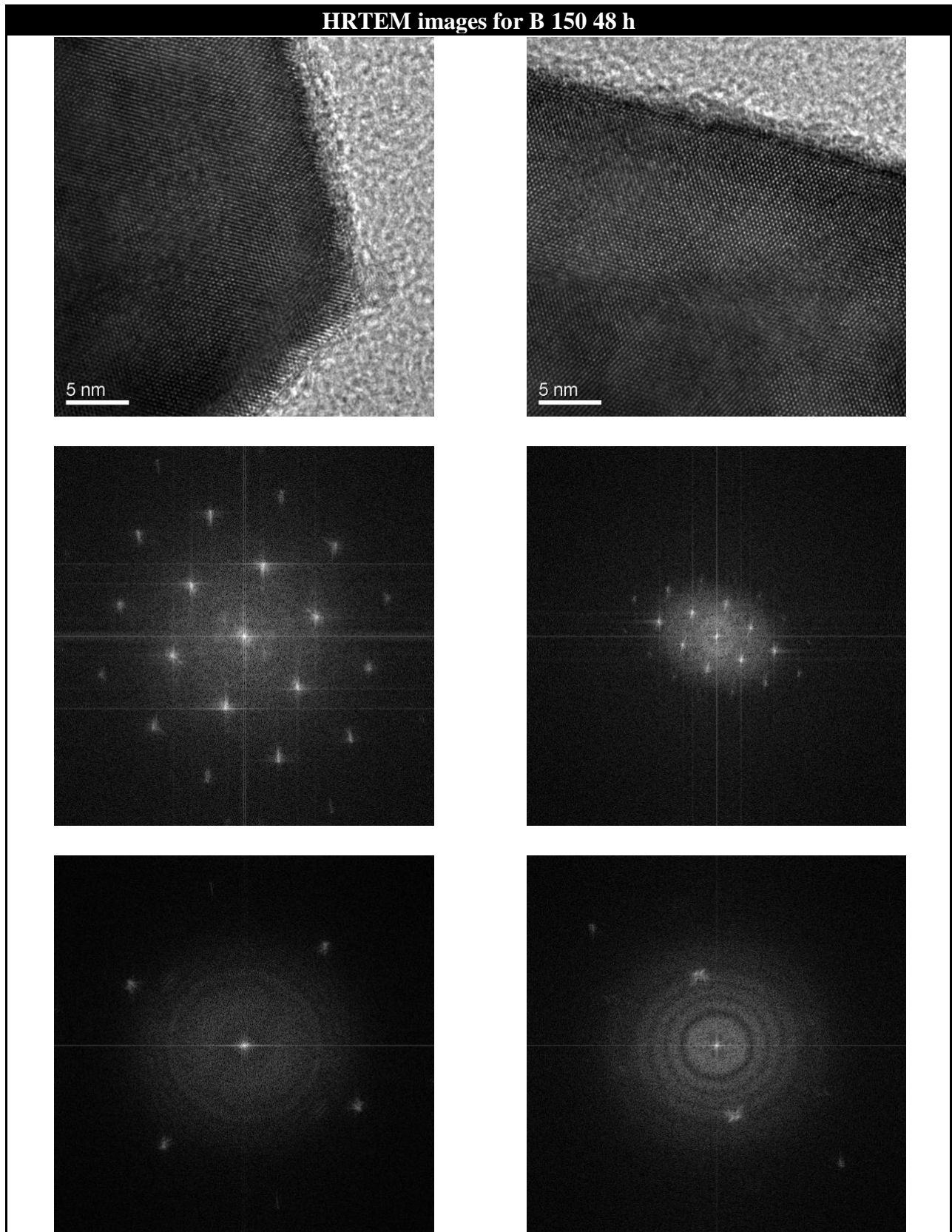
Figure 4-15   HR TEM images computer generated diffractogram for fully crystalline BaTiO$_3$ at 150 ˚C for 48 h using Ti precursor type-B
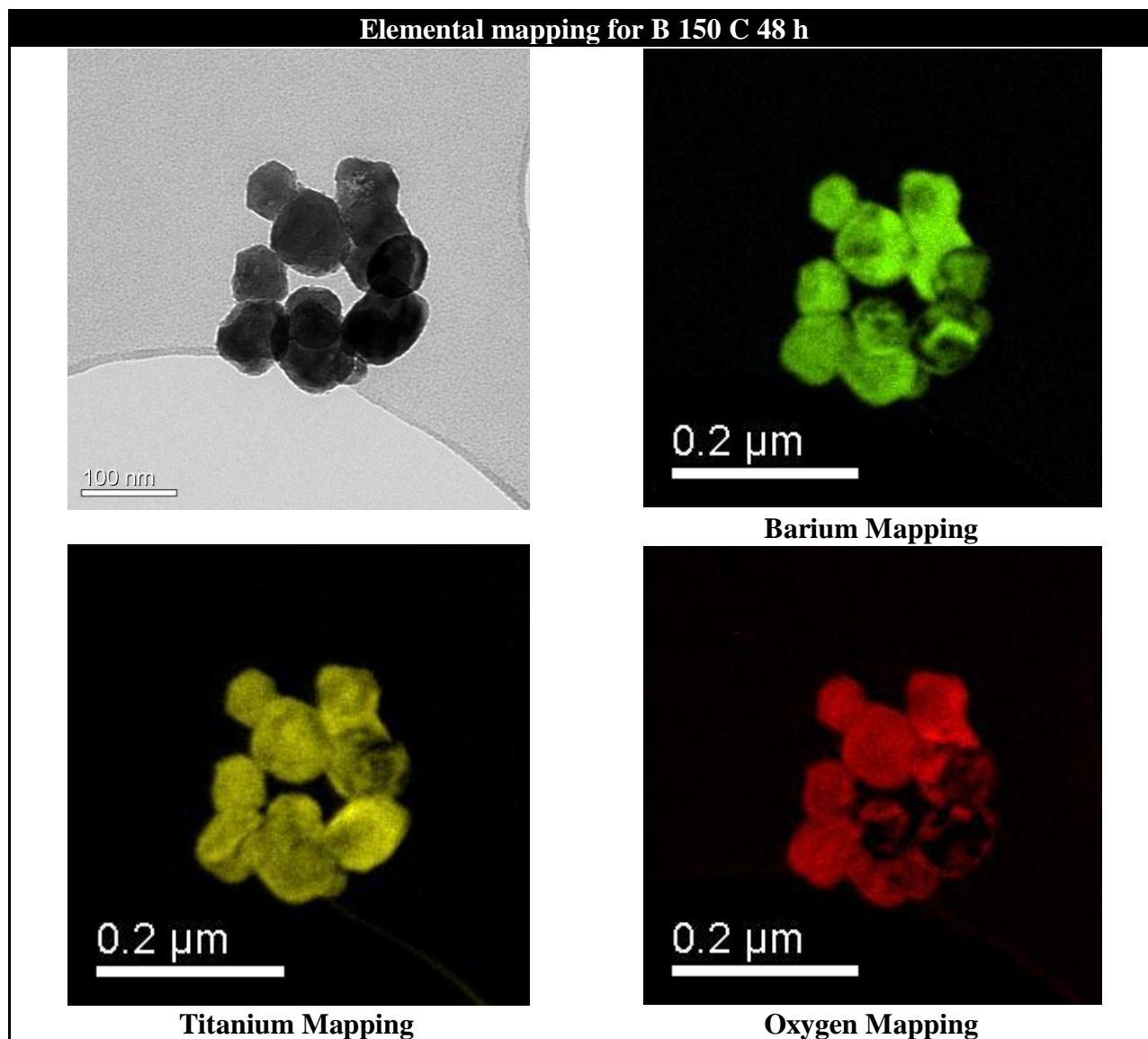
Figure 4-16 EFTEM elemental mapping of Ba, O, and Ti for BaTiO$_3$ obtained at 150 ˚C for 48 h using Ti precursor type-B

SEM micrographs of $BaTiO_3$ obtained using type-B precursor at 60 ˚C for 16 h shows ultrafine agglomerated clusters of particles with uniform size distribution (Figure 4-17). High resolution images show hazy structures of particles with no sharp boundaries. The irregular morphology is very similar to titania precursor used in this case.

The SEM images of samples obtained at 90 ˚C for 24 h and 150 ˚C for 24 h show as well clusters of agglomerates of $BaTiO_3$ nanopartilces. The particles size is in the range of 30 nm to 50 nm. Pores occur in samples at 90 ˚C for 48 h while more compact particles are observable at 150 ˚C for 24 h. The morphology of particles at 90 ˚C for 48 h is appearing to be round and porous. Whereas the sample at 150 ˚C for 24 h shows a fully formed, facetted particle shape (Figure 4-18).
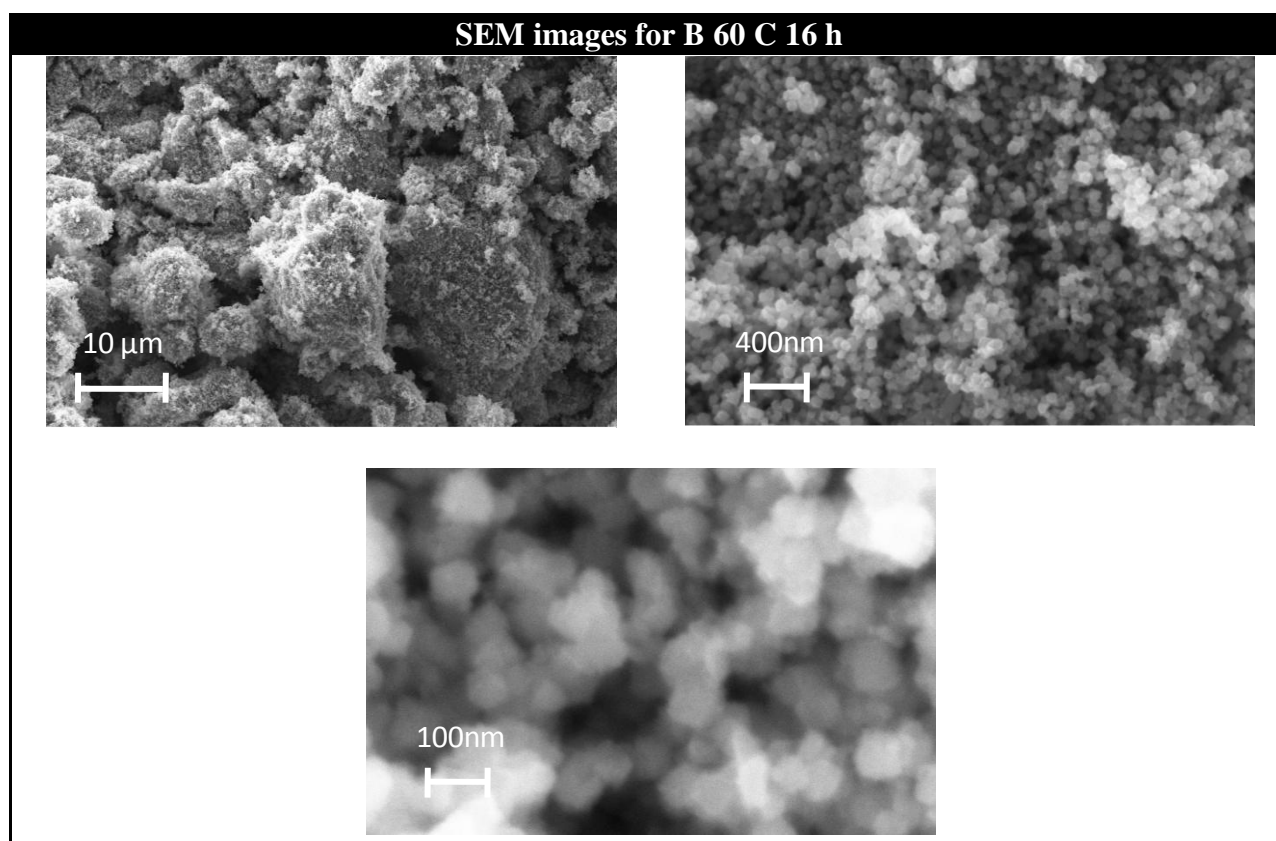
Figure 4-17   SEM micrographs for $BaTiO_3$ obtained at 60 ˚C for 14 h using Ti precursor type-B.
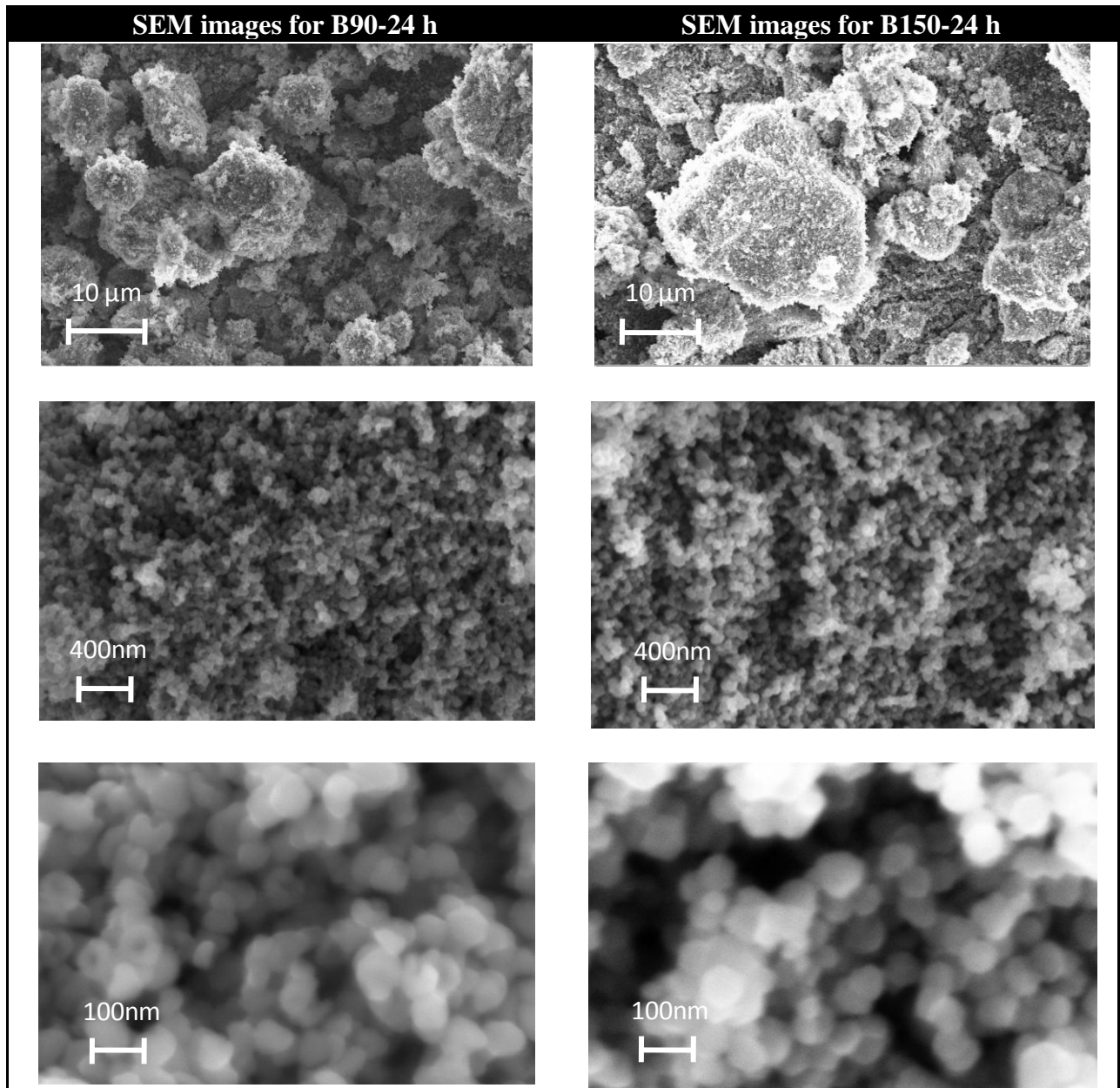
Figure 4-18 SEM micrographs for BaTiO$_3$ obtained at 90 and 150 ˚C for 24 h using Ti precursor type-B

4.1.3 Spindle like TiO$_2$ rutile phase used as Ti-precursor

XRD of samples using spindle like TiO$_2$ show the presence of BaTiO$_3$ perovskite structure along with evident peaks of rutile present in the final product (Figure 4-19). The crystallite size measurement is done using Scherrer's formula for (100) and (110) peaks of XRD diffractogram. The average of the two values was calculated which revealed that crystallite size of obtained BaTiO$_3$ was around 85 nm.

SEM images of the sample show monodispersed BaTiO$_3$ nanoparticles with a particle size in the range between 300 nm to 400 nm with uniform size distribution (Figure 4-20). The morphology of the particles is round which is very different from that of spindle like titania used as titanium precursor. High resolution images reveal some unreacted titania precursor can be found in the final product.
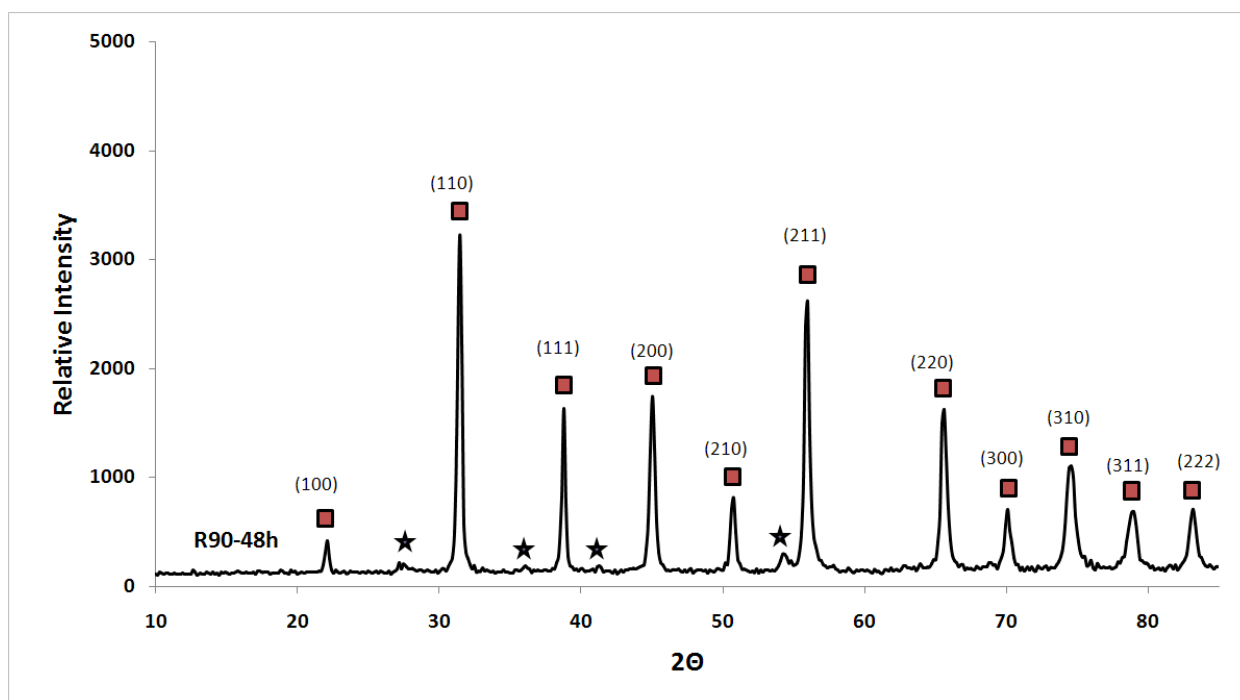
Figure 4-19   X-ray diffraction pattern for BaTiO$_3$ obtained using spindle like TiO$_2$ rutile at 90 ˚C for 48 h reaction times (■ BaTiO$_3$, ⋆ Rutile).
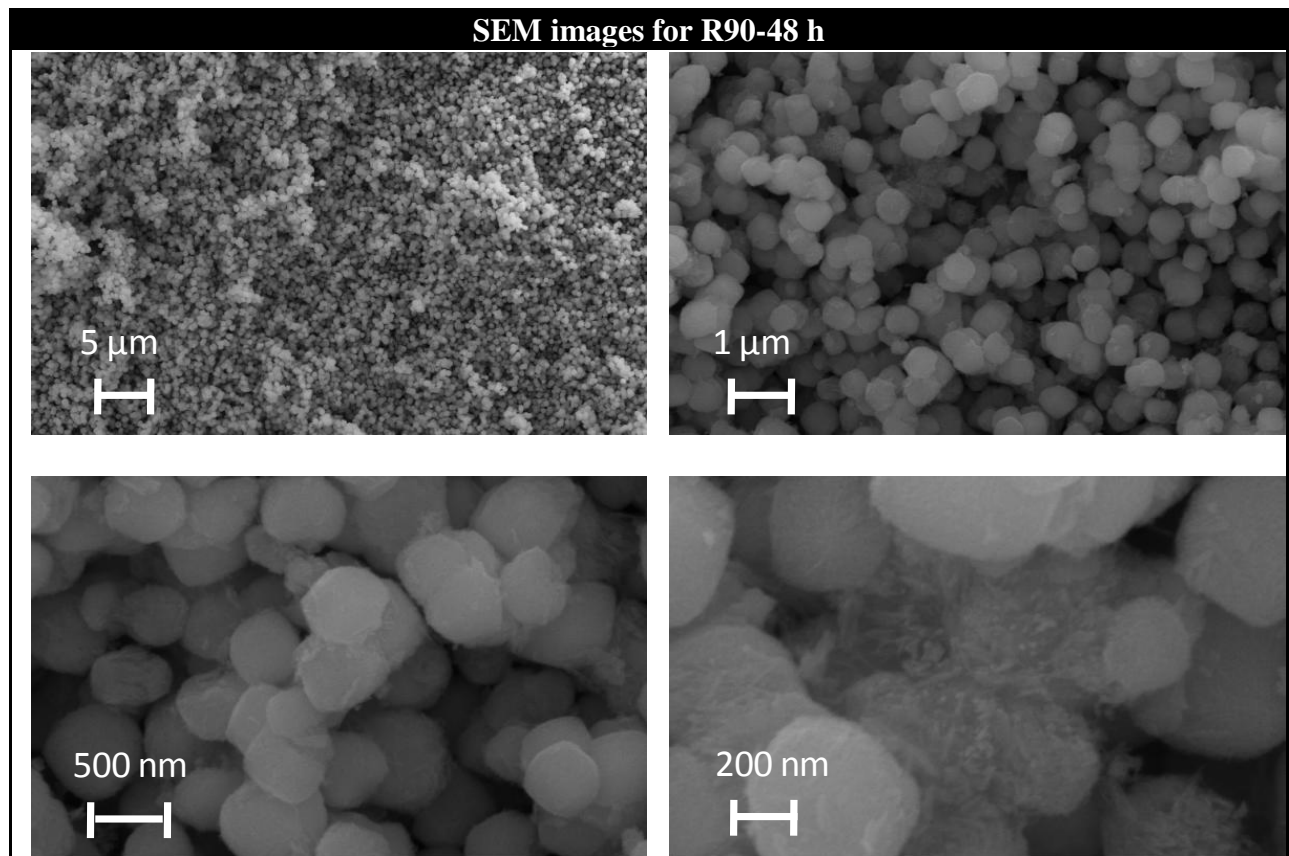
Figure 4-20 SEM images for BaTiO$_3$ obtained using spindle like TiO$_2$ rutile at 90 ˚C for 48 h reaction times, spindles of TiO$_2$ nanofibres are apparent at high resolution.

4.1.4 Use of barium stearate and titanium tetrachloride

Barium stearate $(C_{17}H_{35}COO^{-})_2 Ba^{2+}$ was used instead of Barium Hydroxide, as barium precursor – an effort to obtain in situ surface functionalized $BaTiO_3$. Titanium tetrachloride $(TiCl_4)$ was used as titanium precursor. After the autoclavation of 24 h at 190 ˚C, slurry appeared to contain lot of sticky substance with no presence of ceramic powder. The product was dried to remove water and used for XRD analysis.

XRD patterns of the sample showed no sign of perovskite structure of $BaTiO_3$, indicating that presence of stearate hindered the hydrothermal synthesis of $BaTiO_3$ at 190 ˚C after 24 h of reaction (Figure 4-21).
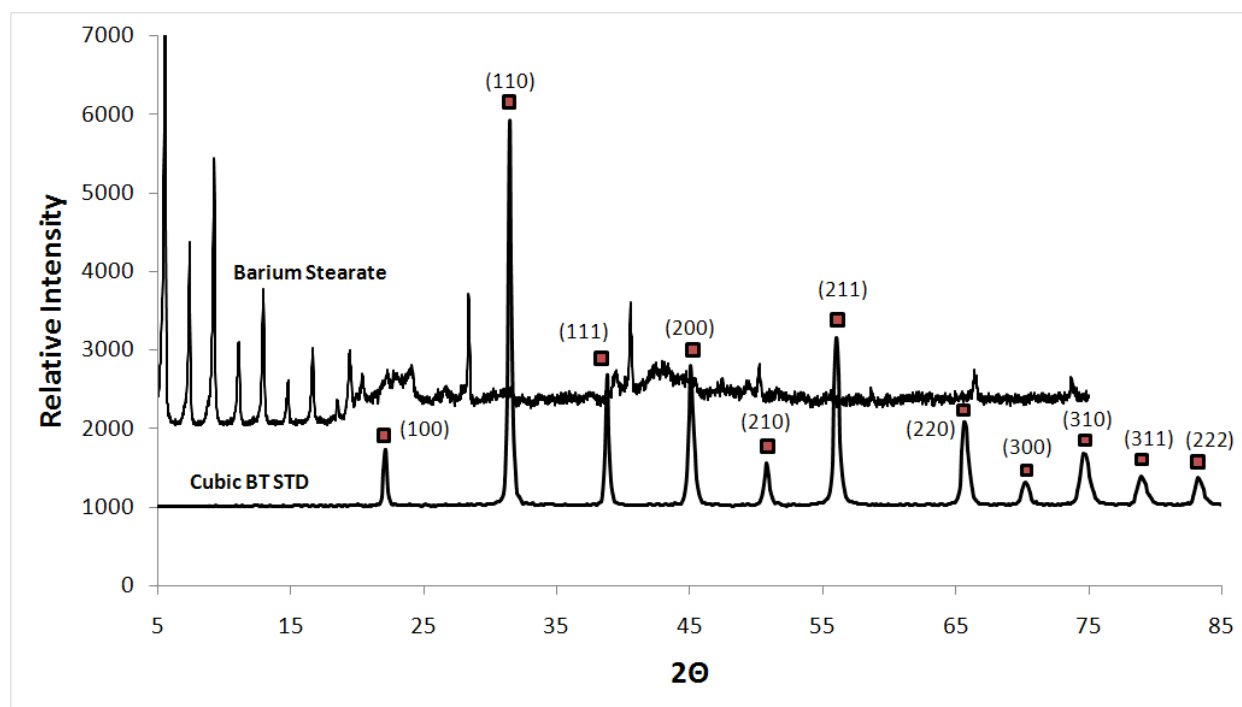
Figure 4-21 XRD pattern for sample obtained using barium stearate as barium precursor at 190 ˚C after 24 h and standard cubic $BaTiO_3$ perovskite peaks for comparison.

4.2 Solvothermal synthesis of BaTiO$_3$

The following set (Table 4-V) of experiments was done as described in experimetal work (section 3.2). The Ba to Ti ratio was kept equal to 2, while TiO$_2$ P25 was used as titania precursor. Solvent ratio in volume percent was kept 50 % ethanol (EtOH) with DI water.

Table 4-V   Samples obtained for solvothermal synthesis of BaTiO$_3$

Sample	Temperature ˚C	Time days	Ti-Precursor A or B	Ba : Ti	EtOH:H$_2$O
1. EtOH-1	185	6	B	2 : 1	1 : 1
2. EtOH-2	185	2 (48 h)	B	2 : 1	1 : 1
3. EtOH-3	235	1 (24 h)	B	2 : 1	1: 1

Figure 4-22 shows XRD patterns for BaTiO$_3$ powders synthesized at 185 ˚C for 2 and 6 days and 235 ˚C for 1 day (24 h),. In all the cases the BaTiO$_3$ perovskite structure is apparent with no sign of unreacted TiO$_2$ rutile phase. Thus a phase pure BaTiO$_3$ final product is achieved under the given reaction conditons with water and ethanol as solvent.

Peaks (002) and (200) are enlarged in Figure 4-23 to compare the powder tetragonality. It compares the powder diffraction pattern in the 40 to 50 2Ɵ regions, at room temperature for BaTiO$_3$ generated from barium hydroxide and TiO$_2$ P25 Degussa. This region of the diffraction pattern is characteristic of the tetragonal versus cubic form of BaTiO$_3$.

The crystallite size measurements were done using Scherrer's formula for peaks (100) and (110). The average of the two values is taken as the final crystallite size for each sample. The sample EtOH-1 reacted at 185 ˚C for 6 days have the largest value of crystallite size i.e., 65nm, while EtOH-2 has a size equal to 58 nm and EtOH-3 has value equal to 56nm.

Figure 4-24 shows the SEM images of BaTiO$_3$ nanopowders obtained at 185 ˚C for 6 days (EtOH-1) and 185 ˚C after 2 days (EtOH-2). The morphology of the particles sample EtOH-1 appears to be round, whereas it has narrow size distribution with average particle size of 120 nm.

In case of EtOH-2 sample morphology is tending more towards elongated cubic shape than rounded structure with narrow size distribution. The estimated average particle size here is about 100 nm.
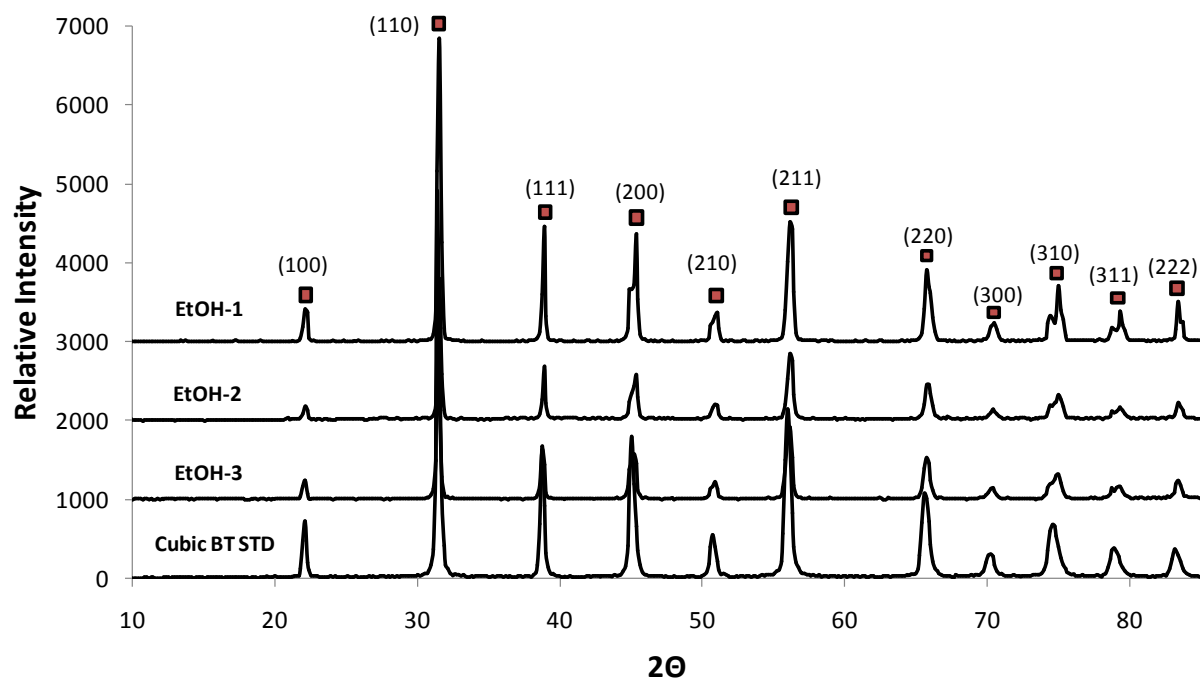
Figure 4-22   XRD patterns for BaTiO$_3$powders obtained solvothermally using ethanol: DI water = 1 : 1
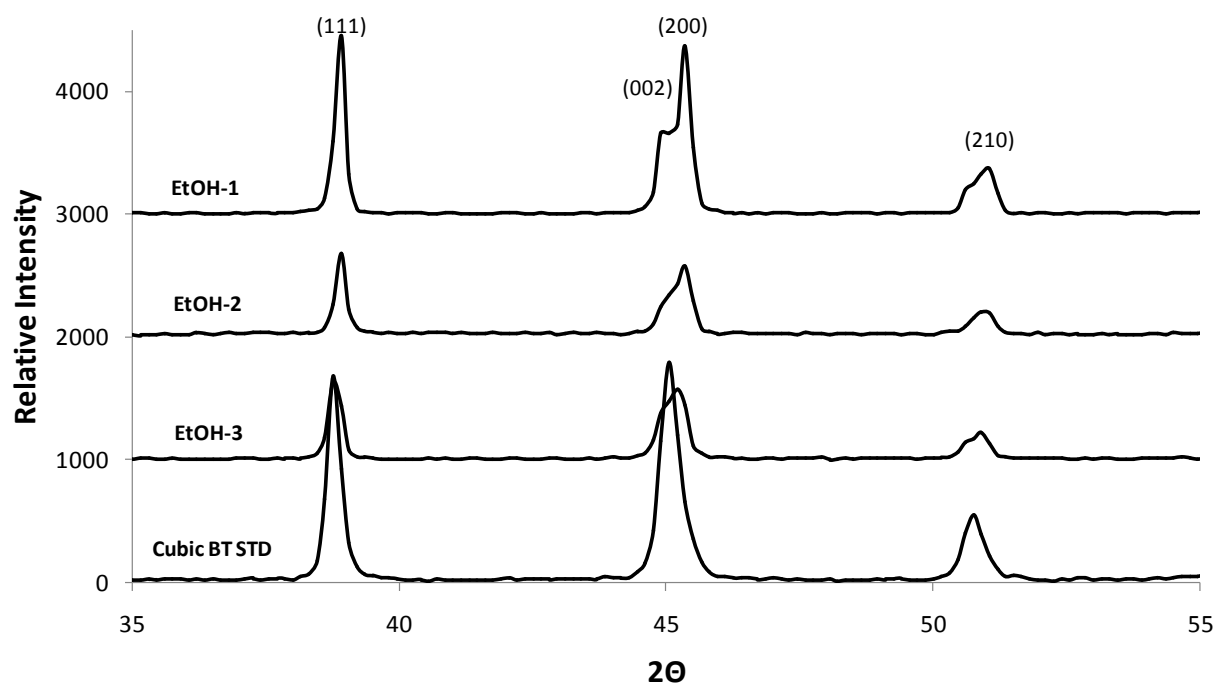
Figure 4-23 Partial enlargement of XRD patterns for solvothermally synthesized BaTiO₃ powders to compare tetragonality
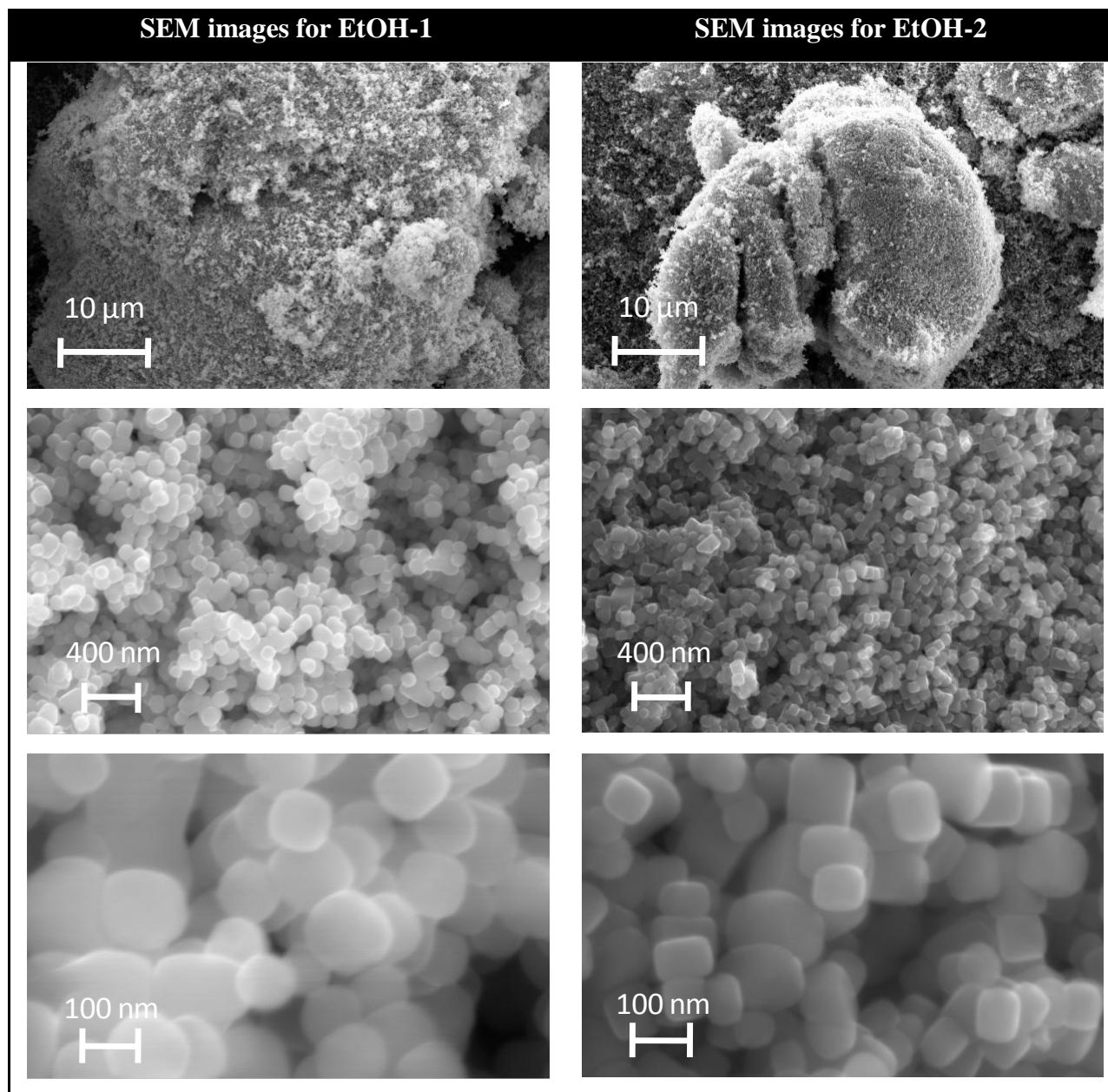
Figure 4-24 SEM images showing the solvothermally synthesised BaTiO$_3$ particles at 185 ˚C for 6 days (EtOH-1) and 185 ˚C for 2 days (EtOH-2)

4.3 Dispersion of BaTiO₃ in PMMA and thin films

4.3.1 Dispersion of BaTiO₃ nanoparticles in different solvents

Among various solvents ethanol was found to be the best with respect to stablity of $BaTiO_3$ suspension. $BaTiO_3$ powder remained suspended in EtOH dispersion for longer time when compared to other solvents, whereas in case of other solvent like acetone and THF the $BaTiO_3$ particles settled down over a short time.

Different samples of $BaTiO_3$ were dispersed in ethanol, to achieve dispersed $BaTiO_3$ sample. There was no such difference found for different $BaTiO_3$ samples.

EtOH and acetone in different ratios (EtOH: Acetone = 1:1, 2, 3, 4, 5, 10) proved to be a good dispersent for dispersing $BaTiO_3$ powders in all above ratios.

4.3.2 Choice of solvent for dissolution of PMMA and different MWs used

Acetone, tetrahydrofuran (THF), chlorobenzene (MCB) and toluene are good solvents for dissolution of PMMA. The solutions in a particular solvent are obtained at different concentration 10 g/L, 20 g/L, 200 g/L and 400 g/L depending on molecular weight of the PMMA. Higher molecular weight resulted in concentrated solutions for same weight percent of PMMA in a solvent when lower molecular weights the viscosity remained low. PMMA solutions were obtained for different molecular weights of PMMA i.e., ACROS 35 000 and Sigma Aldrich 35 0000, and 120 000. MCB can dissolve high concentration of PMMA as compared to THF and toluene.

4.3.3 Vacuum dried BaTiO₃ nanopowders

The vacuum dried $BaTiO_3$ powders appear to better dispersed in dispersions due to removal of water contents in extreme dry condition under vacuum of 0.1 mbar at 110 ˚C for 5 days.

4.3.4 Ultrasonication as mode for deagglomeration of BaTiO₃ nanopowders

Ultrasonication is a common technique for deagglomeration of agglomerated powders. In this work agglomerated $BaTiO_3$ nanopowders were easily deagglomerated by sonicating the powders in certain solvent. For the dispersion to remain stable for longer time a known amount of $BaTiO_3$

powders is added to a certain solvent along with a suitable surfactant and sonicated at room temperature for 15 min to 30 min.The polymer was then added and sonication of the dispersion resulted in stable dispersions of $BaTiO_3$ powders in PMMA. These dispersion were used for obtaining layers and refluxing.

4.3.5 Post functionalization of BaTiO$_3$ particles

Use of stearic acid (Octadeconic acid $C_{18}H_{36}O_2$) for the post functionalization of $BaTiO_3$ powders resulted in better dispersion at lower concentration 1 % to 2 % volume fraction of $BaTiO_3$ fillers in the dispersion in case of PMMA in THF system. The weight fraction of PMMA in solvents was kept 0.56 %.

The $BaTiO_3$ already dispersed in EtOH-acetone when mixed with PMMA in acetone resulted in phase separation of PMMA in the system. The presence of EtOH resulted in water formation in the suspension that caused this phase separation of PMMA in solution.

Stearic acid was dissolved in THF and $BaTiO_3$ already dispersed in THF were mixed with it. PMMA in THF was added subsequently and whole system was agitated using ultrasonication technique. The dispersion obtained remained suspended for lower volume fraction of $BaTiO_3$ i.e., 1 % to 2 % volume fraction, but at higher filler loading lot of aggregation and settling down of $BaTiO_3$ particles was observed. Thin layers were obtained using dip coating method and were characterized under the SEM scanning electron microscopy to observe dispersion of $BaTiO_3$ particle in PMMA (Figure 4-25).

Under electron beam the sample started charging which caused the destruction of the layer as shown in Figure 4-25 a. The hole is appearing in the centre of the image. To avoid charging of the sample, carbon black was used to deposit on the sample before characterization. The Figure 4-25 c shows a SEM sample sputtered with carbon black. It helped to avoid the breaking of the thin polymer film. In future samples a conducting substance (gold, platinum or carbon black) is evaporated under vacuum to deposit a thin conducting layer on the sample to be characterized.

Figure 4-25 c shows that filler in the polymer (PMMA) is quite low and is distributed across the film with some aggregated particles, sedimentation has already occurred before deposition of the thin film using dip coating on glass substrate.

BaTiO₃ PMMA layers obtained using dip coating

a. Charging under SEM

b. Particles covered with polymer

c. Layer sputtered with Carbon black to avoid charging under SEM

d. Agglomerated particles

e. 1 % volume BaTiO₃ in PMMA, 0.56 % weight PMMA in THF, Stearic acid 4 times the weight of BaTiO₃
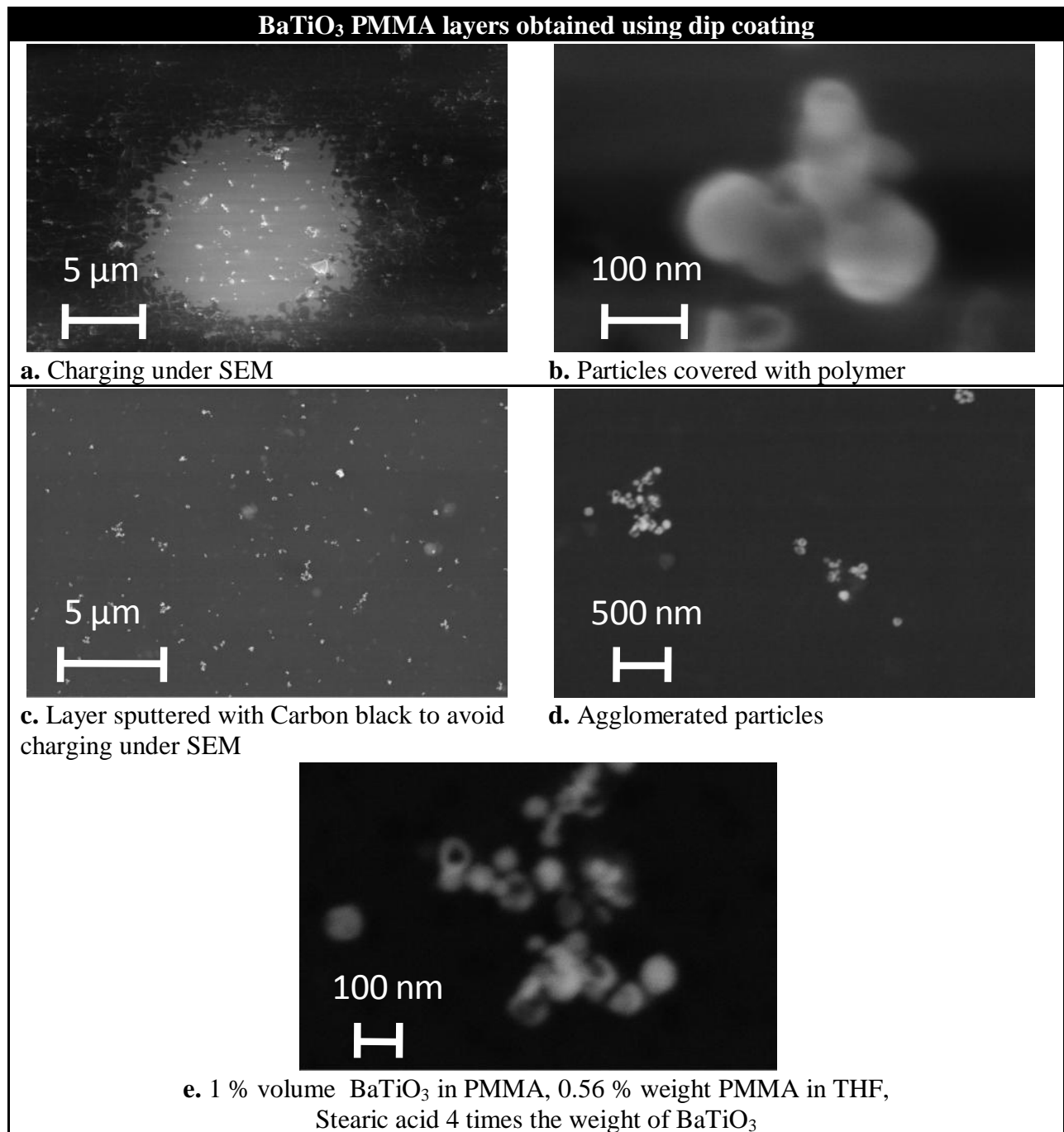
Figure 4-25 BaTiO₃ dispersion using stearic acid at low volume filler fraction

4.3.6 Choice of surfactant for dispersion

The search for one best surfactant for dispersing BaTiO₃ nanoparticles in solvents (THF, toluene or MCB) which are suitable for dissolving PMMA lead to the conclusion that using non-ionic surfactants dispersions remain stable over relatively longer time when compared to ionic or cationic surfactant. Brij 35P and block copolymer poly(methylmethacrylate-co-methacrylic acid) (PMMA-co-MA MW 34 000) were found to be dispersing BaTiO₃ in THF. Slight settling of

BaTiO$_3$ particles was observed with the passage of time. The coagulation of powders was seen for overnight left dispersions.

The dispersion with Brij 35P was used to obtain thin layer using dip coating at various dip speeds i.e., (30, 60 and 85) mm/min. The SEM analysis of the layer showed the homogeneous dispersion of BaTiO$_3$ in PMMA (Figure 4-26).

9% volume fraction BaTiO$_3$ in PMMA 0.56 % weight PMMA in THF, Brij 35P 10 times the weight of BaTiO$_3$
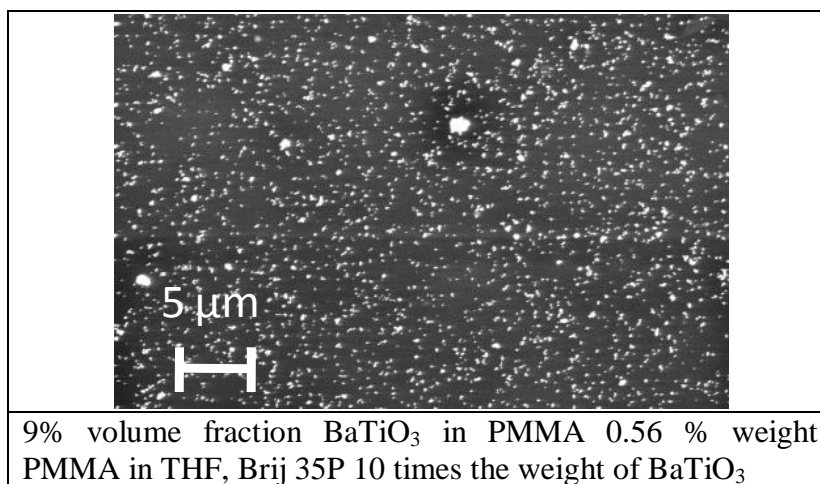
Figure 4-26   SEM image of well dispersed BaTiO$_3$ nanoparticles in PMMA, where Brij 35P was used as surfactant 10 times the weight of the filler

4.3.7   Varying surfactant to BaTiO$_3$ ratio

The ratio of the surfactant to BaTiO$_3$ filler was varied in the range 5, 3.33, 2 and 1 times the weight of the filler in the dispersion while the PMMA in all the case was kept equal to 0.374 weight percent of the THF used to obtain dispersions. The effect of variation of Brij 35P was studied as shown in Table 4-VI.

Table 4-VI   Varying surfactant to BaTiO$_3$concentration

Experiment	Volume % BT in PMMA	Weight % PMMA in THF	Brij 35P Times BT	PMMA-co-MA acid times BT
a)	16.6	0.374	5	0
b)	16.6	0.374	3.33	0
c)	28	0.374	2.5	0
d)	33.2	0.374	2	0
e)	33.2	0.374	2	0.8

At higher concentration of surfactant it was observed that the film had become hazy due to excessive absorption of water (Figure 4-27 **a**, **b,** and **e**). At higher filler loadings and low surfactant to filler ratio (Figure 4-27 **c** and **d**) layer is showing well dispersed BaTiO$_3$ in PMMA. The sedimentation is evident in the suspensions, which causes lower loading of BaTiO$_3$ particles in thin layers obtained using dip coating. The presence of co-polymer PMMA-co-MA acid along with Brij as surfactant shows better dispersion of BaTiO$_3$ in PMMA with closely packed BaTiO$_3$ nanoparticles as depicted in Figure 4-27 **e.** Slight agglomeration is evident in SEM images of all the samples.At 16.5 % volume filler fraction two different dispersion were obtained with PMMA as 0.56 % and 2.73 % weight of solvent while copolymer and Brij were both added as 25 % and 50 % weight of filler in each case respectively as shown inTable 4-VII **a)** and **b)**.

At 16.6 % and 9 % volume fraction of filler in PMMA (1.23 % and 1.56 % wt of solvent) the low concentration of brij and co-polymer were used.

Figure 4-28 shows the well dispersed BaTiO$_3$ nanoparticles in polymer matrix. The higher weight percent of PMMA in solvent leads to excessive close packing in the layer, whereas at low weight percent the BaTiO$_3$ nanoparticles are homogenously distributed over the film. The films obtained using dip coating shows the self assembly of nanoparticles. The agglomerates are observable in case of 2.73 % weight percent PMMA in THF, while at lower weight percent i.e., 0.56 % the film appears to be very homogeneous.

Figure 4-29 shows homogenous distribution of nanofillers in the polymer matrix at two different volume percent fractions i.e., 16.6 % and 9 % volume and almost equal weight percent of PMMA in THF. The self assembly of the nanoparticle is appearing nice and homogenous during dragging off the glass substrate from the dispersion.

Table 4-VII   Usage of copolymer as surfactant along with Brij 35P

Experiment	Volume % BT in PMMA	Weight % PMMA in THF	Brij 35P	PMMA-co-MA acid
a)	16.5	0.56	25 % wt of BT	25 % wt of BT
b)	16.5	2.73	50 % wt of BT	50 % wt of BT
c)	16.6	1.23	2.5 % wt of BT	2.5 % wt of BT
d)	9	1.56	2.5 % wt of BT	2.5 % wt of BT

Effect of variation of Brij concentration on dispersion of BaTiO₃ in PMMA at different % volume fraction of BaTiO₃ in PMMA

a) 16.6 Volume % fraction BaTiO₃ in PMMA 0.374 wt % PMMA in THF Brij 35P 5 X the weight of BaTiO₃

b) 16.6 Volume % fraction BaTiO₃ in PMMA 0.374 wt % PMMA in THF Brij 35P 3.33 X the weight of BaTiO₃

c) 28 Volume % fraction BaTiO₃ in PMMA 0.374 wt % PMMA in THF Brij 35P 2.5 X the weight of BaTiO₃

d) 33.2 Volume % fraction BaTiO₃ in PMMA 0.374 wt % PMMA in THF Brij 35P 2 X the weight of BaTiO₃

e) 33.2 Volume % fraction BaTiO₃ in PMMA 0.374 wt % PMMA in THF Brij 35P 2 X the weight of BT and Copolymer 0.8 times the weight of BaTiO₃

Figure 4-27   Varying surfactant concentration with different filler loading in polymer-ceramic composite

BaTiO₃ PMMA layers obtained using dip coating

16.5 % volume fraction BaTiO₃ in PMMA
2.73 wt % PMMA in THF Brij 35P & PMMA-
co-MA, 25 % wt of BaTiO₃ each

16.5 % volume fraction BaTiO₃ in PMMA
0.56 wt % PMMA in THF Brij 35P & PMMA-
co-MA, 50 % weight of BaTiO₃
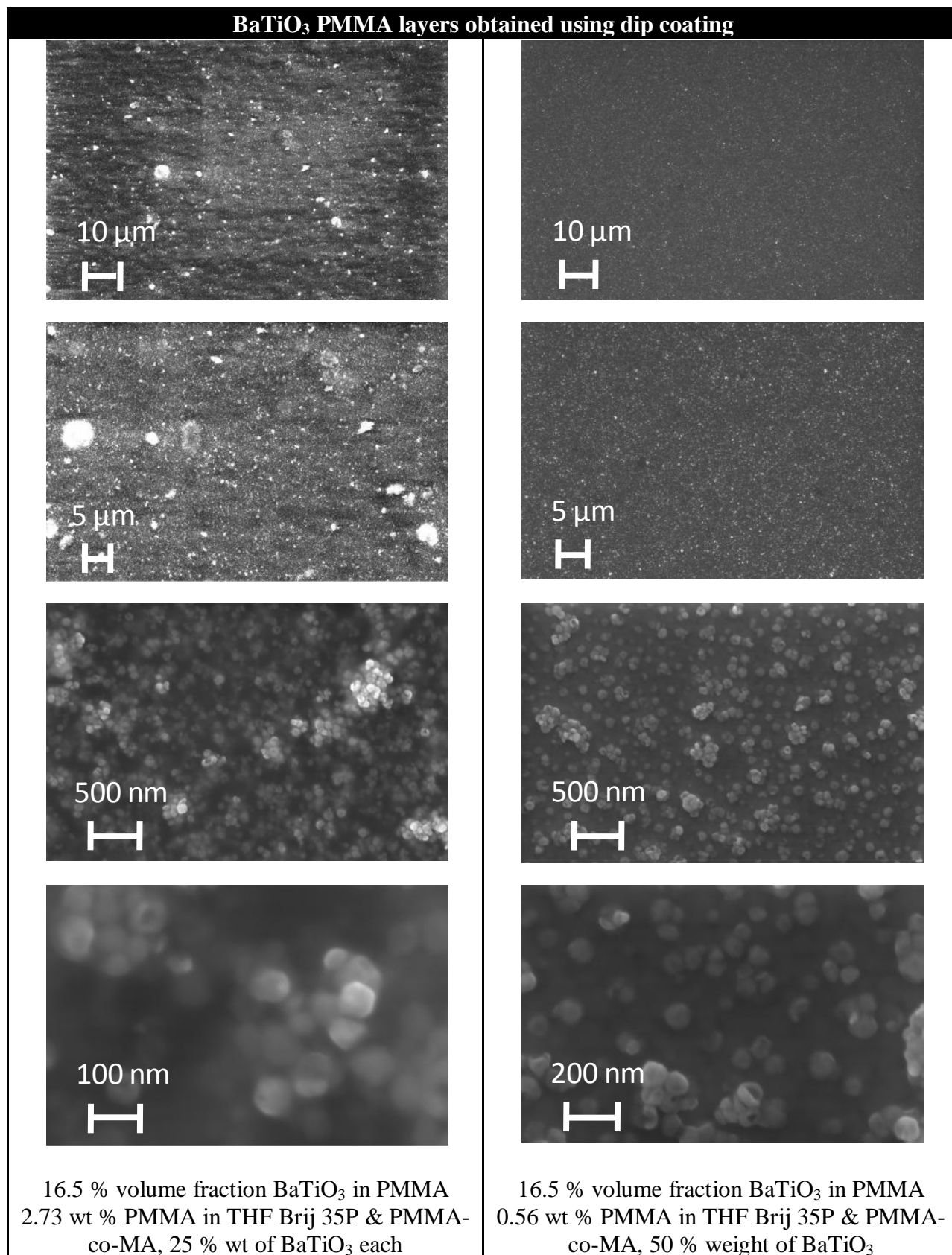
Figure 4-28   Homogeneous distribution of BaTiO₃ in PMMA with PMMA-co MA and Brij 35P
as surfactants

The FIB analysis with milling a crossection in the layer reveal that the filler particles are not just embedded over the polymer during self assembly but as well homogenously distributed within the film (Figure 4-30).

A thin film on antimony doped tin oxide on glass shows good adhesion of dispersion (16.6 volume percent filler fraction and low weight percent PMMA). The dispersion was used after long time (left over standing over a week) and used as it is without stirring or sonicating. The low filler content in the film is a proof of some settling over the time in the dispersion, while good adhesion to oxide layer is proof that our dispersion are attaching well to all oxide layers than to any hydrophilic surfaces.

The ATO layer has some breaking which is evident in the films without and with $BaTiO_3$-PMMA films.

The film thickness measurement of the film on glass for the same dispersion using optical profilometer is shown in Figure 4-32.

$BaTiO_3$ PMMA layers obtained using dip coating

16.63 % volume fraction $BaTiO_3$ in PMMA 1.23 % wt PMMA in THF Brij 35P & PMMA-co-MA 2.5 % wt of $BaTiO_3$

9 % volume fraction $BaTiO_3$ in PMMA 1.58 % wt PMMA in THF Brij 35P& PMMA-co-MA 2.5 wt % of $BaTiO_3$
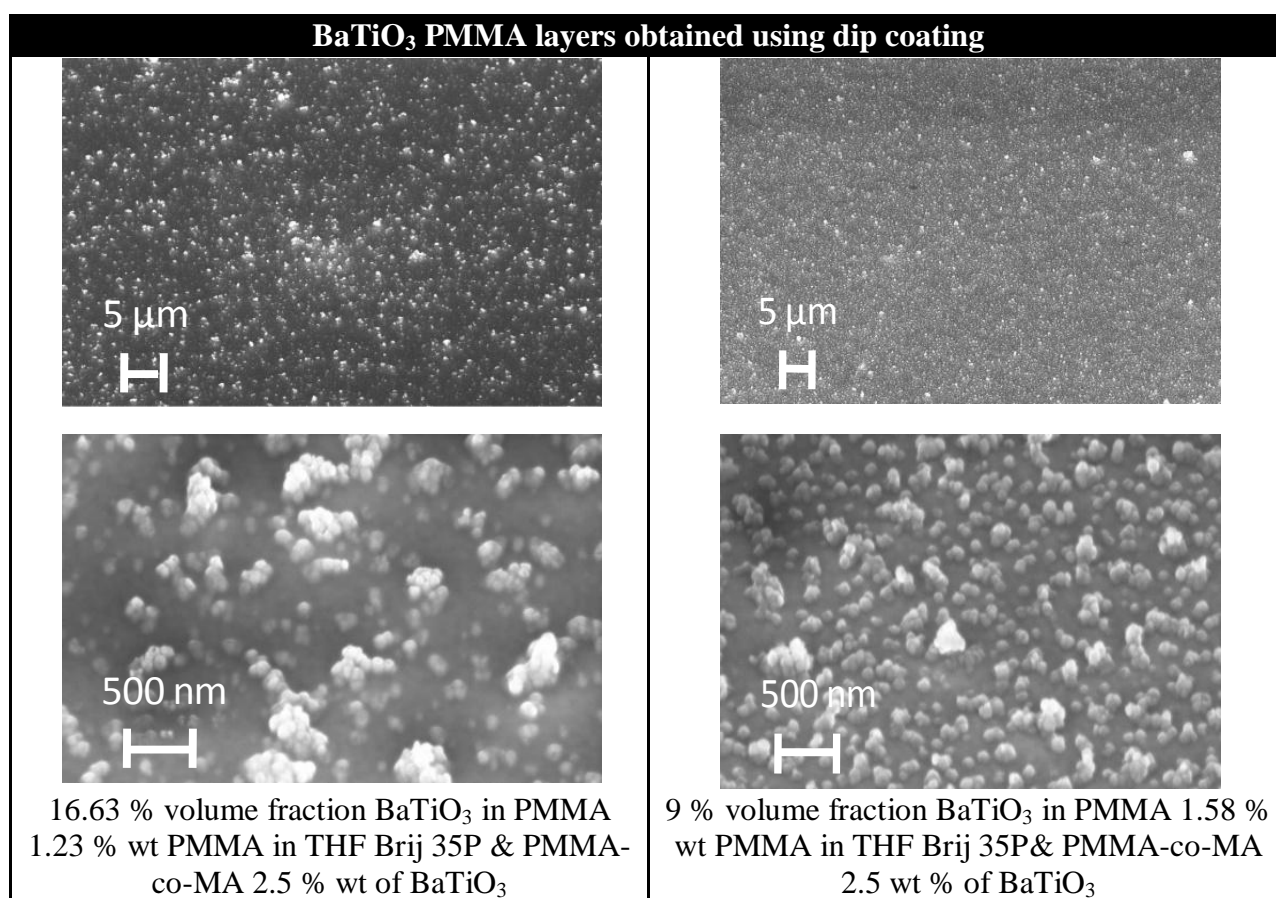
Figure 4-29 Homogeneous distribution of $BaTiO_3$ in PMMA at low concentration of Brij and copolymer as surfactant

FIB analysis of thin film and HR SEM image

9 % volume fraction BaTiO$_3$ in PMMA 1.58 % wt PMMA in THF Brij 35P& PMMA-co-MA 2.5 wt % of BaTiO$_3$
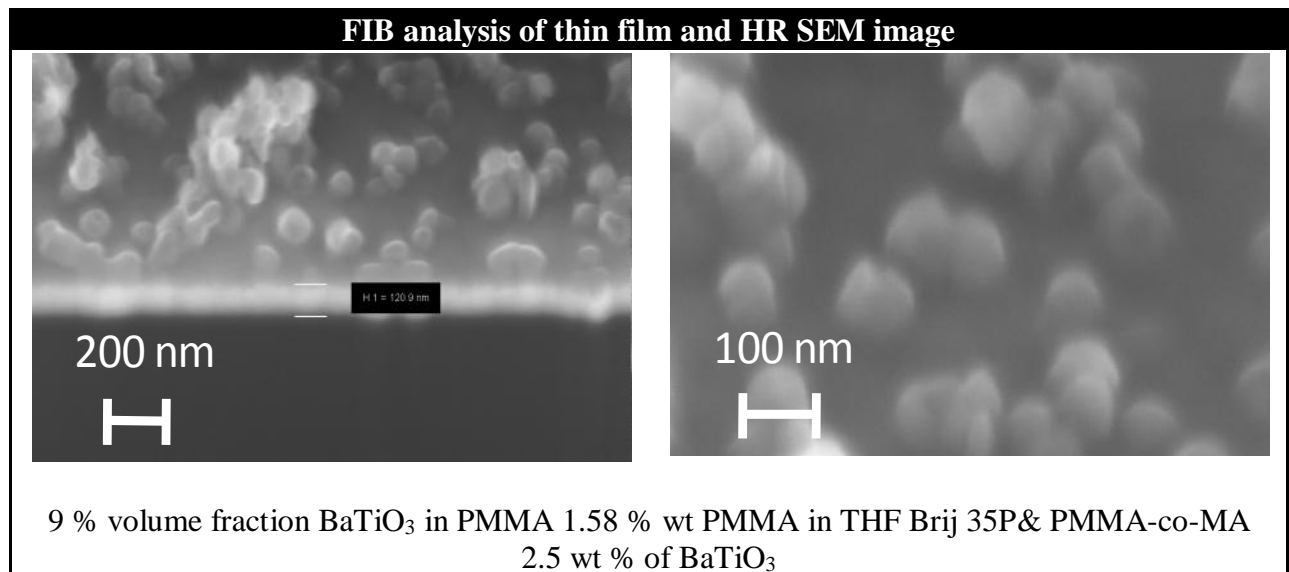
Figure 4-30 Crossection milled using focused ion beam of electrons for thin film and image of surface

BaTiO$_3$ PMMA layers obtained on ATO using dip coating

16.6 % volume fraction BaTiO$_3$ in PMMA 0.8 % wt PMMA in THF Brij 35P& PMMA-co-MA 2.5 wt % of BaTiO$_3$ on ATO obtained after a week
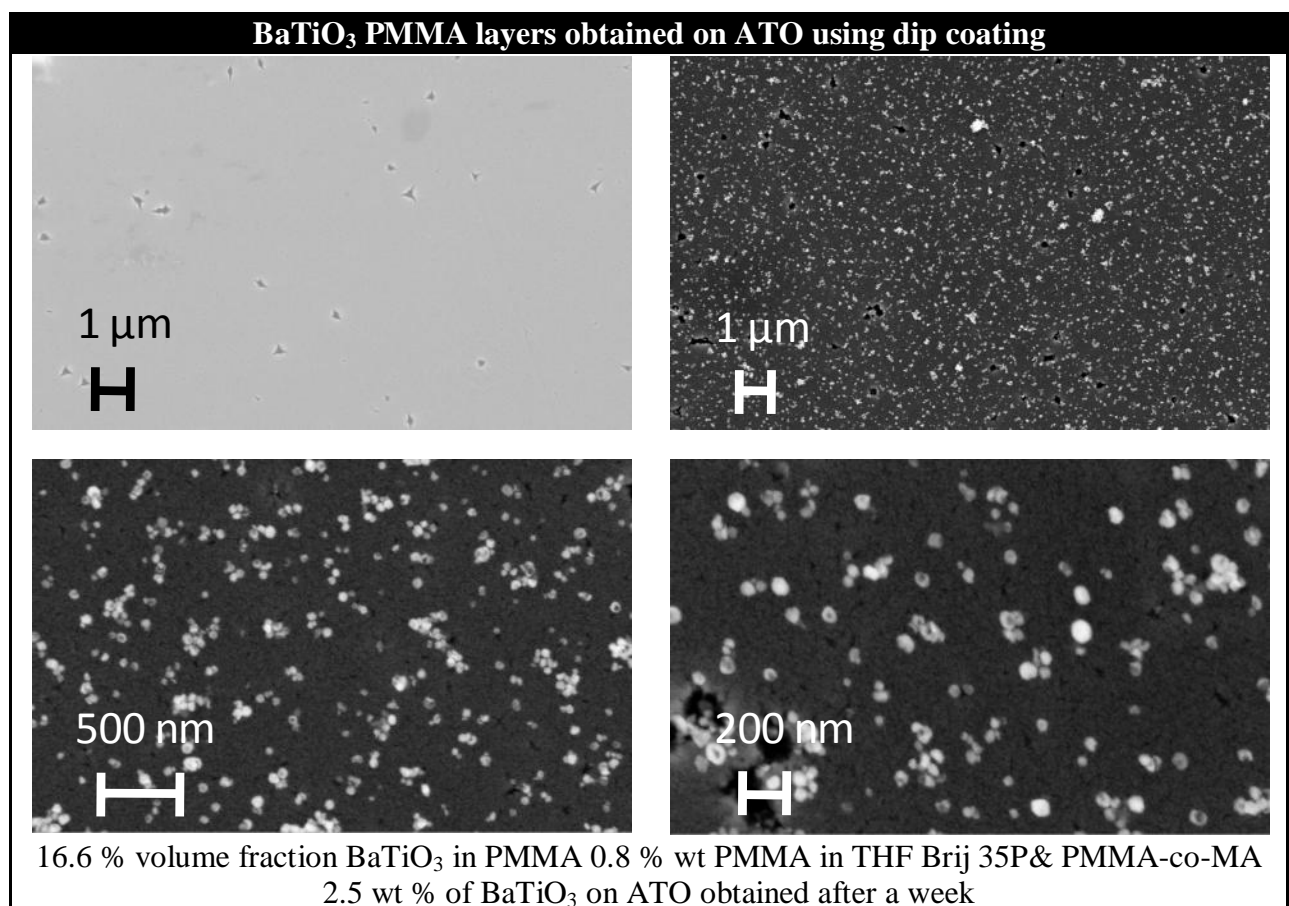
Figure 4-31 Thin film on ATO shows well dispersed BaTiO$_3$ with low filler fraction in already settled dispersion.

Layer thickness measurement using optical profilometer

16.6 % volume fraction BaTiO$_3$ in PMMA 0.8 % wt PMMA in THF Brij 35P & PMMA-co-MA 2.5 wt % of BaTiO$_3$ on glass slide
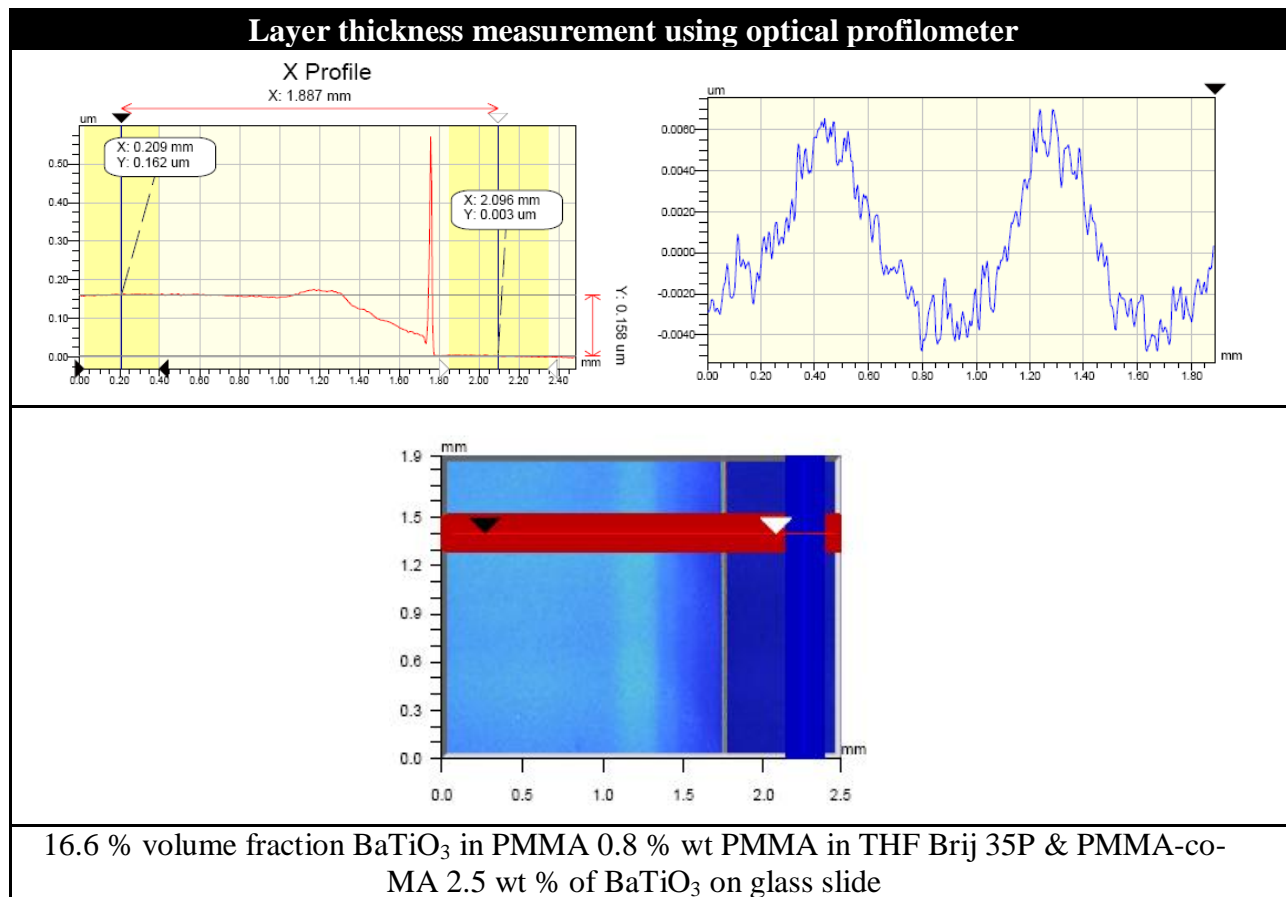
Figure 4-32   Layer thickness measurement using optical profilometer

4.3.8   Substrates for film deposition

Among various substrate used oxide surfaces showed better adherence to films deposition from the dispersion of BaTiO$_3$-PMMA.

Self assembled monolayer

Self assembled monolayer (SAM) of thiols on gold sputtered substrate Si wafers was achieved. The idea was to increase compatibility between gold layer on Si wafer and PMMA film which is to be deposited on the Au sputtered substrate. HS bonds well with gold and the hydrophobic groups on other side may increase the adhesion of BaTiO$_3$-PMMA dispersions. The SAM layers as did not improve the adhesion of thin films. The surface appeared to be lipophobic when tested for thedeposition of film via dispersions.

ITO (tin-doped indium oxide)

Layers of tin-doped Induim oxide (ITO) proved to be good substrate for the deposition of thin films. The dispersion in THF, Toluene and MCB had similar adhesion properties on ITO

4.3.9 Brij HLB observations

It was observed that moderate HLB values support the suspension of $BaTiO_3$ in THF (Figure 4-33). Details are in Table 4-VIII.

Table 4-VIII   Brij used with different HLB values

Sample	Brij	HLB value	Amount	Remarks
1	Brij35P	16.9	5 wt % of BT	Moderate settling
2	Brij 78	15.3	5 wt % of BT	Least settling
3	Brij 700	18	5 wt % of BT	Moderate settling
4	Brij 76	12	5 wt % of BT	Least settling
5	Brij 30	9	5 wt % of BT	Lot of settling

Figure 4-33 $BaTiO_3$ settling after 1h with Brij HLB variation for $BaTiO_3$ dispersion in THF, samples 5, 1, 3, 4, and 2 are shown in the figure for details of samples please see Table 4-VIII

4.3.10 Copolymer as surfactant

Poly(methylmethacrylate-co-methacrylic) (PMMA-co-MA) acid MW 34 000 was used as polymer surfactant in different ratios and for different $BaTiO_3$ samples details are given in Table 4-IX. It was observed that for different ratios of surfactant mostly all the $BaTiO_3$ samples are stable except R90-iii obtain hydrothermally using rutile phase TiO_2. Slight settling is observed after keeping overnight in all samples.

Table 4-IX   Varying polymer surfactant (PMMA-co-MA) ratios for different $BaTiO_3$ samples

$BaTiO_3$	Surfactant Wt %of BT	THF (ml)	Observation after 1 h	Observation overnight
cubic B90-III	5	10	stable	Slight settling
cubic B90-III	10	10	stable	Slight settling
cubic B90-III	20	10	stable	Slight settling
cubic B90-III	50	10	stable	Slight settling
cubic B90-III	100	10	stable	Slight settling
Tetragonal EtOH1	2.5	10	stable	Slight settling
tetragonalEtOH1	5	10	stable	Slight settling
R90-iii	5	10	settling	Settled mostly
EtOH2	5	10	stable	Slight settling

4.3.11 Comparison of non ionic surfactants Brij and PMMA-co-MA

In comparison of a) Brij, b) polymer surfactant PMMA-co-Ma acid and, c) Brij + polymer surfactant. Overnight left dispersion with surfactant as 5 wt % of $BaTiO_3$ (B90-III) showed least settling for dispersion containing polymer surfactant. Details are in Table 4-X.

Table 4-X   Comparison of Brij and PMMA-co-MA as surfactant

Sample	Brij 78	PMMA-co-MA	Remarks
1	5 % wt of BT	-	Moderate settling
2	-	5 % wt of BT	Least settling
3	2.5 %wt of BT	2.5 % wt of BT	Least settling

4.3.12 Use of THF as solvent for obtaining dispersions for thin and thick films

THF has a low boiling point of 69 ˚C and can dissolve PMMA well. It is used mainly to obtain BaTiO$_3$-PMMA polymer nanocomposite. THF is used to dissolve PMMA with different molecular weights i.e., MW 35 000, 120 000, and 350 000.

Low volume fraction of BaTiO$_3$ in PMMA

Most of the dispersions discussed in previous sections were obtained using THF. The following further experiment were performed to test the layers for electrical properties. Low volume fraction of BaTiO$_3$ was used initially to obtain thin film as increased filler fraction causes agglomeration.The following set of dispersions was obtained in first round. Details are given in Table 4-XI. Thin layers were obtained using the dispersions. Dip coating and spin on techniques were used to take thin film on ITO and charcterised for electric properties. Details of whole set of layers is given in Table 4-XII and Table 4-XIII.

Thin films obtained were characterized for layer thickness using optical profilometer (for example Figure 4-35), ellipsometery (for example Figure 4-34) and step/ditch height measurement using atomic force microscopy (AFM) in contact mode (Figure 4-36).

A comparison between ellipsometery, AFM, and optical profilometery shows that layer thickness measurements done using optical profilometery for a sample R agrees well with step height measurement on film surface of the same sample using AFM (Figure 4-35, Figure 4-36). Whereas the value of thickness calculated using ellipsometery is too high to be accepted (Figure 4-34).

Table 4-XI   Dispersions obtained using THF at low volume fraction of BaTiO$_3$

Sr. Nr	% Vol fraction of BT in PMMA	% Weight of PMMA in THF	PMMA MW	BaTiO$_3$	PMMA-co-MA % wt of BaTiO$_3$
1	1	14	120000	Cubic BT B90-III	2.5
2	2	8.5	350000	Cubic BT B90-III	2.5
3	3	6.5	35000	Cubic BT B90-III	2.5
4	4	12	35000	Cubic BT B90-III	2.5
5	4	12	35000	Tetragonal EtOH1	2.5

Table 4-XII   Detail of thin films using dip coating for lower BaTiO$_3$ filler loadings in PMMA

Sample Layers	% Volume fraction of BT in PMMA	% Weight of PMMA in THF	Dip speed (mm/min)	Film thickness nm
A	2	8.5	85	2632
B	2	8.5	60	540
C	2	8.5	85	1600
D	2	8.5	85	200
E	1	14	85	2107
F	1	14	85	1681
G	1	14	30	400

Table 4-XIII Detail of thin films using spin coating for lower BaTiO$_3$ filler loadings in PMMA

Sample Layers	% Volume fraction of BT in PMMA	% Weight of PMMA in THF	Spin speed (rpm/min)	Film thickness nm
L	3	6.5	6000	524
M	3	6.5	6000	534
O	4	6.5	4000	1452
P	4	6.5	4000	1560
Q	4	6.5	8000	888
R	4	6.5	4000	1309
S	4	12	6000	900

The layer thickness values given for vaious samples in Table 4-XII and Table 4-XIII are measured using optical profilometry. The X-prolfile images for measurements done using optical profilometry for the samples are shown in Figure 4-37 and Figure 4-38.

Layer thickness measurements using ellipsometry is shown in Figure 4-39. The experimental and generated model curves were drawn for ψ and Δ i.e., stokes parameters. ψ and Δ describe the polarization state of electromagnetic radiation. The values of ψ and Δ for generated curve were calculated using Fresnel equations.

The electrical characteriztion of these films is coming in the section 4.4.2

Generated and Experimental

3	r	2789.4 nm
2	srough	0 nm
1	ito	130 nm
0	bk7_u	1 mm

- Model Fit
- Exp Ψ-E 60°
- Model Fit
- Exp Δ-E 60°
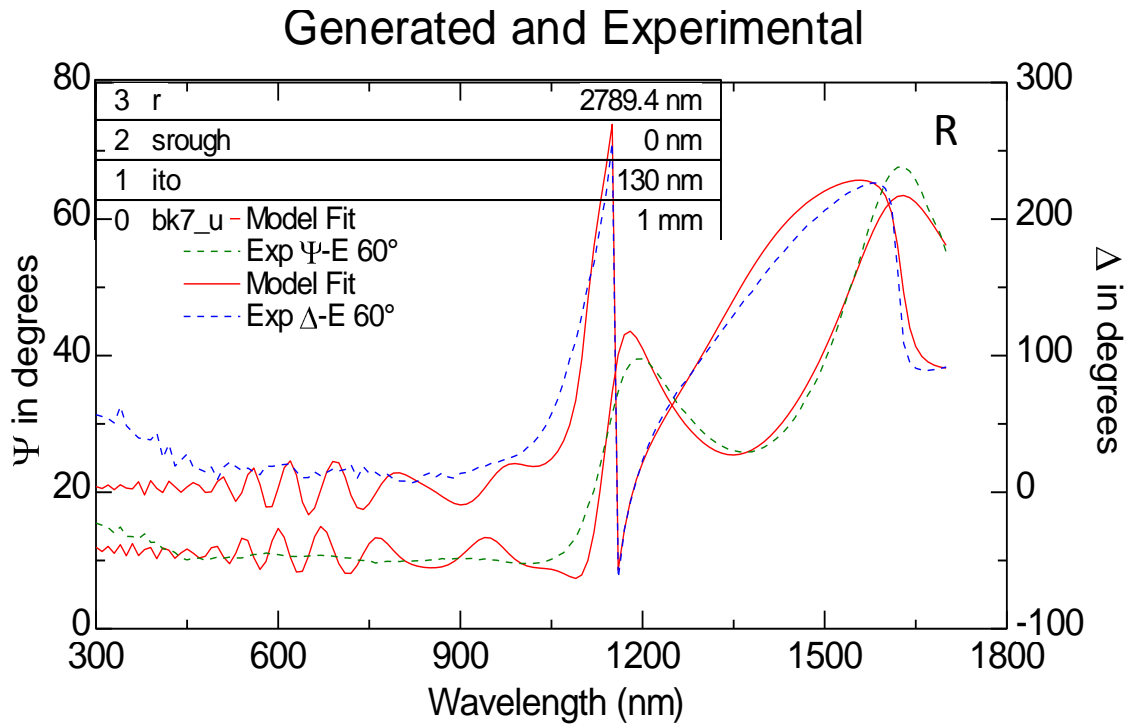
Figure 4-34 Layer thickness measurement using ellipsometry; the experimental curve and generated model curve obtained using Fresnel equations for obtaining ψ and Δ are shown

Layer thickness of films measured using optical profilometer

4 %Volume Fraction of BaTiO₃ in PMMA

12 % Weight of PMMA in THF

Layer thickness (profilometer) = 1309 nm

Layer thickness AFM = 1300-1400 nm

Layer thickness ellipsometery = 2789 nm
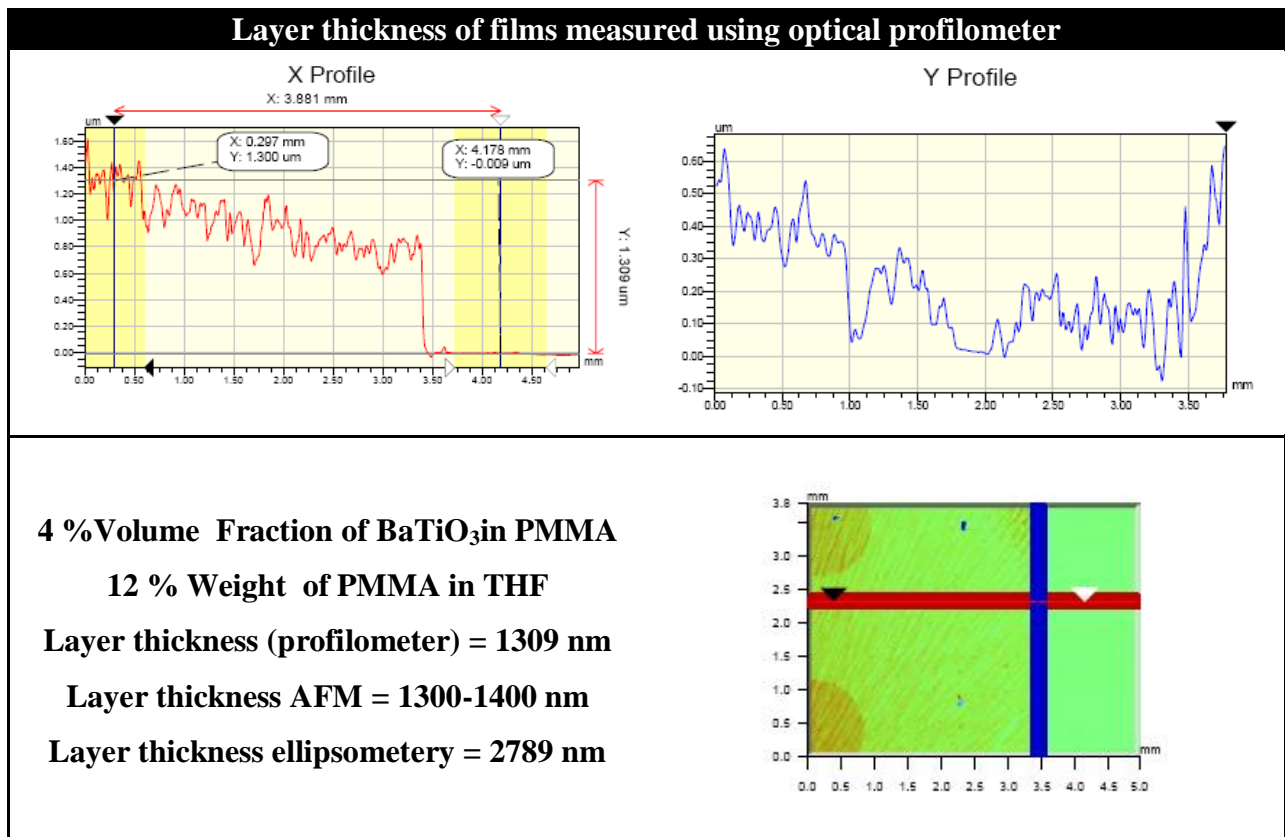
Figure 4-35 Layer thickness for thin film measured using optical profilometery.
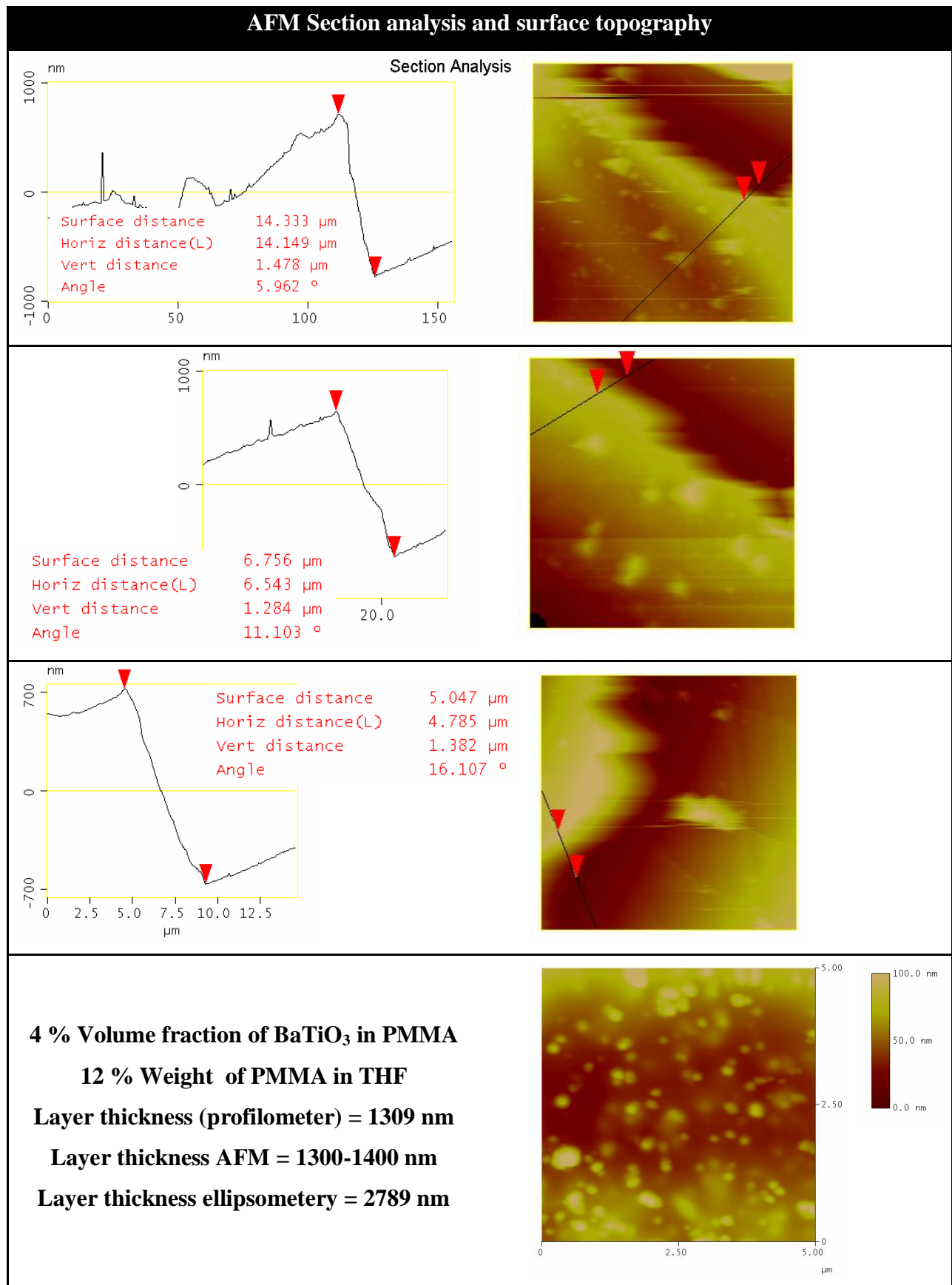
Figure 4-36   Layer thickness using atomic force microscopy and topographic image of surface
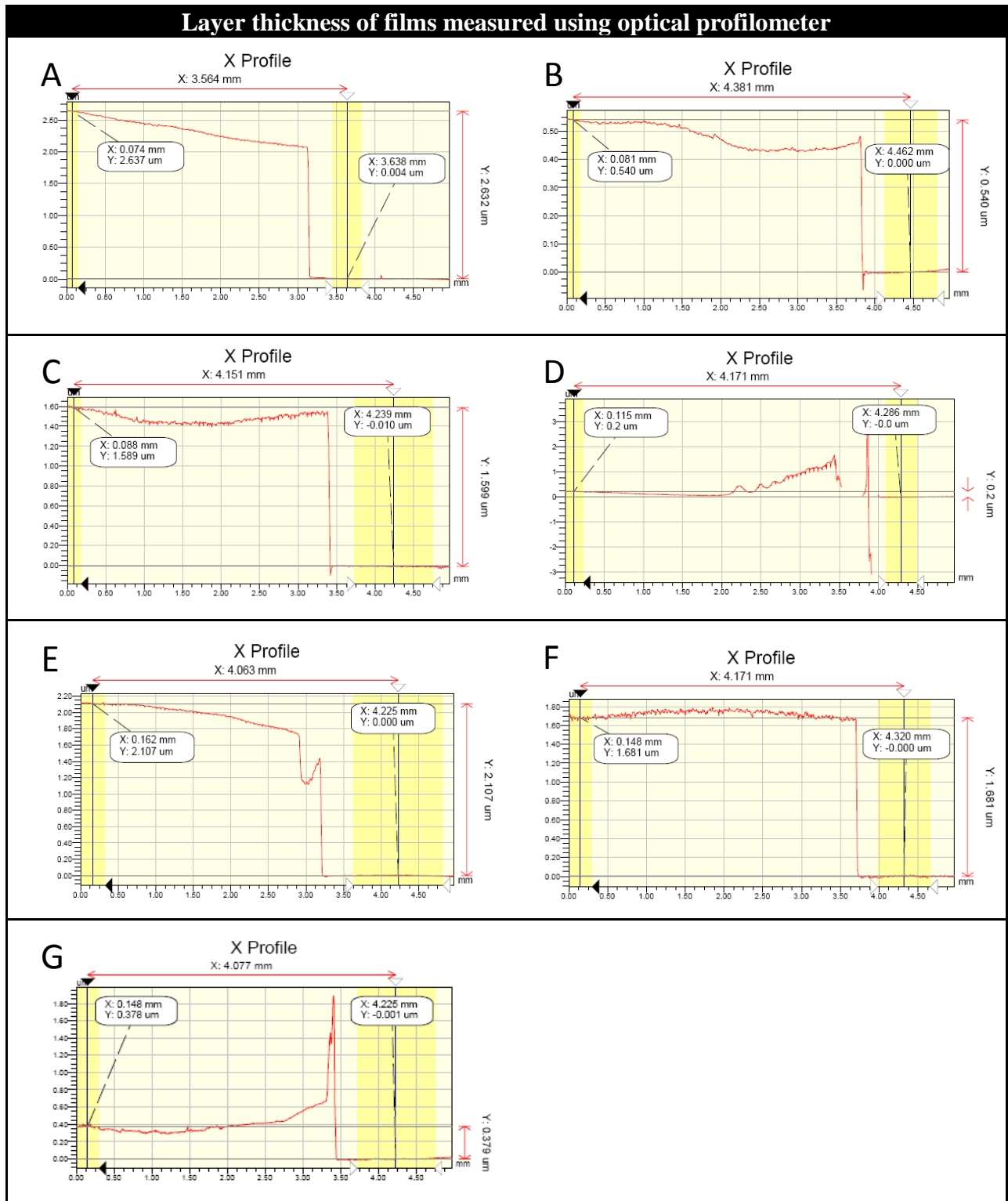
Figure 4-37 X profile images for layer thickness measurements of thin films using optical profilometery
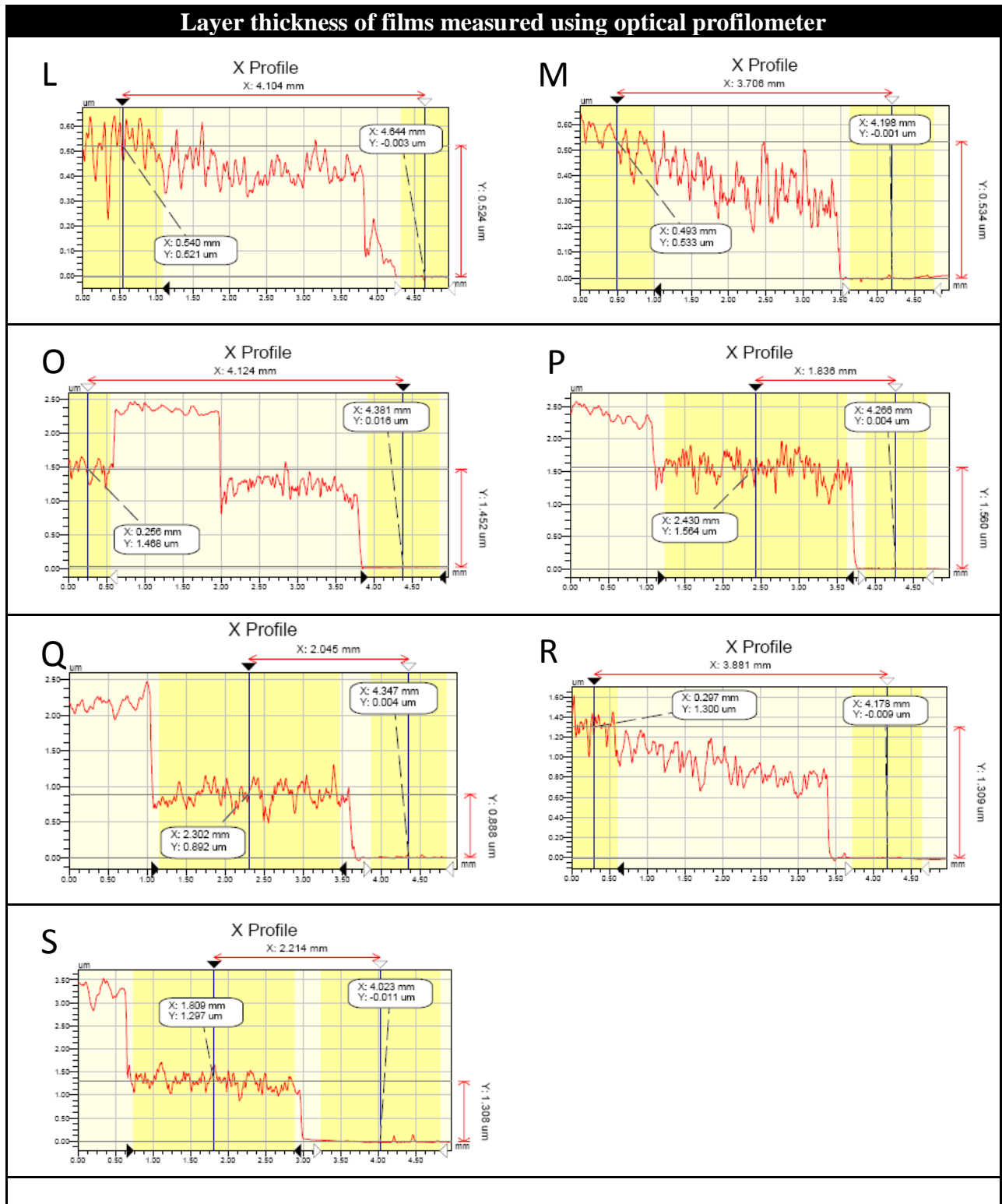
Figure 4-38 X profile images for layer thickness measurements of thin films using optical profilometery
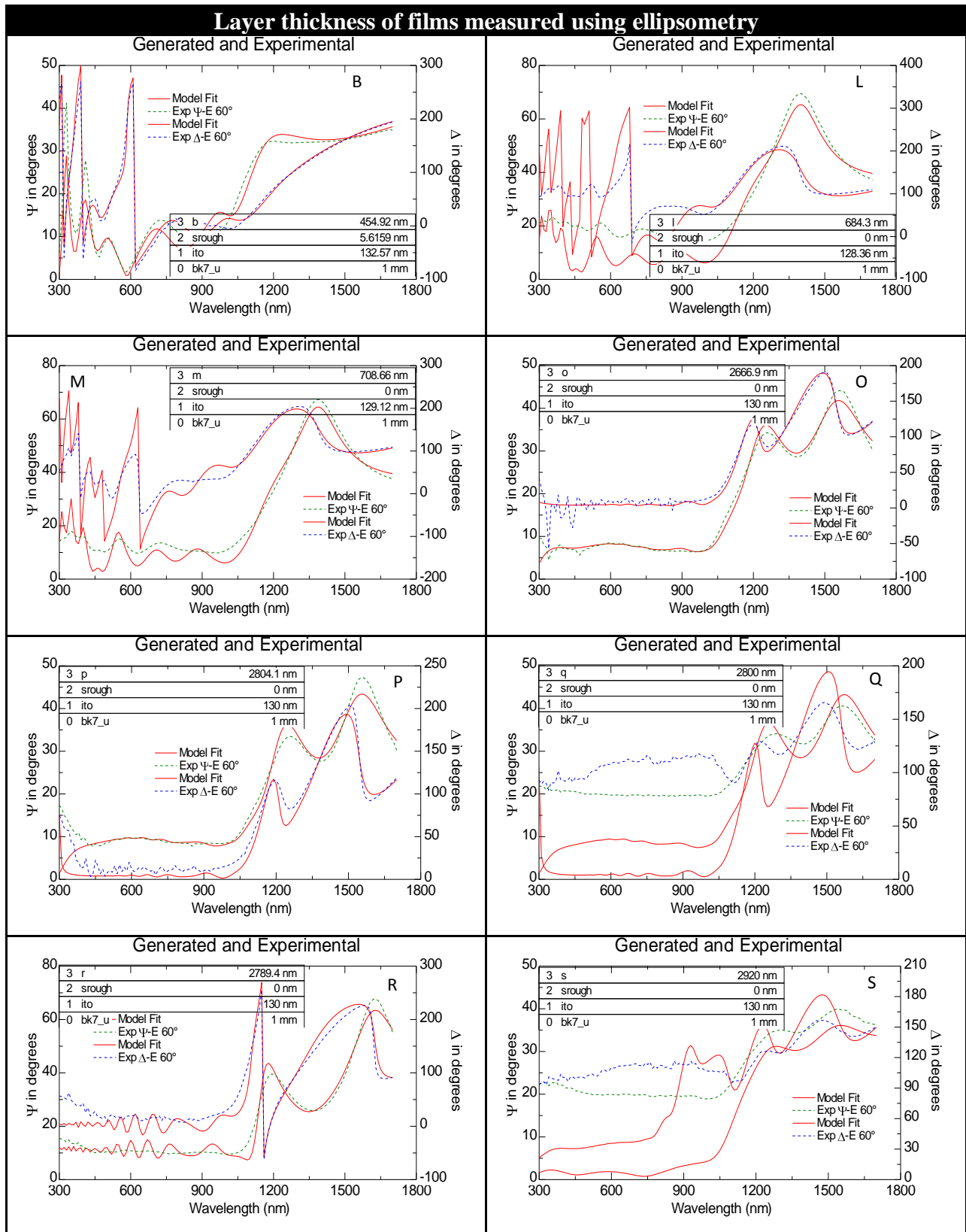
Figure 4-39 Layer thickness measurements using ellipsometry; the experimental curve and generated model curve obtained using Fresnel equations for obtaining ψ and Δ are shown

Higher volume fraction of BaTiO$_3$ in PMMA

To improve the dielectric properties of thin film a systemtic variation of volume fraction of BaTiO$_3$ in PMMA (from 4-30 %) and weight percent of PMMA in solvent (from 2-8 %) was carried out. details are in Table 4-XIV.

Table 4-XIV Dispersion with different volume percent fraction of filler in polymer with different weight percent of PMMA in THF

Sr. Nr	% Volume fraction of BT in PMMA	% Weight of PMMA in THF	PMMA MW	BaTiO$_3$	PMMA-co-MA % wt of BaTiO$_3$
1	0	22, 15, 11	35000	-	-
2	4	8.7	35000	B90-48 h	2.5
3	8	6.5, 5.2, 4.3	35000	B90-48 h	2.5
4	12	5.2, 4.3, 3.7	35000	B90-48 h	2.5
5	13	6.7, 6.0, 5.5, 5.0	35000	B90-48 h	2.5
6	16	5.7, 3.3, 2.6, 2.2, 1.9	35000	B90-48 h	2.5
7	20	4.7, 3.7, 3.3, 2.9, 2.6, 2.4, 2.0, 1.7	35000	B90-48 h	2.5
8	24	3.7, 3.3, 2.9, 2.6, 2.4, 2.0, 1.7	35000	B90-48 h	2.5
9	30	3.5	35000	B90-48 h	2.5

Thin films were obtained on ITO as substrate using dispersions listed in Table 4-XIV at 1000, 2000, 4000, 6000, and 8000 rpm spin speeds and 1000, 2000, and 4000 rpm^2 acceleration for 30 s. Details are mentioned in Table 4-XV.

The films obtained were deposited with platinum (Pt) as top electrode (~ 60 nm) by sputtering a platinum target under vacuum. A shadow mask was applied on the rest of the film and platinum was sputtered under high vacuum to achieve top electrode for electrical property characterization.

Samples VII-I, XI, Xa ans XIVa were charaterised under SEM to observer the filler distrbution in polymer (Figure 4-40, Figure 4-41 and Figure 4-43). It is evident that at low filler loading i.e., 12 % volume fraction of BaTiO$_3$ in PMMA the distrbution of BaTiO$_3$ in PMMA is homogenous

in the film with some agglomerates on the surface of the film. At higher filler loadings that is 30 volume percent of $BaTiO_3$ in PMMA, the wave in the films are evident, which shows uneven distribution of filler in the film.

Lower weight percent 2.4 of PMMA in solvent and high filler loading 24 % volume fraction (Figure 4-43) results in uneven distribution of filler in film when compared to same filler loading at high 3.7 weight percent PMMA in solvent (Figure 4-40 **b)**).

SEM FIB milling was used for a $BaTiO_3$-PMMA layer (XIV-a: 24 % volume fraction of $BaTiO_3$ in PMMA, 2.4 % weight PMMA in THF and 2.5 % wt PMMA-co-MA as surfactant of $BaTiO_3$) to mill an area over the film surface and height of the step was seen under scanning electron microscopy. The thickness measurement with optical profilometery again agrees well thickness measurement using FIB SEM technique (Figure 4-42 and Figure 4-43).

Table 4-XVI gives the layer thickness and surface roughness of the samples characterised for capacitance with higer filler loadings by optical profilometer.

Table 4-XVII gives the layer thickness and surface roughness for samples obtained by using dispersion with 20 % volume fraction of $BaTiO_3$ in PMMA and 3 % weight of PMMA in THF. The layer thickness at this filler loading remained between 100 nm to 350 nm with a roughness around 50 nm to 80 nm.

Figure 4-44 shows the x profile obtained using the optical profilometery for the layer thickness measurement of the film samples mentioned in Table 4-XVI and Table 4-XVII.

Table 4-XV Detail of layers obtained using dispersions at different filler loading in THF

Sample Layers	% Volume fraction of BT in PMMA	% Weight of PMMA in THF	Spin speed (rpm)	Acceleration rpm²
I	4	8.7	4000	1000
II	4	8.7	4000	1000
III	4	8.7	4000	1000
IV	8	6.5	4000	1000
V	8	6.5	4000	1000
VI	8	6.5	4000	1000
IV-I	8	5.2	4000	1000
IV-II	8	4.3	4000	1000
V-I	8	5.2	4000	1000
VI-I	8	5.2	4000	1000
VII	12	5.2	4000	1000
VII-I	12	4.3	4000	1000
VII-II	12	3.7	4000	1000
VII-III	12	5.2	6000	2000
VIII	16	3.3	4000	1000
VIII-a	16	3.3	6000	2000
VIII-I	16	2.6	4000	1000
VIII-Ia	16	2.6	6000	2000
VIII-II	16	2.2	4000	1000
VIII-IIa	16	2.2	6000	2000
VIII-III	16	1.9	4000	1000
VIII-IIIa	16	1.9	6000	2000
VIII-IV	16	1.6	4000	1000
VIII-IVa	16	1.6	6000	2000
IX	20	3.7	4000	1000
IX-a	20	3.7	6000	2000
IX-Ia	20	3.25	6000	2000
IX-IIa	20	2.9	6000	2000
IX-IIIa	20	2.6	6000	2000
IX-IVa	20	2.4	6000	2000
IX-Va	20	2.0	6000	2000

Continued Table 4-XV

Sample Layers	% Volume fraction of BT in PMMA	% Weight of PMMA in THF	Spin speed (rpm)	Acceleration (rpm²)
IX-VIa	20	1.7	6000	2000
X	24	3.7	4000	1000
X-a	24	3.7	6000	2000
X-Ia	24	3.3	6000	2000
X-IIa	24	2.9	6000	2000
X-IIIa	24	2.6	6000	2000
X-IVa	24	2.4	6000	2000
X-Va	24	2.0	6000	2000
X-VIa	24	1.7	6000	2000
XI	30	3.5	4000	1000
XI-a	30	3.5	6000	2000
XI-b	30	3.5	8000	4000
XIIa	21	4.7	6000	2000
XIIb	21	4.7	8000	4000
XIIIa	16	5.7	6000	2000
XIIIb	16	5.7	8000	4000
XIVa	13	6.7	6000	2000
XIVb	13	6.7	8000	4000
XIV-Ib	13	6.0	8000	4000
XIV-IIb	13	5.5	8000	4000
XIV-IIIb	13	5.0	8000	4000
PMMA b	0	22	8000	4000
PMMA d	0	15	8000	4000
PMMA f	0	11	8000	4000

Distribution of BaTiO₃ at higher filler loading

a) 12 % volume BaTiO$_3$ in PMMA, 4.3 % weight PMMA in THF

b) 24 % volume BaTiO$_3$ in PMMA, 3.7% weight PMMA in THF
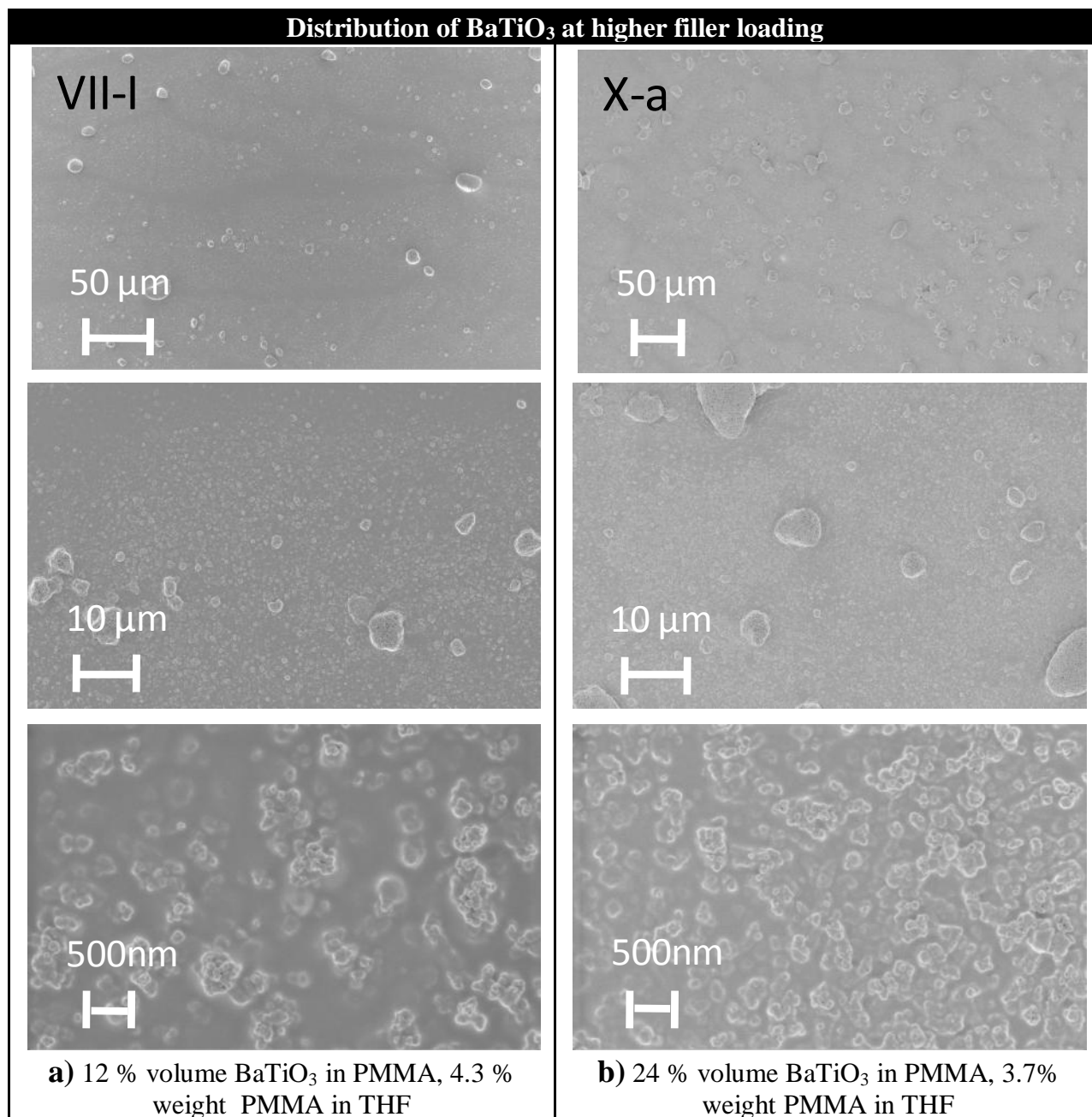
Figure 4-40   SEM images of thin films revealing distribution of BaTiO$_3$ in PMMA

Distribution of BaTiO₃ at higher filler loading

30 % volume BaTiO$_3$ in PMMA, 3.5 % weight PMMA in THF
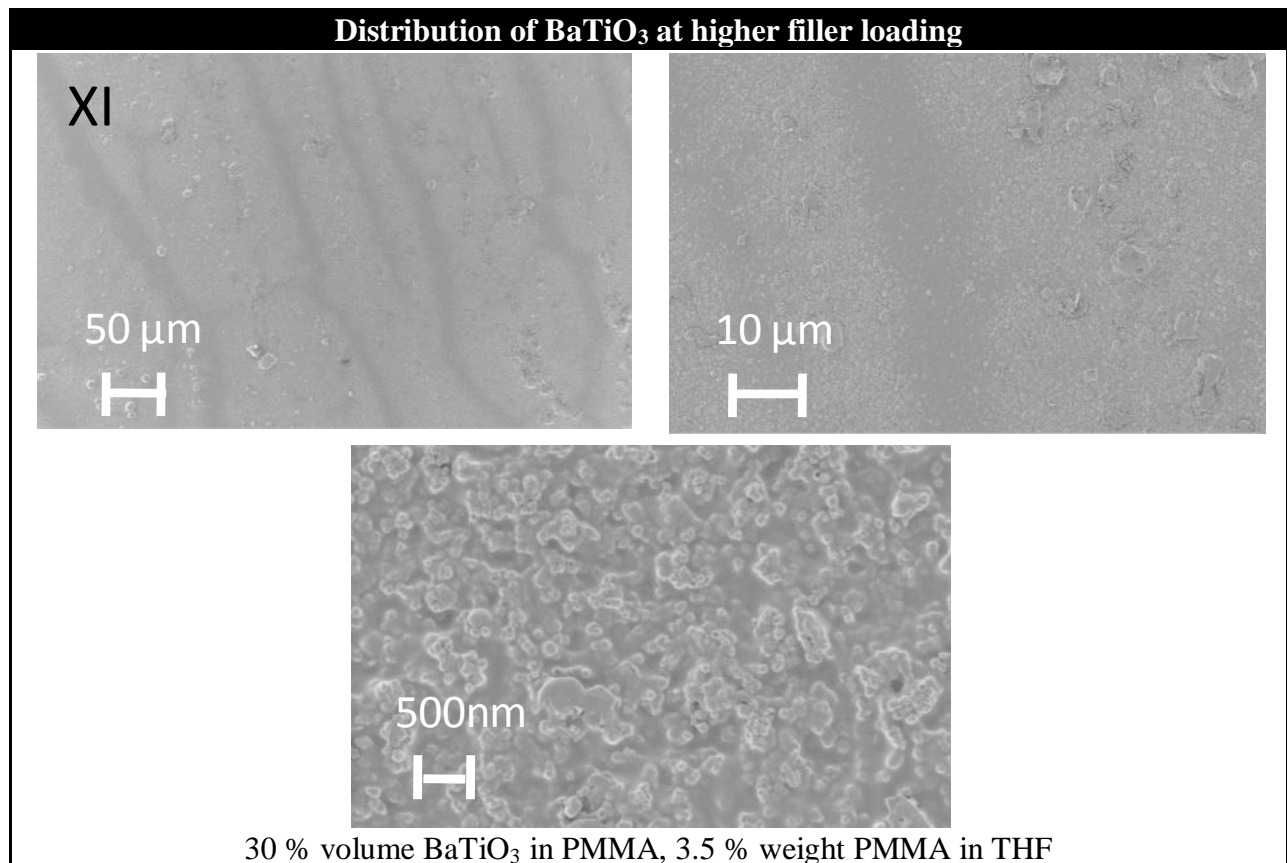
Figure 4-41   SEM images of thin films revealing distribution of BaTiO$_3$ in PMMA

Layer thickness of films measured using optical profilometer

24 % volume fraction of BaTiO$_3$ in PMMA

2.4 % weight of PMMA in THF

Layer thickness (profilometer) = 698 nm

Layer thickness FIB/SEM = 700 nm
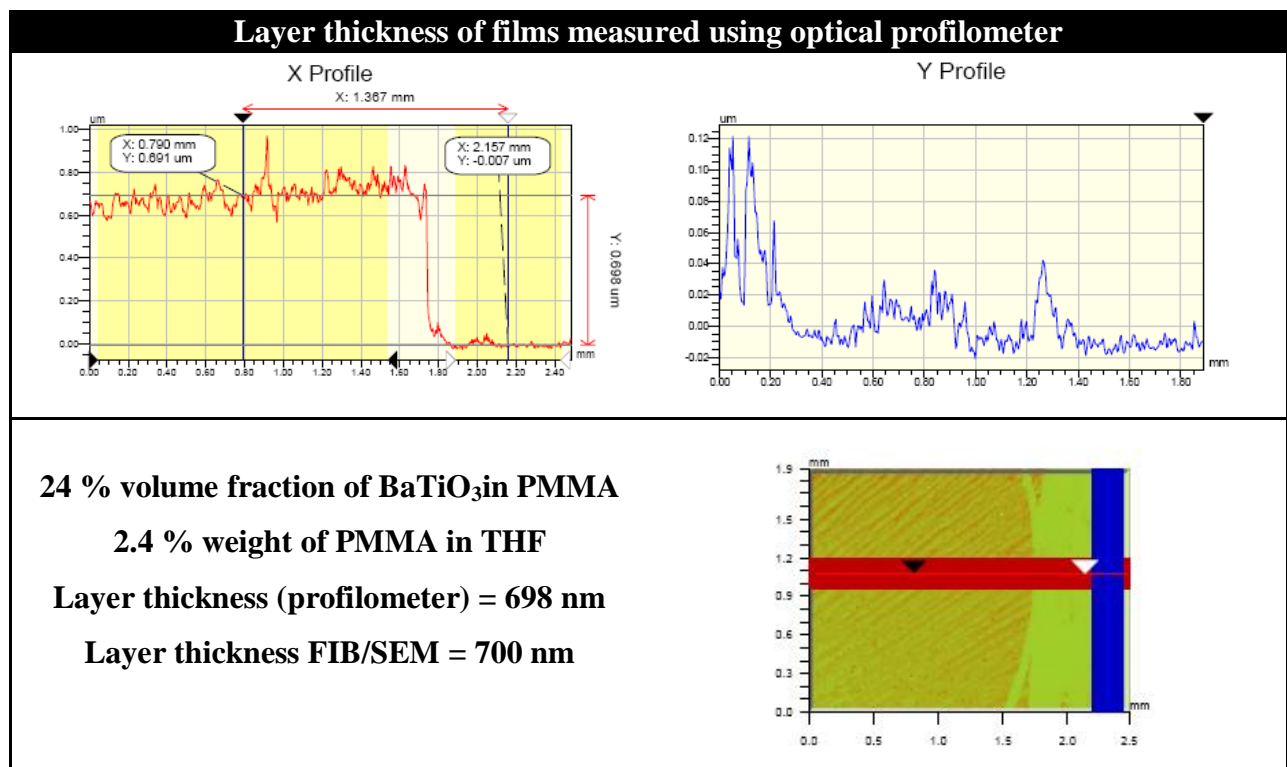
Figure 4-42   Layer thickness for thin film measured using optical profilometery

24 % volume fraction of BaTiO₃ in PMMA, 2.4 % weight PMMA in THF, 2.5 % weight PMMA-co-MA
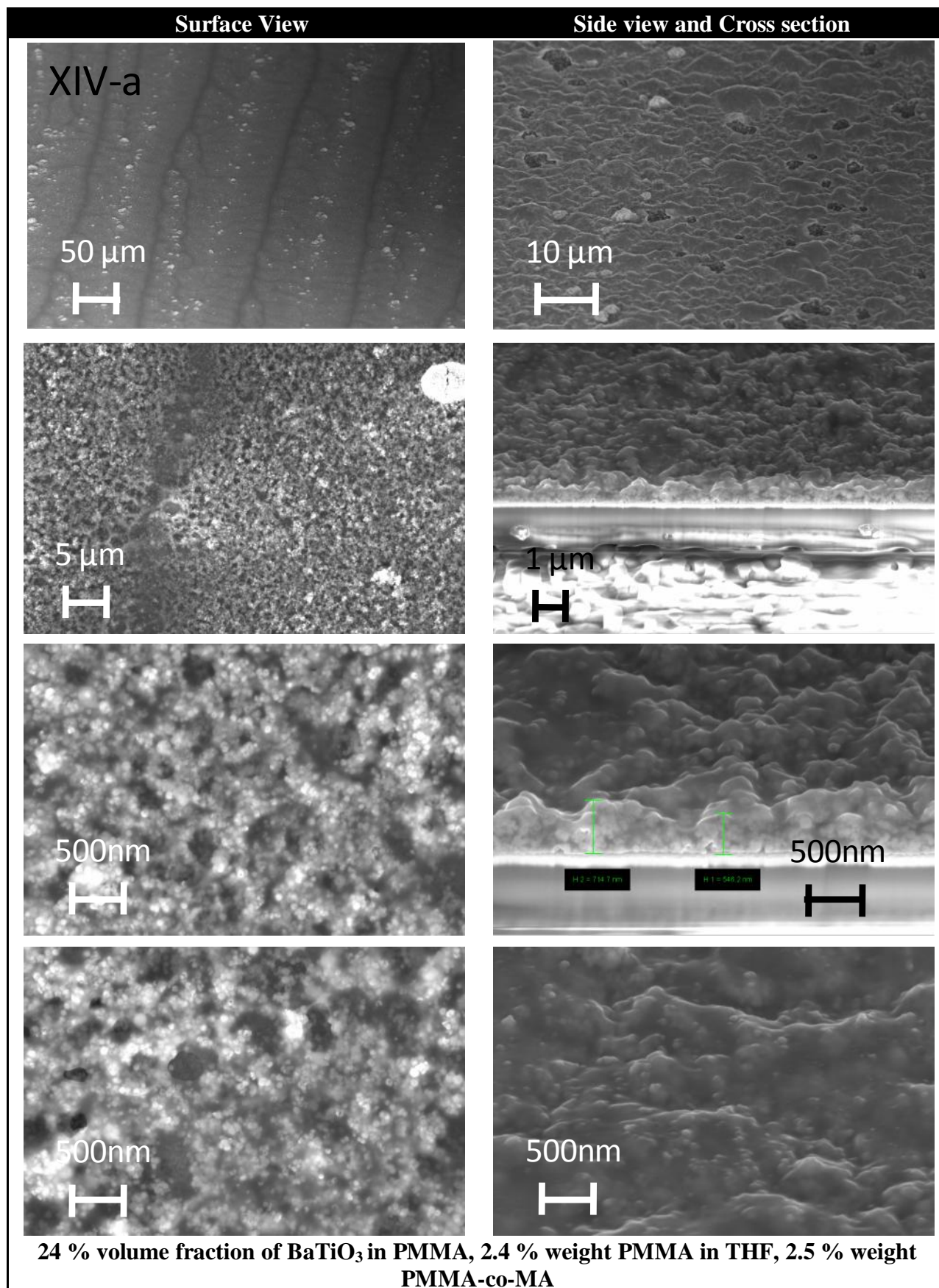
Figure 4-43   SEM images and FIB analysis of thin film revealing distribution of BaTiO₃ in PMMA and film thickness

Table 4-XVI Layer thickness and surface roughness for samples measured for capacitance for higher filler loadings

Sample Layers	Thickness (nm)	Roughness (nm)	% Volume fraction of BT in PMMA	% Weight of PMMA in THF	Spin speed (rpm)
IX	204	127	20	3.7	4000
IX-a	91	69	20	3.7	6000
IX-Ia	283,271	46	20	3.25	6000
X	190	123	24	3.7	4000
XI	298,300	116	30	3.5	4000
XI-a	136	89	30	3.5	6000
XII-b	236	72	21	4.7	8000
XIV-a	698,590, 593	134,100	13	6.7	6000
XIV-III-b	178	89	13	5.0	8000
PMMA-1	1706	431	0	22	8000
PMMA-2	976	129	0	15	8000
PMMA-3	537	82	0	11	8000

Table 4-XVII Layer thickness and surface roughness for samples measured for capacitance for higher filler loadings

Sample Layers	Thickness (nm)	Roughness (nm)	% Volume fraction of BT in PMMA	% Weight of PMMA in THF	Spin speed (rpm)
AH1-IV-r	193	59	20	3	6000
AH1-IV	98	72	20	3	4000
AH1-I-rs	281	57	20	3	6000
AH1-I-r	229	76	20	3	4000
AH1-II-rs	270	49	20	3	6000
AH1-III-r	245	63	20	3	4000
AH1-II-r	363	71	20	3	6000
AH1-III	160	79	20	3	6000
AH1-II	253	77	20	3	6000
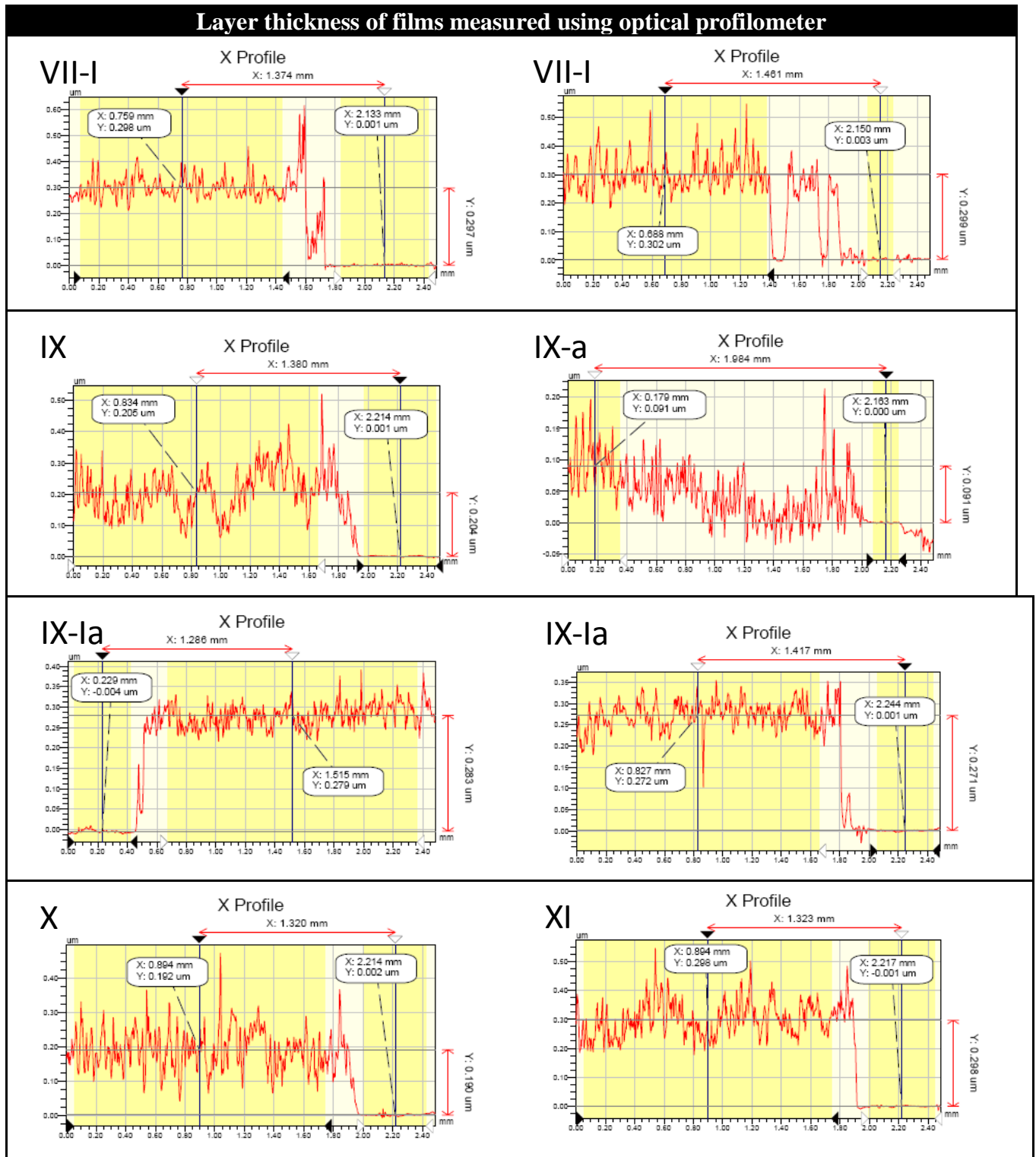
Figure 4-44 X profile for layer thickness measured using optical profilometery for samples obtained using dispersions at different spin speeds and filler loadings

Continued Figure 4-44

Layer thickness of films measured using optical profilometer

Continued Figure 4-44

Layer thickness of films measured using optical profilometer
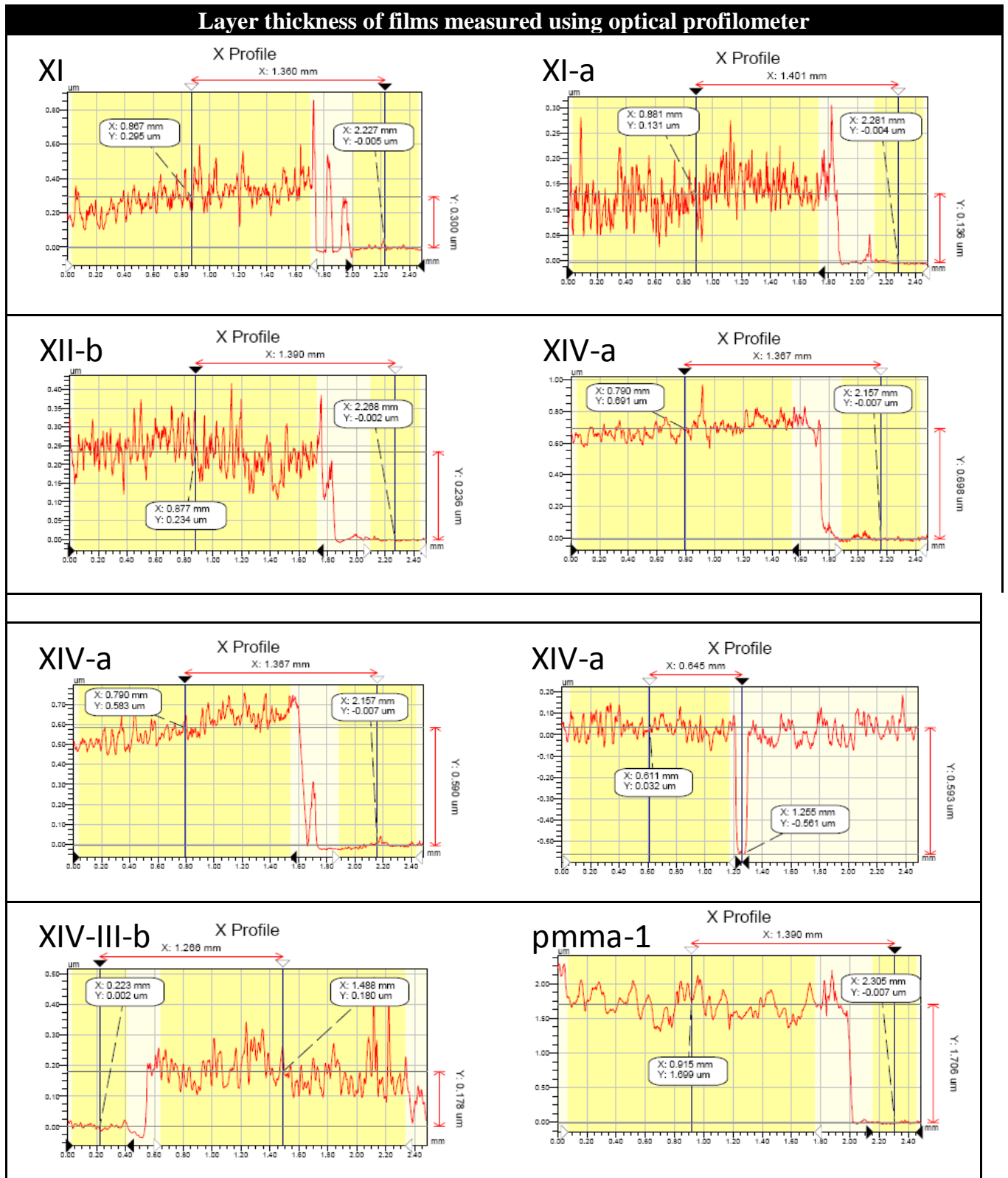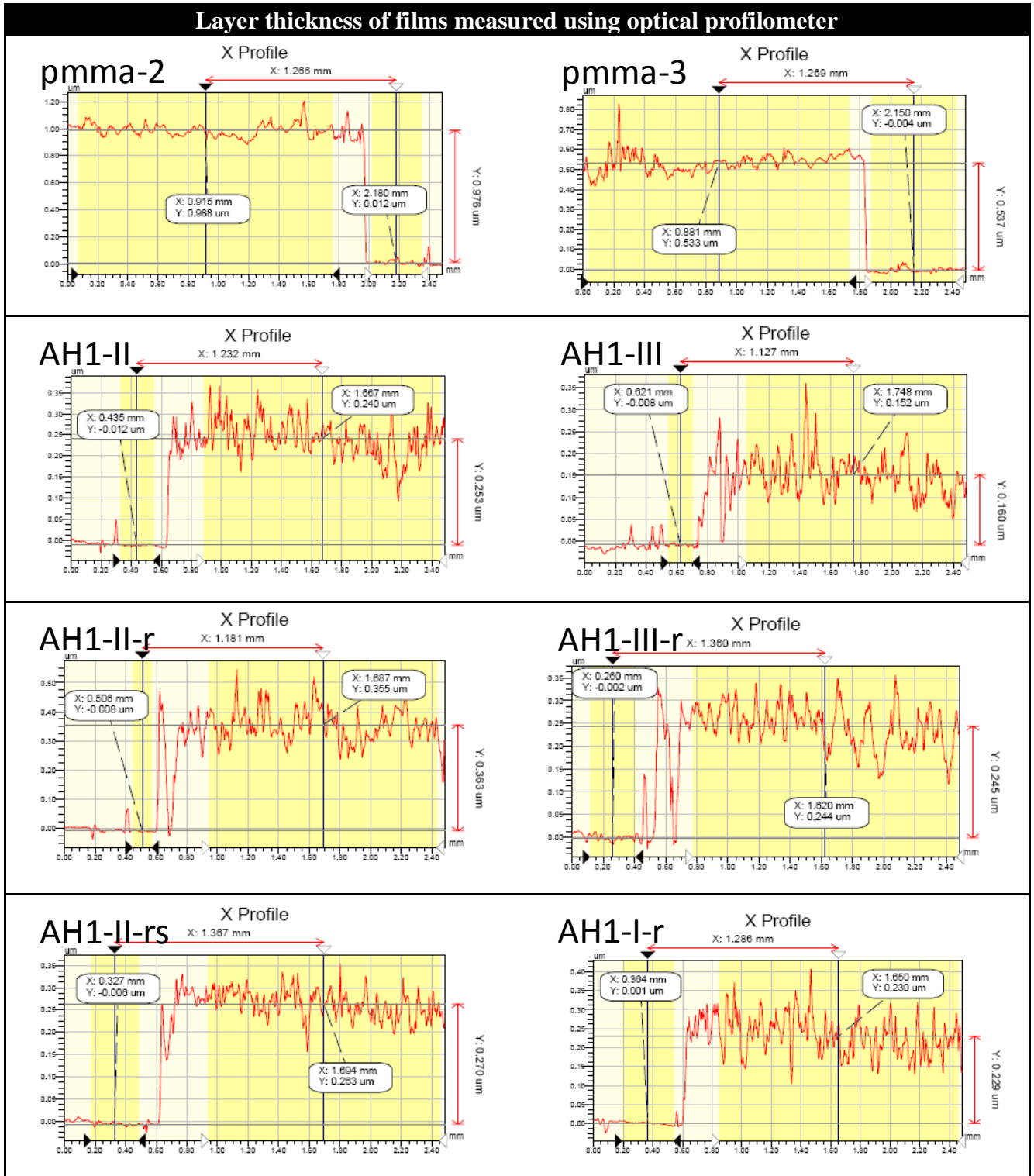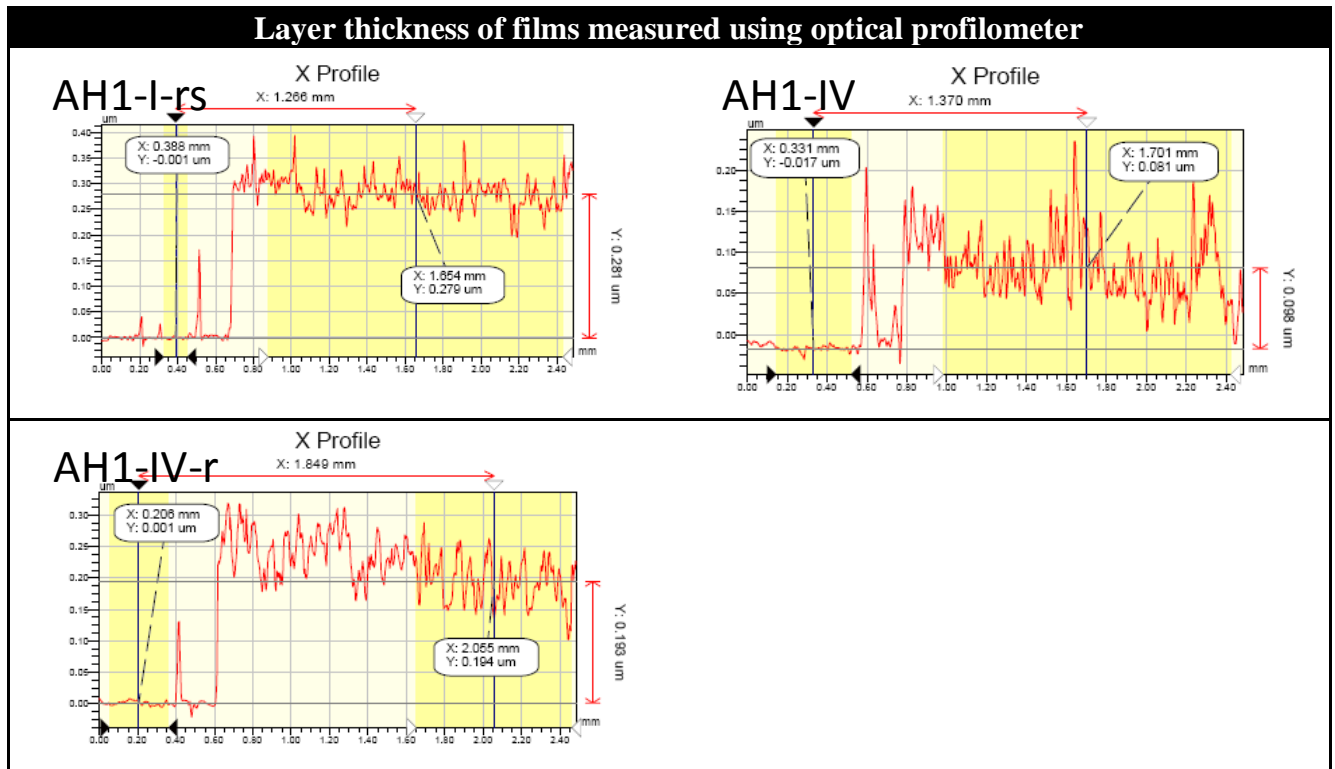
Conitnued Figure 4-44

4.3.13 Use of Toluene as solvent for obtaining thin and thick films

Toluene is a good solvent for PMMA. It is as well tested for obtaining dispersions using cubic and tetragonal $BaTiO_3$ in different PMMAs MW 35 000 and 350 000.

Dispersions obtained using toluene as solvent are described in Table 4-XVIII.

In first dispersion 2.5 wt % of PMMA-co-MA was dissolved in toluene and $BaTiO_3$ was added to solution and sonicated in ultrasonic bath for 15 min and kept overnight to observe the settling down of $BaTiO_3$ particles over time. It was found that some sedimentation has occurred over night yet still the suspension has been hanging.

Dispersion 2, 3 and 4 listed in Table 4-XVIII were used to obtained thick and thin films.
Thick film obtained using dispersion 4was observed under SEM. The film was mounted in a dye to hold it vertically for crossectional examination under SEM. The crossectional and surface view of thick film reveals well distributed $BaTiO_3$ in PMMA. The thickness of the film is 16.3µm. The upper portion of the film is affected due to the use of ethanol while removing the thick film from glass substrate as shown in (Figure 4-45).

Table 4-XVIII   Dispersions in Toluene

Sr. Nr.	% Volume fraction of BT in PMMA	%Weight PMMA in toluene	PMMA MW	BaTiO$_3$	PMMA-co-MA wt %	Remarks
1	0	0	-	Cubic BT	2.5	Sonication 15 min
2	2	8.8	35000	Cubic BT	2.5	Refluxing overnight 115°C
3	2	8.8	350000	Cubic BT	2.5	Refluxing overnight 115°
4	2	8.8	350000	Tetrago-nal BT	2.5	Refluxing overnight 115°

Surface view of thick film	Crossectional view of thick film

2 % volume fraction BaTiO$_3$ in PMMA 8.8 % wt PMMA in Toulene,
PMMA-co-MA 2.5 wt % of BaTiO$_3$
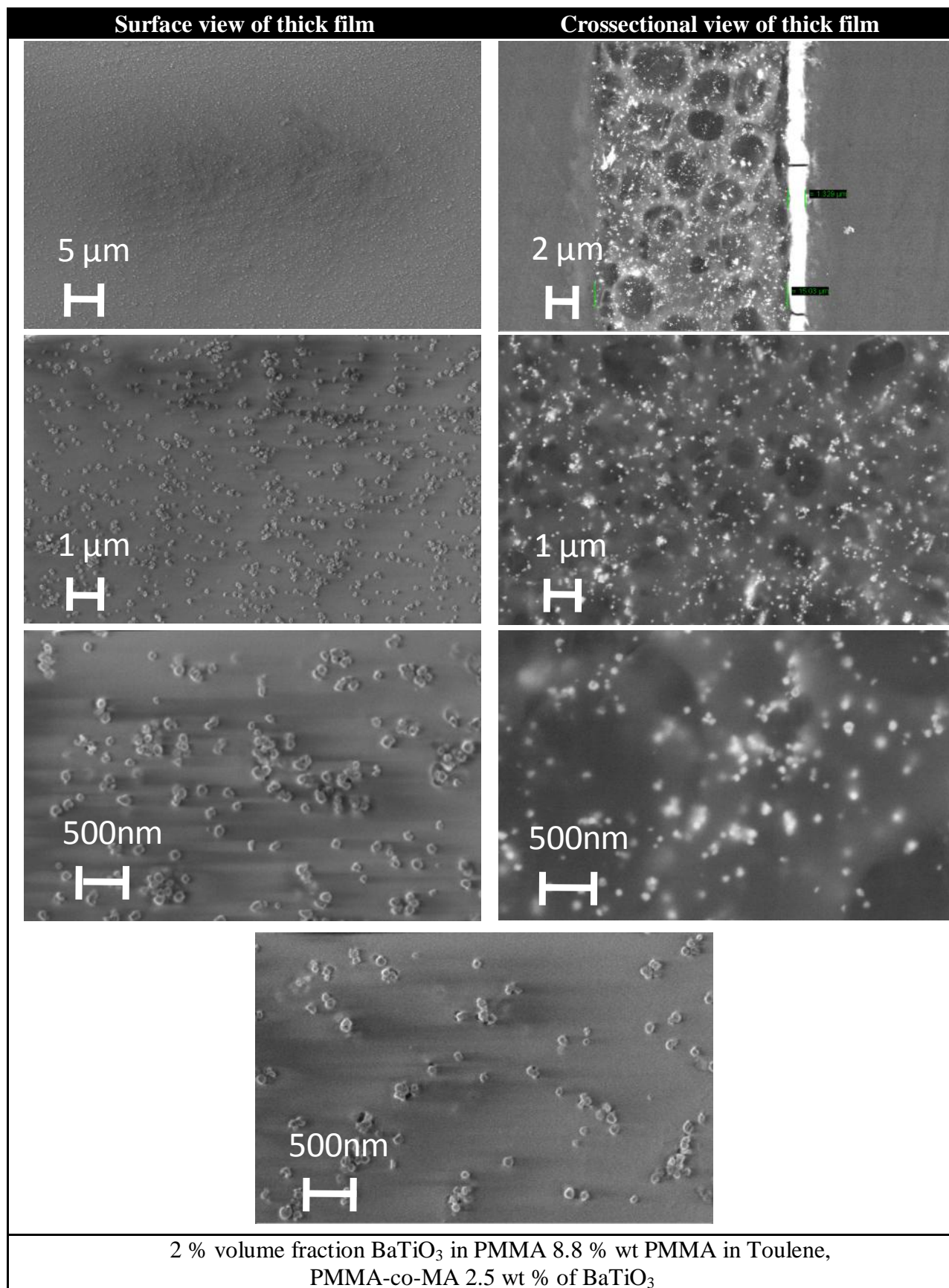
Figure 4-45   Surface and crossectional view of thick film BaTiO$_3$ in PMMA

4.3.14 Use of Chlorobenzene as solvent for obtaining dispersions for thin films

Chlorobenzene (MCB) used has a boiling point of 130 ˚C. A study is conducted here to dissolve our PMMA MW 35 000 in MCB and obtaining dispersion of our $BaTiO_3$ nanoparticles with surfactant i.e., PMMA-co-MA acid (Table 4-XIX). Thin films were obtained using spin on technique and characterize it under SEM and using optical profilometery to compare effect of MCB as solvent with other solvent used here. Detail of surface roughness is given in Table 4-XX.

The HRSEM images (Figure 4-46) for 10 % and 30 % volume percent filler loadings in 3.5 weight percent PMMA. At 30 % volume fraction the homogenously distributed closely packed nanoparticle of $BaTiO_3$ within the film can be observed whereas for 10 % volume fraction the agglomerated and with wide gap is obseravable. The aggolmeration on surface is evident in both cases. The film thickness measured using optical profilometery for 30 % volume fraction is 274 nm with surface roughness of 52 nm.

Layers obtained were measured for thickness using profilometery, X profile of the measurements is given in Figure 4-47.

Table 4-XIX Dispersions in Monochlorobenzene

Dispersion	Volume % BT	Weight % PMMA	PMMA MW	BaTiO$_3$	Copolymer wt %
1	10	3.5	35000	Cubic BT	10
2	20	3.5	35000	Cubic BT	10
3	20	5	35000	Cubic BT	10
4	25	4	35000	Cubic BT	10
5	30	3.5	35000	Cubic BT	10

Table 4-XX   Details of layers thickness and surface roughness obtained using MCB as solvent

Sample Layers	% Volume fraction of BT in PMMA	% Weight of PMMA in THF	Spin speed (rpm)	Layer thickness (nm)/ Roughness (nm)
AH4-II-II	20	5	4000	80/74
AH4-II-I	20	5	4000	210/110
AH4-I-II	25	4	4000	123/71
AH4-I-I	25	4	4000	242/84
AH4-III	30	3.5	4000	245/54
AH4-II	30	3.5	4000	274/52
AH4-I	30	3.5	4000	243/107
AH3-F-I	10	3.5	4000	86/17
AH3-F	10	3.5	4000	93/24
AH3-III	10	3.5	4000	206/18
AH3-II	10	3.5	4000	198/42
AH3-I	10	3.5	4000	191/25
AH2-VIII	20	3.5	4000	136/52
AH2-VII	20	3.5	6000	173/51
AH2-VI	20	3.5	4000	100/10
AH2-V	20	3.5	6000	112/12
AH2-IV	20	3.5	4000	79/5
AH2-III	20	3.5	6000	155/12
AH2-II	20	3.5	4000	108/7

Distribution of BaTiO₃ in PMMA at higher filler loading in MCB

10 % volume BaTiO₃ in PMMA, 3.5 % weight PMMA in MCB, 10 % weight copolymer | 30 % volume BaTiO₃ in PMMA, 3.5 % weight PMMA in MCB, 10 % weight copolymer
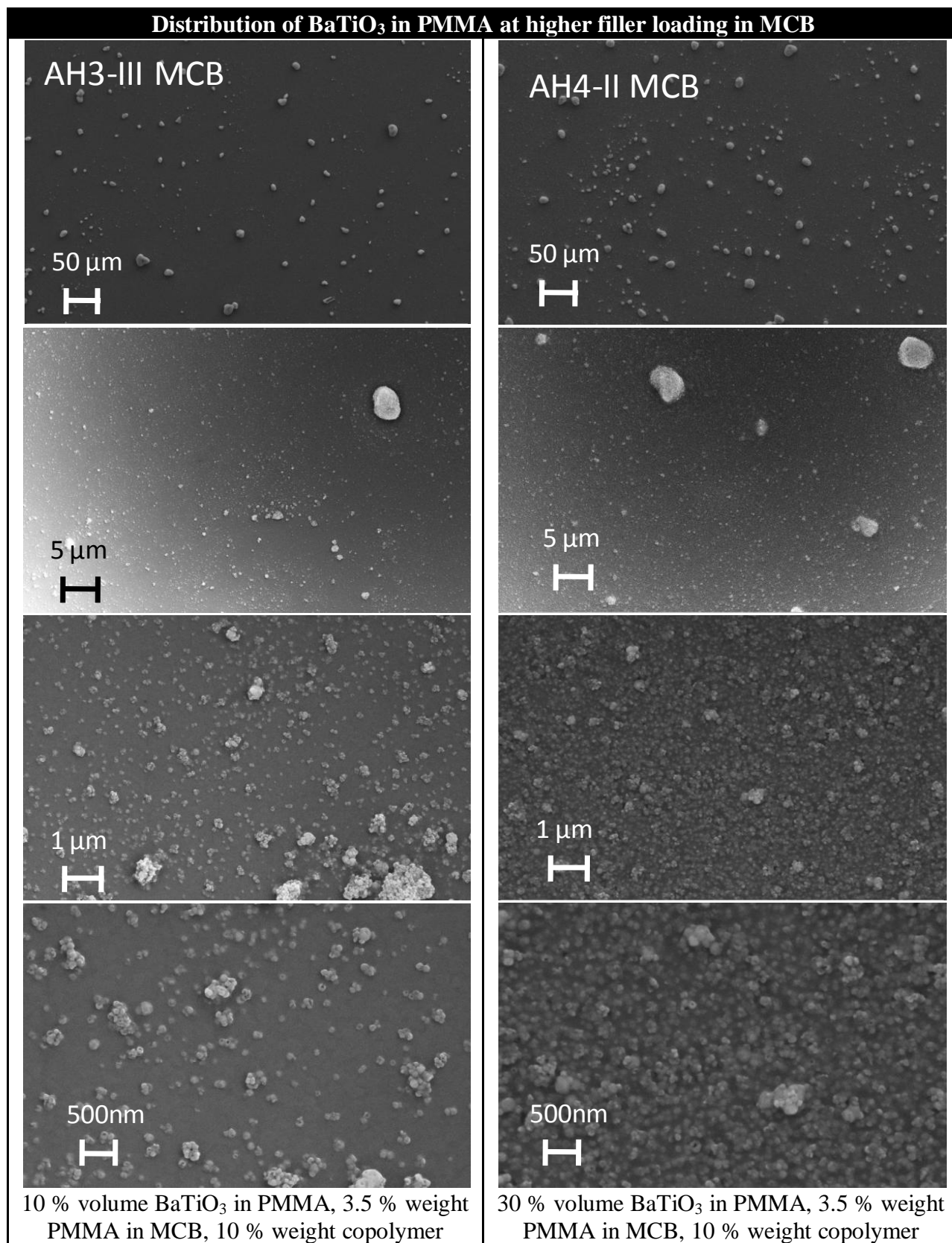
Figure 4-46   SEM images of thin films obtained using spin coating at 10 % and 30 % volume fraction of BaTiO₃ in PMMA in MCB
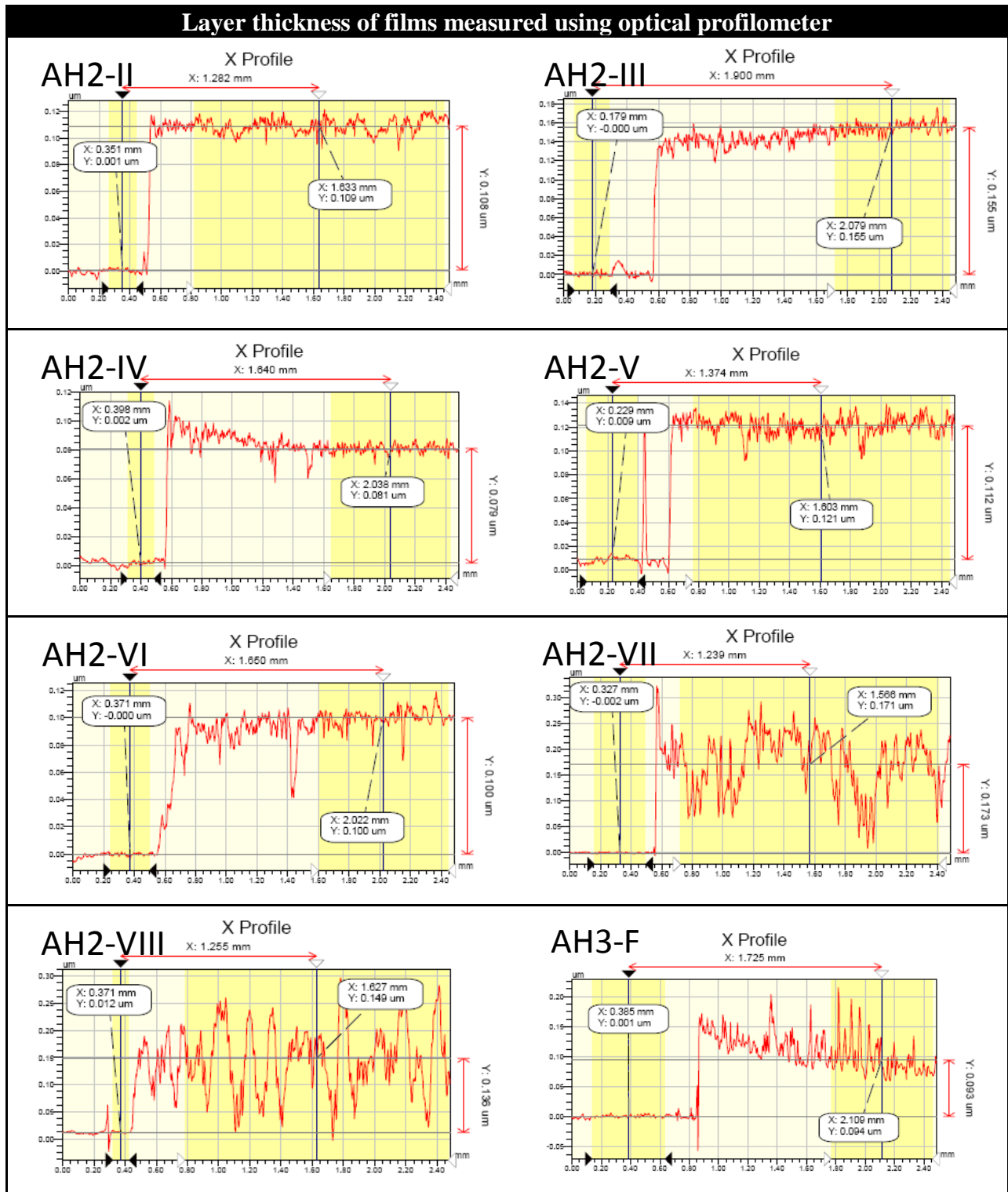
Figure 4-47   X profile for layer thickness measured using optical profilometery for samples obtained using dispersions at different spin speeds and filler loadings in MCB

Layer thickness of films measured using optical profilometer

Continued Figure 4-47

Layer thickness of films measured using optical profilometer
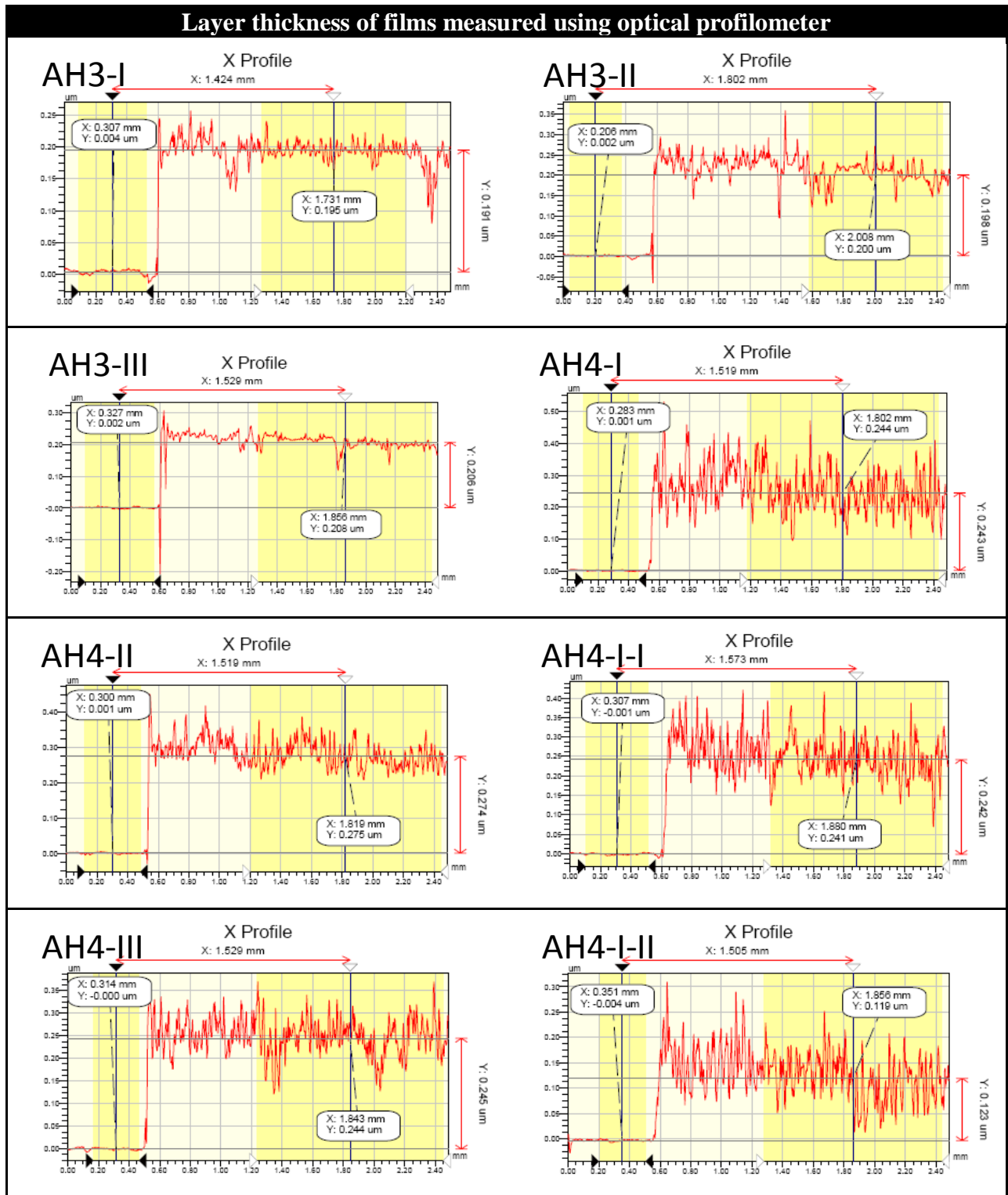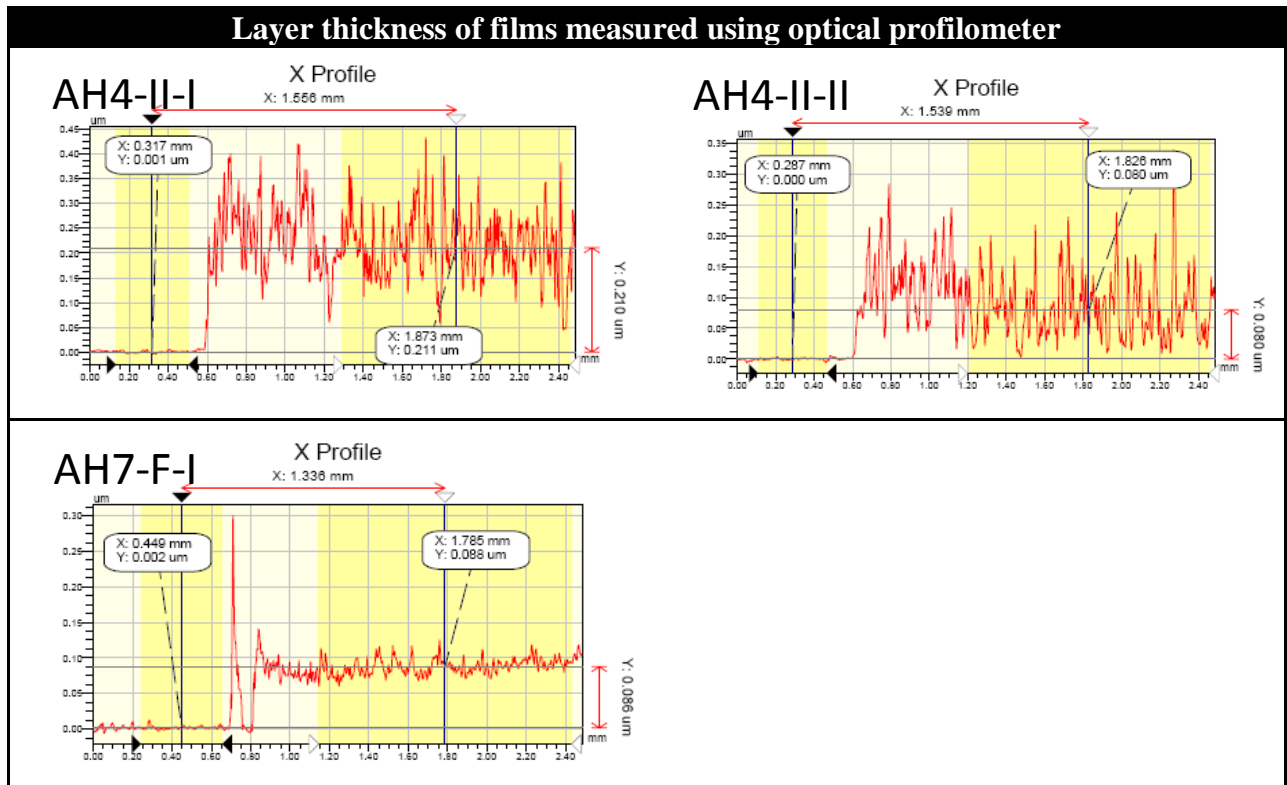
Continued Figure 4-47

4.4   Electrical property measurements of thick / thin dielectric layer

Different dispersions were obtained using THF and Toluene. The cubic and tetragonal $BaTiO_3$ obtained via hydrothermal or solvothermal synthesis respectively were used in these dispersion. Thick and thin films were obtained using dispersions. These layers were characterised using LCR meter for their electrical properties.

4.4.1   Electrical property measurements of thick layers

Thick layers were obtained using the dispersions with 2 % volume fraction of $BaTiO_3$ in PMMA, 8.8 % weight of PMMA in solvent by sliding apparatus on glass plates. The wet thickness of the obtained layer was 200 µm. The dried layers were characterised for thickness, and distribution of filler within the layer using SEM and screw gauge. The dried sample thickness was measured using screw gauge at various spots to obtain mean of the layer thickness value. It was found to be in the range of 0.016mm. Whereas SEM image of thick film shows that thickness is about 0.0163 mm.

Effort to increase the filler loading to 4 % and 8 % volume fraction in PMMA with MW 35 000 resulted in layers which were impossible to peel off from the glass substrate for characterization.

Two different solvents THF and toluene were used to obtain dispersion for thick films.

The distribution of $BaTiO_3$ in PMMA was observed by mounting the crossection of layer in silica sample holder and observing it under SEM. The homogenous distribution of $BaTiO_3$ in PMMA is evident in SEM images in crossectional and surface view of the layer in Figure 4-45.

The capacitance of the layer was measured by holding tight thick film between two copper electrodes of known diameter. The area of the electrode (1.76×10^{-4} m^2) was calculated to use in calculation for dielectric constant measurement using the formula given below;

Equation 4-1 $$C = \varepsilon_0\varepsilon_r A/t$$

Where C is the capacitance of the film, A is area of film held between electrodes, t is the thickness of sample, ε_0 is relative permittivity of vacuum (8.85×10^{-12} F/m), and ε_r is the dielectric constant of the film.

Air and PMMA of same thickness were used as reference to compare the capacitance and dielectric constant measurements.

There is marked increase in the capacitance and dielectric constant of thick polymer nanocomposite films with the addition of $BaTiO_3$ as filler. The electrical property of thick is shown in Figure 4-48 and Figure 4-50. The capacitance has attained the value of 120 pf at 2 % volume fraction of $BaTiO_3$ filler for the same area for which the capacitance for pure PMMA is 50 pF and air is 20 pF.

The dielectric constant has risen between 6.7 and 6.5 at this low filler loading while the dielectric constant for same thickness PMMA film was measured to be in the range 2.7 to 2.6 over the frequency range 10-200000 Hz.

The use of tetragonal $BaTiO_3$ instead of cubic $BaTiO_3$ has also proved to affect the electrical properties of thick films. The dielectric constant for the layer with 2 % volume fraction of tetragonal $BaTiO_3$ has attained a value of 7.4 at 10 KHz, when with same loading and thickness for film loaded with cubic $BaTiO_3$ was 6.7.

Figure 4-49 shows enlarged part of the capacitance values measured for thick films using tetragonal and cubic $BaTiO_3$ at 2 % volume filler fraction. The three different samples with same filler loading of cubic $BaTiO_3$ show a good agreement in the measured capacitance values, whereas Figure 4-51 shows dielectric constant for these three samples.

Figure 4-48 Capacitance measurement for thick film (approx. 16.3 μm) polymer nanocomposite films tetragonal and cubic BaTiO$_3$ as filler in PMMA in comparison to PMMA and air

Figure 4-49 Capacitance measurement for thick films using tetragonal and cubic BaTiO$_3$ at same filler loading in PMMA in comparison to PMMA and air
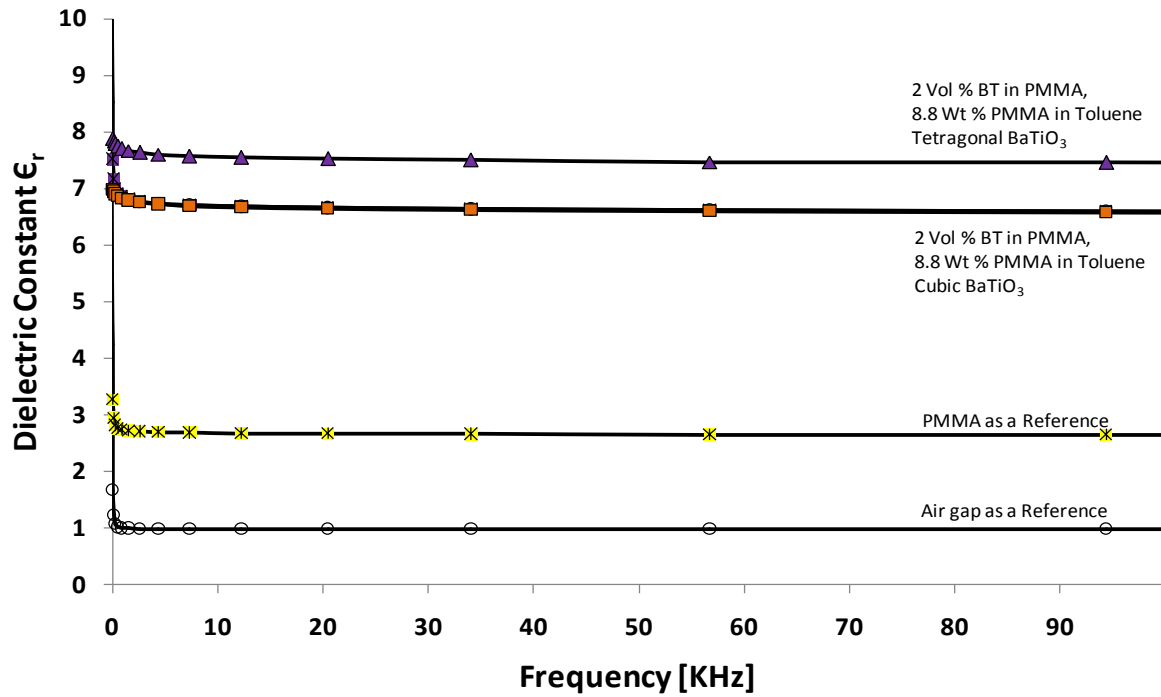
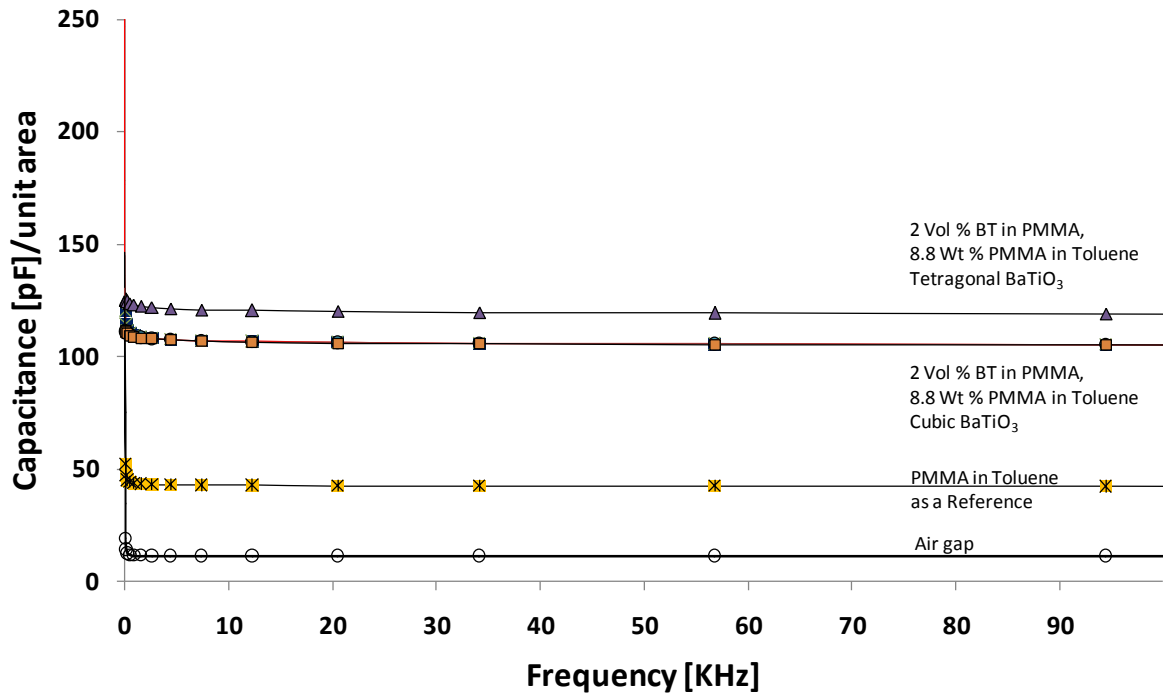Figure 4-50 Dielectric constant measurement for thick film (approx. 16.3 µm) polymer
nanocomposite films tetragonal and cubic $BaTiO_3$ as filler in PMMA in comparison
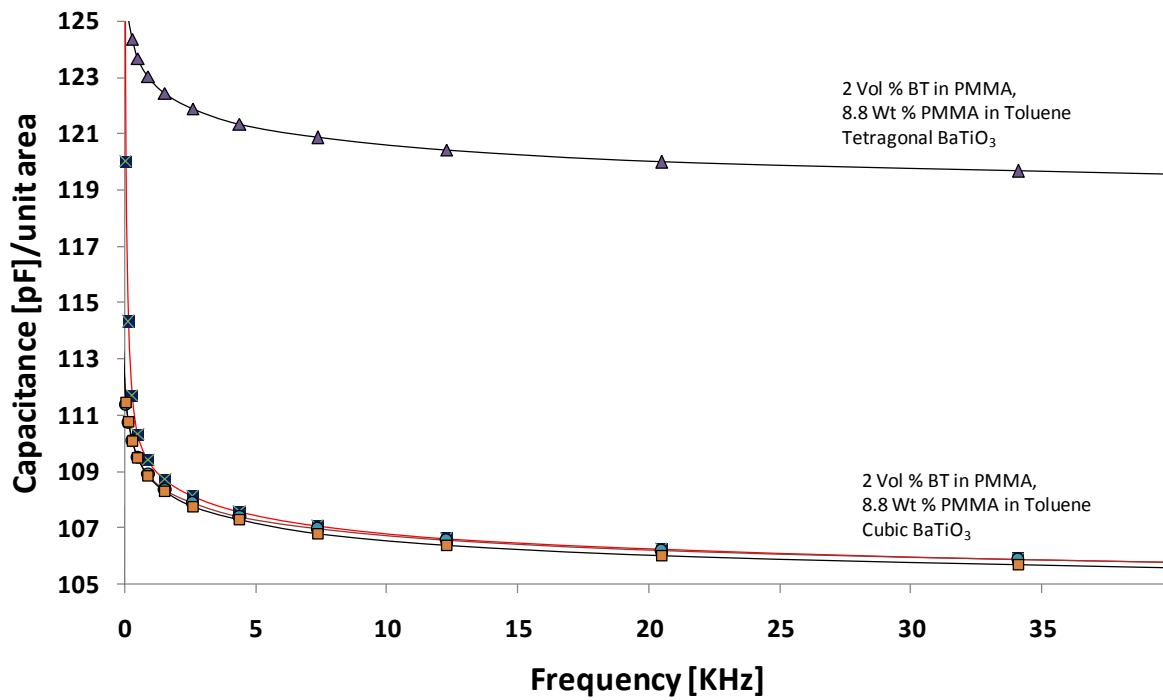to PMMA and Air
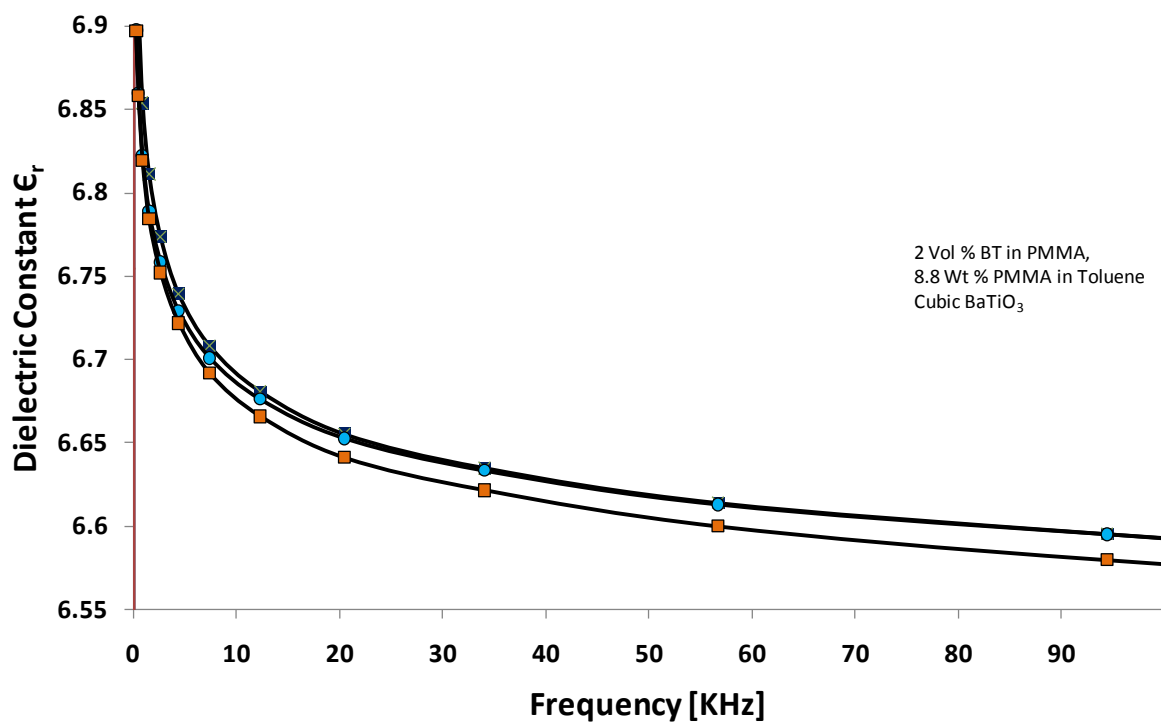
Figure 4-51 Dielectric constant for three different samples obtained at same filler loadings using
cubic $BaTiO_3$.

4.4.2 Electrical property measurements of thin films with lower filler loading

Dip coating and spin on technique were used to obtain thin films on ITO. Thin dielectric films obtained at a volume fraction between 0 % & 4 % volume fraction of $BaTiO_3$ in PMMA were characterised for dielectric constant and dielectric loss over a frequency sweep of 42 Hz to 5 GHz at applied voltage of 1V. Thin films with filler loading between 8 % & 30 % volume fraction were obtained using spin on technique. These films were characterised for capacitance measurement over a frequency range of 1000-10000 Hz with constant applied voltage of 1 V.

Thin films were deposited with aluminium (Al) top electrode by applying a mask on the film and sputtering the aluminium in a vacuum chamber. Thin films are already on ITO, which acts as a bottom electrode. The sample is mounted on a needle probe apparatus to have fixed contact without destroying thin film via top and bottom electrodes. The Hoiki LCR meter was used to measure the electrical properties of the films. The apparatus was tested for open and short circuit before sample measurement. The area of the electrode was measured under microscope. Al as top electrode, samples mounted on the needle probe and the measurement of area of electrode are shown in Figure 4-52.

Capacitance was measured using the HIOKI 3532-50 LCR meter and the dielectric constant was calculated using the Equation 4-1.

Use of cubic $BaTiO_3$ as filler

Figure 4-53 shows the dielectric constant values over a broad frequency range from 100 Hz-100 kHz for thin films using cubic $BaTiO_3$ as filler. The variation of filler loading has resulted in the increase of dielectric constant of the thin film. PMMA with no filler loading is shown as a reference. The increase of 2 % & 3 % filler fraction shows low increase of dielectric constant of about 2.8 & 3.2 respectively, while for 4 % volume fraction dielectric constant value is 3.5 (Figure 4-53). The tangent loss (dissipation factor-DF) measured for said thin film is between 0.033 and 0.038 at 10 kHz (Figure 4-54).

Use of tetragonal BaTiO$_3$ as filler

Figure 4-55 shows the dielectric constant changes with increased filler loading of tetragonal BaTiO$_3$ in thin film. At 1 % volume fraction there is no change seen in the dielectric constant of the thin film as the values of dielectric constant overlap that of PMMA. While for 2 % volume fraction loadings the dielectric constant at 10 kHz is about 4.2, with further increase in filler loading to 4 % volume fraction the dielectric constant at 10 kHz is in the range of 4.7 to 5 as measured for two different samples.

Another interesting fact observed during observation of low filler constant in our thin films is that a buffer layer of PMMA at top of our BaTiO$_3$ –PMMA film at 2 % volume fraction has caused a low dielectric value of 3.05, when without the buffer layer it was 4.2.

The dissipation factor (DF) is another important parameter which is looked for capacitors along with their dielectric constant. It is measure of electric power lost in a dielectric materials, usually in the form of heat. DF is expressed as the ratio of the resistive power loss to the capacitive power, and is equal to the tangent of the loss angle (δ). It is also referred as the loss tangent or tan δ.

The loss tangent measured for thin films loaded with tetragonal BaTiO$_3$ show that at 1-2 volume percent these values remain low between 0.03 to 0.04 over broad frequency range, while for 4 volume percent the values are in the range 0.05 to 0.09 between 10 kHz to 30 kHz (Figure 4-56).

Arrangements for capacitance measurement for thin films
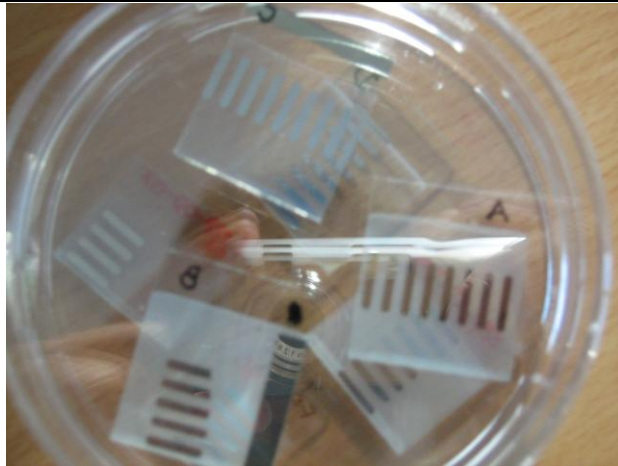
Al deposited top electrode on thin film

Sample connected on needle probe appar.

12,44 mm²

12,33 mm²

12,50 mm²
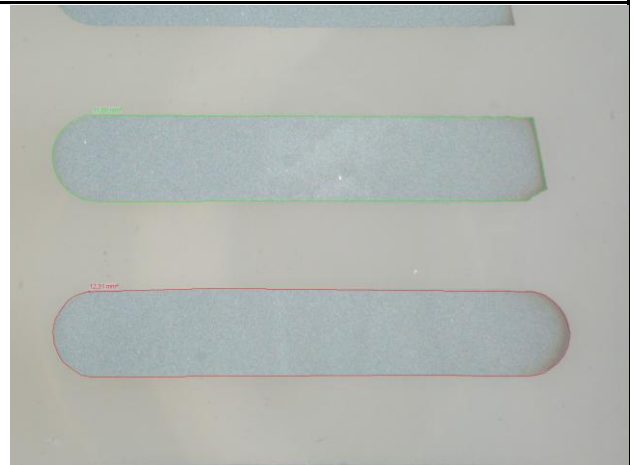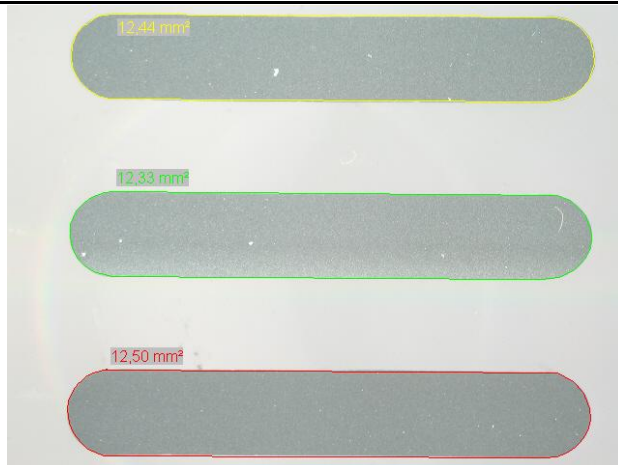
Area of top electrodes measured using microscopy

Room temperature condition and LCR meter used for capacitance measurements

Figure 4-52 Al deposited top electrode on thin film, the thin film on needle probe and area of the electrode measured under optical microscope and LCR meter used during electrical property measurement under room temperature conditions
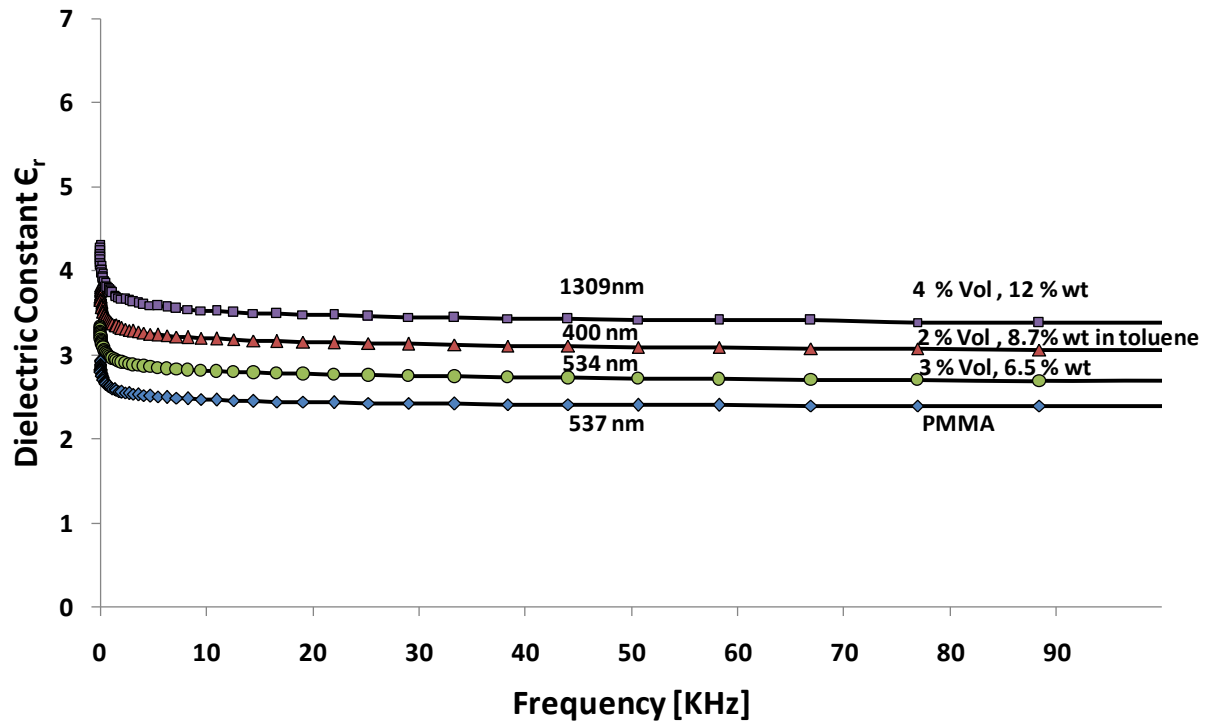
Figure 4-53 Dielectric constant of thin films with low filler loading using cubic BaTiO$_3$
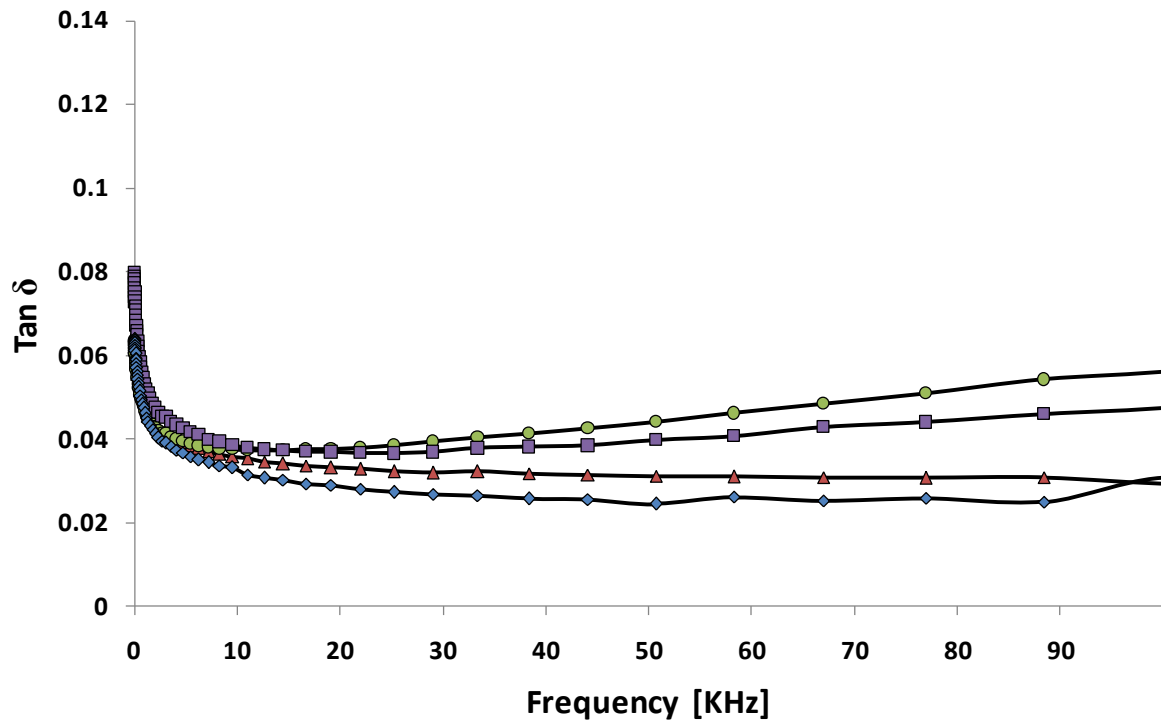
Figure 4-54 Loss tangent for thin films at lower filler loading using cubic BaTIO$_3$
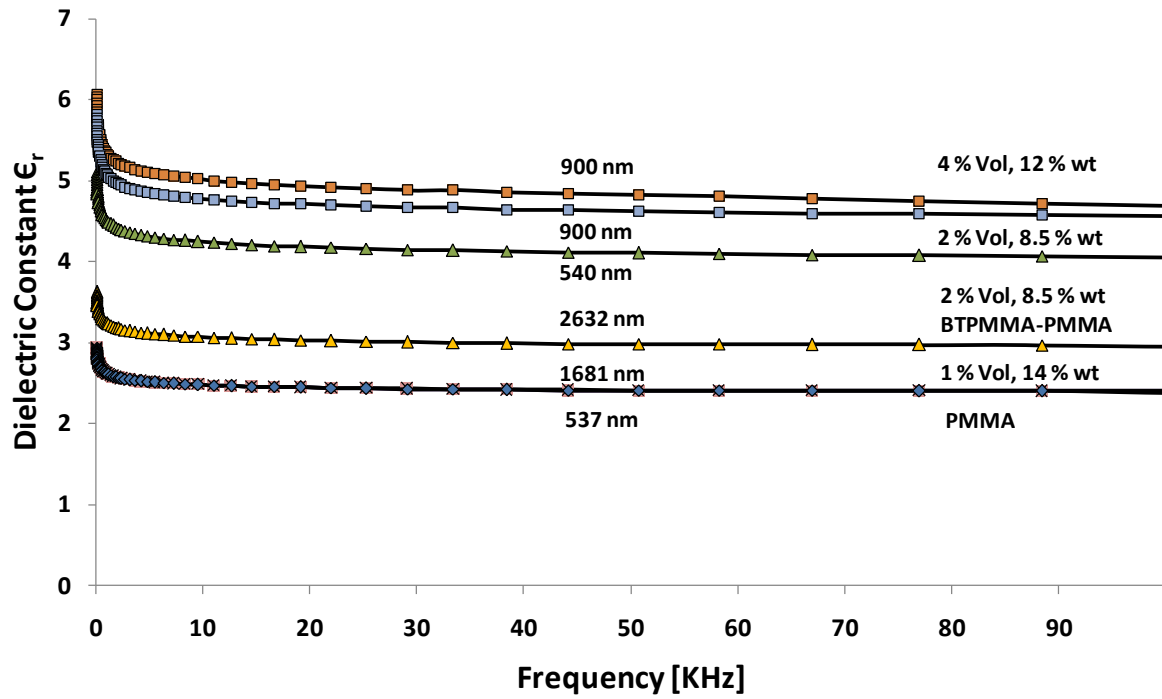
Figure 4-55 Dielectric constant of thin films with low filler loading using tetragonal BaTiO$_3$
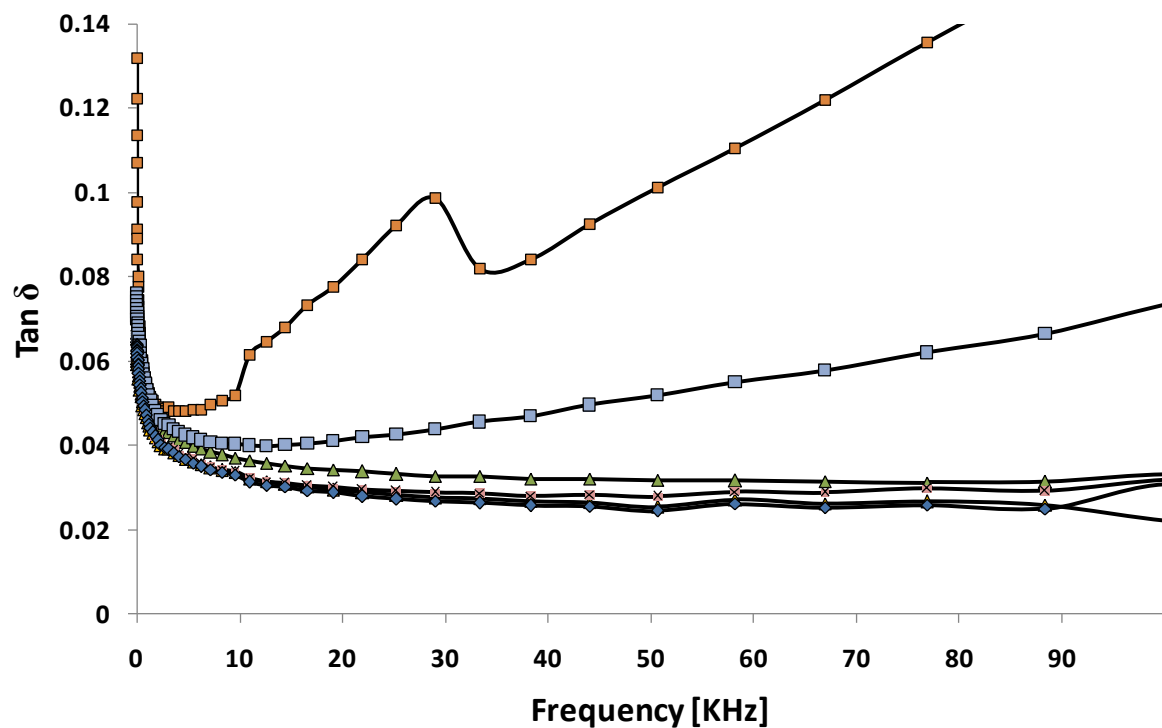
Figure 4-56 Loss tangent for thin films at lower filler loading using tetragonal BaTIO$_3$

4.4.3 Dielectric constant measurements of thin films with higher filler loading

At lower filler loadings the value of dilectric constant reamined low, to improve the dielectric constant with effecting the films mechanical stability. A systematic variation of volume percent fraction of filler and weight percent of PMMA was carried out. Thin dielectric films obtained at different volume fraction of $BaTiO_3$ and weight percent of PMMA in sovlent to reach the optimal loading of $BaTiO_3$ in PMMA with good electrical and mechanical stable thin layers.

The thin films obtained on ITO were deposited with platinum electrodes by sputtering the samples covered with mask in a vacuum chamber to achieve top electrode for characterisation of thin film by agilant LCR meter in the frequency range 1000 Hz to 10 000 Hz.

4.4.4 Capacitance measurements

Thin dielectric films obtained at high volume fraction of $BaTiO_3$ were characterised for dielectric constant and dielectric loss at 1 kHz to 10 kHz frequency at applied voltage of 1 V.

Figure 4-57 Capacitance density over frequency range for thin films (thickness in 'nm' shown on respective curve) loaded with cubic $BaTiO_3$ as filler, '% vol' stands for volume fraction of $BaTiO_3$ in PMMA and '% wt' for weight fraction PMMA in solvent used to obtain dispersion

The samples with platinum as top electrodes and ITO as bottom electrode were attached to an LCR meter on a needle probe apparatus. The LCR meter used and area of the top Pt electrode is shown in Figure 4-58. The LCR meter was tested for short and open on gold standard substrate before sample measurements.

Due to poor quality of electrode on film surface or the film itself, in some cases samples were unable to be tested, yet certain values of capacitance achieved using the same arrangement are shown in the Figure 4-57.

A marked increase in the capacitance of the thin films up till 136nm thickness was observed at 13 %, 20 %, 24 %, and 30 % volume fraction.

Arrangements for capacitance measurement for thin films

Agilent 4284A precision LCR meter   **Area of Pt top electrode on the film**
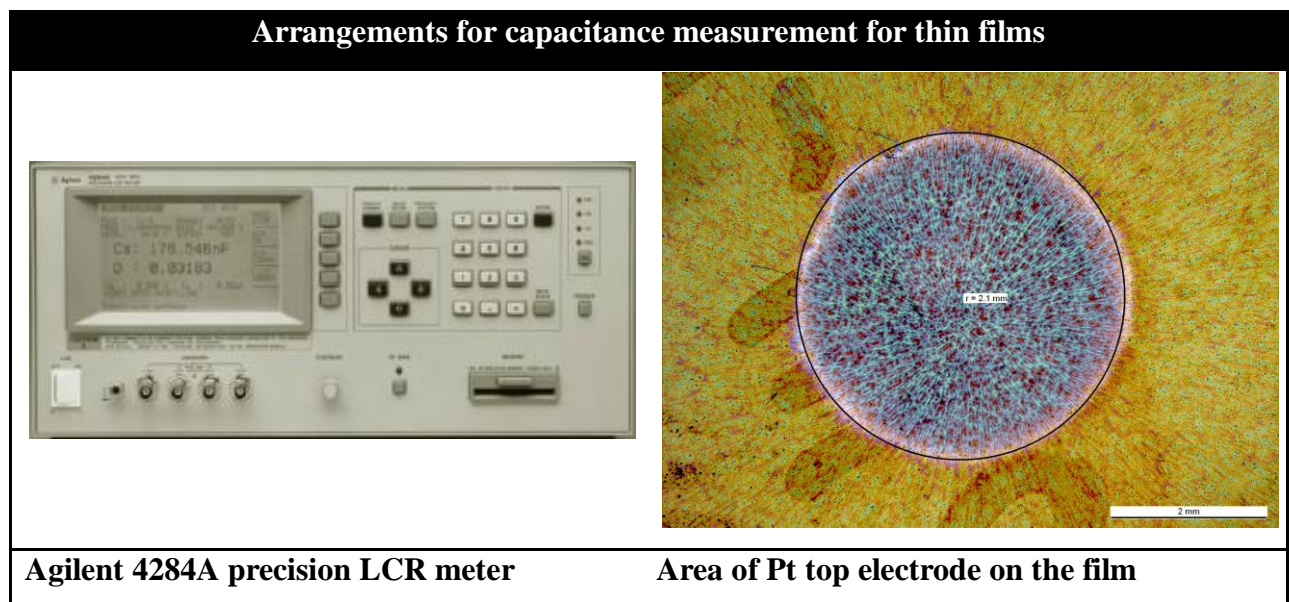
Figure 4-58 LCR meter used for capacitance measurement and area of platinum electrode on film surface

4.4.5   Dielectric constant measurements

Dielectric constant was measured using capacitance measured and area of electrode and thickness of the film. The Equation 4-1 was used to calculate the dielectric constant of these thin films.

A marked increase in dielectric constant of film loaded with cubic $BaTiO_3$ was achieved. At 20 % volume filler fractionof $BaTiO_3$ in PMMA when 3.25 % weight of PMMA in solvent was

used for obtaining the dispersion. The value of dielectric constant measured has reached to 9 at 10 kHz which is 3.46 time the value of dielectric constant of pure PMMA at this frequency.

At 24 %, and 30 % volume fraction a decrease in the dielectric constant shows that an optimal filler loading for thin film (100 nm to 280 nm) in this work is 20 % volume fraction of PMMA while the weight fraction of PMMA in solvent is 3.25 % (Figure 4-59).

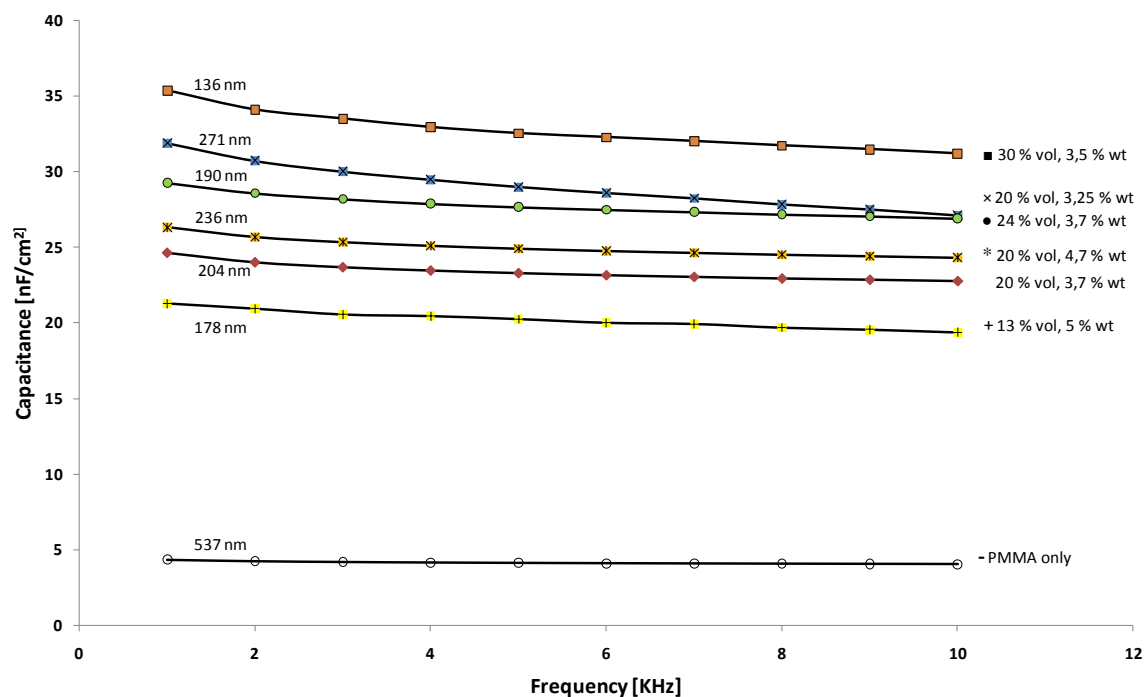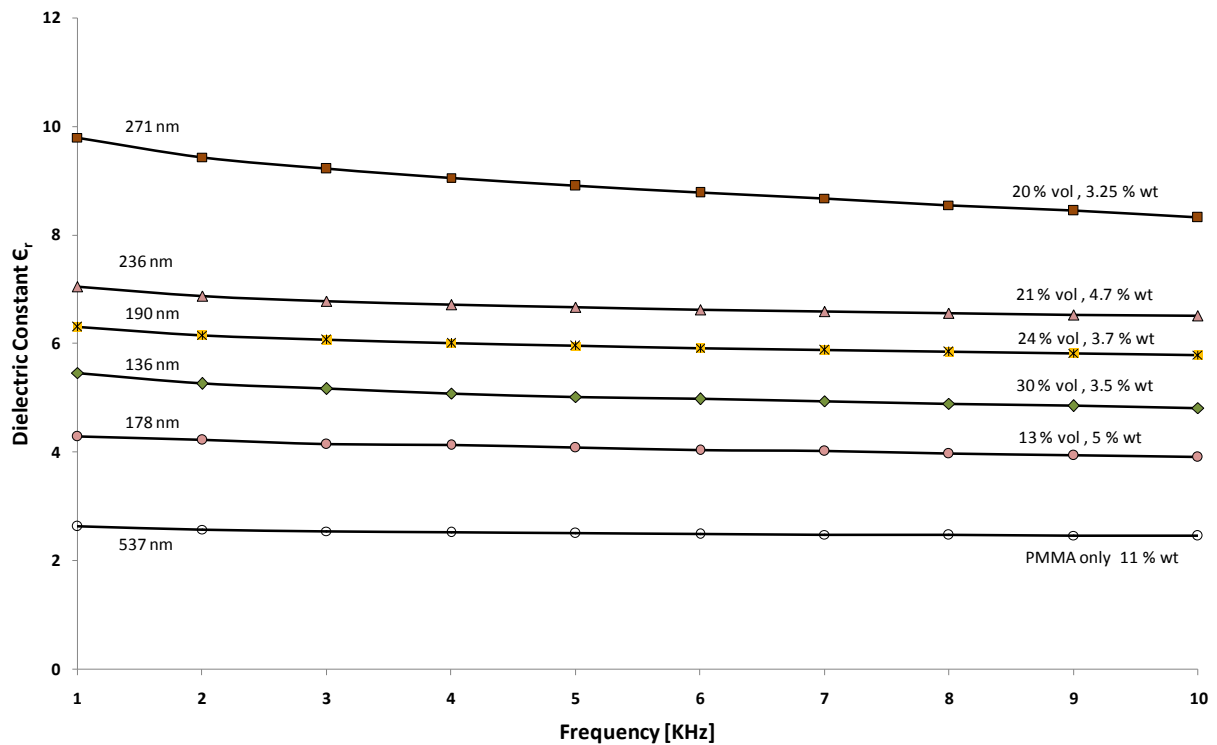Figure 4-59 Dielectric constant over frequency range for thin films (thickness in 'nm' shown on respective curve) loaded with cubic $BaTiO_3$ as filler, '% vol' stands for volume fraction of $BaTiO_3$ in PMMA and '% wt' for weight fraction of PMMA in solvent used to obtain dispersion

5   Discussion

5.1   Hydrothermal synthesis of BaTiO$_3$

The dynamic nature of hydrothermal synthesis process has been recognized in the literature [39] since the nature of crystals has been found to change with both time and temperature of the synthesis. The particle size of titania precursor as well considerably affects the obtained BaTiO$_3$ nanoparticles.

In our experiments mostly Ba (OH) $_2$·H$_2$O was used as Ba precursors. For titanium precursor we used different titania namely TiO$_2$ Tronox (average particle size approx.125 nm), TiO$_2$ P25 Degussa (average particle size approx. 25 nm), and spindle like rutile phase TiO$_2$.

Barium stearate was tried as Ba precursor along with TiCl$_4$ as titanium precursor to synthesis the in- situ surface functionalized BaTiO$_3$ during hydrothermal synthesis. It was found that presence of stearate did not allow the precipitation of perovskite BaTiO$_3$.

A systematic study was conducted using Tronox (type-A) and P25 Degussa (type-B) as titanium precursor for hydrothermal synthesis of BaTiO$_3$. The reactions were carried out at different temperatures i.e., 60 ˚C, 90 ˚C, 120 ˚C, and 150 ˚C for 16 h, 24 h, 48 h, and in some cases for 72 h.

The characterization of obtained BaTiO$_3$ particles using different titania precursors gave insight into formation mechanism and effect of temperature, time, particle size of titania precursor on the synthesis of BaTiO$_3$. During hydrothermal synthesis of BaTiO$_3$ the parameters temperature and time have strong influence on crystal growth, morphology and phase stabilization under highly alkaline conditions.

Use of spindle like TiO$_2$ resulted in BaTiO$_3$ nanoparticles with spherical morphology, which was quite different from the morphology of TiO$_2$ precursor used. It will be discussed at the end of discussion.

First of all our discussion will be focused on the systematic study conducted for hydrothermal synthesis of $BaTiO_3$ using type-A and type-B titania with $Ba(OH)_2$.

5.1.1 Influence of temperature on synthesis of $BaTiO_3$ using Tronox and Degussa TiO_2

The reaction of $Ba(OH)_2$ and Tronox TiO_2 (type-A precursor) at 60 °C for 48h yielded incomplete reaction; unreacted anatase was observed by XRD analysis, besides $BaTiO_3$ perovskite structure (Figure 4-1). Contrary, the XRD patterns of $BaTiO_3$ samples obtained using TiO_2 Degussa (type-B precursor) showed that the perovskite structure had started appearing at 60 °C for 16 hwith no big peaks of unreacted titania were observable (Figure 4-8).

The reactions at 90, 120 and 150 °C for type-A Ti precursor yielded $BaTiO_3$ with some TiO_2 as anatase present in all the samples (Figure 4-1, Table 5-I). This may be attributed to the formation of $BaCO_3$ due to reaction with atmospheric CO_2 causing reduction of Ba content for reaction with TiO_2. For phase pure $BaTiO_3$ formation from solution Ba/Ti ratio > 1 is proposed in literature [107, 108], and avoiding the atmospheric CO_2 is suggested by Lencka et al. [17].They reported that in open system with respect to CO_2, the desirable $BaTiO_3$ did not form at all because $BaCO_3$ is inherently more stable. In the closed system such as a tightly closed autoclave, which drastically reduces the availability of CO_2 (g) $BaCO_3$ precipitates at molar concentration of Ba higher than 10^{-5}m. Therefore, the precipitated $BaTiO_3$(s) will be always contaminated with some amount of $BaCO_3$(s) if the solution is concentrated.

The reactions at higher temperatures i.e., 90, 120 and 150 °C using type-B precursor yielded $BaTiO_3$ with fully formed perovskite structure (Figure 4-8). Here the unreacted anatase and rutile were seen in 60 °C samples obtained after 48 h reaction time, and in 90°°C, 120°°C, and 150°°C samples obtained after 16h. But at 60 °C after 72h and 90°°C, 120°°C, and 150 °C after 24 h and 48 h no peaks of anatase and rutile were observed (Table 5-II). In samples obtained at 90°°C and 120 °C after 24 h, peaks of barium formate as impurity were observed, which is due to washing with formic acid for removing $BaCO_3$. These peaks were not observed in other samples, due to better washing of powders with DI water after 1M formic acid washing. The presence of barium formate was quite low in all samples.

Table 5-I   Presence of unreacted anatase (Δ) in samples obtained using type-A titanium precursor reacted at 60, 90, 120, 150 ˚C for 16, 24, 48 h. NA stands for samples not obtained

Temperature/ Time	16 h	24 h	48 h	72 h
60 ˚C	Δ	Δ	Δ	NA
90 ˚C	Δ	Δ	Δ	Δ
120 ˚C	Δ	Δ	Δ	NA
150 ˚C	Δ	Δ	Δ	NA

Table 5-II   Presence of unreacted anatase (Δ) and rutile ($\bullet$) in samples obtained using type-B titanium precursor reacted at 60, 90, 120, 150 ˚C for 16, 24, 48 h

Temperature/ Time	16 h	24 h	48 h	72 h
60 ˚C	Δ, $\bullet$	Δ, $\bullet$	$\bullet$	-
90 ˚C	Δ, $\bullet$	-	-	NA
120 ˚C	Δ, $\bullet$	-	NA	NA
150 ˚C	Δ, $\bullet$	-	-	NA

The crystallite size of obtained $BaTiO_3$ powders using Scherrer's equation was found to be in the range of 40 nm to 90 nm using type-A precursor of titania while in case of type-B precursor it remained in the range 35 nm to 60 nm. The graphs drawn using this variation of crystallite size for various sample of $BaTiO_3$ indicated a decrease in the calculated crystallite size for higher reaction temperatures in case of type-A precursor, a similar trend was observed for type-B precursor with a few exceptions (Figure 5-1). Qi et al. [109] rejected the idea of Ba^{2+} diffusion in TiO_2, while supporting short range dissolution mechanism of TiO_2, suggested that the reaction of $[Ti(OH)_x]^{4-x}$ species with Ba^{2+} results in smaller particle size as Ba/Ti ratio increases.

a)

b)
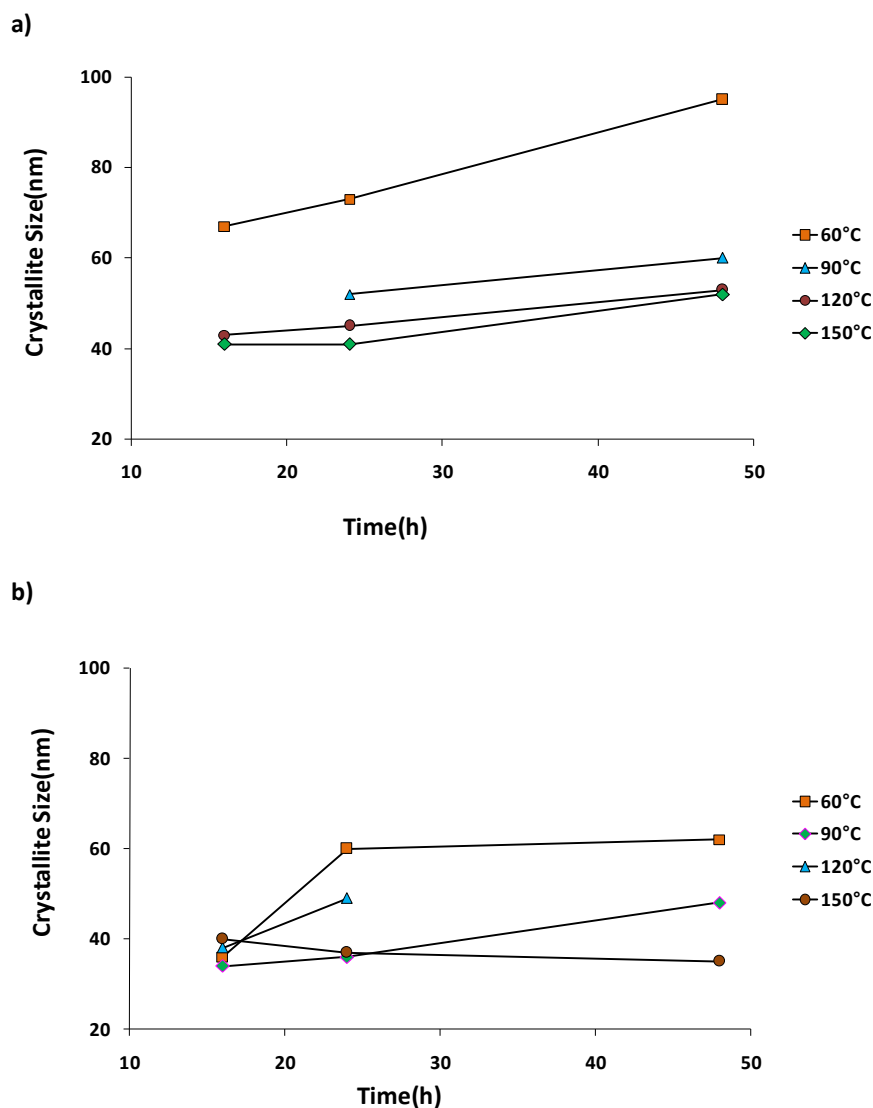
Figure 5-1   Crystallite variation of BaTiO$_3$ with temperature and time using a) type A and b) type-B titanium precursor

5.1.2   Morphology and mechanism

TEM and SEM images of the samples obtained using type-A and type-B titania revealed the changes in morphology and composition of BaTiO$_3$ with synthesis temperature. In case of type-A precursor the BaTiO$_3$ particles obtained at various temperatures showed morphology similar to that of the type-A precursor. The same is true for the BaTiO$_3$ particles obtained using type-B titanium precursor as shown in Figure 5-2. At first sight it appears that an in situ transformation mechanism occurs, involving diffusion of Ba^{2+} through the BaTiO$_3$ shell layer formed around the titania particle, and subsequently reaction with the TiO$_2$ core. As authors suggested in literature [29, 30] the shape and morphology of BaTiO$_3$ remains same as TiO$_2$ used in the reaction in case

of in situ transformation mechanism. While arguing against the Ba^{2+} diffusion in TiO_2, Qi et al. [109] supported short range dissolution of TiO_2 and suggested that the reaction of $[Ti(OH)_x]^{4-x}$ species with $Ba^{2+}$ results in smaller particle size as Ba/Ti ratio increases, which as well result in the formation of $BaTiO_3$ with a morphology similar to that of the TiO_2 titania precursor.

The decrease in crystallite size at higher temperature in our work can be explained by higher $BaTiO_3$ nucleation rate on the TiO_2 particles surface. Due to the core shell structure during crystal growth of $BaTiO_3$, the increase in number of nucleation sites on the surface of TiO_2 resulted in smaller crystal size in the final product.

The surface morphology of the $BaTiO_3$ obtained using type-A titania at 90 °C after 48 h shows less pores than the particles obtained at 120 °C after 48 h and 150 °C after 24 h. The cubic morphology of $BaTiO_3$ has changed to more porous particles for the same samples (Figure 5-2). Whereas, in case of type-B precursor for the sample at 60 °C for 16 h and 48 h, irregular morphology of particles with no sharp edges is observed in SEM and TEM images (Figure 5-2, Figure 5-3). The high resolution images of same samples in Figure 5-5 shows amorphous and crystalline portion, indicating incomplete reaction in the final product which is as well seen by the XRD patterns.

TEM bright and dark field images (Figure 5-3, Figure 5-4) of $BaTiO_3$ for type-A show that pores and strains in the particles are evident in the samples obtained at 90 °C after 48 h. The large strain in the TEM photograph is indicated by the contrast variation across a particle. If the particle is single crystalline and has no strain, it should be uniform in contrast. However, for a single-crystalline particle, if the image shows dark-bright variation in contrast, it is likely to have a high strain. Strain affects the diffraction behavior of the electrons, resulting in dramatic contrast change [63]. The HRTEM images for same particles shows fully crystalline particle with same orientation of plane with in a particle, which indicate that these $BaTiO_3$ are single crystals.

SEM images of $BaTiO_3$ obtained using type-B titania show the circular porous morphology for the sample at 90 °C for 24 h and 48 h. Finally it can be seen that particles are pore-free with compact facetted morphology in the sample obtained at 150 °C for 48 h (Figure 5-2). TEM bright field images for sample reacted at 90 °C for 48 h show the round morphology of the particles with bright and dark variation in contrast indicating strains in the particles. However samples at

150 ˚C for 48 h shows facetted nature of the particles with well defined boundaries and no bright and dark variation in contrast is observable on bright and dark field images (Figure 5-3, Figure 5-4). The pores seen before in samples at 90 ˚C cannot be seen here, which indicates that the particle are strain free and fully compact. SEM images of sample obtained at 150 ˚C after 24 h show that facetted particles without pores have started to appear (Figure 5-2). The removal of the pores from the particle surface is reported by Nakano et al. [110] at 855 ˚C or more during in-situ TEM observation of $BaTiO_3$ particles on a hot stage. Hennings et al. [111] reported that hydrothermally synthesized $BaTiO_3$ contains nanometre sized intragranular pores, these pores migrates to the grain boundaries and disappear at temperatures greater than 800 ˚C. In this work it was observed that under hydrothermal conditions, the pore free compact $BaTiO_3$ was obtained at 150 ˚C after 48 h.

The elemental analysis by EFTEM shows homogenous distribution of Ba, Ti, and O in the samples produced at 90 ˚C and 150 ˚C after 48 h for both type-A and type-B. Whereas, EFTEM spectrum for sample grown at 60 ˚C after 48 h using type-B titania precursor shows regions containing unreacted TiO_2 with no Ba (Figure 5-6). This may be due to the fact that Ba^{2+} has not yet diffused the core of TiO_2, if the in situ transformation or short range dissolution is taken into consideration as mechanism responsible for the formation of $BaTiO_3$.

Morphology of titania precursors and obtained BaTiO₃ samples

Type-A TiO₂ Tronox

Type-B TiO₂ P25 Degussa

A90 ˚C 48 h

B60 ˚C 16 h

A120 ˚C 48 h

B90 ˚C 24 h

A150 ˚C 24 h

B150 ˚C 24 h
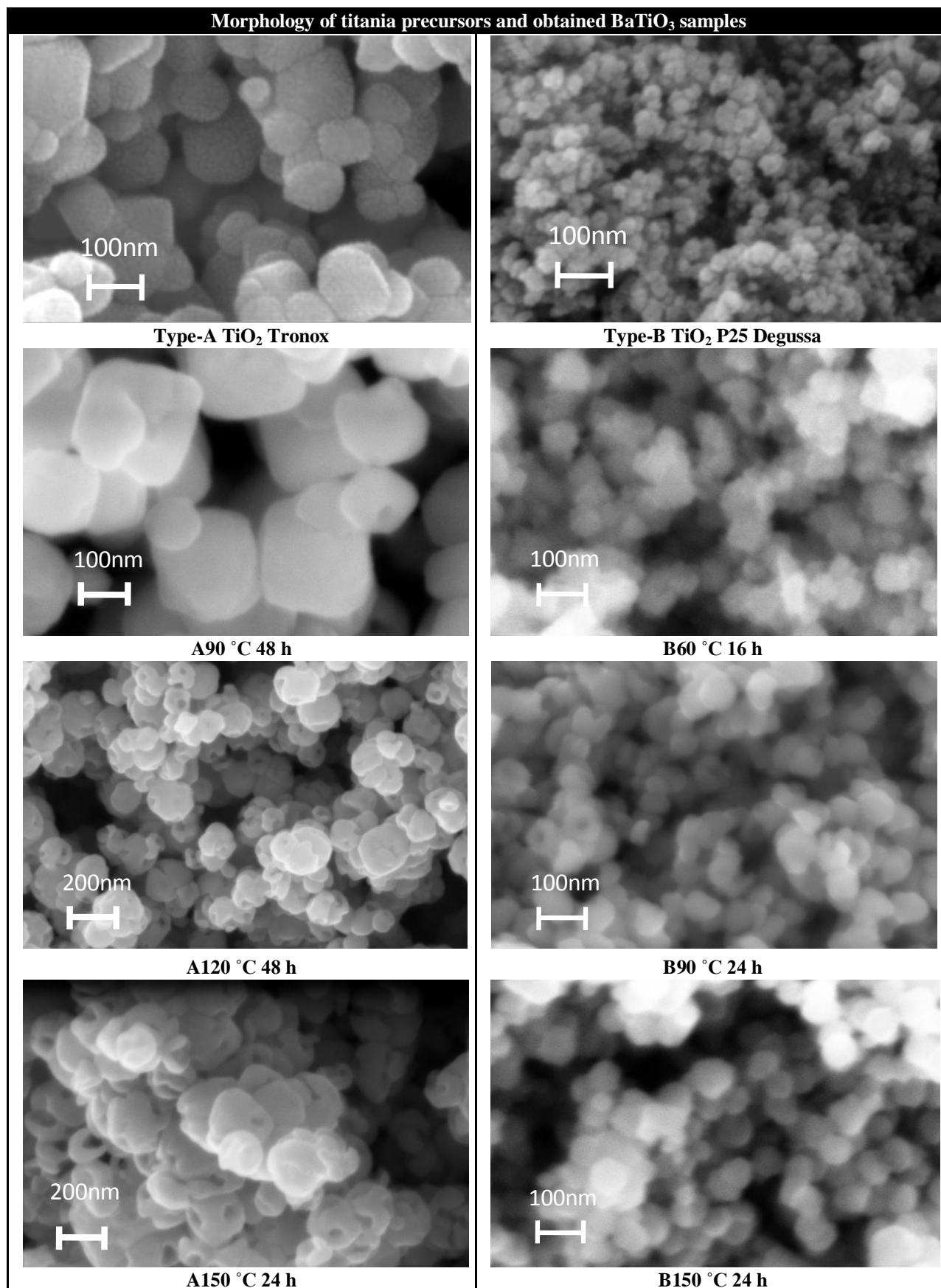
Figure 5-2   SEM images for Type-A and B titania and BaTiO₃ samples obtained using them

Figure 5-3   TEM bright field images for BaTiO₃ samples obtained at 90 ˚C after 48 h for type-A titania and at 60, 90, and 150 ˚C, after 48 h for type-B titania
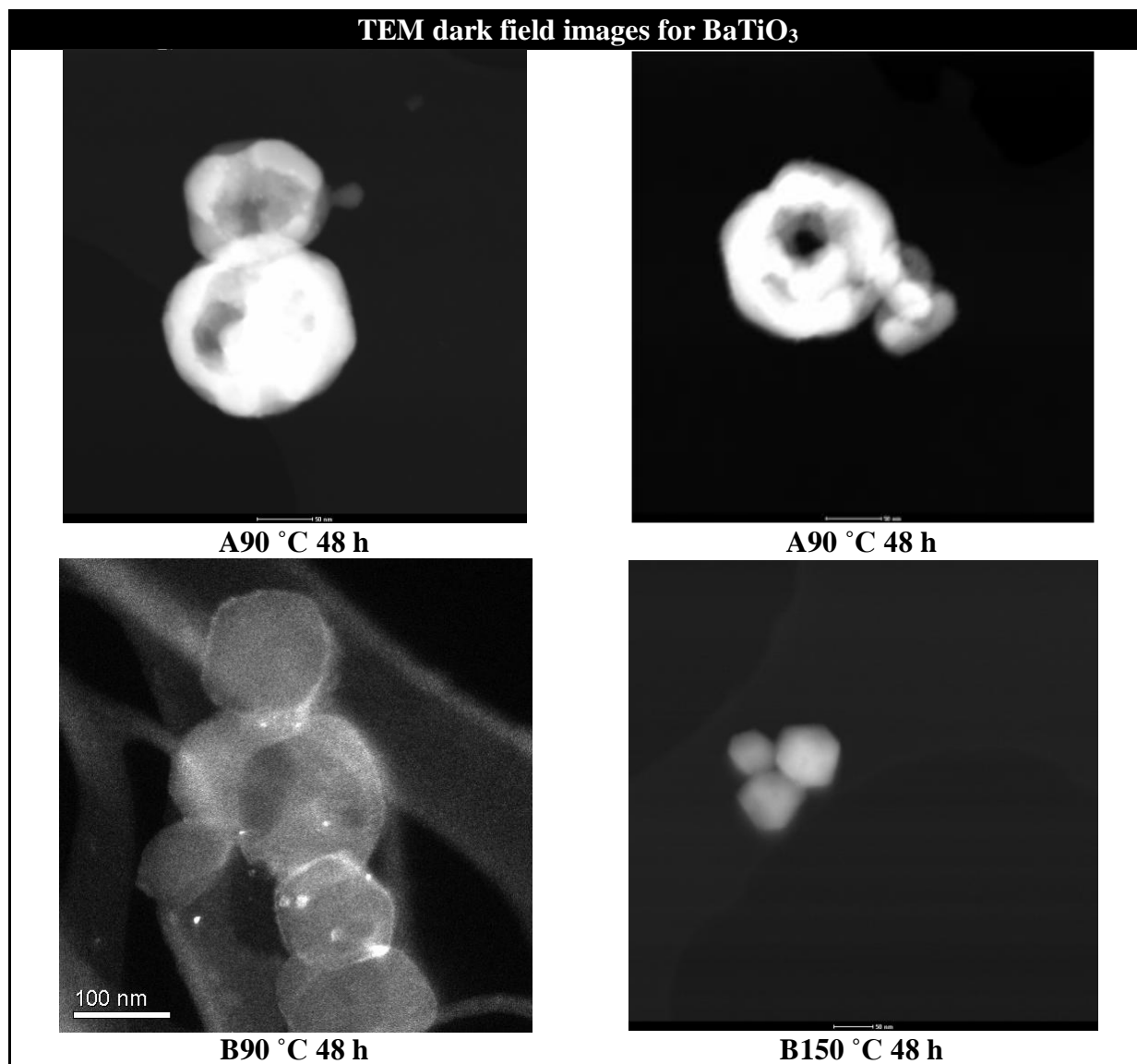
Figure 5-4   TEM dark field images for BaTiO₃ samples obtained at 90 ˚C after48 h for type-A titania and at 90 and 150 ˚C, after 48 h for type B titania

HR TEM images for BaTiO₃

A90 ˚C 48 h

B60 ˚C 48 h

B90 ˚C 48 h

B150 ˚C 48 h
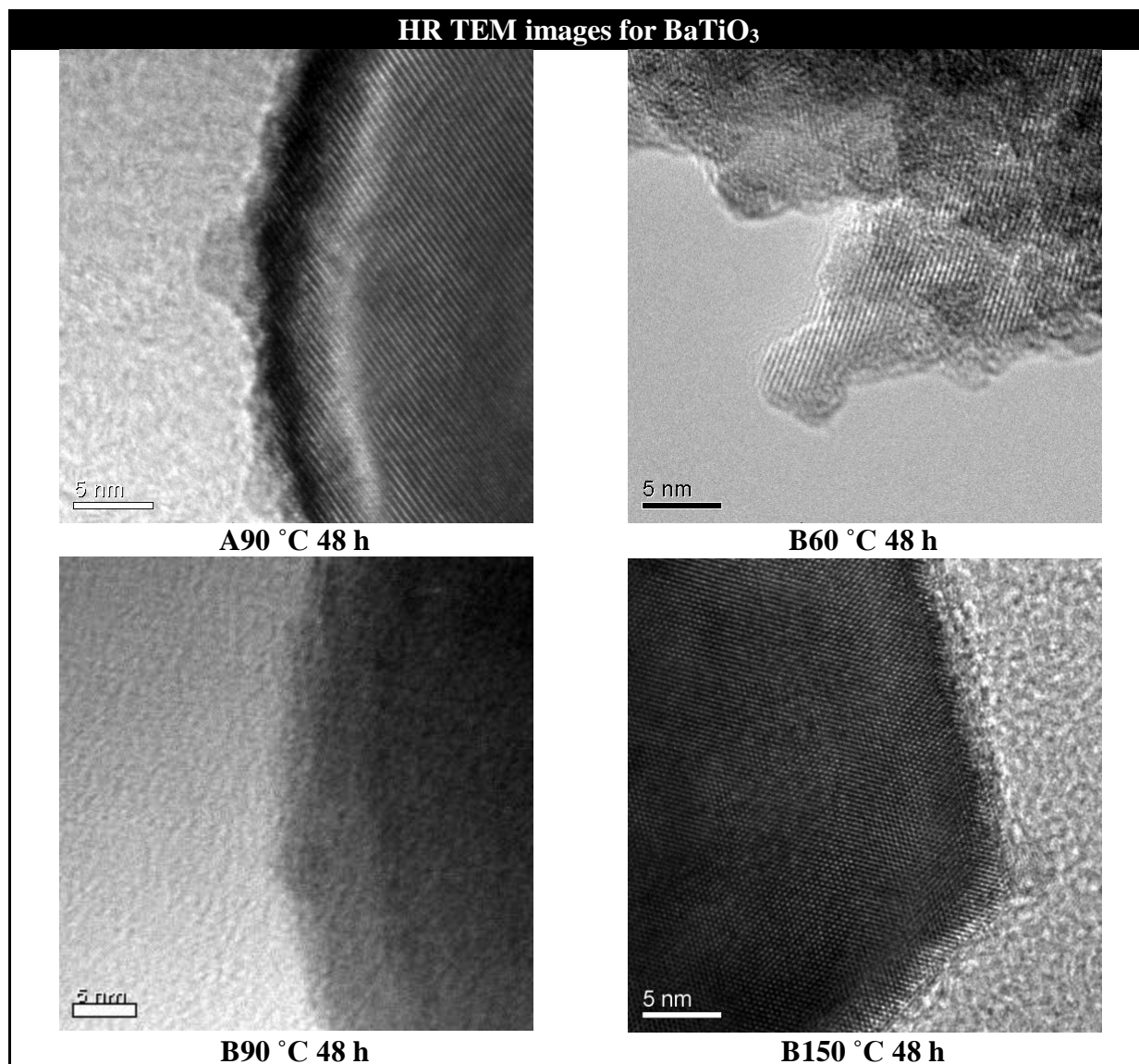
Figure 5-5 HRTEM images for BaTiO₃ samples obtained at 90 ˚C after 48 h for type-A titania and at 60, 90, and 150 ˚C, after 48 h for type-B titania
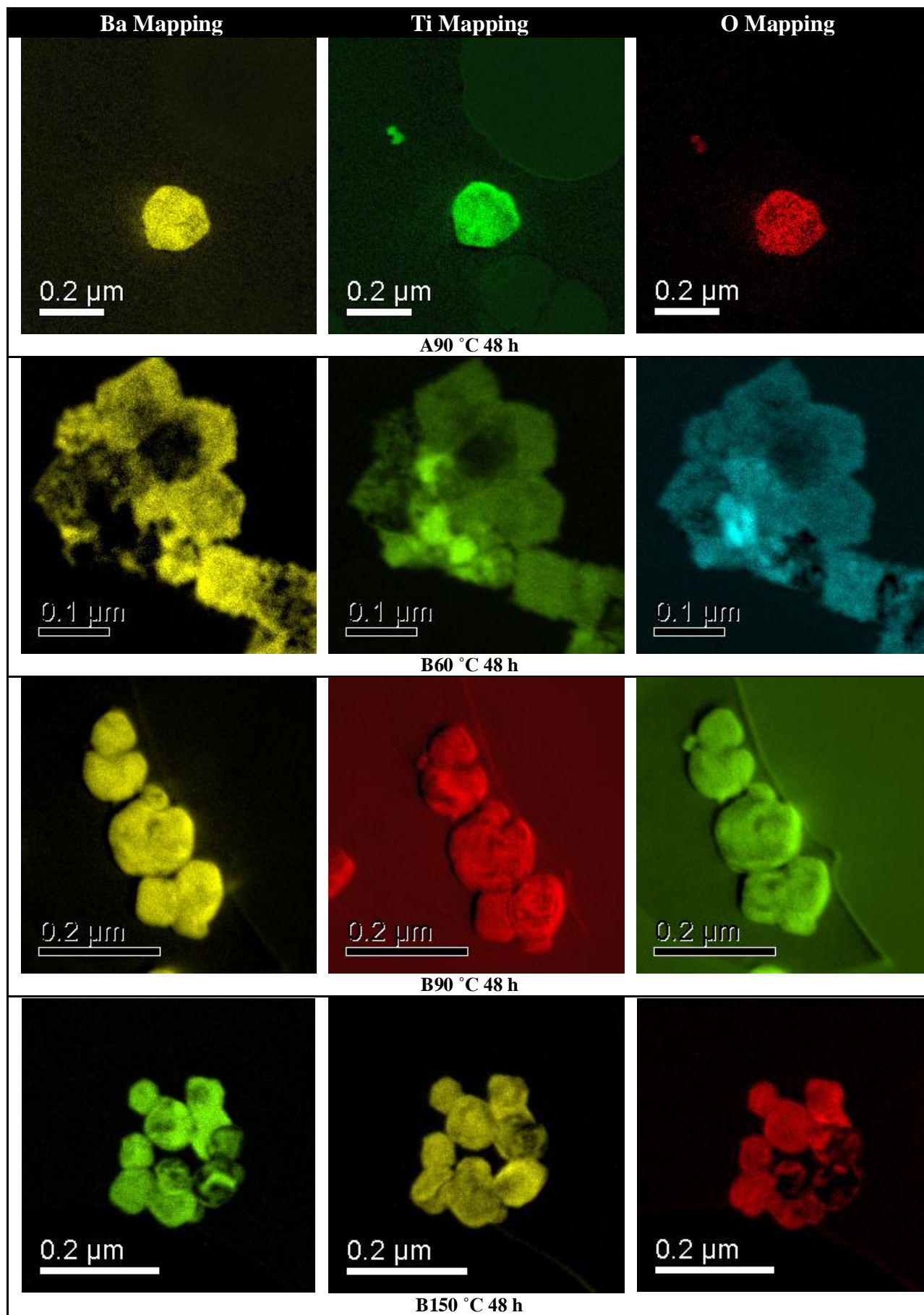
Figure 5-6   Elemental mapping of Ba, Ti and O for obtained BaTiO$_3$ using titania type-A&-B

5.1.3   Influence of time on synthesis of BaTiO$_3$ using Tronox and Degussa TiO$_2$

Generally longer reaction time favours the hydrothermal crystallization of BaTiO$_3$. The samples obtained at 60 °C after 16, 24 and 48 h using type-A titanium precursor show the evident peaks of unreacted anatase in the XRD patterns indicating that 60 °C is too low temperature for the completion of BaTiO$_3$ crystallization from Tronox TiO$_2$ as titanium precursor under our reaction conditions. The perovskite structure has started appearing at 60 °C even after 16 h reaction time. XRDs were obtained under same sample preparation method and XRD arrangements. The change in the peak intensity gives a rough idea of the amount of substances increasing or decreasing in the samples. This suggests that the amount of anatase decreased with longer reaction times and peaks of the cubic BaTiO$_3$ for longer reaction time shows increased intensity. This indicates that with time the conversion of TiO$_2$ to BaTiO$_3$ is increasing (Figure 5-7).

The XRD observation of BaTiO$_3$ sample at 60 °C using type-B precursor for 16 h reveals presence of unreacted titania as anatase and rutile phases. The intensity of the peaks was not as sharp as was in the case of type-A titania at same conditions of temperature and time. This suggests that hydrothermal crystallization of BaTiO$_3$ is completing even at 60 °C after 16 h. After 48 h no anatase phase can be detected in the same sample while rutile was still present. This may be attributed to the fact that anatase phase of TiO$_2$ reacts faster than rutile [112]. J. Moon et al. [31] reported the hydrotherm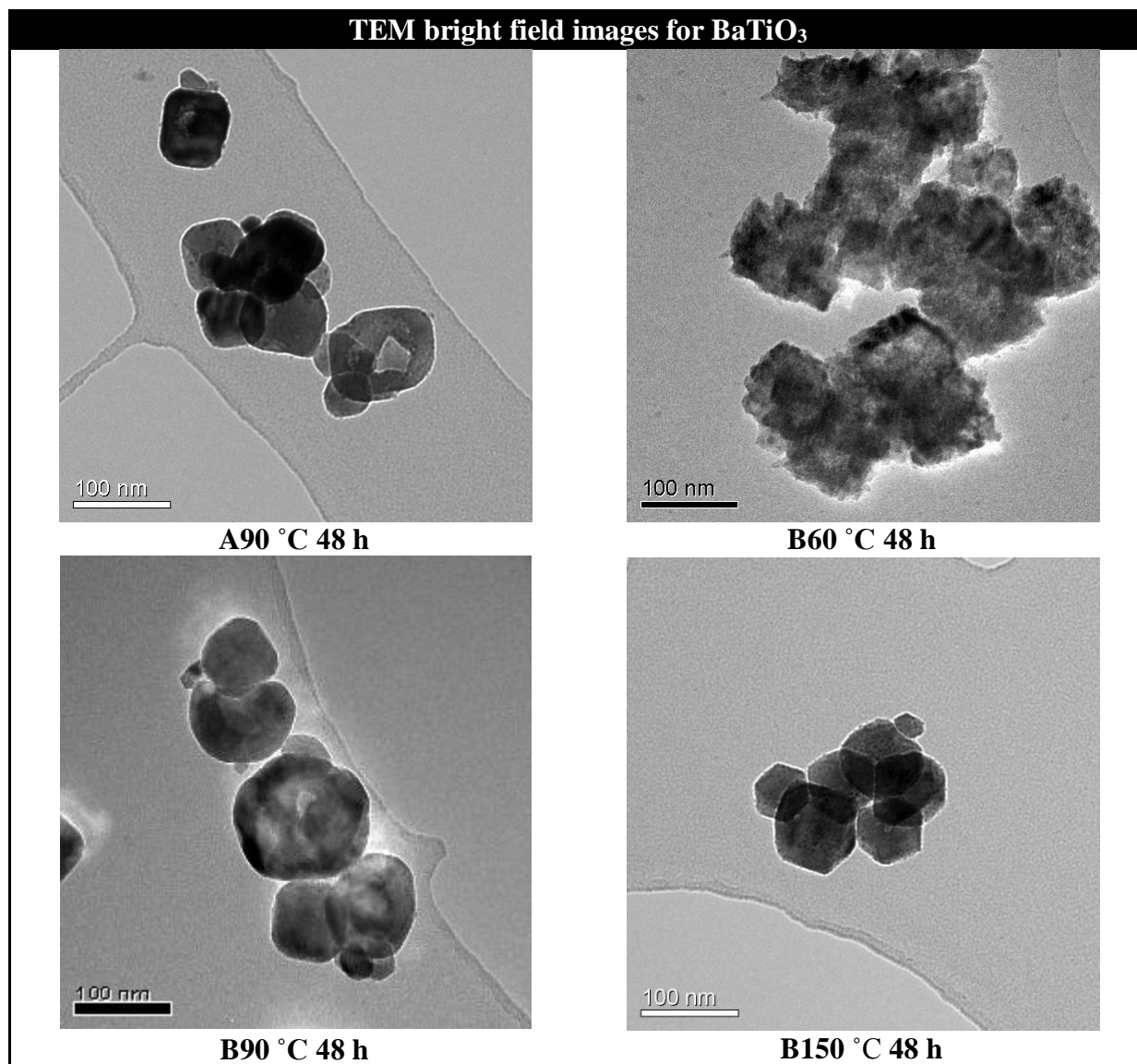al synthesis of BaTiO$_3$ using metal alkoxide precursor under highly alkaline condition at 50 °C after 12 h. While synthesis of BaTiO$_3$ at 85 °C at equilibrium water vapour pressure (15-65 atm.) was reported in the literature [23, 24].

At 90, 120, and 150 °C slight amount of anatase was present in the samples till 48 h for type-A titania (Figure 4-1) while for type-B titania, the anatase and rutile as impurities are observable for reaction at 90, 120, and 150 °C over duration of 16 and 24 h, but after 48 h no rutile or anatase are observed (Figure 4-8). This implies that longer reaction time helps to complete the crystallization of BaTiO$_3$.

A reaction time dependence on BaTiO$_3$ crystallite size (Figure 5-1) reveals no predictable trend via hydrothermal route in our study.

5.1.4   Effect of particle size and phase of TiO_2 on hydrothermal synthesis of $BaTiO_3$

Table 3-I indicates the properties and Figure 3-1 shows the SEM images of TiO_2 precursors; type-A and type-B used in the systematic study of $BaTiO_3$ synthesis. Type-A titania is coarser than P25 Degussa TiO_2, while it constitutes mainly the anatase phase of titania, whereas the type-B precursor of titania is 30 % anatase and 70 % rutile with very fine grains of about 25 nm as observed by SEM images.

The reaction of type-A titania with $Ba(OH)_2$ at low temperature reveals that at 60 ˚C excess of anatase is left after 16 h reaction time. The amount of anatase appear to decrease for reaction at 60 ˚C for longer time whereas the XRD diffractograms of samples reacted at 60 ˚C for type-B show that finer particles complete the reaction at lower temperatures and in shorter time which indicates, that reaction rate might depend on the surface area of titania precursor (Figure 5-7, Figure 5-8). This agrees with the observation of Chen et al. [113] who reported that the reaction rate is possibly dependent on particle size of titania while studying the conversion of three different titania precursor to $BaTiO_3$ via hydrothermal route. Whereas, Kutty et al. [112] found that reaction rate depends on phase of titania precursor. They observed amorphous gel of titania reacted fastest, anatase reacted at intermediate rates and rutile reacted most slowly.

The morphology of the $BaTiO_3$ obtained at 90 ˚C for 48 h using type-A precursor is very similar to original Tronox powder used as titania precursor in this case. While the same is true for morphology of $BaTiO_3$ obtained using type-B precursor at 60°C samples (Figure 5-2).

At higher temperature $BaTiO_3$ obtained using type-A and type-B precursors have comparable size to their respective TiO_2 precursors. The coarse grained titania precursor yielded coarser $BaTiO_3$ while the fine grained p25 Degussa the $BaTiO_3$ obtained was very fine (Figure 5-2). This shows that initial size of TiO_2 precursor strongly influence the size of obtained $BaTiO_3$ via hydrothermal synthesis, which lead researchers [29] conclude that conversion of TiO_2 to $BaTiO_3$ is in-situ transformation mechanism, i.e., formation of continuous $BaTiO_3$ layer at surface of TiO_2 by reaction with dissolved barium, more Ba-ions must diffuse through this $BaTiO_3$ layer to continue the reaction.

XRD pattern for the $BaTiO_3$ sample obtained using spindle like TiO_2 show evident peaks of TiO_2 present in the final product as rutile phase (Figure 4-19). The crystallite size of obtained $BaTiO_3$ was around 85 nm measured by Scherrer's equation.
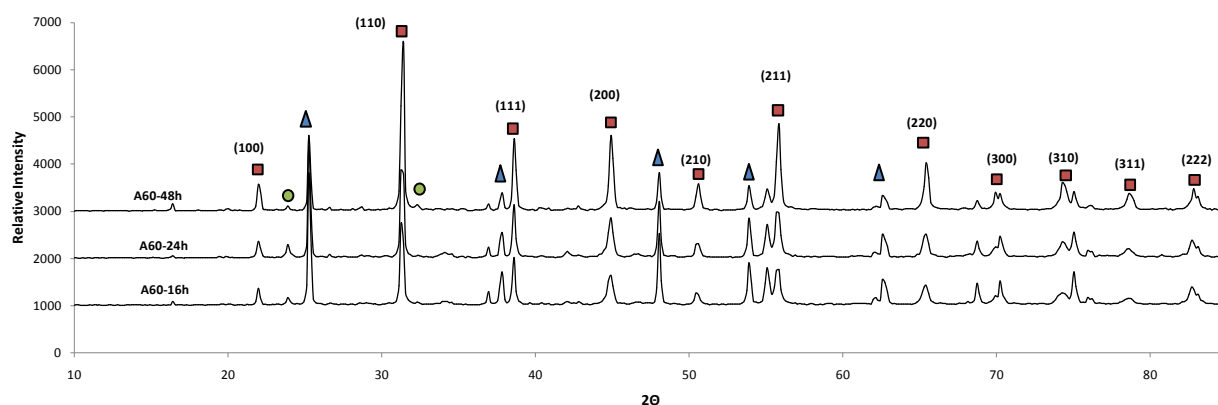
Figure 5-7   XRD patterns for BaTiO$_3$ samples obtained at 60 ˚C at different temperature for type-A titanium precursor
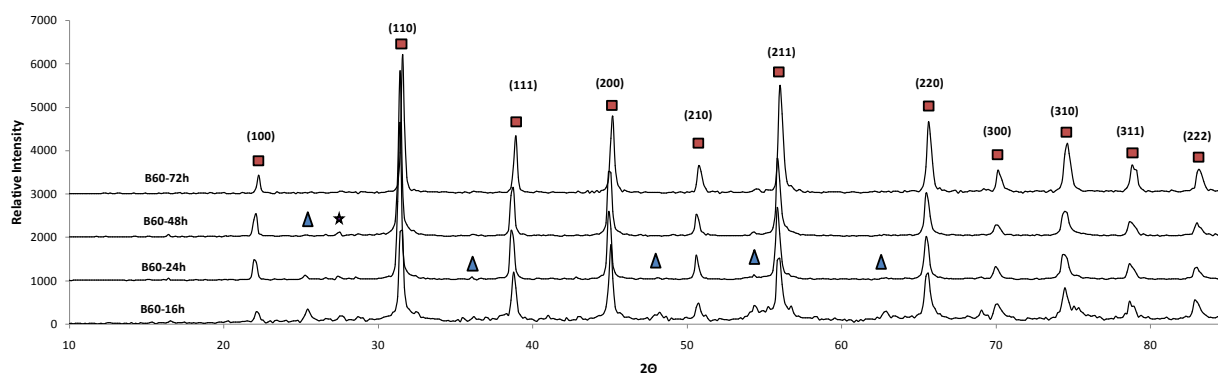
Figure 5-8   XRD patterns for BaTiO$_3$ samples obtained at 60 ˚C at different temperature for type-B titanium precursor

SEM images of the sample show monodispersed BaTiO$_3$ nanoparticles ~ 300-400 nm with uniform size distribution (Figure 5-9). The morphology of the particle is round which is very different from that of spindle like titania used as titanium precursor. A careful observation of high resolution images reveal some unreacted titania precursor can be found in final product which is as well observed in the XRD peaks of the sample. The nature of the BaTiO$_3$ particles obtained is look like weaved cotton balls with lot of strings like structure hanging out of the particles. This may be the case that in-situ or short range dissolution mechanism of TiO$_2$ has occurred in the formation of BaTiO$_3$ and formed BaTiO$_3$ particles on core TiO$_2$ have rolled into the shape of ball like spherical morphology.
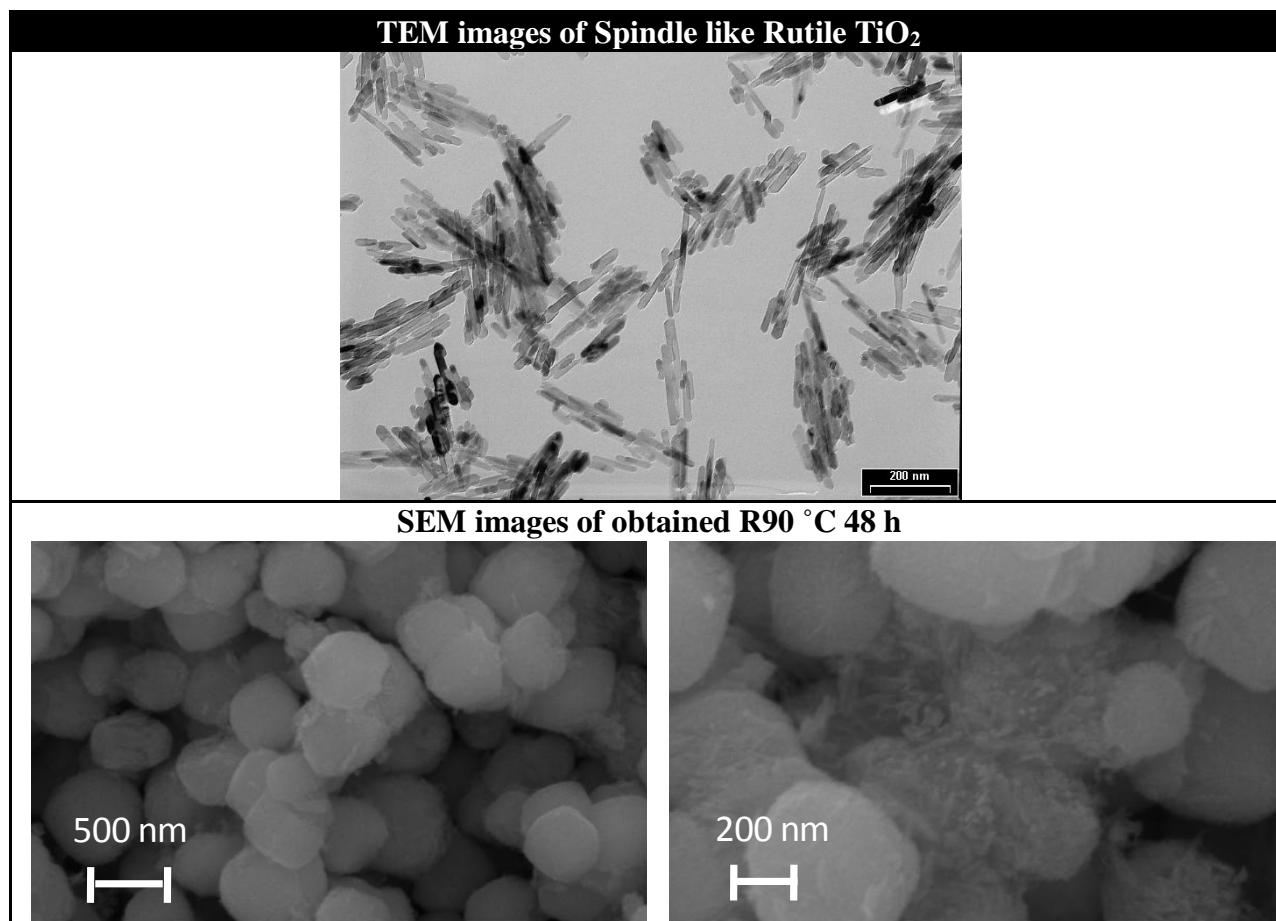
Figure 5-9   TEM image of spindle like TiO_2 and SEM images for resulted $BaTiO_3$ product after
reaction at 90 °C for 48 h

5.2 Solvothermal synthesis of barium titanate and tetragonal phase stabilization

$BaTiO_3$ powders were prepared by solvothermal method using barium hydroxide octahydrate and P25 Degussa TiO_2 (type-B titania). The XRD patterns for three samples shows the perovskite structure of $BaTiO_3$ with no impurity peaks, It is usually reported that Ba:Ti >1 results in stabilization of phase pure barium titanate [107, 108].

The XRD patterns of obtained $BaTiO_3$ for samples reacted at 185 °C for 6 days shows a clear split of (002) and (200), peaks at 44.85° 2θ and 45.38° 2θ. This splitting of the (200) reflection with the lower angle shoulder indexed at (002). is an indication of tetragonal form of $BaTiO_3$ [63, 114-116]. In the cubic form this peak remains unsplit. The overlapping double peak is obvious in the case of samples reacted at 235 °C for 1 day and at 185 °C for 2 days. The inset in Figure 5-10 shows the splitting peaks clearly. This indicates that stabilization of tetragonal phase

of $BaTiO_3$ is depending more on time than on temperature of reaction. The higher temperature i.e., 235°C for 1 day shows the least splitting effect for two peaks, while for 185 for 2 days the overlapping peaks show presence of some tetragonality in the sample and at 185 °C for 6 days resulted in clear split of peaks (002) and (200).

In all cases presence of eythanol (EtOH) helps to form tetragonal phase of $BaTiO_3$ as claimed by Kwon et al. [51]. The OH^- must play a vital role in this process since in its absence $BaTiO_3$ is not formed. The mechanism of formation of $BaTiO_3$ from Ba^{2+} and Ti species is not well understood. Two proposed mechanisms involve a condensation reaction of Ti $(OH)_6^{2-}$ with Ba^{2+} [40] and migration of Ba^{2+} into the TiO_2 structure with resulting breakage of TiOTi bands and incorporation of Ba^{2+} [41]. In the latter mechanism, the role of OH- could be to facilitate the hydrolysis of TiOTi bands.

The longer reaction time is as well another important factor for stabilization of tetragonal phase as founded by Dutta et al. [19] who were able to synthesis of tetragonal $BaTiO_3$ at 240°C for 1 week reaction time in the presence of chloride ions, whereas Wu et al. [47] prepared tetragonal $BaTiO_3$ hydrothermally using $Ba(OH)_2 \cdot H_2O$ and TiO_2 (anatase), in the absence of anions (Chloride ions), at 220 °C after several days reaction time.

The crystallite size of the sample EtOH-1 as calculated by Scherrer's formula is 65 nm. The particles size estimated using SEM images for the sample is around 120 nm. Earlier literature [8, 19, 43-46] reported that to stabilize tetragonal $BaTiO_3$, it is important that crystal sizes exceed 1 μm so as to accommodate the strains caused by the transformation from cubic to tetragonal structure. Few successful cases of tetragonal $BaTiO_3$ powder synthesis below 100 nm size have been reported recently [49-51, 63].

The crystallite size obtained for the sample EtOH-2 is about 58 nm, whereas for EtOH-3 it was found to be 56 nm. The increase in crystallite is apparent with longer reaction time. The EtOH-3 sample has approximately same size as for sample EtOH-2.
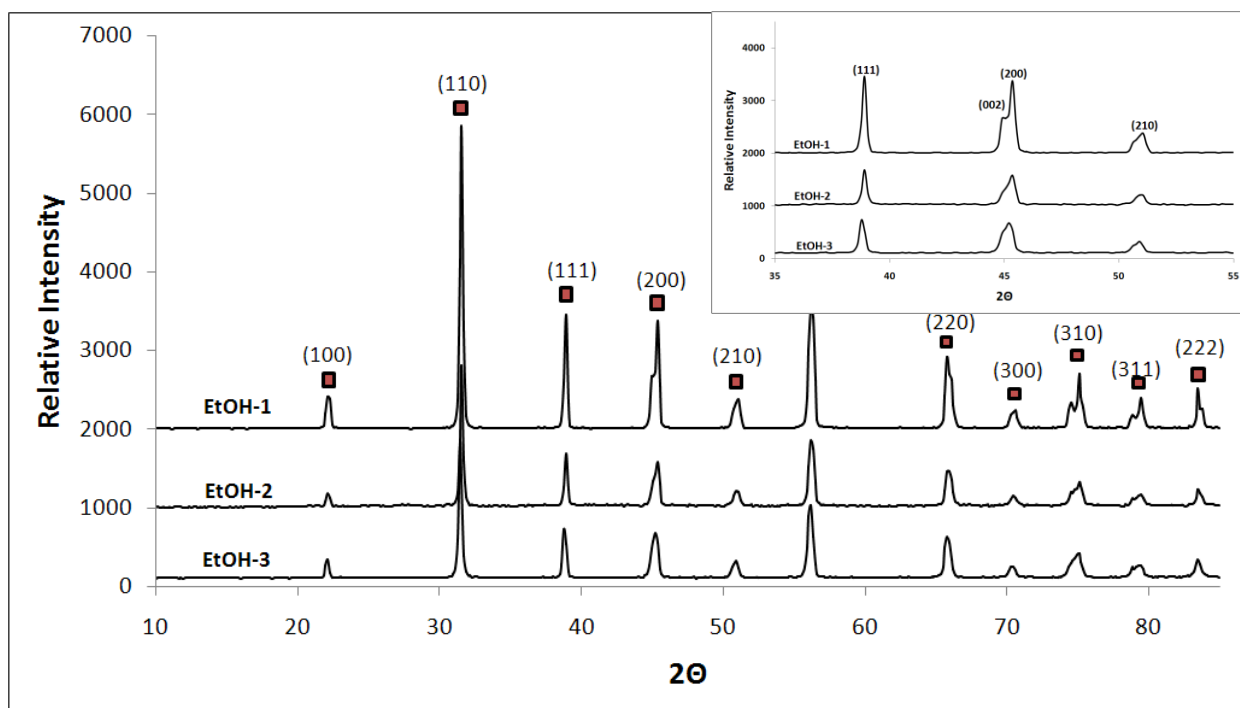
Figure 5-10 XRD patterns for BaTiO₃ samples obtained at 185 ˚C for 6 days (EtOH-1) and 2 days (EtOH-2) and at 235 ˚C after 1 day (EtOH-3). Inset shows the splits in peaks at 44.85˚ and 45.38˚
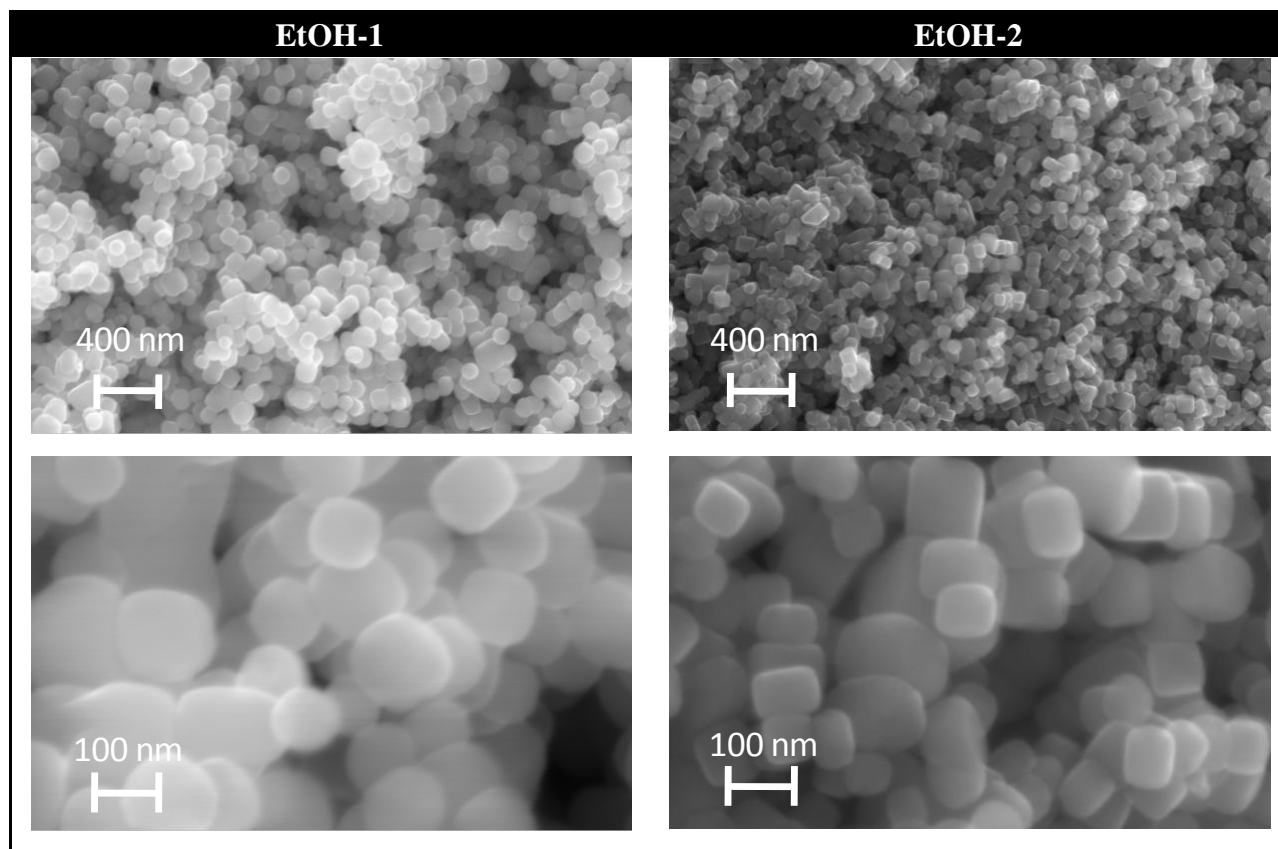
Figure 5-11 SEM images for BaTiO₃ obtained at 185 ˚C for 6 (EtOH-1) and 2 days (EtOH-2)

5.3 Dispersion of BaTiO₃ in PMMA

5.3.1 Dispersion of BaTiO₃ nanoparticles in different solvents

Shanefield [70], while describing the test for effectiveness of dispersion states that if a ceramic (particle size around 1 µm to 5 µm) which is well dispersed in a particular solvent is left to settle by force of gravity only, will form a fairly dense compact ceramic layer at the bottom of the vessel after a few hours. The solvent lubricates the particles well as they fall, letting them pack better. Therefore, the sedimentation height of the settled powder has been used as a quantitative measure of dispersion effectiveness [117, 118]. Finer particles (0.9 µm to 0.01 µm) will not settle at all if they are better dispersed, still it depend on how much the particle loading a dispersion can take.

Different solvents were tested and it was found that ethanol and ethanol plus acetone proved to be good dispersing solvents for BaTiO₃ due to their polar nature. The hydrogen bonding of OH groups on powder surface to polar ethanol help to disperse BaTiO₃ better in ethanol and ethanol acetone mixture.

5.3.2 Choice of solvent for dissolution of PMMA

Amorphous (glassy) polymers such as PMMA, polystyrene, and polycarbonate (PC) are commonly used for many engineering applications because of their excellent transparencies and relative ease of processing.

The polymer used here is PMMA in form of powder with bead size about 50 µm to 150 µm. PMMA was dissolved in different suitable solvents. Three different solvents were chosen depending on their boiling points and dielectric constants. tetrahydrofuran, a non polar solvent has a low boiling point of 69 ˚C and dielectric constant of 5.72. Toluene is a non polar solvent with a boiling point of 110 ˚C and a dielectric constant of 2.4, chlorbenzene has a boiling point of 130 ˚C and a dielectric constant of 5.6.

Solvents with different boiling points were used to observe the effect of layer formation due to different evaporation rate of each solvent. It is known that layer formation strongly depends on the boiling point of the dispersion solvent. If the boiling point is higher it is expected to result in thicker layers because of a lower evaporation rate.

It was observed that viscosity of PMMA (MW 35 000) solution differ in THF, toluene and MCB. The latter was found to be the most suitable solvent regarding the amount of PMMA it can dissolve. With THF 200 g/L was a workable viscous concentration where as MCB dissolved 400 g/L.

5.3.3 Vacuum dried BaTiO$_3$ nanopowders

BaTiO$_3$ powders obtained by hydrothermal are always covered by water. Water is highly polar and polarity is a major aspect of the van der Waals force. The hydrated surfaces of BaTiO$_3$ need to be dried so that dispersion of BaTiO$_3$ in PMMA can be achieved. Therefore the slurries obtained after hydrothermal synthesis were dried once under ambient conditions and than dried in vacuum furnace at 110 ˚C for 5 days and kept in a dessicator to avoid readsorption of moisture from atmosphere.The drying did not affect the powders particle size as observed by McNeal et al. [35]. Annealing BaTiO$_3$ particles at 500 ˚C for 3 h does not affect the particle size.

5.3.4 Ultrasonication as mode for deagglomeration of BaTiO$_3$ nanopowders

Markovic et al. [84] reported deagglomeration of BaTiO$_3$ powder (particle size of 1.4 µm), by high-intensity ultrasound irradiation for 10 min, 60 min, and 180 min ultrasonication times. It was found that the particles size of the BaTiO$_3$ powder was influenced by ultrasonic treatment, while its tetragonal structure was maintained. They proposed ultrasonic irradiation as an environmental-friendly, economical, and effective tool for the deagglomeration of barium titanate

In this work ultrasonic treatment is used to deagglomerate the strongly held nanoparticles in solvents and solvent with surfactants. As we have started from already dried BaTiO$_3$ powder, nanofillers are in form of agglomerated clusters (Figure 5-12). If these clusters of nanoparticles are added to polymer as it is, it would result in the agglomerated particles trapped in polymer. Therefore, before adding nanofiller to polymer; it is devised to achieve dispersion of nanofillers with the use of surfactants in a proper solvent and then adding the polymer into this dispersion.

Powders in agglomerate form before dispersion

EtOH-1   EtOH-2

B90-24 h   B150-24 h
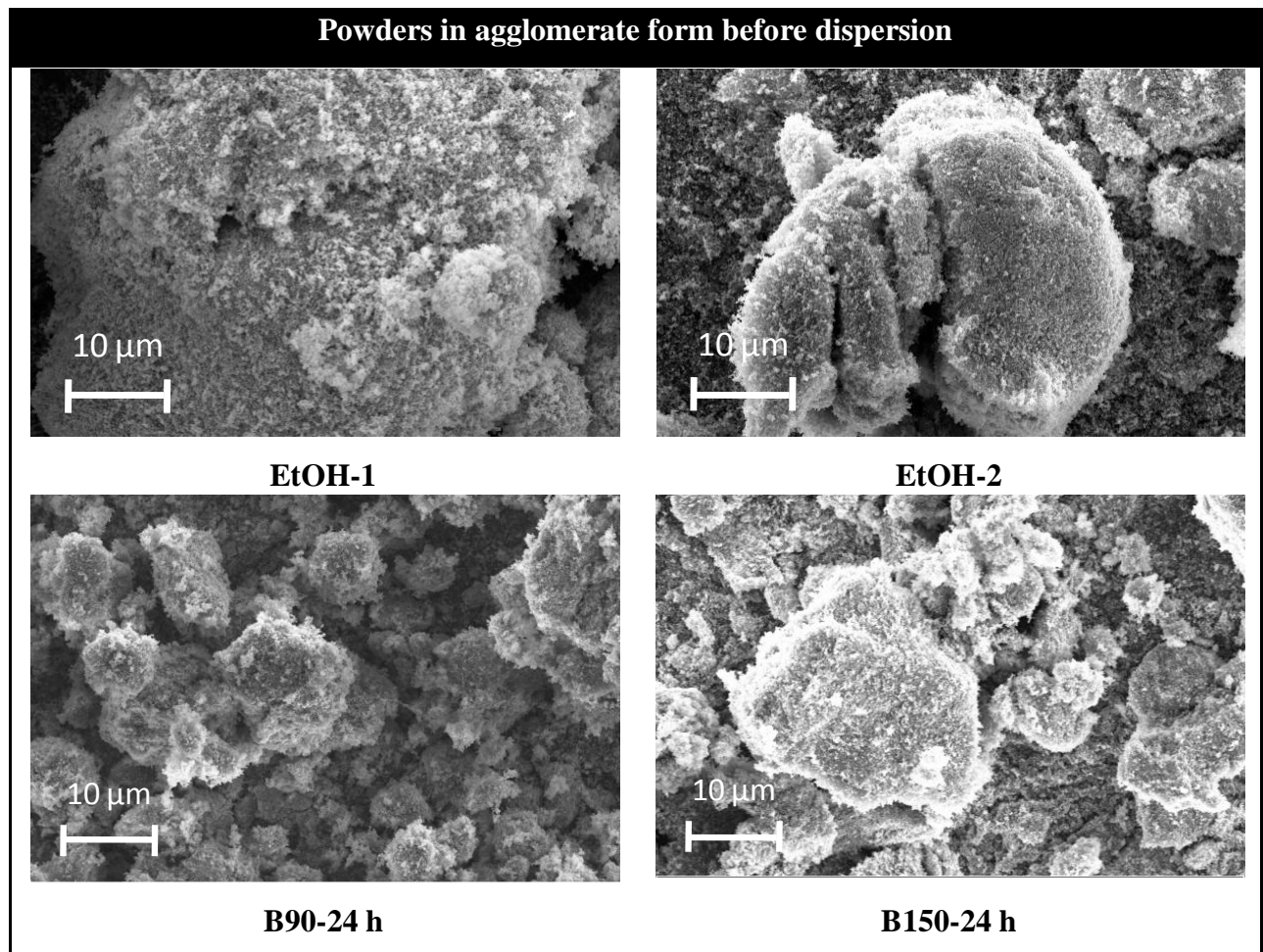
Figure 5-12   Agglomerated cluster of nanopowders of $BaTiO_3$ obtained via hydrothermal and solvothermal synthesis

5.3.5   Post functionalization of $BaTiO_3$ nanoparticles

The incorporation of nanoceramics with extremely large surface area into polymer influences their electrical and mechanical properties. The uniform dispersion of nanofillers in the polymer matrix is a general prerequisite to achieve the desired physical and electrical properties. The dispersion of nanoceramics in the polymer is rather poor due to their incompatibility with polymers and large surface to volume ratio. Due to van der Waals forces the agglomeration in the polymer starts occurring. Organic surfactants are often used to improve dispersion of these nanofillers in the polymer.

Mostly ceramic oxides are hydrophilic and proper modification of the powder surface with surfactants is needed. Due to their extremely large surface area these nanofillers tend to

agglomerate during the processing of the nanocomposite. Techniques like ultrasonic activation and surfactant addition are commonly used to disperse ceramic particles in polymers.

5.3.6   Choice of surfactant for dispersion

The non ionic surfactant proved to be better dispersants in case of $BaTiO_3$ / PMMA in THF, toluene or MCB. Since non ionic surfactants can not impart an electrostatic charge on the ceramic, they can only work as dispersants by steric hinderance [119]. In non polar solvents such as THF, toluene and MCB, the amount of ionization is possibly insufficient to stabilize dispersions. Therefore steric hinderance is the dominant stabilizing mechanism by which dispersants operate in very non polar systems [120, 121].

The surfactants are used to link the inorganic ceramic powders to organic matrix. The surfactants are usually amphipathic; having a polar head and a non polar tail. If a surfactant is working well for a certain powder, it means that the polar head of the surfactant has attached to hydrophilic surface or hydroxyl groups of the ceramic powder surface, while the non polar tail is hanging out in the nonpolar solvent. The solution of PMMA in nonpolar solvent, when added to such dispersion where surfactant is already attached to ceramic surface will readily get attached to outward lying tails of that surfactant. This results in the stable dispersion of ceramic fillers in the polymer matrix.

5.3.7   Varying surfactant to $BaTiO_3$ ratio

Viscosity is another measure of dispersion effectiveness, the lower the viscosity the better is the dispersion [70]. A monolayer of dispersant on powder surface is looked for to achieve the minimum viscosity of dispersion. Shanefield suggested that approximately 1 g of surfactant per 100 g of powder can be a rough estimate for obtaining such a monolayer, although the amount of surfactant needed may increase with the increase in srufce area of the powerd. Different authors reported different amounts of dispersants for obtaining minimum viscosity for their systems for example 0.8 % weight fraction was used by Karas et al. [122], 1.2 % weight fraction was used by Takabe et al. [123] and 1.7% weight fraction was used by Shanefield et al. [70] for dispersing half micron powders. These amounts depend on density of powder, surface area of powder and size of dispersant molecule etc.

In this work amount of surfactant was varied from 500 % (i.e., 5 times the weight of BaTiO₃) to 2.5 % weight of BaTiO₃. In excessive amounts of dispersants the films obtained showed haziness in SEM images. It is seen that dispersion was quite stable at low concentration of surfactant i.e., 2.5 % by weight of BaTiO₃.

5.3.8   Brij HLB observations

Moderate values of HLB (12 to 15) proved to be better dispersant in case of several brijs used for obtaining dispersions.

5.3.9   Copolymer as surfactant

Poly(methylmethacrylate–co-methacrylic acid) (PMMA-co-MA) MW 34 000 proved to be a good dispersant for the dispersion of BaTiO₃ in PMMA in all the solvents used here i.e., THF, toluene and MCB. Being a copolymer dispersant with both polar (methacrylic acid) and non polar parts (PMMA) it proved to be more effective than Brij. The hygroscopic nature of Brij was another disadvantage to use it as surfactant. The films obtained using Brij at different weight fractions caused the degradation of film, as lot of water absorption was observed in the samples. Whereas, PMMA-co-MA with polar head attached to OH groups of BaTiO₃ and non polar part sticks out into solvent to mechanically fend off other particles and in the presence of PMMA in solution attach to it.

5.3.10 Comparison of non ionic surfactants Brij and PMMA-co-MA

In an effort to observe effect of brij, PMMA-co-MA and their combination, it was found that presence of PMMA-co-MA led to better dispersion of BaTiO₃ in PMMA. This may be due to better joining of outward lying gropus of polymer surfactant to PMMA that improve the dispersion. The hygroscopic Brij in low or high concentrations lead to absorption of water in the films. The use of brij was avoided to obtain water free films, as it affects the mechanical stability of films.The use of PMMA-co-MA was preferred for obtaining dispersions in solvents.

5.3.11 Use of THF, toluene and MCB for obtaining dispersions for thin and thick films

THF proved to better solvent regarding the quality of films obtained, In case of toluene in thick films it was observed that at surface the BaTiO₃ started to get separated from the polymer

(Figure 4-45), therefore the use of toluene in thin films was mostly avoided. In case MCB , although a good solvent for PMMA yet SEM images at different concentrations did not show homogeneous distribution of $BaTiO_3$ in films (Figure 4-46). It might be that this solvent system has a different optimal filler loading of $BaTiO_3$ in PMMA which can yield better dispersion. As shown in the SEM images of 30 % volume fraction the films.

5.3.12 Low filler fraction

The films obtained using lower filler fractions of 1 % to 4 % showed film thickness in the range of 500 nm to 2600 nm when dip coating was used. The high weight percent of PMMA in THF and high dip and removal speed appear to be the cause of increase in film thickness for 1 % to 2 % filler fractions. While in case of 3 % and 4 % volume fraction the spin coating was use to obtain thin film on ITO. The film thickness remained between 500 nm to 1500 nm depending upon the spin speed on which film was obtained. The profilometery is preferred as a mode of layer thickness for all the samples as it agrees with the direct step height measurement by AFM. While the FIB analysis as well showed good agreement with layer thickness measurement by profilometery. The effect of lower filler loading on electrical properties is discussed in section 5.4.

5.3.13 High filler fraction

The use of higher filler fraction in PMMA led to agglomeration in films obtained. Yet the phase separation started occurring for samples at 24 % and 30 % volume fraction. The film thickness measured for different layers at filler fraction of 4 % to 30 % remained between 100 nm to 700 nm, whereas the roughness of films varied 45 nm to 130 nm.

Addition of alumina nanoparticles usually does not lead to enhancement of stiffness in PMMA. They act as toughening agent rather than reinforcing materials [106]. This fact lead to conclude that addition of nanoceramic will not lead to better mechanical stability of thin films; it would rather increase the brittleness of the films.

5.4 Electrical property measurements of thick / thin dielectric layer

Organic polymers have relatively low dielectric constant, usually within the range of 2 to 10. In exceptional cases the dielectric constant of a pure polymer exceeds 10 (e.g., for poly (vinylidene fluoride) $\varepsilon = 12$) [124]. The high dielectric materials like $BaTiO_3$, lead magnesium niobate–lead titanate (PMN–PT) have been used as fillers to improve the dielectric properties of different polymers [90, 91, 93, 95-97]. All except Kobayashi et al. [97] have reported the property of polymer composite with high-k dielectric fillers for thick films of few microns.

Kobayashi et al reported the dielectric property of thin film in the range of 150 nm to500 nm.

5.4.1 Electrical property measurements for thick films

Thick films with a wet thickness of 200 µm and 16.3 µm after drying and peeling off were tested for their electrical properties using an LCR meter. The film samples were held between copper electrodes of an area 1.76×10^{-4} m^2. These films were obtained using dispersions with 2 % volume fraction of $BaTiO_3$ in PMMA (MW 35 000) and 8.8 % weight fraction of PMMA in toluene. Effort to increase filler concentration to 4 % and 8 % volume fraction of $BaTiO_3$ in PMMA (MW 35 000) lead to cracking of the film while removing from the glass substrate.

An increase in the capacitance density was observed for the films loaded with cubic $BaTiO_3$ (particle size about 35 nm) at 2 % volume fraction. The dielectric constant has increased from 2.6 of PMMA films without any filler to 6.7 at 10 kHz. This increase in dielectric constant of the film can be attributed to better distribution of filler within the film as evident by the SEM images of the thick films (Figure 4-45). Agarwal et al. [89] reported dielectric constants of their composites varied between 30 and 74 depending on the dispersion and packing characteristics.

With tetragonal $BaTiO_3$ (particle size about 120 nm) increase in the dielectric constant of 7.5 at 100 kHz was observed for the same thickness films at 2 % volume fraction filler loading. This increase in the dielectric constant of film may be due to the increase in particle size and tetragonal phase of the $BaTiO_3$. The tetragonal phase of barium titanate has high dielectric constant due to its ferroelectric electric structure. Kobayashi et al. [97] reported an increase in the $BaTiO_3$ crystal size from 10.5 nm to 34.6 nm in the polyvinylidene fluoride (PVDF) film at a particle volume fraction of 30 % caused the dielectric constant of the film to increase from 20.1 to 31.8. The particle size and phase is often quoted to be responsible for the dielectric properties of $BaTiO_3$ [8, 90, 125].

5.4.2   Electrical property measurements for thin films

Thin film were prepared and characterized in two steps at lower filler loadings up till 4 % volume fraction of $BaTiO_3$ in PMMA and at higher filler loadings from 8 % to 30 % volume fraction. As it is usually reported that polymer nanocomposites achieve the desired physical and mechanical characteristic at low filler loading where the fillers are evenly distributed in the system [106]. The inclusion of these fillers at higher filler loadings lead to agglomeration of the nanoparticles to microparticle. Then there is no benefit of adding the nanofillers as they will be acting like micro fillers in the polymer and not result in the characteristics which are aimed at.

At lower filler concentrations the dielectric constant of 3.5 at 4 % volume fraction of cubic $BaTiO_3$ in PMMA was achieved whereas at the same filler loadings of tetragonal $BaTiO_3$ has resulted in an increase in dielectric constant to 4.7 or 5 as seen for two different sample. There is a low increase in dielectric constant for thin film at 4 % volume fraction when compared to thick films. Thick film can be thought to act bulk like where even lower loadings have contributed well to improve the dielectric constant of the film.

The increase of dielectric constant with tetragonal $BaTiO_3$ phase in case of thin and thick films supports the argument that increase in size and phase has an influence on the dielectric properties of the film. Kobayashi et al. [126] reported the preparation of polyvinylpyrrolidone (PVP) thin films containing barium titanate nanoparticles (av. size of approx. 7 nm and a tetragonal cryst. phase). The authors claimed to achieve capacitances of 12 nF/cm^2 to 157 nF/cm^2 with inclusion of tetragonal $BaTiO_3$.

The lower filler loading could not obtain the high dielectric constant of polymner nanocomposite thin film lead to increase the filler loading upto 30 % volume fraction $BaTiO_3$ in PMMA, while the weight fraction of PMMA was as well varied. It was observed the capacitance density of the films increased up till 35 nF/cm^2 at 30 % volume fraction. Kobayashi et al. [97] achieved $BaTiO_3$ in the range 10 nm to 36 nm particle size via alkoxide route and dispersed them in PVDF. They reported an increase in the dielectric constant from 12 (for PVDF) to 31 with $BaTiO_3$ (particle size approx. 36 nm) as filler in their polymer nancomposite thin films which correspond to capacitance density of 63 nF/cm^2.

The dielectric constant increased with increase in the filler loading as can be seen in Figure 5-14. A gradual increase of filler from 2 %, 4 %, 13 % and 20 % volume fraction of $BaTiO_3$ resulted in the increase of dielectric constant. Anomalous attitude is observed for the layers with 20 %, 24 %, and 30 % volume fraction of $BaTiO_3$ in PMMA. SEM images of the samples at 20 %, 24 %, and 30 % volume fraction reveals that the sample films have different distribution of $BaTiO_3$ within the film. The inhomogeneous distribution in higher filler loadings i.e., 24 and 30 volume fraction lead to poor dielectric properties in the films. Whereas a difference in the values of dielectric constant for 20 % volume fraction of $BaTiO_3$ sample shows that there is an optimum filler loading in PMMA which results in homogenous distribution of $BaTiO_3$ in the film. This lead to an increase in the dielectric values of the films. This work indicates that a 20 % volume fraction of $BaTiO_3$ in PMMA and a 3.25 % weight fraction of PMMA in THF resulted in achieving a dielectric of 9 at 10 kHz films with a film thickness of 271 nm.

Several quantitative rules of mixture models have been proposed for predictions of the dielectric constant of heterogeneous two-component systems on the basis of dielectric properties of the components [90, 92, 99]. However, while different models had been developed, usually little or no experimental evidence was provided to support the derived equations, and it turns out that most of these theoretical models fail when it comes to prediction of the dielectric constant of ferroelectric ceramic/polymer composites, where there is a large contrast between the dielectric constant of the components, especially at high filler contents [90, 124, 127]. In this work a general trend of increase in dielectric constant of polymer nanocomposite with filler loading is observed.
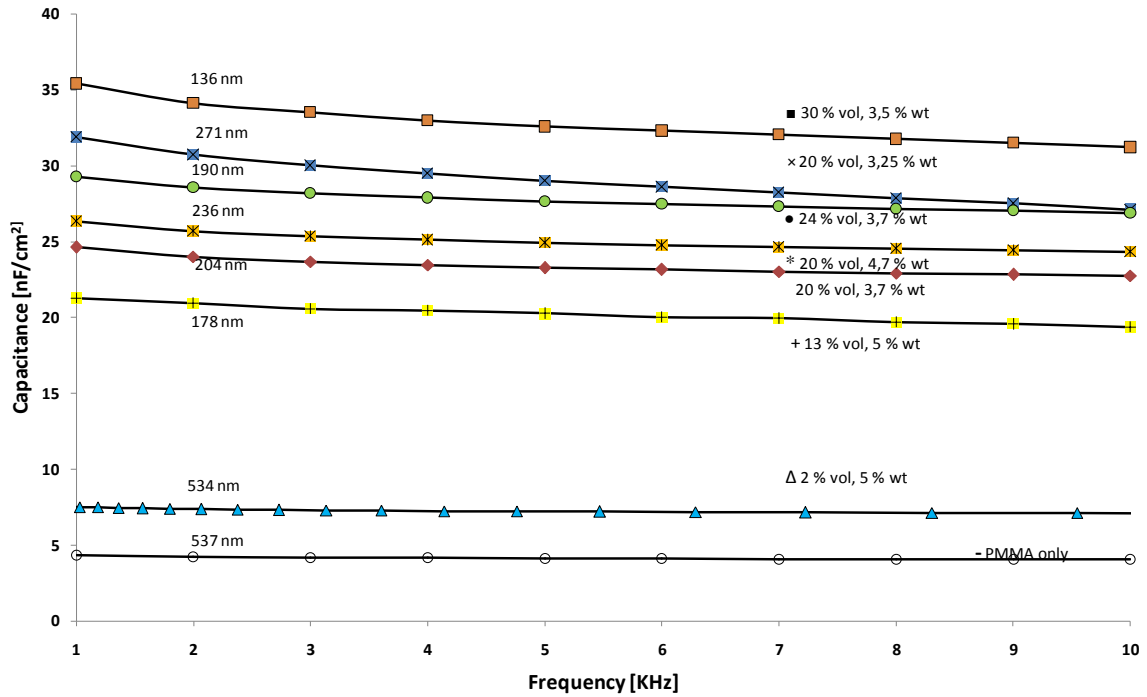
Figure 5-13   Capacitance density over a frequency range (1 kHz to 10kHz) for thin films (thickness is shown over respective curve) loaded with cubic $BaTiO_3$ as filler, '% vol' stands for volume fraction of $BaTiO_3$ in PMMA and '% wt' for weight fraction of PMMA in solvent used to obtain dispersion
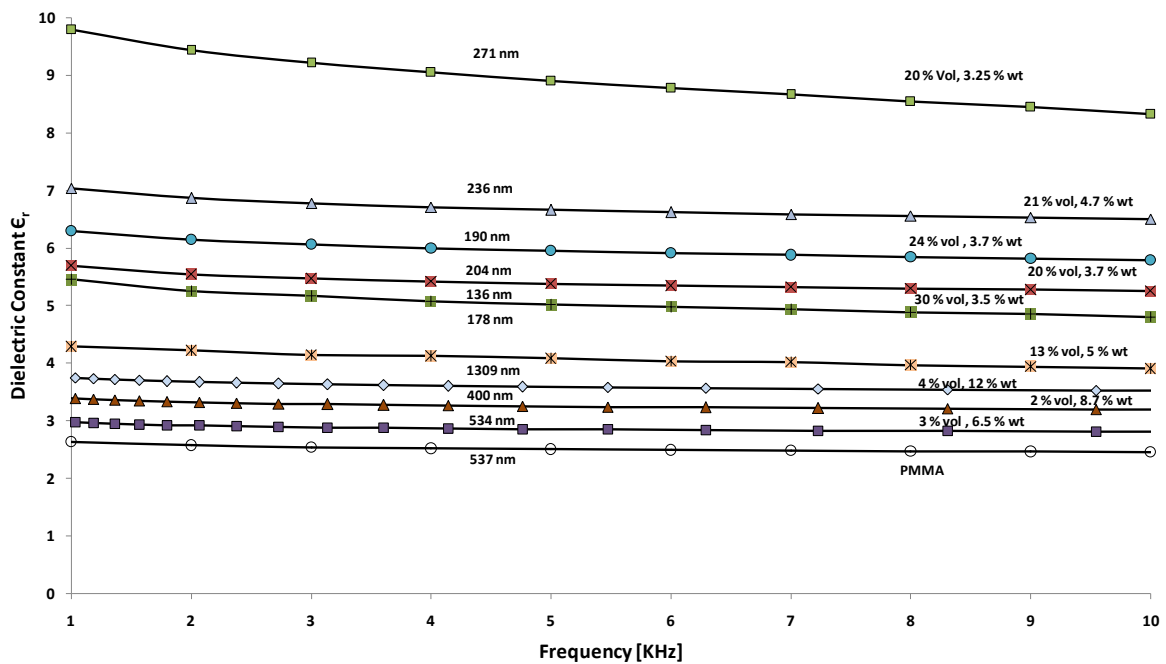

Figure 5-14   Dielectric constant over a frequency range for thin films (thickness is shown over respective curve) loaded with cubic $BaTiO_3$ as filler, '% vol' stands for volume fraction of $BaTiO_3$ in PMMA and '% wt' for weight fraction of PMMA in solvent used to obtain dispersion

6   Conclusion

A study is conducted to achieve thin dielectric films (approx. 100 nm to 500 nm) for organic field effect transistors (oFETs) by a ceramic polymer nanocomposite development method. Polymer nanocomposite by definition requires the incorporation of nanometeric particles in a polymer matrix. In this work high-k dielectric material $BaTiO_3$ is synthesised via hydrothermal and solvothermal route. Nanoparticles of $BaTiO_3$ are synthesised via these routes and characterised for their perovskite structure, size and morphology. The nanoparticles usually have high surface energies, which are to be reduced by surface functionalization. The post functionalization of already obtained $BaTiO_3$ nanofillers helped to achieve better dispersions in polymer. Poly(methylmethacrylate) (PMMA) is used as polymer matrix. PMMA has a low dielectric constant and is used as a gate dielectric in oFETs. The idea was to improve the dielectric constant of PMMA by imbedding the high k dielectric nanomaterial like $BaTiO_3$.

To achieve thin films it is necessary that the fillers in the polymer should be in nanometer regime and have good dielectric properties, as final properties of the polymer nanocomposite strongly depend on the two components used to obtain it. The methods of hydrothermal and solvothermal synthesis of $BaTiO_3$ is adopted to obtain the nanoparticle in lower limit of nanometer range. The tetragonal phase of $BaTiO_3$ is famous for better dielectric characteristics. Tetragonal $BaTiO_3$ powders are synthesised via solvothermal route. The powders synthesised in water of course have higher water and hydroxyl group contents. Vacuum heat treatment helped to remove excess water and OH groups from particle surfaces.

6.1   Hydrothermal synthesis of $BaTiO_3$ using various TiO_2 precursors

A systematic study for the synthesis of $BaTiO_3$ was carried out for two different titania precursors TiO_2 Tronox (average particle size 120 nm, anatase phase) and TiO_2 P25 Degussa (average particle size 25 nm, 70 % anatase and 30 % rutile phase). $Ba(OH)_2 \cdot 8H_2O$ was used as barium precursor. The reaction of precursors under alkaline condition (pH 9 to 10) was studied at 60 ˚C, 90 ˚C, 120 ˚C and 150 ˚C for reaction time 16 h, 24 h, and 48 h.

The characterization of obtained $BaTiO_3$ particles using two titania precursors gave insight into formation mechanism and effect of temperature, time, and particle size of titania precursor on the synthesis of $BaTiO_3$. It was observed that a fine grained TiO_2 precursor reacts faster due to large

surface area for reaction of Ba with TiO_2. Higher reaction temperature and longer reaction time helped to complete crystallization of $BaTiO_3$ by hydrothermal route. The crystallite size of $BaTiO_3$ calculated from XRD data is observed to decrease at higher temperature, while no trends regarding the dependence of crystallite size on time can be predicted in this study.

Samples synthesized at low temperature shows unreacted core of TiO_2 in $BaTiO_3$, while size and morphology of $BaTiO_3$ depend on the initial titania precursor. This supports the idea of in-situ transformation mechanism or short range dissolution-precipitation to be responsible for the formation of $BaTiO_3$ from particulate precursors.

In case of TiO_2 Tronox precursor porous particles are evident at 150 ˚C, whereas compact particle are obtained at 150 ˚C using TiO_2 P25 Degussa precursor.

Use of spindle like TiO_2 (aspect ratio of 0.2, with the width being approx. 20 nm) to investigate the effect of particle size and morphology reveals that obtained $BaTiO_3$ has very different size and morphology when compared to $BaTiO_3$ using other titania precursors, namely Tronox and P25 Degussa. In case of Tronox and P25 Degussa the final product resemble to initial titania precursor in morphology whereas for spindle like titania it is very different. The crystallite size of obtained $BaTiO_3$ was around 85 nm calculated by Scherrer's equation. The crystallization after dissolution of TiO_2 must be responsible for the crystal growth up to 300 nm to 400 nm particle.

6.2 Solvothermal synthesis of $BaTiO_3$

For solvothermal synthesis ethanol and water were used as solvent in equal ratio. A barium to titanium ratio equal to two results in stabilization of a phase pure $BaTiO_3$ product. High reaction temperature and longer reaction time favours tetragonal phase stability in solvothermal synthesis of $BaTiO_3$. Morphology of the final product differs from that of the titania precursor shows dissolution precipitation mechanism to be the evident phenomena in crystallization of $BaTiO_3$ via solvothermal route. Longer reaction time caused an increase in particle size while morphology tends from cubic at 185 ˚C after 2 days to round for sample obtained at 185 ˚C after 6 days.

6.3   Dispersion of $BaTiO_3$ in PMMA

Dispersion of $BaTiO_3$ in PMMA dissolved in THF, toluene or chlorobenzene (MCB) is achieved using a polymeric surface active agent: Poly(methylmethacrylate-co-methacrylic acid) MW 34 000.The weak interactions are responsible for the attachment of methacrylic acid groups to the surface hydroxyl groups of hydrothermally or solvothermally synthesised $BaTiO_3$. The presence of PMMA in the surfactant as well helped to link surface functionalized $BaTiO_3$ to polymer matrix.

A self assembly of $BaTiO_3$ particles is evident in thin films obtained using dip coating at 16 % volume fraction when PMMA in THF was as low as 0.56 % by weight. Higher filler loading i.e., 24 % and 30 % volume fraction in the dispersions resulted in agglomeration of nanoparticles.

6.4   Electrical properties of thick and thin films

At low filler loading i.e., 2 % volume fraction of $BaTiO_3$ and 8.8 % weight PMMA in toluene an increase in the dielectric constant of the PMMA is observed in thick films of 16.3 µm. A dielectric constant of 6.5 is achieved for cubic $BaTiO_3$ (average particle size approx. 35 nm) in host matrix of dielectric constant of 2.6 while inclusion of tetragonal $BaTiO_3$ resulted in further increase to 7.4.

In thin films at lower loadings 4 % a dielectric constant of 4 and 5 is attained by inclusion of cubic and tetragonal $BaTiO_3$ respectively. Here as well an increase in dielectric constant is evident with larger of $BaTiO_3$ and tetragonal phase of $BaTiO_3$.

Thin films obtained using higher filler loadings resulted in increase in the capacitance density and dielectric constant up to 20 % volume fraction. With further increase in filler contents in dispersion thin layers obtained using spin on technique resulted in excessive agglomeration and phase separation of filler and matrix. This caused a decrease in the dielectric constant of the film with filler loading in PMMA when THF was used as solvent. For 20 % volume fraction an optimal weight percent PMMA in THF was found to be 3 % to 3.5 %. The dielectric constant at this optimal filler loading and weight percent of PMMA attained a value of 9 and a capacitance density of 32 nF/cm^2 at 10 kHz. The surface roughness of films using spin on technique was as low as 50 nm.

7 References

1. Dimitrakopoulos, C.D., et al., *Low-Voltage Organic Transistors on Plastic Comprising High-Dielectric Constant Gate Insulators.* Science, 1999 **283**: p. 822-24.

2. Horowitz, G., *Organic Field-Effect Transistors.* Advanced Materials, 1998. **10**(5): p. 365-77.

3. Katz, H.E., *Organic molecular solids as thin film transistor semiconductors.* Journal of Material Chemistry, 1997. **7**(3): p. 369–376.

4. Kato, Y., et al., *High mobility of pentacene field-effect transistors with polyimide gate dielectric layers.* Applied Physics Letters, 2004. **84**(19): p. 3789-91.

5. Klauk, H., et al., *High-mobility polymer gate dielectric pentacene thin film transistors.* Journal of Applied Physics, 2002. **92**(9).

6. Horowitz, G., *Theory of the organic field-effect transistor.* Synthetic Metals 1999. **101**: p. 401-04.

7. Stadlober, B., et al., *High-mobility pentacene organic field-effect transistors with a high-dielectric-constant fluorinated polymer film gate dielectric* Applied Physics Letters, 2005. **86**: p. 242902-1.

8. Arlt, G., D. Hennings, and G. de With, *Dielectric properties of fine grained barium titanate ceramics.* Journal of Applied Physics 1985. **58**(4): p. 1619-1625.

9. Yoon, D.-H. and B.I. Lee, *$BaTiO_3$ properties and powder characteristics for ceramic capacitors.* Journal of Ceramic Processing Research. , 2002. **3**(2): p. 41-47.

10. Dickson, J.G., L. Katz, and R. Ward, *Compounds with the hexagonal barium titanate structure.* Journal of the American Chemical Society, 1961. **83** p. 3026-29.

11. Clarke, R., *Phase Transition Studies of Pure and Flux-Grown Barium Titanate Crystals.* Journal of Applied Crystallography, 1976. **9** p. 335-338.

12. Merz, W.J., *The electric and optical behavior of barium titanate single-domain crystals.* Physical Review, 1949. **76**(8): p. 1221-1225.

13. Uchino, K., E. Sadanaga, and T. Hirose, *Dependence of the crystal structure on particle size in barium titanate.* Journal of the American Ceramic Society, 1989. **72**(8): p. 1555-58.

14. Kyoichi Kinoshita and A. Yamaji, *Grain-size effects on dielectric properties in barium titanate ceramics.* Journal of Applied Physics, 1976. **47**(1): p. 371-73.

15.   Lines, M.E. and A.M. Glass, *Principles and Applications of Ferroelectric and Related Materials*. 1997, Oxford: Clanrendon Press.

16.   Eckert, J.O.J., et al., *Kinetics and Mechanisms of Hydrothermal Synthesis of Barium Titanate*. Journal of the American Ceramic Society, 1996. **79**(11): p. 2929-2939.

17.   Lencka, M.M. and R.E. Riman, *Thermodynamic Modeling of Hydrothermal Synthesis of Ceramic Powders*. Chemistry of Materials, 1993. **5**: p. 61-70.

18.   Lencka, M.M. and R.E. Riman, *Thermodynamics of the Hydrothermal Synthesis of Calcium Titanate with Reference to Other Alkaline-Earth Titanates*. Chemistry of Materials 1995. **7**: p. 18-25.

19.   Dutta, P.K. and J.R. Gregg, *Hydrothermal Synthesis of Tetragonal Barium Titanate*. Chemistry of Materials, 1992. **4**: p. 843-846.

20.   Dawson, D.W., *Hydrothermal synthesis of advanced ceramic powders.* . Ceramic Bulletin, 1988. **67**(10): p. 1673-1678.

21.   Komarneni, S., et al., *Hydrothermal route to ultrafine powders utilizing single and diphasic gels*. Advanced Ceramic Materials, 1986. **1**(1): p. 87-92.

22.   Christensen, A.N., *Hydrothermal preparation of barium titanate by transport reactions*. Acta Chemica Scandinavica, 1970. **24**: p. 2447-2452.

23.   Vivekanandan, R. and T.R.N. Kutty, *Hydrothermal synthesis of Ba(Ti, Sn)O$_3$ fine powders and dielectric properties of the corresponding ceramics*. Ceramic International, 1988. **14**: p. 207-216.

24.   Hennings, D., G. Rosenstein, and H. Schreinemacher, *Hydrothermal preparation of barium titanate from barium-titanium acetate gel precursors*. Journal of the European Ceramic Society, 1991. **8**: p. 107-115.

25.   La Mer, V.K. and R.H. Dinegar, *Theory, production and mechanism of formation of monodispersed hydrosols*. Journal of the American Chemical Society, 1950. **72**(11): p. 4847-4854.

26.   Kumazawa, H., S. Annen, and E. Sada, *Hydrothermal synthesis of barium titanate fine particles from amorphous or crystalline titania*. Journal of Material Science, 1995. **30**: p. 4740-4744.

27.   Wada, S., T. Suzuki, and T. Noma, *Preparation of barium titanate fine particles by hydrothermal method and their characterization*. Journal of the Ceramic Society of Japan, 1995. **103**(Dec): p. 1220-7.

28. Urek, S. and M. Drofenik, *The Hydrothermal Synthesis of BaTiO₃ Fine Particles using Hydroxide-Alkoxide Precursors.* Journal of the European Ceramic Society, 1998. **18**: p. 279-286.

29. Hu, M., et al., *Wet-chemical synthesis of monodispersed barium titanate particles-hydrothermal conversion of TiO₂ microspheres to nanocrystalline BaTiO₃.* Powder Technology, 2000. **110**: p. 2-14.

30. Chen, K.-Y. and Y.-W. Chen, *Preparation of monodispersed spherical barium titanate particles.* Journal of Materials Science, 2005. **40**(4): p. 991-998.

31. Moon, J., et al., *Phase development of barium titanate from chemically modified amorphous titanium (hydrous) oxide precursor.* Journal of the European Ceramic Society 2002. **22**: p. 809–815.

32. Hertl, W., *Kinetics of Barium Titanate Synthesis.* Journal of the American Ceramic Society, 1988. **71**(10): p. 879-883.

33. Johnson, W.A. and R.F. Mehl, *Reaction Kinetics in Processes of Nucleation and Growth.* Trans. Am. Inst. Min. Metall. Eng., 1939. **35**: p. 416-458.

34. Avrami, M., *Kinetics of Phase Change I: General Theory.* Journal of Chemical Physics 1939. **7**(10): p. 1103-12.

35. McNeal, M.P., S.-J. Jang, and R.E. Newnham, *The effect of grain and particle size on the microwave properties of barium titanate (BaTiO₃).* Journal of Applied Physics, 1998. **83**(6): p. 3288-3297.

36. Kingery, W.D., H.K. Bowen, and D.R. Uhlmann, *Introduction to Ceramics.* 2nd edition ed. 1976,, New York,: Wiley,. 969.

37. Jaffe, B., W.R. Cook, and H. Jaffe, *Piezoelectric Ceramics.* 1971, London and New York: Academic Press. 54.

38. Hench, L.L. and J.K. West, *Principles of Electronic Ceramics.* 1990, New York: Wiley. 246.

39. Kajiyoshi, K., N. Ishizawa, and M. Yoshimura, *Preparation of tetragonal barium titanate thin film on titanium metal substrate by hydrothermal method.* Journal of the American Ceramic Society, 1991. **74**(2): p. 369-74.

40. Vivekanandan, R., S. Phillip, and T.R.N. Kutty, Materials Research Bulletin, 1986. **22**: p. 99.

41. Kiss, K., et al., *Ferroelectrics of Ultrafine Particle Size: I, Synthesis of Titanate Powders of Ultrafine Particle Size.* Journal of the American Ceramic Society, 1966. **49**: p. 291-95.

42.   Fukai, K., et al., *Preparation and properties of uniform fine perovskite powders by hydrothermal synthesis.* Ceramics International, 1990. **16**(5): p. 285-90.

43.   Arlt, G., *The role of domain walls on the dielectric, elastic and piezoelectric properties of ferroelectric ceramics.* Ferroelectrics, 1987. **76**(3-4): p. 451-8.

44.   Kanata, T., T. Yoshikawa, and K. Kubota, *Grain-size effects on dielectric phase transition of barium titanate ceramics.* Solid State Communications, 1987. **62**(11): p. 765-7.

45.   Buessem, W.R., L.E. Cross, and A.K. Goswami, *Phenomenological theory of high permittivity in fine-grained barium titanate.* Journal of the American Ceramic Society, 1966. **49**(1): p. 33-6.

46.   Bell, A.J., A.J. Moulson, and L.E. Cross, *The effect of grain size on the permittivity of barium titanate(IV)* Ferroelectrics, 1984. **54**: p. 487-90.

47.   Wu, M., et al., *Hydrothermal Synthesis of Tetragonal Barium Titanate from Barium Hydroxide and Titanium Dioxide under Moderate conditions.* Journal of the American Ceramic Society, 1999. **82**(11): p. 3254-56.

48.   Xu, H., L. Gao, and J. Guo, *Hydrothermal Synthesis of tetragonal Barium titanate from Barium Chloride and Titanium Tetrachloride under Moderate conditions.* Journal of the American Ceramic Society, 2002. **85**(3): p. 727-29.

49.   Zhang, M.S., et al., *Study of structural and photoluminescent properties in barium titanate nanocrystals synthesized by hydrothermal process.* Solid State Communications, 2001. **119**: p. 659-63.

50.   Xu, H. and L. Gao, *Tetragonal nanocrystalline barium titanate powder: preparation, characterization, and dielectric properties.* Journal of the American Ceramic Society, 2003. **86**(1): p. 203-205.

51.   Kwon, S.-G., et al., *Solvothermally Synthesized Tetragonal Barium Titanate Powders using H2O/EtOH solvent.* Journal of the European Ceramic Society 2006. **26**: p. 1401-1404.

52.   Chattopadhyay, S.A., et al., *Size induced diffuse phase transition in the nanocrystalline ferroelectric PbTiO$_3$.* Physical Review B, 1995. **52**: p. 13177.

53.   Hsaing, H.I. and F.S. Yen, *Effect of crystallite size on the ferroelectric domain growth of ultrafine BaTiO$_3$ powders.* Journal of the American Ceramic Society, 1996. **79**: p. 1053.

54.   Begg, B.D., E.R. Vance, and J. Nowotny, *Effect of particle size on the room-temperature crystal structure of barium titanate.* Journal of the American Ceramic Society, 1994. **77**(12): p. 3186-92.

55. Kobayashi, Y., et al., *Size Effect on Crystal Structures of Barium Titanate Nanoparticles Prepared by a Sol-Gel Method.* Journal of Sol-Gel Science and Technology 2004. **29**: p. 49–55.

56. Niepce, J.C., *Surfaces and Interfaces of Ceramic Materials.* 1989, Dordrecht, Netherlands: Kluwer Academic Publishers. 512.

57. Vivekanandan, R. and T.R.N. Kutty, *Characterization of barium titanate fine powders formed from hydrothermal crystallization.* . Powder Technology, 1989. **57**(3): p. 181-92.

58. Takeuchi, T., et al., *Thickness of Cubic Surface Phase on Barium Titanate Single-Crystalline Grains.* Journal of the American Ceramic Society, 1994. **77**(6): p. 1665-68.

59. Hennings, D. and B.S. Schreinemacher, *Characterization of hydrothermal barium titanate.* Journal of the European Ceramic Society, 1992. **9**(1): p. 41-46.

60. Lobo, R., D. Mohallem, and R. Moreira, Journal of the American Ceramic Society, 1995. **78**(5): p. 1343-46.

61. Li, X. and W. Shih, Journal of the American Ceramic Society, 1997. **80**(11): p. 2844-52.

62. Jiang, B., et al., Physica B, 2000. **291**: p. 203-12.

63. Lu, S.W., et al., *Hydrothermal synthesis and structural characterization of BaTiO$_3$ nanocrystals.* Journal of Crystal Growth 2000. **219**: p. 269-276.

64. Kniekamp, H. and W. Heywang, *Depolarization effects in polycrystalline barium titanate.* Zeitschrift fuer Angewandte Physik 1954. **6**: p. 385-90.

65. Jonker, G.H. and W. Noorlander, *Science of Ceramics*, ed. G.H. Stewart. 1962, London and New York: Academic Press. 255.

66. Sharma, N.C. and E.R. McCartney, *Dielectric properties of pure barium titanate as a function of grain size.* Journal of the Australian Ceramic Society 1974. **10**(1): p. 16-20.

67. Kinoshita, K. and A. Yamaji, *Grain-size effects on dielectric properties in barium titanate ceramics.* Journal of Applied Physics, 1976. **47**(1): p. 371-73.

68. Arlt, G., *The influence of microstructure on the properties of ferroelectric ceramics.* Ferroelectrics, 1990. **104**: p. 217-227.

69. Frey, M.H. and D.A. Payne, *Grain-size effect on structure and phase transformations for barium titanate.* Physical Review B, 1996. **54**(5): p. 3158-68.

70. Shanefield, J.D., *Organic Addititives and Ceramic Processing: With Applications in Powder Metallurgy, Ink, and Paint*. 1 ed. 1995, Boston: Kluwer Academic Publishers.

71. Puigdollers, J., et al., *Pentacene thin-film transistors with polymeric gate dielectric.* Organic Electronics, 2004. **5**: p. 67-71.

72.   Ash, B.J., A. Eitan, and L.S. Schalder, *Polymer nano composites with particle and carbon nanotube fillers*, in *Dekker Encyclopedia of nanoscience and nanotechnology*, J.A. Schwarz, C.I. Contescu, and K. Putyera, Editors. 2004, Marcel Dekkar: New York, Basel. p. 2917-30.

73.   Caseri, W., *Nanocomposites of polymers and metals or semiconductors: Historical background and optical properties.* Macromolecular Rapid Communications, 2000. **21**(11): p. 705–722.

74.   Schubert, U. and N. Husing, *Synthesis of Inorganic Materials*. 2nd ed. 2005, Weinheim, Germany: Wiley-VCH Verlag GmbH & Co. 409.

75.   Siegel, R.W., *Nanophase Materials*, in *Encyclopedia of Applied Physics*, G.L. Trigg, Editor. 1994, VCH Publishing: Weinheim.

76.   Hergeth, W.-D., et al., *Polymerization in the presence of seeds. Part IV: Emulsion polymers containing inorganic filler particles.* Polymer, 1989. **30**(2): p. 254-258.

77.   Ding, W., et al., *Direct Observation of Polymer Sheathing in Carbon Nanotube-Polycarbonate Composites.* Nano Letters 2003. **3**(11): p. 1593-1597.

78.   Mackay, M.E., et al., *General Strategies for Nanoparticle Dispersion.* Science, 2006. **311**: p. 1740-43.

79.   Hooper, J.B. and K.S. Schweizer, *Theory of Phase Separation in Polymer Nanocomposites.* Macromolecules, 2006. **39**: p. 5133-5142.

80.   Sharma, S., et al., *Control of Dewetting Dynamics by Adding Nanoparticle Fillers.* Nano Letters, the American Chemical Society, 2001. **1**(10): p. 511-514.

81.   Krishnamoorti, R., *Strategies for dispersing nanoparticles in polymers.* Materials Research Bulletin, 2007. **32**: p. 341-347.

82.   Everett, D.H., *Basic principles of colloid science*. 1988, Whitstable, Kent, UK.: The Royal Society of Chemistry, print.

83.   Horn, R.G., *Ceramic Processing*. 1st ed, ed. R.A. Terpstra, P.P.A.C. Pex, and A.H. de Vries. 1995, London: Chapman and Hall.

84.   Markovic, S., et al., *Ultrasonic de-agglomeration of barium titanate powder.* Ultrasonics Sonochemistry, 2008. **15**(1): p. 16-20.

85.   Usuki, A., et al., *Three-Dimensional Observation of Structure and Morphology in Nylon-6 / Clay Nanocomposite.* Nano Letters, 2001. **1**(5): p. 271-272.

86.   Holmberg, K., et al., *Surfactants and Polymers in Aqueous Solutions*. 2nd ed. 2002, West Sussex, England: John Wiley & Sons Ltd. 527.

87.   Goodwin, J.W., *Colloids and Interfaces with Surfactants and Polymers– An Introduction*. 2004: John Wiley & Sons Ltd. 281.

88.   Ogitani, S., S.A. Allen, and P. Kohl. *An investigation of the fundamental factors influencing the permittivity of composite for embedded capacitor* in *Proceedings of the IEEE 49th Electronic Components and Technology Conference*. 1999.

89.   Agarwal, V., et al. *Improvements and recent advances in nanocomposite capacitors using a colloidal technique*. in *Proceedings of the IEEE 48th Electronic Components and Technology Conference*. 1998.

90.   Windlass, H., et al., *Colloidal Processing of Polymer Ceramic Nanocomposite Integral Capacitors.* IEEE Transactions on Electronics Packaging Manufacturing, 2003. **26**(2): p. 100-105.

91.   Khastgir, D. and K. Adachi, *Piezoelectric and dielectric properties of siloxane elastomers filled with barium titanate.* Journal of Polymer Science: Part B: Polymer Physics, 1999. **37**: p. 3065–3070.

92.   Bruggemann, D.A.G., *Dielektrizitätskonstanten und Leitfähigkeiten der Mischkörper aus isotropen Substanzen.* Annalen der Physik (Leipzig), 1935. **24**(5): p. 636.

93.   Rao, Y., J. Qu, and T. Marinis. *A Precise Numerical Prediction of Effective Dielectric Constant for Polymer-Ceramic Composite Based on Effective Medium Theory*. in *IEEE Transactions on Composite and Packaging Technologies*. 2000.

94.   Bhattacharya, S. and R.R. Tummala, *Integral passives for next generation of electronic packaging: application of epoxy/ceramic as integral capacitors.* Microelectronics Journal, 2001. **32**: p. 11-19.

95.   Popielarz, R., et al., *Dielectric Properties of Polymer/Ferroelectric Ceramic Composites from 100 Hz to 10 GHz.* Macromolecules, 2001. **34**: p. 5910-15.

96.   Vrejoiu, I., et al., *Flexible Ceramic-Polymer composites films with temperature-insensitive and tunable dielectric permitivity.* Applied Physics A 2002. **74**: p. 407-409.

97.   Kobayashi, Y., et al., *Fabrication and dielectric properties of the $BaTiO_3$–polymer nano-composite thin films.* Journal of the European Ceramic Society, 2007. **28**(1): p. 117-122.

98.   Kymakis, E. and G.A.J. Amaratunga, *Optical properties of polymer-nanotube composites.* Synthetic Metals 142 (2004) 161–167, 2004. **142**: p. 161–167.

99.   Garnett, M.J.C. and J. Larmor, *Colours in metal glasses and metallic films* Royal society (GB). Philosophical transactions of the Royal society of London . Series A, Mathematical and physical sciences, 1904. **203**: p. 385.

100. Gregor, L.V., *Polymer Dielectric Films.* IBM Journal 1968.

101.   Whitehead, S., *Dielectric Breakdown of Solids*. 1951, Oxford: Clarendon Press

102.   O'Dwyer, J.J., *Theory of Dielectric Breakdown of Solids*. 1964, Oxford: Clarendon Press.

103.   Ku, H.Y. and F.G. Ullman, *Capacitance of Thin Dielectric Structures*. Journal of Applied Physics, 1964. **35**: p. 265.

104.   Love, J.C., et al., *Self-Assembled Monolayers of Thiolates on Metals as a Form of Nanotechnology*. Chemical Review, 2005 **105**: p. 1103-1169.

105.   Medvedovski, E. and k.M. Olsson. *Advanced indium tin oxide ceramic sputtering targets and transparent conductive thin films*. in *31st International conference on advanced ceramics and composites*. 2007. Daytona Beach, FL: The American Ceramic Society.

106.   Tjong, S.C., *Structural and mechanical properties of polymer nanocomposites*. Materials Science and Engineering R, 2006. **53**: p. 73-197.

107.   Kaneko, S. and F. Imoto, *Synthesis of Fine Grained Barium titanate by a Hydrothermal Reaction*. Nippon kagaku Kaishi, 1975. **6**: p. 985-90.

108.   Ovramenko, N.A., et al., *Kinetics of Hydrothermal Syntheiss of Barium metatitanate*. Doklady Akademii Nauk SSSR, 1979. **248**(4): p. 889-91.

109.   Qi, L., et al., *Short-range dissolution-precipitation crystallization of hydrothermal barium titanate*. Journal of the European Ceramic Society, 2004. **24**: p. 3553-3557.

110.   Nakano, H., et al., *Characterization of Internal Pores in Hydrothermally Synthesised BaTiO₃ Particle by Transmission Electron Microscopy*. Journal of the American Ceramic Society, 2004. **87**(8): p. 1594-1597.

111.   Hennings, D.F.K., C. Metzmacher, and B.S. Schreinemacher, *Defect Chemistry and Microstructure of Hydrothermal Barium Titanate*. Journal of the American Ceramic Society, 2001. **84**(1): p. 179-182.

112.   Kutty, T.R.N., R. Vivekanandan, and P. Murugaraj, *Precipitation of Rutile and Anatase (TiO₂) Fine powders and their Conversion to MTiO₃ (M = Ba, Sr, Ca) by Hydrothermal Method*. Materials Chemistry and Physics, 1988. **19**(6): p. 533-546.

113.   Chen, H.-J. and Y.-W. Chen, *Hydrothermal Synthesis of Barium Titanate*. Industrial & Engineering Chemistry Research, 2003. **42**: p. 473-483.

114.   M. Wu, et al., Journal of Material Science, 1996. **31**: p. 6201.

115.   Xia, C.T., et al., Journal of the European Ceramic Society, 1995. **15**: p. 1171.

116.   Dutta, P.K., et al., *Hydrothermal Synthesis and Dielectric Properties of Tetragonal BaTiO₃*. Chemistry of Materials, 1994. **6**: p. 1542-1548.

117.   Okuyama, M., et al., *Dispersion of silicon carbide powders in nonaqueous solvents*. Journal of the American Ceramic Society 1989. **72**(10): p. 1918-24.

118. Abel, J.S., et al., *Sedimentation in flocculating colloidal suspensions.* Journal of Materials Research, 1994. **9**(2): p. 451-61.

119. Vogel, E.M., American Ceramic Society Bulletin, 1979. **58**: p. 453.

120. R. G. Horn, Journal of the American Ceramic Society, 1990. **73**: p. 1117.

121. Patel, S.S., Annual Review of Physical Chemistry, 1989. **40**: p. 597.

122. Karas, A., T. Kumagai, and W.R. Canon, Advanced Ceramic Materials, 1988. **3**: p. 374.

123. Takabe, H., Journal of the Ceramic Society of Japan, 1992. **100**: p. 750.

124. Popielarz, R. and C.K. Chiang, *Polymer composites with the dielectric constant comparable to that of barium titanate ceramics.* Materials Science and Engineering B 2007. **139**: p. 48–54.

125. Shaikh, A.S., R.W. Vest, and G.M. Vest, *Dielectric Properties of Ultrafine Grained BaTiO₃.* ÍEEE Transactions on ultrasonics, ferroelectrics, and frequency control, 1989. **36**(4): p. 407-412.

126. Kobayashi, T., *Fabrication of high capacitance ceramic-polymer nano-composite films* Materials Forum (Advanced Materials Processing), 2005. **29**: p. 268-273.

127. Bai, Y., et al., *High-dielectric-constant ceramic-powder polymer composites.* Applied Physics Letters 2000. **76**(25): p. 3804-06.

Curriculum Vitae

AMIR HABIB

Surface Engineering Group
Functional Materials
ARC Seibersdorf, Austria
Tel.:+43-(0)50550-2737
amir.habib@arcs.ac.at
habib_amir@hotmail.com
www.arcs.ac.at
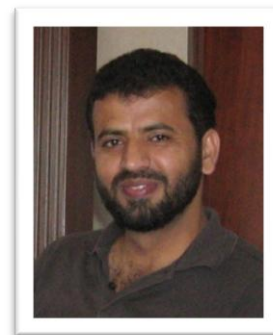
EDUCATION

Vienna University of Technology, Austria	
Ph.D. Fellow in Technical and Analytical Chemistry	**2008**
Govt. College, Lahore (PU Lahore)	
M.Sc. in Physics 1st Div	**1995**
Thesis: "Stress relaxation behavior in pure polycrystalline Titanium"	
Petroman Training Institute, Islamabad	
Diploma in Computer Application and Software 1st Div	**1993**
Govt. College, Attock (PU, Lahore)	
1. B.Sc. 1st Div	**1992**
Mathematics A&B Courses, Physics	
2. F.Sc. 1st Div	**1989**
Pre. Engg.	
F.G. Public High School, Attock	
S.S.C. 1st Div	**1987**

PUBLICATIONS

- A. Habib, R. Haubner, N. Stelzer, "*Effect of Temperature, Time and Particle Size of Ti- Precursor on Hydrothermal Synthesis of Barium Titante*", Journal of Material Science and Engineering B, Elsevier. 2008

- A. Habib, R. Haubner, N. Stelzer, "*Fabrication of BaTiO₃-PMMA Polymer Nano-composite Thin / Thick Films and their Dielectric Properties*", Oral presentation in E-MRS Fall Meeting at Warsaw University of Technology 15-19 Sept 2008

- A. Habib, R. Haubner, N. Stelzer, "*Effect of Temperature, Time and Particle Size of Ti- Precursor on Hydrothermal Synthesis of Barium Titante*", Poster presentation 4th International Workshop on Nanoscience and Nanotechnologies Thessaloniki, Greece 2007

- A. Habib, R. Haubner, Georg Jakopic, N. Stelzer: "*Synthesis of Barium Titanate (BT) via Hydrothermal Route for the production of BT-Polymer Nano Composite*", Oral presentation Sharjah. AIP Conference Proceedings (2007), 929 (Nanotechnology and Its Applications), 157-161

- A. Habib, N. Stelzer, R. Haubner:"*Hydrothermal Synthesis of Barium Titanate Temperature, Time and Particle Size of Ti-precursor Dependence*"; Poster: Nano and Photonics Mauterndorf 2006, Mauterndorf, Austria; 15.03.2006- 17.03.2006

- M. Amir, A. Habib, M.Z. Butt, A. Ul Haq: "Stress Relaxation in Titanium Polycrystals" Journal of Natural Sciences and Mathematics, vol. 37 No. 1&2 (April & October 1997) pp. 21-29

AWARDS

- 1st Prize for Poster Competition among PhD Students in Austrian Research Centers Seibersdorf, Austria	**2006**